UNIVERSITÀ
DEGLI STUDI
FIRENZE

DOTTORATO DI RICERCA IN FISICA E ASTRONOMIA

CICLO XXVIII

COORDINATORE Prof. Roberto Livi

Coevolution of black holes and host galaxies

Settore Scientifico Disciplinare: FIS/05 Astronomia e Astrofisica

Dottorando
Dott. Carniani Stefano

_____

Tutor
Prof. Marconi Alessandro

_____

Coordinatore
Prof. Roberto Livi

_____

Anni 2012/2013-2013/2014-2014/2015

Contents

List of Acronyms and Symbols

BH: super-massive Black Hole
AGN: Active Galactic Nucleus
BLR: Broad Line Region
NLR: Narrow Line Region
QSO: Quasi-Stellar Object or quasar
SF: Star Formation
SFR: Star Formation Rate
SFH: Star Formation History
LF: Luminosity Function
SMG: Sub-Millimetre Galaxies
ULIRG: Ultra Luminous Infrared Galaxy
S: flux density or intrinsic intensity in unit of Jy
S/N: signal-to-noise
SN: SuperNovae
EBL: Extragalactic Background Light
CIB: Cosmic Infrared Background
COB: Cosmic Optical Background
CMB: Cosmic Microwave Background
DM: Dark Matter
UV: UltraViolet
IR: Infrared
ISM: Inter-Stellar Medium
IGM: Inter-Galactic Medium
FIR: Far-Infrared
SED: Spectral Energy Distribution
ALMA: Atacama Large Millimetre/submillimetre Array
VLT: Very Large Telescope
SINFONI: Spectrograph for INtegral Field Observations in the Near Infrared
SDSS: Sloan Digital Sky Survey
WISE: Wide-field Infrared Survey Explorer
2MASS: Two Micron All Sky Survey

Introduction

One of the most important astronomical discoveries of the last 20 years is that most local massive galaxies host a supermassive black hole (hereafter BH), with mass of $\sim 10^6 - 10^{10}$ $M_\odot$, in their centre.

The most relevant discovery supporting a connection between a BH and its host galaxy is the tight correlation between the BH mass and the velocity dispersion of the stars in the bulge, which corresponds to the whole galaxy for the elliptical ones. Together with similar correlations with bulge luminosity and mass, this led to the belief that BHs and bulges coevolve by regulating each other's growth. However, the difference of nine orders of magnitude between the typical spatial scales of BHs and bulges seems to preclude a direct casual connection.

What makes the study of the coevolution scenario very appealing to the astronomical community is the fact that the nature of this mechanism is still little understood.

Many processes have been proposed to unveil the connection between these two classes of objects, including galaxy major mergers, star-formation winds, and AGN-driven outflows. Although there are clear evidences for many of these processes, we are still trying to figure out which is the engine driving the overall BH-galaxy growth. An important factor is the impact that the energy released by accretion has on the surrounding gas. In fact, a growing BH releases plenty of energy into the host galaxy: the thermal energy of the host gas in a 10^{13} $M_\odot$ dark-matter halo is 10^{61} erg, while the total accretion energy for a 10^9 $M_\odot$ BH is 10^{62} erg. The Active Galactic Nucleus (AGN) should, therefore, be able to disrupt its surrounding environment and to regulate both its own growth and the star formation activity in the host galaxy.

One possible evolutionary path suggests that major-merger processes or galaxy interactions modify the gravitational potential so that the gas is driven into the central region through a series of gravitational instabilities that help overcoming the gas angular momentum conservation. In this scenario the AGN is obscured by the surrounding gas that accretes onto the central BH. The BH grows until the energy released by accretion is large enough to unbind the gas not only from the host galaxy, but from the entire surrounding halo. This so-called "negative feedback" is responsible for the observed BH-galaxy correlation since it shuts down both BH growth and that of its host galaxy. This mechanism would be an important physical process to understand the BH-galaxy co-evolution, but there are no clear evidences for it in the local Universe.

The goal of this thesis is a comprehensive investigation of the BH-galaxy coevolution over cosmic time and, in particular, of the main processes connecting a BH to its host galaxy. To analyse the evolution of star-forming galaxies over the cosmic history, we made use of data obtained at different wavelength ranges thanks to the new generation telescopes, such as the astronomical interferometry Atacama Large Millimetre/submillimetre Array (ALMA). In the last three years ALMA has shown its capabilities in detecting and resolving sources at high redshift permitting the observation of dusty obscured regions in the Universe that are usually not detectable by optical facilities. In addition to millimetre observations, we took advantage of images obtained with the Spectrograph for INtegral Field Observations in the Near Infrared (SINFONI). In the last 5 years integral field unit observations have played a relevant role, showing kpc-scale energetic outflows in a non-negligible fraction of the galaxy population at high-redshift. The aim of SINFONI observations was to constrain AGN-driven outflow properties. Since models and observations predict that most powerful AGN and outflows should be observed at high redshift, we focused only on sources lying at redshift $z > 2$.

This Phd thesis therefore addresses the following topics:

- Dusty, star-forming galaxies play an important role in the assembly of stellar mass and the evolution of massive galaxies. Far-infrared and millimetre wavelength surveys have established the properties of bright galaxies belonging to this dusty population, but the characteristics of the faint population are still unknown. We exploited the deepest ALMA observations to detect faint, dusty, star-forming galaxies aiming at determining their role in galaxy evolution by comparing the millimetre number counts with predictions from recent models.

- Although bright starburst galaxies are not representative of the bulk of the star-forming galaxy

population, they may indicate a key phase between spiral and passive elliptical galaxies. To test this scenario, we analysed the [CII] emission lines in BR1202-0725, a major-merger system composed by a bright submillimetre galaxy and a quasar, both characterised by a high star formation rate. The kinematics of [CII] allows to determine which is the origin of the starburst activity. Moreover, this system is one of the few where we can observe the presence of galaxies in different phases of evolution in the same environment.

- Finally, in the last part of this thesis we focused on revealing a clear proof of "negative feedback". We analysed the ionised outflows in six luminous quasars ($L > 10^{46}$ erg/s) and their interaction with the host galaxies. Constraining the properties of ionised outflows may help to understand the mechanisms leading to AGN-driven outflows .

In summary, in this thesis we made use of facilities at different wavelengths targeting high-z galaxies in different phases of the galaxy evolution track, with the aim on shedding light on the BH-galaxy coevolution puzzle.

Chapter 1

Black Holes and Galaxies Evolution

Super-massive ($> 10^6$ $M_\odot$) black holes (BHs) are ubiquitous at the centre of galaxy bulges. The closest BH is in the centre of our Galaxy, the Milky Way, and it was discovered with measurements of stellar orbits close to Galactic centre. Our knowledge of BHs has increased over the last decades thanks to the development of modern and more sensitive instruments, which have allowed deep sky investigations. One of the main discoveries obtained from extensive studies of such kind of objects is that BHs are no mere ornaments of galaxies, but plays a crucial role in the host galaxy evolution process. As a matter of fact, coevolution of BHs and host galaxies is invoked by models to explain the results from large surveys carried out in the local Universe. Indeed, the properties of BHs and local galaxies suggest that the evolution of these two populations is driven by a series of interlinked physical processes. Recent multi-wavelength observations of neutral and ionised fast winds produced by BH accretion mechanisms and able to quench star formation in host galaxies support the coevolution scenario. However, at the moment, the main physical mechanisms connecting the two populations are still largely unknown.

In this Chapter, I will provide an overview of the essential scientific context that is necessary to understand the BH-galaxy coevolution paradigm. In Section 1.1, I will present the main properties of galaxy populations supporting the hypothesis that Active Galactic Nuclei (hereafter AGNs) have an impact on their host galaxy and hence are related to galaxy formation. Then I will describe the different classes of AGNs (Section 1.2) and the observed correlation with host galaxies (Section 1.3). Finally in Section 1.4 I will present the model predictions regarding BH and host galaxy coevolution explaining how AGNs interact with their surrounding environment.

1.1 Galaxy Properties

A galaxy is a dynamically bound system consisting of stars, gas, dust and dark matter. Galaxies can be either isolated or gravitationally bound in groups (< 100 galaxies) or cluster ($\sim 100 - 1000$ galaxies). They can be classified and studied according to different physical properties like luminosity, size, mass, morphology, colour, age of the stellar population, nuclear activity. These properties of galaxies are fundamental for understanding their formation and evolution.

1.1.1 Hubble Tuning Fork Diagram

The first classification of galaxies ever proposed, still currently in use, is based on their morphological properties and was made by Edwin Hubble in 1936. Hubble classified galaxies into three main categories that populate the so called Hubble sequence (Figure 1.1):

- Ellipticals. As suggested by their name, these galaxies are characterised by an elliptical shape. They are usually labelled as E# with the number # describing their ellipticity, which is defined as $1 - (b/a)$ where b, a are the semi-minor and the semi-major axis, respectively.

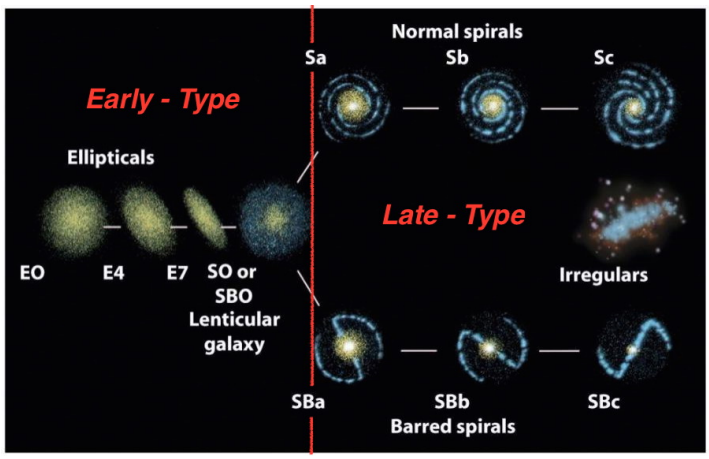

Figure 1.1: Hubble's tuning-fork diagram. Galaxies are classified depending on their morphology. E, S SB denote elliptical, spiral, and barred spiral galaxies, respectively. For the ellipticals, numbers from 0 to 7 refer to the increasing ellipticity of the galaxy. For Spirals and Barred Spirals letters a,b, and c indicate how tight around the bulge the spiral arms are and how prominent the bulge is. S0 and SB0 (usually named Lenticulars) are galaxies with intermediate properties falling between those typical of Ellipticals and Spirals. Ellipticals and Lenticulars are also known as early-type galaxies, while Sprials, Barred Sprials, and Irregulars are named late-type galaxies.

- Spirals. This class of galaxies, named after the spiral structures extending from their centre towards the disk, includes the following sub-categories: S0, Sa, Sb, and Sc. As a matter of fact, S0 is now separate from the actual spiral class since it includes objects with properties in between those of ellipticals and spirals. For actual spiral galaxies, the lower-case letter (a,b,c) is directly connected to the spiral structure itself.

- Barred Spirals. These objects are like spiral galaxies but also show a central bar-shaped structure. They are usually labelled SB galaxies with SB0 (or lenticular galaxy) indicating an intermediate galaxy between elliptical and proper SB galaxies. As for regular spirals, a lower-case letter is used to indicate the morphology of the spiral structure.

Through the years, Hubble's classification has been modified to include also irregular (Irr) galaxies, that, as suggested by their name, have no regular shape.

Hubble originally identified an evolutionary sequence for the galaxies from "early" to "late" type from left to right across the diagram, respectively. Although this is now known to be not correct, the terms "early-type" and "late-type" are still used on a regular basis in order to distinguish Ellipticals and Lenticulars from Spirals (including the barred ones) and Irregulars. In conclusion the Hubble sequence is not a evolutionary sequence, but is a galaxy classification based on morphological properties (Baldry 2008).

With the advent of colour measurements[1] ,,,, morphology-colour relations were established. Holmberg (1958) showed that E and S0 are redder than S and Irr, and the trend from red to blue is nearly monotonic along the Hubble sequence (from left to right).

Photometric and spectroscopic observations revealed that stars in Ellipticals and Lenticulars are predominately old, move in random orbits, and have a large range of inclinations and eccentricities. Measurements reveal that elliptical galaxies come in a large range of sizes, from the rare giant ellipticals found in the centres of galaxy clusters and stretching over hundreds of kpc with mass up to 10^{13} $M_{\odot}$, to the very common dwarf ellipticals which may have diameters as small as 0.3 kpc with mass of 10^{7} $M_{\odot}$. Ellipticals are gas poor systems suggesting that they have passed the star formation epoch and most of the gas has already been used to form stars. Indeed, most massive galaxies observed in the Local Universe are Ellipticals with low star formation activity. Spiral galaxies consist in flat, rotating

[1]The colour of a galaxy is defined as the difference between the magnitude in two different passbands. The colour depends mainly on the stellar population dominating the galaxy itself (e.g. red colours indicate passive-evolving galaxies with old stellar populations while blue colours are associated to star formation activity.)

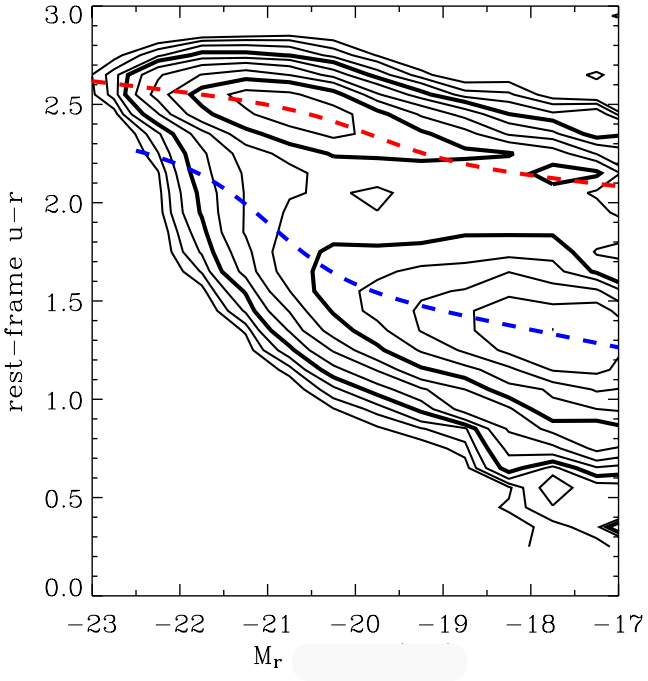

Figure 1.2: Colour-magnitude distributions by Baldry et al. (2004). The colour-axis is defined as the difference between the magnitude in the u (~ 365 nm) and r-band (~ 658 nm). The contours are in a logarithmic scale of number density and the dashed lines represent the colour-magnitude fitted relations of the red and blue sequences. Galaxies on the red sequence (top line) are more luminous, more massive, and redder than those on the blue sequence (bottom line).

discs containing stars, gas, dust and showing the characteristic arms, plus a structure located in the centre known as bulge. Spiral arms are regions of intense star formation and, hence, are populated by young blue stars. On the other hand, the bulge lacks in gas and is dominated by old red stars. The spectral emission of a spiral galaxy is dominated by the light emitted from the young blue stars and it appears bluer than that of elliptical galaxies. Spiral mass spans a range of 10^9 – 10^{12} $M_\odot$, with disk diameters from 5 to 100 kpc. Finally, irregular galaxies have ongoing star formation activity and are composed of young stellar populations. Irregular galaxies are on average smaller (1-10 kpc) and less massive than Spirals and Ellipticals, with masses in the range 10^8 – 10^{10} $M_\odot$. The lack of a regular velocity profile as a function of distance from the centre make difficult any guess on whether or not this type of galaxies are surrounded by a dark matter halo.

To summarise, late-type galaxies are characterised by a blue colour associated with young stellar population, while early-type galaxies are red and show the presence of old stellar populations.

1.1.2 Bimodality Distribution

About 80 years after Hubble's first galaxy classification, Baldry et al. (2004) identified two separated and distinct populations analysing the distribution in colour versus absolute magnitude[2] of a sample of galaxies at $z \lesssim 0.1$ from the Sloan Digital Sky Survey (SDSS) [3]. As shown in Figure 1.2, the galaxies are divided into two well separated populations: the blue and red sequence. The former mainly includes S and Irr galaxies, while the latter is dominated by E and S0 galaxies. Briefly:

- the blue sequence, also known as blue cloud, consists mostly of star-forming, low-mass galaxies

[2]The absolute magnitude of a galaxy is the magnitude of the galaxy would have if it was placed at a distance of 10 parsecs from Earth.

[3]The SDSS is a major multi-filter imaging and spectroscopic redshift survey carried out with a dedicated 2.5-m wide-angle optical telescope located at the Apache Point Observatory in New Mexico (USA).

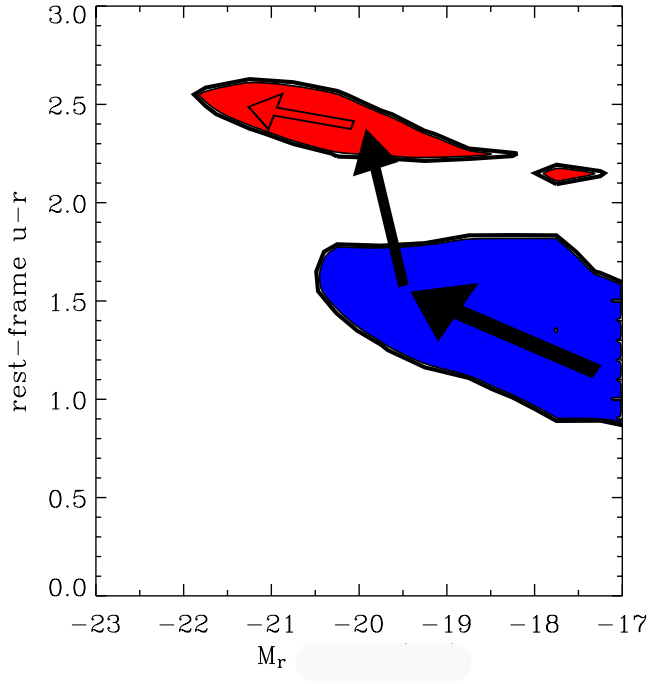

Figure 1.3: Schematic picture of galaxy evolution. Evolutionary tracks are plotted on the colour-mass diagram. A galaxy evolves over the blue sequence increasing its mass. The black solid arrows tracks the quenching mechanism which moves the galaxy from the main sequence to the red sequence. In order to obtain a bi-modal distribution the quenching tracks should last 1-2 Gyr (Newberry et al. 1990; Barger et al. 1996; Poggianti et al. 1999). Once a galaxy reaches the red sequence, it may evolve slowly along it (open arrows).

which are disc-dominated;

- the red sequence consists mostly of high-mass spheroidal galaxies with little or no star formation activity, usually known as “red and dead” galaxies.

To a more careful analysis, the colour-magnitude distribution showed a intermediate region, called the “green valley”, hosting a transition population between the blue cloud and the red sequence galaxies (e.g. Bell et al. 2004; Faber et al. 2007; Martin et al. 2007; Schiminovich et al. 2007; Wyder et al. 2007; Mendez et al. 2011; Gonçalves et al. 2012). The shortage of galaxies in this region suggests a fast transition between blue and red sequence, otherwise there would be no observed bi-modal distribution (Faber et al. 2007; Martin et al. 2007). However, it is still unclear whether there exists a connection between star-forming galaxies and read-and-dead ones.

The existence of the bi-modal distribution could be explained by a rough picture of galaxy evolutionary tracks (e.g. Faber et al. 2007; Lilly et al. 2013), as showed in Figure 1.3. A typical galaxy evolves along the star-forming sequence, increasing mass through the accretion of cold gas from the cosmic web and through mergers with other galaxies. As it reaches a critical mass, the star formation is strongly reduced, the supply of gas is shut off, and the galaxy then evolves into the passive population. Some works (Newberry et al. 1990; Barger et al. 1996; Poggianti et al. 1999) found that stellar populations become red enough to join the red sequence just $\sim 1-2$ Gyr after the star formation activity stopped. Such a short time scale explains the shortage galaxies in the green valley region. Faber et al. (2007) suggested that there are three mechanisms leading to migration: (i) the quenching of star formation in blue galaxies, (ii) the merging of less luminous already quenched red galaxies, or (iii) some combination of the two. Once a galaxy evolves into a read-and-dead elliptical, it has to remain in the red sequence population. The request for the galaxy to stay in the red sequence is that the star formation remains low.

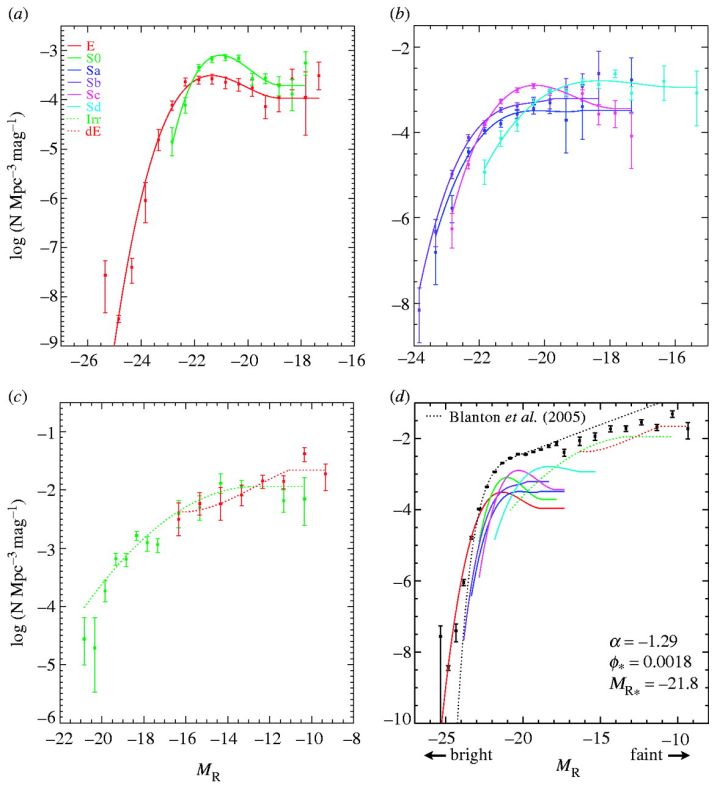

Figure 1.4: Spline-fit of the luminosity function for different Hubble types of galaxies (colour-coded as in the legend on the top left panel): (a) Elliptical and S0, (b) Spirals (c) irregulars and (d) combined luminosity function. The combined luminosity function in the bottom right panel. The dotted line in the (d) panel is a Schechter function by Blanton et al. (2005), whose parameter are listed in the bottom right corner of the panel. The x and y-axis indicate the logarithm of number of galaxies (N) per Mpc^3 per magnitude (mag) and the magnitude in the R-band (~ 658 nm), respectively. Figure by Read & Trentham (2005).

So far it is still debated what is this the mechanism able to halt star formation and whether the mass scale at which quenching occurs pertains to the stellar mass or the dark matter halo mass.

1.1.3 The Luminosity and Stellar Mass Function of Galaxies

The luminosity of galaxies spans a very wide range of values, but astronomical observations have revealed that, at a fixed redshift, the number of galaxies with lower luminosity is larger than that of bright galaxies.

The galaxy luminosity function (hereafter LF) Φ(L) is defined such that Φ(L)dLdV is the number of galaxies with luminosities between L and L+dL within a co-moving volume element dV. Figure 1.4 shows the LFs for the different classes of galaxies in the Hubble sequence obtained from all SDSS galaxies and those in nearby groups (Trentham & Tully 2002; Trentham & Hodgkin 2002; Trentham et al. 2005). The LF is very steep at bright luminosities and has a significantly flatter faint end.

Globally the LF is well described by the Schechter parametrisation (Schechter 1976):

$$\Phi(L)dL = \Phi_0 \left(\frac{L}{L_0}\right)^{\alpha} e^{-\frac{L}{L_0}} \frac{dL}{L_0}, \tag{1.1}$$

where Φ_0 is a normalisation factor, α is the slope at the faint end, and L_0 indicates a cut-off for bright galaxies over which the number density drops exponentially. At $L < L_0$, i.e. at low luminosities, the function is described by a power-law with slope α, i.e. $\Phi(L) \propto L^{\alpha}$, that means that galaxies with lower luminosities are more common. At $L > L_0$, i.e. at high luminosities, the function is represented by an exponential cutoff in the form $\Phi(L) \propto e^{-L}$, which means that very luminous galaxies are rare. The

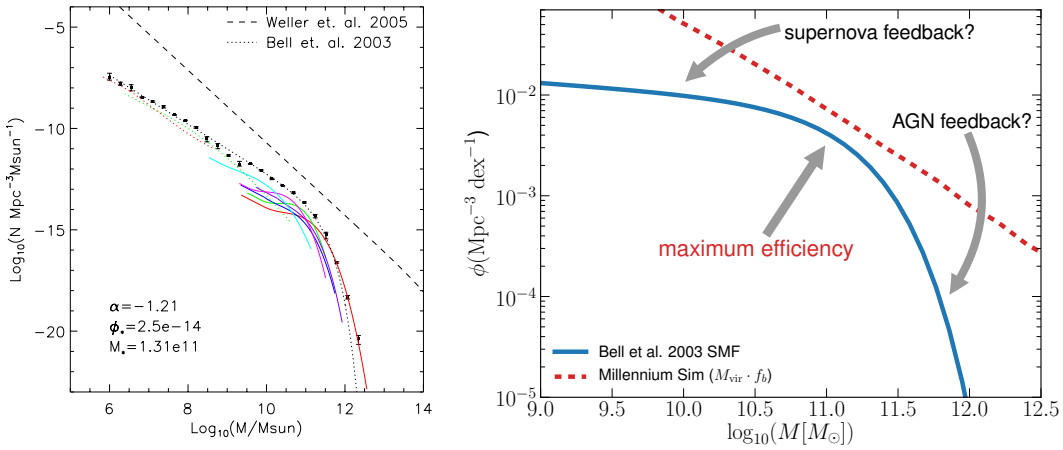

Figure 1.5: Galaxy mass function. *Left panel*: Spline fits split by Hubble sequence (colour-coded as in the legend in the upper left panel of Figure 1.4). The Cosmic Dark Matter mass spectrum from the numerical simulations by Weller et al. (2005) is also shown in dashed black line. Figure by Read & Trentham (2005). *Right panel*: Comparison of the observed galactic stellar mass function (blue solid line; Bell et al. 2003) and the halo mass function from the Millennium Simulation (red dashed line; Springel & Hernquist 2003). The halo mass function has been multiplied by the universal baryon fraction in order to demonstrate the maximum possible stellar mass content as a function of halo mass. The closer the stellar mass function to this line, the more efficient the star formation activity in halos with that mass. If galaxies were to form stars with a fixed efficiency at all halo masses, then the slope of the stellar mass function would be identical to that of the halo mass function. Slopes that are different both in the high and low masses regime indicates that the star formation (as a function of halo mass) is less efficient in these regimes. At low masses, this is commonly attributed to efficient gas ejection due to supernova feedback, whereas at high masses energy injection from central super-massive BHs is thought to be able to effectively reduce the efficiency of gas cooling. However, it should be noted that many other physical processes could have a non-negligible contribution in both regimes. Figure by Mutch et al. (2013).

equation 1.1 can be also expressed in terms of magnitude:

$$\Phi(M)dM = 0.4\ln(10)\Phi_{M_0}10^{0.4(M_0-M)^{1+\alpha}}e^{-10^{0.4(M_0-M)}}dM.$$

Typical values for α lie in the range $-1.5 < \alpha < -1$, so integrating over all luminosities the total number of galaxies diverge, but the total luminosity $\int L\Phi(L)dL$ remains finite.

Since the total luminosity of a galaxy is proportional to its stellar mass, we can derive the stellar mass distribution of galaxies, usually known as galaxy mass function. The analysis of the galaxy mass function allows us to estimate the average mass of a galaxy population and to infer an upper limit for the massive galaxy. The mass-to-light ratio (M/L) is, in general, a function of galaxy type, age, metallicity, and luminosity. From the M/L of each type of galaxy we can derive the global galaxy mass function as the one shown in Figure 1.5 (Read & Trentham 2005). The galaxy mass distribution is characterised by slopes that are similar to those of a LF with a steep bright-end distribution and a flatter faint-end profile. Moreover, it is generally parametrised with a Schechter function, as done for the LF.

As mentioned above, the density of galaxies increases with decreasing luminosity and a steep faint-end slope is a general prediction of a galaxy formation models based on hierarchical clustering (White & Rees 1978; Kauffmann et al. 1993; Cole et al. 1994). Assuming that the dark matter interacts gravitationally with itself and is not subject to any dissipative force, dark matter halos form hierarchically, i.e. the small ones form first and then aggregate into progressively larger system. The baryonic matter, i.e. gas, gravitationally coupled with dark matter, collapses to the halo centre due to gravitational instability. The gas cools via radiative processes during the collapse and eventually settles into centrifugal equilibrium at the centre of the halo potential-well, forming a rotationally supported disc of gas provided that some angular momentum is retained during the collapse. The cold dense gas that accumulates at the centre of the halos starts to form stars. Massive galaxies grow by merging of

individual galaxies. However the only hierarchical mechanism of accretion is not sufficient to explain the drop of the LF at bright luminosities. White & Rees (1978) argued that an additional process, feedback, was needed to make small galaxies more diffuse so that they would be less successful at surviving the merging process, thus avoiding the production of more faint galaxies than are observed.

The dotted line in the left panel of Figure 1.5 corresponds to the Cosmic Dark Matter (hereafter CDM) mass function obtained from simulation (Weller et al. 2005). The halo mass function has been multiplied by the universal baryon fraction in order to demonstrate the maximum possible stellar mass content as a function of halo mass. The normalisation for the baryonic component in galaxies is much lower, reflecting the fact that galaxy masses are dominated by dark matter ($> 90\%$), not baryons. Additionally, the mass function has a very different shape from the CDM one as we observe in the right panel of Figure 1.5 as well. The discrepancy between these two profile at both low and high masses suggests that the efficiency of star formation is lower in these regimes. At the faint end, where galaxies are heavily dark-matter dominated, the baryonic distribution is flatter than that of the CDM. This is the famous missing satellites problem: a disagreement between the expected and observed number of dwarf galaxies around the Milky Way and Andromeda (Kauffmann et al. 1993; Klypin et al. 1999). Recent results suggest that the shallow gravitational potential provided by the dark matter halos allows supernovae[4] to efficiently eject gas and dust away from the galaxy, slowing the star formation activity. In addition to supernovae, the intergalactic medium (IGM) is heated by stellar photoionisation reducing the efficiency of star formation in this regime (Benson et al. 2002 and references therein). For massive halos the situation is slightly more complicated, the LF is steeper than the CDM one, indicating that there is a "powerful" mechanism capable of preventing the formation of massive galaxies. The energy released by supernovae or injected by stellar photoionisation is not sufficient to overcome the dark matter gravitational potential. Recent models (see references in Section 1.4) claim that the energy released by BH accretion mechanisms could contrast the gravitational potential and sweep up the interstellar gas from the host galaxy, quenching the star formation. This mechanism slows the growth of massive galaxies and may explain the drop in the LF (or in the galaxy mass function) in the bright luminosities regime. Objects hosting an accreting BH are called Active Galactic Nuclei (AGNs) and will be discussed in detail in Section 1.2.

1.1.4 Star formation rate and Main sequence

The star formation rate (hereafter SFR) of a galaxy depends on the amount of gas converted into stars in a given time and is usually measured in unit of solar masses per year ($M_\odot$/yr). Ground-based and space-based surveys over a wide redshift range have revealed that the star formation history (SFH) of the Universe is a rapidly changing quantity. In detail, the cosmic star formation rate density reaches a maximum around $1 < z < 3$ and steeply declines towards higher and lower redshift (Lilly et al. 1996; Madau et al. 1996). Questions on the main drivers of this rapid evolution are still raised and finding an answers to them is at the forefront of new studies.

One insightful finding, revealed by comparing the SFRs of galaxies with different stellar masses (hereafter $M_\star$), is the distribution of galaxies on the SFR-$M_\star$ plane, a valuable clue to trace the evolution of galaxies during cosmic time. Deep multi-wavelength extragalactic surveys have revealed that star-forming galaxies follow a tight correlation between their $M_\star$ and SFR (Figure 1.6). This correlation, usually known as "galaxy main sequence", has been established from the local to the high-z Universe (e.g. Brinchmann 2004; Daddi et al. 2007; Pannella et al. 2009; Peng 2010; Rodighiero et al. 2010, 2011) and it is usually expressed as:

$$Log_{10}(SFR) = \alpha(Log_{10}M_\star - 10.5) + \beta$$

where α and β are the slope and normalisation factor, respectively. It is well established that β depend on redshift. The normalisation parameter reaches its maximum at $z \sim 2-3$ (Karim et al. 2011) when the cosmic SFR density peaks (Lilly et al. 1996; Madau et al. 1996), and remains roughly

[4] A supernova is a stellar explosion that releases a large amount of energy ($E \sim 10^{51}$ erg/s)

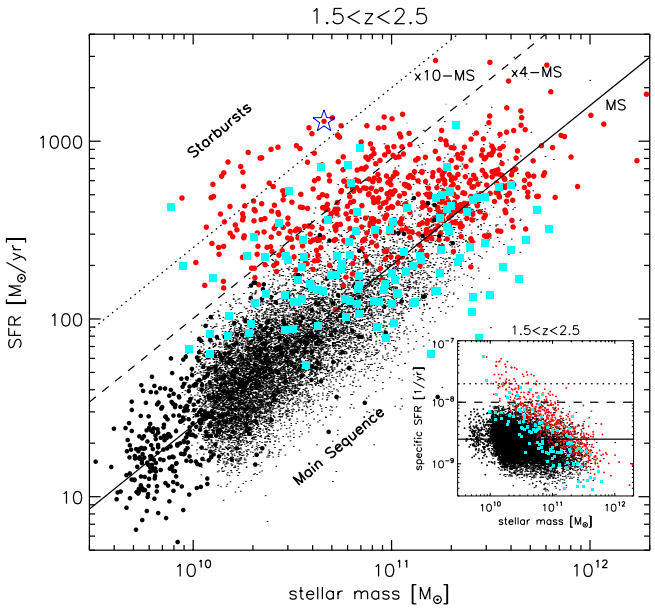

Figure 1.6: Stellar mass-star formation rate (SFR-$M_\star$) plane at $1.5 < z < 2.5$ (Rodighiero et al. 2011). Different colours and symbols refer to different samples of galaxies. The solid black line indicates the main sequence for star-forming galaxies at $z \sim 2$ defined by Daddi et al. (2007), the dotted and dashed ones mark the loci 10 and 4 times above the main sequence, respectively.

constant up to $z \sim 7$ (González et al. 2010). The slope parameter α spans a range between ~ 0.6 and ~ 1 and recent studies claim it to be redshift-dependent (Karim et al. 2011; Whitaker et al. 2012). Since both α and β depend on redshift, we observe that, for a fixed stellar mass, the SFR decreases at a steady rate by a factor of $\sim$30 from $z \sim 2$ to $z = 0$ (Daddi et al. 2007).

Both the slope and the normalisation factor of the galaxy main sequence play a crucial role in the growth of galaxies and in the evolution of their mass function (Renzini 2009; Peng 2010). The tight correlation suggests that star formation is regulated by the balance between the rate at which cold gas is accreted onto galaxies and feedback mechanisms (Dutton et al. 2010; Bouché et al. 2010)

Starburst Galaxies

Not all galaxies lie on the Main Sequence. Starburst galaxies have, indeed, a significantly higher star formation activity compared to normal galaxies on the main sequence. In the SFR-$M_\star$ plane the starburst population lies well above the main sequence as shown in Figure 1.6. Observational results have established that starburst galaxies are predominantly driven by galaxy merging (Sanders et al. 1988) in contrast with smooth accretion for galaxies on the main sequence (e.g. Daddi et al. 2010). The merging of galaxies is an alternative and turbulent way for the gas-supply, and it occurs when two galaxies gravitationally interact with each-other. If the two galaxy have similar dynamical mass, we refer to a major-merger event, while all the other cases are grouped under the minor-merger class. During a major-merger event the large amount of gas leads to a starburst with SFR higher than 1000 $M_\odot$/yr

High luminosity, local starburst galaxies are the so-called Ultra-Luminous Infrared Galaxies (ULIRGs) while at high-z starburst galaxies are called Sub-Millimetre Galaxies (SMGs). These names come from the high luminosity ($> 10^{12}$ $L_\odot$) at infrared (ULIRGs) or millimetre wavelengths (SMGs). Both ULIRGs and SMGs are mostly driven by interactions between systems (Engel et al. 2010). As mentioned above ULIRGs and SMG do not lie over the main sequence: for a fixed stellar mass the SFR of a starburst galaxy is at lest 10 times larger than the one measured for a typical main sequence galaxy (Figure 1.6). If starburst galaxies continue to form star at the currently observed rate, they will exhaust the entire supply of star-forming material, i.e. gas and dust, over a short time scale. For sake of clarity

we recall that in typical starburst galaxy, the gas depletion time scale is shorter than 10^8 years, that is less than 1% of the age of the Universe.

Since the existence of the main sequence suggests a secular trend, the question is whether starburst galaxies contribute a significant fraction to the global SFR at different epochs. Several studies have revealed that major mergers are relatively unimportant for the formation of stars (Robaina et al. 2009; Elbaz et al. 2011; Rodighiero et al. 2011). At $z \sim 2$, where the SFR density is peaked, starburst galaxies seem to contribute to $\sim$ 10% of the total cosmic star formation rate. However, this merging-driven starburst may be a crucial phase for the transformation of star-forming galaxies into passive ellipticals. Massive starbursts at high redshifts, triggered by major mergers and thereby shaping their elliptical morphologies are hence likely the progenitors of the earliest massive quiescent galaxies observed in the local Universe. It is a open question if the number densities of both population match. Moreover, the time life of a starburst is similar to that inferred for the green valley population, suggesting that these galaxies lie on the intermediate region of the bi-modality distribution observed in the local Universe. Hence, we consider that off-sequence galaxies are likely to be crucial objects for our understanding galaxy formation and evolution.

The search for extreme starbursts at high redshifts is also motivated by the fact that their high SFRs (typically several hundreds of solar masses per year) may give rise to a significant contribution to the global SFR density at z> 2. Given their large dust reservoirs there might more dust-obscured star formation activity happening in the early Universe than what is currently assumed (Michałowski et al. 2010). Explaining how the large amounts of interstellar dust observed in these extreme starbursts have been produced at such early time is an ongoing challenge (e.g. Michałowski et al. 2010; Dwek et al. 2011).

1.2 Active Galactic Nuclei

In addition to starburst galaxies, another exotic galaxy population consist in the active galaxies, i.e. luminous galaxies hosting an AGN in their centre.

In detail, an AGN is a compact, bright region at the centre of a galaxy whose luminosity (L $> 10^{40}$ erg/s) cannot be attributed to star emission. Galaxies hosting an AGN are generally referred to as "active galaxies" and host a massive accreting BH with Eddington ratio exceeding the limit of $L_{\rm AGN}/{\rm L_{edd}} = 10^{-5}$ (Netzer 2015), where $L_{\rm AGN}$ is the bolometric luminosity of the AGN and $\rm L_{edd}$ is the Eddigton luminosity[5]

The AGNs are the most luminous, compact sources known in the Universe. The typical bolometric luminosity of an AGN (hereafter $L_{\rm AGN}$) spans in a range from 10^{40} erg/s to 10^{47} erg/s and, in some cases, the emitted energy at visible wavelengths ($\lambda \sim 390-700$ nm) is brighter than the energy emitted by all of the stars in the galaxy (i.e. $\sim 10^{44}$ erg/s). Even though the spectral energy distribution (hereafter SED) depends on the specific type of AGN we are observing, all of them show an emission spread widely across the whole spectrum, often peaked in the ultraviolet (UV; $\lambda \sim$ 10 - 320 nm) with significant contribution on the X-ray ($\lambda \sim$ 0.003 - 10 nm) and InfraRed (hereafter IR; $\lambda \sim$0.75 - 300 μm) domain.

Based on the form of the energetic output, the population of AGN can be divided in two main groups: "radiative mode" and "jet mode" AGN (Antonucci 2012; Heckman & Best 2014).

- **Radiative mode.** Most of the energetic output is emitted by the AGN in form of electromagnetic radiation produced by mass accretion into the central BH. Active galaxies hosting this type of AGN are called Seyferts or quasars (hereafter QSOs) and have an Eddington ratio $\gtrsim$0.01. Most of radiative-mode AGN are radio-quiet; namely, a radio-quiet source is an astronomic source having a ratio of radio, 5 GHz, to optical, B-band (λ = 444 nm), flux $F_{\rm 5GHz}/F_{B-band} \leq$ 10 (Kellermann et al. 1989). Only a small fraction ($\sim$ 10%) of these sources are radio-loud

[5]The Eddigton luminosity is the maximum luminosity that an astronomic source can achieve to guarantee an hydrostatic equilibrium between the force of radiation acting outward and the gravitational force acting inward.

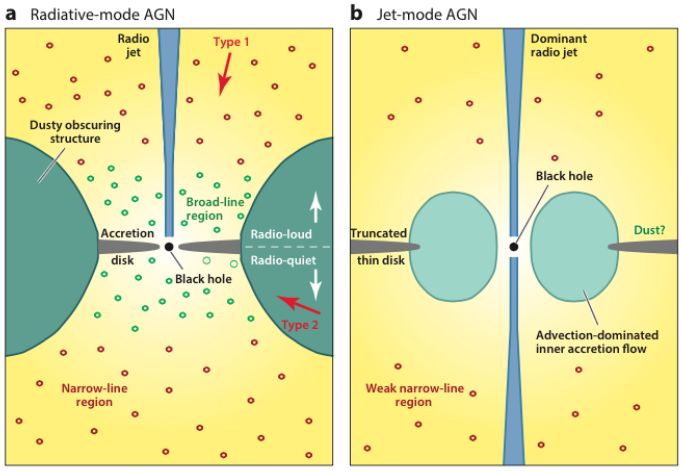

Figure 1.7: Schematic picture of the central AGN structure. The scheme is not to scale. *Left panel*: Radiative-mode AGNs are characterised by a geometrically thin, optically thick accretion disk, reaching into the radius of the innermost stable orbit around the central supermassive black hole. Luminous UV radiation from this accretion disk illuminates the broad-line and narrow-line emission regions. An obscuring structure of dusty molecular gas prohibits direct view of the accretion disk and broad-line regions from certain lines of sight (Type 2 AGN), whereas they are visible from others (Type 1 AGN). In a small proportion of sources (predominantly toward the high end of the range of black hole masses), powerful radio jets can also be produced. *Right panel*: In jet-mode AGNs the thin accretion disk is replaced in the inner regions by a geometrically thick advection-dominated accretion flow. At larger radii (beyond a few tens of Schwarzschild radii, the precise value depending upon properties of the accretion flow, such as the Eddington-scaled accretion rate), there may be a transition to an outer (truncated) thin disk. The majority of the energetic output of these sources is released in bulk kinetic form through radio jets. Radiative emission is less powerful, but can ionise weak, low-ionisation narrow-line regions, especially where the truncation radius of the thin disk is relatively low.

($F_{5\mathrm{GHz}}/F_{B-band} \geq 10$) showing a collimated, relativistic radio jet. Left panel of Figure 1.7 shows a schematic drawings of radiative-mode AGN. A geometrically thin, but optically thick, accretion disk is located around the central BH which an inflow occurs. The accretion disk has a radial temperature gradient and emits a thermal continuum radiation from the UV to the optical band. The accretion disk is surrounded by a hot corona that Compton-up-scatters the soft photons from disk into the X-ray regime. The X-ray spectral energy distribution is, then, modified, through fluorescence and reflection off the accretion disk. The radiation from the disk and corona heats and photoionises the dense gas clouds ($n_{\mathrm{H}} = 10^{9.5} - 10^{13}$ cm^{-3}) located on scales of light-days to light-years for the centre. The heated clouds emit UV- optical-, and near-IR-permitted emission lines, while forbidden emission lines are collisionally de-excited. Since the orbital speed of a cloud increase as the distance from the central BH decreases, the gas velocity in this region is several thousands of kilometres per seconds leading a Doppler broadening (FWHM > 5000 km/s) of the permitted emission lines. This region surrounding the BH and accretion disk and filled by dense, fast gas clouds is called the Broad Line Region (hereafter BLR). BH, accretion disk and BLR are surrounded by an optically thick torus of molecular gas and dust grains. The UV/visible emission from the accretion disk and the soft X-rays from the corona are absorbed by dust, and are re-emitted at the IR wavelengths as thermal emission. The internal radius of the torus is set at a distant such that the dust temperature is below the sublimation temperature[6](T_{sub}), which depends on the properties of the dust, i.e. grain size and composition, (e.g. the sublimation temperature for silicate is $T_{\mathrm{sub}} \simeq 1400$ K). From Barvainis (1987) and Netzer (2015), we can estimate the minimum radius where a grain can survive the local radiation field:

[6]the maximum temperature attend by a dust grain before it evaporates

$$R_{\rm sub} \simeq 1.3 L_{46}^{0.5} \left(\frac{1500}{T_{\rm sub}}\right)^{2.6} f(\theta) \quad pc, \tag{1.2}$$

where $L_{46} = L_{\rm AGN}/10^{46}$ erg/s and $f(\theta)$ is the angular term that depend on the anisotropy radiation of the central source (Netzer & Trakhtenbrot 2014). Assuming $L_{46} = 1$ and $f(\theta) = 1$, we infer an inner radius of the torus of $\sim$ 1.6 pc. The inferred total column density of these structures is $N_H \sim 10^{23} - 10^{24}$ cm^{-2} and, in the extreme case of $N_H \sim 10^{25}$ cm^{-2} , the torus is even able to absorb X-ray photons with energy > 10 keV. In this latter case, AGN are defined Compton-thick. Because of the shape of the torus, most of the AGN radiation emitted along the plane of the disk is absorbed by surrounding dust, while the radiation emitted along the polar axis photoionizes gas up to few thousands parsecs. The region ionised by AGN continuum emission has a bi-conical shape. The gas located within ionisation cones is less dense than that composing the BLR and the efficiency of the electron collisions is not sufficient to de-excite the forbidden emission lines that emit mainly in a radiative manner. These external regions are characterised by permitted and forbidden emission line with FWHM< 1000 km/s, and are hence called Narrow Line Regions (hereafter NLR).

Based on the torus inclination with respect to the line of sight, the SED changes its profile. Observing face-on AGN, i.e. when the line of sight is very close the polar axis, we directly detect the emission originated from the accretion disk, corona, BLR and NLR, and, in this case, the spectra show broad (FWHM > 1000 km/s) permitted and semi-forbidden emission lines. These object are called Type 1 or unobscured AGN. In the literature we usually refer to these sources as Seyfert 1 or quasars (QSOs). On the other hand, when we look at an edge-on AGN, i.e. along the equatorial plane of the dusty torus, we observe only the thermal radiation emitted by the torus and the electromagnetic spectrum associated to the NLR, while the central emission is obscured by the thick torus itself. The spectrum is, then, characterised by strong narrow (FWHM $\sim$ 300-1000 km/s) NIR-optical-UV permitted and forbidden emission lines that show a clear indication of photoionisation by a non-stellar source. This group is called Type 2 or obscured AGN. To summarise, there are two population of radiative-mode AGN, Type 1 and Type 2, that differ only in the viewing angle from which the AGN is observed, according to the standard unified model for radiative-mode AGN (Antonucci 1993; Urry & Padovani 1995; Urry et al. 2002).

- **Jet-Mode AGN**. This type of AGN is radiatively inefficient with the bulk of the energetic output in kinetic form. The right panel of Figure 1.7 shows a schematic picture of the central structure of a jet-mode AGN. The central thin disk typical of radiative-mode AGN is replaced by a geometrically thick structure in which the inflow time is much shorter than the radiative cooling time (Narayan & Yi 1995; Quataert 2001; Narayan & Quataert 2005; Ho 2008). In this case the low accretion rates are inefficient in emitting powerful radiative energy and $L_{\rm AGN}/L_{\rm edd} < 0.01$. The energetic output emitted is kinetic energy transported by two-sided jets moving along the pole axis. The typical radiation of these jets, extending over megaparsec scales, is emitted through the synchrotron mechanism, so they are mainly visible at the radio wavelengths. The radio jets travel at relativistic velocities (Lorent's Gamma factor of several) when launched, but appear to rapidly decelerate ad destabilise as they interact with the gas of the host galaxy and transition to subsonic turbulent plumes. Based on the radio morphology and total radio power, active galaxies can be distinguished into two distinct sub-classes (Fanaroff & Riley 1974):

  - First class or FR-I, i.e. sources whose luminosity decreases as the distance from the AGN engine increases showing extended plumes and tails with no distinct termination of the jet.
  - Second class or FR-II, i.e. sources that exhibit an increasing luminosity and narrow, well-collimated jets with clear termination points called "hot spot".

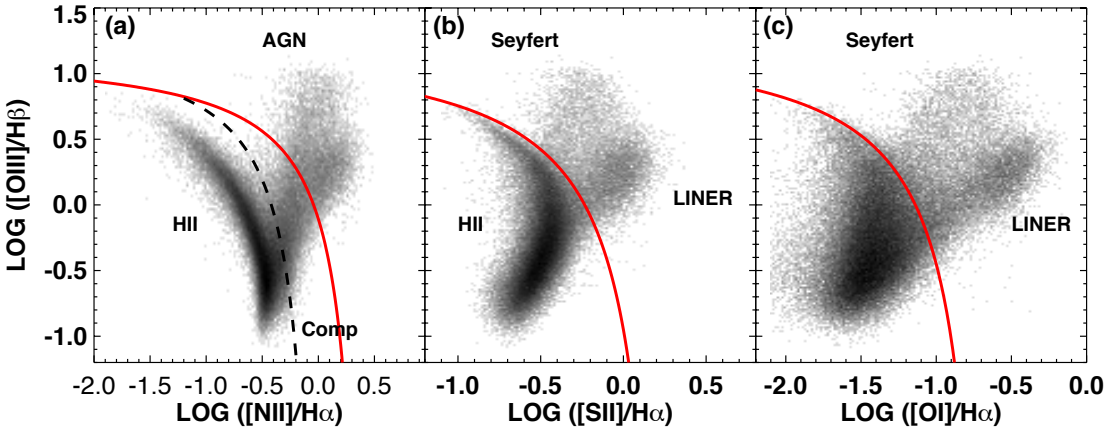

Figure 1.8: A set of diagnostic diagrams for the Sloan Digital Sky Survey main galaxy sample taken from Kewley et al. (2006). The red line is the maximal starburst line from Kewley et al. (2001), whereas the dashed line in panel a shows the more stringent dividing line between pure star-forming galaxies and AGNs adopted by Kauffmann et al. (2003a). The separation between star-forming galaxies and AGNs is most cleanly done using panel a, whereas panels b and c can be used to separate Seyferts from LINERs.

In addition to these two main classes (radiative and jet mode), there is a further group of AGN called LINERs (Low-Ionisation Nuclear Emission-line Regions) including objects characterised by low luminosity (L< 10^{37} erg/s) and low ionisation ([OIII]λ5006/Hβ< 3). Since this thesis is focused on luminous AGN interacting with the host galaxy, we are not interested in a closer examination of this class of objects; for a comprehensive review on LINERs see Ho (2008).

The broad emission lines (FWHM ~ 1000-20000 km/s) and strong non-stellar continuum emission in Type 1 AGNs allow us to identify the presence of the AGN in the centre of a galaxy. On the other hand, the narrow, ionised emission lines typical of Type 2 radiative-mode and jet-mode AGNs are also produced by ordinary population of O stars associated with ongoing star formation. So the presence of these kind of ionised lines in the observed spectrum is not sufficient to claim whether the radiation is emitted by an AGN or not. For this reason, in the past years a large effort has been made to find a way to distinguish star forming regions from AGNs. In 1981, Baldwin et al. (1981) proposed spectroscopic diagnostics based on emission line ratios between permitted and forbidden emission lines. The most famous is the [OIII]λ5006/Hβ vs [NII]/Hα diagram, often referred to as the BPT diagram (for Baldwin, Phillips, & Terlevich 1981). Figure 1.8 shows the BPT diagram for a main galaxy sample extracted from the SDSS (Kewley et al. 2006; Groves 2007). The point distribution on this plane highlights the presence of two populations: AGNs and HII star-forming regions. Since photons emitted from AGN are harder than those coming from the massive stars in the HII regions, the optical collisionally excited lines (i.e. [OIII]λ5006, [NII]) are brighter with respect to recombination lines (i.e. Hβ, Hα) than in the case of ionisation by massive stars only. Based on photoionisation and stellar population synthesis models, Kewley et al. (2001) defined an upper boundary for the locus occupied by star-forming galaxies in the BPT diagram (red line in Figure 1.8), above which the sample hosts only AGN objects. Two years later, analysing the properties of 22623 galaxies within the redshift range 0.02< z <0.3 and hosting AGNs, Kauffmann et al. (2003a) set an alternative demarcation (dotted line in Figure 1.8) that should provide a more complete census of the AGN population. Nowadays, the BPT diagram is still used to distinguish emission-line galaxies in three classes: AGNs (above the Kewley line, on the right), star-forming galaxies (below the Kauffmann line) and composites (between the Kweley and Kauffmann lines). In addition to this two limits, other authors have suggested further refinements to this division (e.g., Kewley et al. 2006; Stasińska et al. 2006; Cid Fernandes et al. 2001), but we are not going into details now.

Later on, Veilleux & Osterbrock (1987) suggested two additional diagrams: [OIII]λ5006/Hβ vs [SII]/Hα and [OIII]λ5006/Hβ vs [OI]/Hα. These two new emission-line diagnostic diagrams shown

in Figure 1.8 offer a further method to discern between the AGN emission and the one from star-forming regions. Even for these two diagram, Kewley et al. (2001) proposed an upper limit for the HII population. It is interesting to note the [SII]/Hα and [OI]/Hα diagrams, allow us to separate Seyfert (Type 1 AGN) from LINERs on the basis of a different levels of ionisation: Seyfert galaxies lie on the upper branch while LINERs are on the lower branch.

1.3 AGN Population

The luminosity function (LF) defines the number of galaxies per luminosity interval per volume. Usually, up to very high redshifts ($z \sim 8$; e.g. Bradley et al. 2012; Schmidt et al. 2014), the galaxy LF seems to be well described by a Schechter function (equation 1.1), despite ground-based studies claiming a power-law trend at bright magnitudes (Bowler et al. 2014). On the other hand, the QSO luminosity function is generally described by a double power law distribution (Pei 1995; Boyle et al. 2000; Croom et al. 2004):

$$\Phi(L) = \frac{\Phi_0}{\left(\frac{L}{L_0}\right)^{\alpha} + \left(\frac{L}{L_0}\right)^{\beta}}$$

where α is the faint-end slope and β the steepness of the bright-end.

In the last 20 years, the advent of AGN deep surveys has resulted in more that a 10-fold increase in the number of known QSOs and early measurements of QSO LFs have shown a strong evolution in this population as a function of redshift. In particular the comoving number density of luminous QSOs peaks between $z \sim 2-3$ (hereafter called "Quasar Epoch") and then converges rapidly at higher redshifts (e.g. Richards et al. 2006). The observed evolution of QSOs, together with the known paradigm that AGNs are powered by mass accretion onto a BH suggested that the BHs observed in the Local Universe should be the "relics" of AGN activity. To verify this assumption, the observed BH mass function has been compared to that inferred by known AGN luminosity function. Taking into account that a fraction of AGN are obscured by dust, Marconi et al. (2004) found that the BH mass function inferred by QSO evolution is perfectly consistent with the local BH mass function, indicating that BHs mainly grow during the AGN active phase.

In Section 1.1 we illustrated how both the colour-mass bi-modal distribution and galaxy LFs may be explained by energy released by mass accretion onto BH. The energetic output interacts with the host galaxy over kpc scales shutting off the supply of gas and quenching the SF. Since BH observed in nearby galaxies are relics of AGN activity and assuming that the coevolution paradigm occurs, we expect to observe some correlations between the properties of BHs and host galaxies in the nearby Universe.

The earliest BH demographic works based on small samples of objects (5-7 sources Dressler 1989; Kormendy & Richstone 1992) suggested the existence of a correlation between the BH mass M_{BH} and the luminosity of the bulge component (L_{bulge}) in the host galaxy. Later on, larger BH samples showed that almost all galaxy bulges contain a BH in their centre and satisfy this M_{BH}-L_{bulge} correlation. Further analysis was then performed on larger samples, on different types of galaxy or assuming different M_{BH} quality cuts (e.g Ho 1999; Merritt & Ferrarese 2001; Kormendy 2001; McLure & Dunlop 2001; Marconi & Hunt 2003; Ferrarese & Ford 2005; Graham 2007; Sani et al. 2011; Kormendy & Bender 2011; Vika et al. 2012; McConnell & Ma 2013; Kormendy & Ho 2013). An interesting result was achieved by Marconi & Hunt (2003), who analysed for the first time the correlation between BH and bulge luminosity in the K band (~ 2 μm) rather than the visible-light wavelength range. This choice significantly reduced the scatter on the M_{BH}- L_{bulge} relation, minimising the L_{bulge} error due to contamination of internal absorption and young stars emission.

Since L_{bulge} is directly correlated with the bulge mass (hereafter M_{bulge}), the M_{BH} - L_{bulge} relation could translate in terms of M_{bulge}. Several studies (e.g. McLure & Jarvis 2002; Marconi & Hunt 2003; Häring & Rix 2004) are in agreement with an inferred linear relation:

$$\left\langle M_{BH}/M_{bulge} \right\rangle \sim 0.001 - 0.002.$$

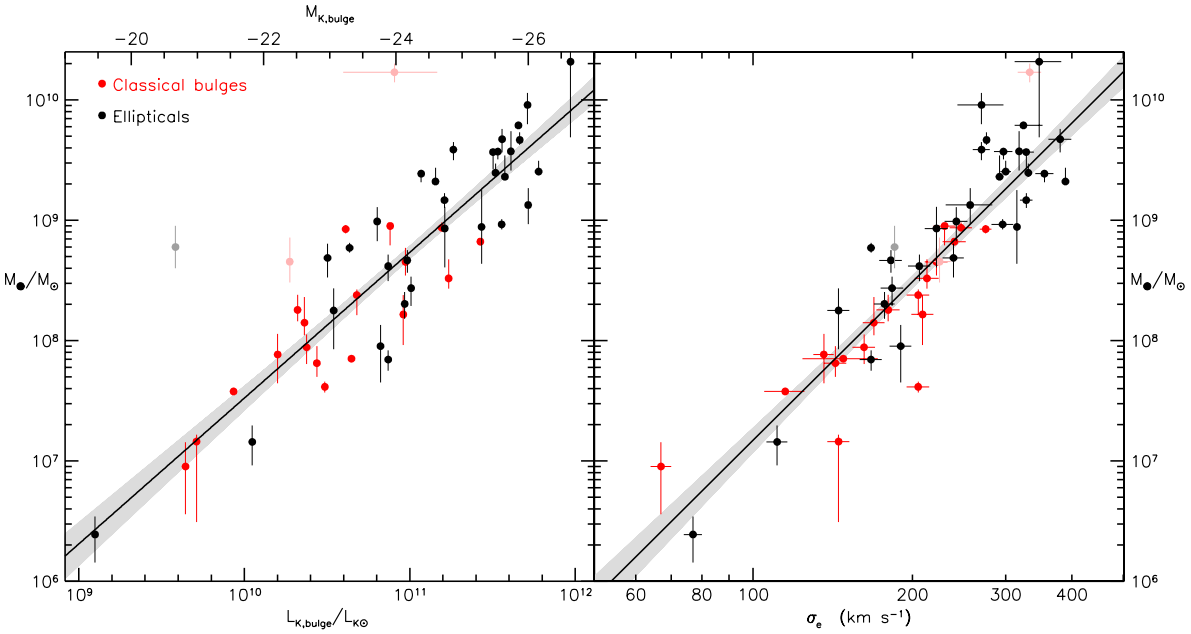

Figure 1.9: Correlation between the measured M_{BH} and the K-band absolute magnitude $M_{K,bulge}$ and luminosity $L_{K,bulge}$ (left panel), and the velocity dispersion σ_e for (red) classical bulges and (black) elliptical galaxies (right panel). The lines indicate symmetric least-squares fits to all the points except the 'monsters' (points in light colours) and the grey shaded region indicates its statistical uncertainty.

The correlation between M_{BH} and M_{bulge}(or L_{bulge}) remains a well established result, suggesting the paradigm of BH-host-galaxy coevolution. However, the typical ratio between the two masses, $M_{bulge} \sim 1000 M_{BH}$, kindled suspicions that the BH could affect the whole galaxy growth.

Another hint to the strong link between BH formation, galaxy formation, and AGN is the tight correlation between M_{BH} and the stellar velocity dispersion (hereafter σ_e) in the host galaxy. The first announcement of this discovery was claimed by Ferrarese & Merritt (2000) and Gebhardt et al. (2000), who measured BH masses and velocity dispersions in a sample of elliptical and spiral galaxies. Following studies (Merritt & Ferrarese 2001; Kormendy 2001; Tremaine et al. 2002; Marconi & Hunt 2003; Ferrarese & Ford 2005; Wyithe 2006; Graham 2007, 2008; Hu 2008; Sani et al. 2011; Kormendy & Bender 2011; McConnell et al. 2011; Beifiori et al. 2012; Graham & Scott 2013; McConnell & Ma 2013) relied on larger samples decreasing the M_{BH}-σ_e scatter error and showed that this correlation is also applicable to other kind of objects (i.e. AGNs, globular cluster) observable both in the Local Universe and at high redshifts.

Figure 1.9 shows the updated M_{BH}- L_{bulge} (left panel) and M_{BH}- σ_e (right panel) correlations found by Kormendy & Ho (2013). The black lines are the best fits to all points :

$$Log\left(\frac{M_{BH}}{10^9 M_\odot}\right) = -(0.266 \pm 0.052) - (0.484 \pm 0.034)(M_K + 24.21)$$

and

$$Log\left(\frac{M_{BH}}{10^9 M_\odot}\right) = -(0.510 \pm 0.049) - (4.377 \pm 0.290) Log\left(\frac{\sigma_e}{200\ km/s}\right)$$

where M_K is the K-band luminosity of the bulge measured in magnitude unit. The intrinsic scatter in the M_{BH}- L_{bulge} relation is almost the same as the intrinsic scatter in M_{BH}- σ_e. This is important to support the BH-bulge correlation. Indeed M_{BH} is generally calculated using the stellar velocity dispersion, so, when plotting M_{BH}vs σ_e, we are to some degree plotting a function of σ_e against σ_e. Seeing the same small scatter in the M_{BH}- L_{bulge} correlation is therefore compelling. The tight correlation between M_{BH} and the bulge velocity dispersion and mass suggests that BH growth and galaxy formation are somehow connected.

Unless these findings are mere coincidences, these correlations are indirect proofs of coevolution between BHs and host galaxies. Although M_{BH} is only 0.1% of M_{bulge} the binding energy of a BH (see Section 1.4) is much larger than that of the host bulge and in fact, if a small fraction of the AGN energy output coupled to gas in the forming galaxy, all the gas would blow away. This means that AGN feedback could significantly affect star formation in the host galaxy.

1.4 AGN Feedback

AGN feedback mechanisms are invoked by recent models and simulations to explain galaxy evolution (e.g. Kauffmann & Haehnelt 2000; Granato et al. 2004; Di Matteo et al. 2005; Springel et al. 2005; Croton 2006; Hopkins et al. 2006; Ciotti et al. 2010; Alexander & Hickox 2012; Zubovas & King 2012; Fabian 2012; Heckman & Best 2014; Zubovas & King 2014; Nayakshin 2014; Costa et al. 2014, 2015; King & Pounds 2015). Although the nine orders of magnitude difference between the physical size of a BH and a typical host galaxy, it is easy demonstrate that the energetic output due to matter accretion onto the central BH can have a significant effect on the surrounding environment within the host galaxy. The energy released by BH accretion mechanism could be written as

$$E_{\rm BH} = \eta M_{\rm BH} c^2,$$

where η is the radiative efficiency for the accretion process (usually $\eta \sim 10\%$; e.g. Fabian & Canizares 1988), and c is the speed of light. On the other hand, the binding energy of the galaxy bulge is

$$E_{\rm gal} \sim M_{\rm gal} \sigma_e^2,$$

where $M_{\rm gal}$ is the galaxy mass and $\sigma_{\rm e}$ the stellar velocity dispersion. Since recent observations (Kormendy 2001; Merritt & Ferrarese 2001; Häring & Rix 2004) claim $M_{\rm BH} \approx 10^{-3} M_{\rm gal}$, we derive

$$\frac{E_{\rm BH}}{E_{\rm bulge}} \approx 10^{-3} \eta \left(\frac{c}{\sigma}\right)^2 \approx 10^{-4} \left(\frac{c}{\sigma_e}\right)^2.$$

Assuming a typical velocity dispersion $\sigma_{\rm e} \sim$ 200 km/s, we obtain $E_{\rm BH}/E_{\rm bulge} \sim 200$. The energy produced by the accretion process onto a central BH is about two orders of magnitude larger than the binding energy of the galaxy. Hence the energy expelled by BH accretion may contribute to the evolution of the host galaxy and its star-formation history.

In Section 1.2 we defined two different classes of AGN based on their energetic output: radiative and jet mode. Here we illustrate how the energy released by a radiative-mode process ($L \sim L_{\rm Edd}$), which is larger than one emitted by a jet-mode AGN, may lead to the $M_{\rm BH}$-$\sigma_{\rm e}$ correlation observed in the Local Universe (Section 1.3). A simple way to obtain the observed $M_{\rm BH}$ versus stellar velocity dispersion relation is balancing the outward radiation force ($F_{\rm outward}$) and the inward one ($F_{\rm inward}$) due to gravity:

$$\frac{4\pi {\rm G} M_{\rm BH} {\rm m_p}}{\sigma_{\rm T}} = \frac{L_{\rm Edd}}{c} = F_{\rm outward} = F_{\rm inward} = \frac{{\rm G} M_{\rm gal} M_{\rm gas}}{r^2}, \tag{1.3}$$

where G is the gravitational constant, m_p is the proton mass, and σ_T is Thomson cross section for electron scattering. Assuming that the gas mass is a fraction f of the total galaxy mass ($M_{\rm gas} = f M_{\rm gal}$) and supposing the galaxy spheroid as an isothermal sphere $M_{\rm gal} = 2\,{\sigma_{\rm e}}^2 r/{\rm G}$, we get:

$$\frac{4\pi {\rm G} M_{\rm BH} {\rm m_p}}{\sigma_{\rm T}} = \frac{{\rm G} f M_{\rm gal}^2}{r^2} = \frac{{\rm G} f 4 \sigma_e^4 r^2}{r^2 {\rm G}^2} \Rightarrow M_{\rm BH} \propto \sigma_e^4, \tag{1.4}$$

in agreement with the observational relation. When the BH achieves a critical luminosity ($L \sim L_{Edd}$),

the emitted radiation overcomes the gravity force and sweeps away gas and matter, slowing the BH growth and the star formation in the host galaxy. The model predictions expect the radiative mode feedback occurs at $z \sim 2-3$, when the QSO activity peaks and galaxies are most gas rich. Once a host galaxy has no gas reservoir left, matter accretion is no longer radiative efficient and the AGN luminosity drops ($L \lesssim 0.01 L_{Edd}$). In this case the jet-mode feedback is fundamental to support the M_{BH}-σ_e correlation. Indeed, the kinetic output deposits energy into the local intergalactic medium preventing re-accretion of gas and maintaining the galaxy on the red sequence (e.g. Croton 2006; Bower et al. 2006; Best et al. 2006; Fabian et al. 2006).

Please note that this thesis is not focused on jet-mode feedback, but we are rather interested in understanding the radiative mode feedback that is still poorly understood.

1.4.1 Radiation Pressure vs Wind Mode

The impact of AGN feedback on star-forming galaxies is still an open question. AGN feedback can operate via different physical mechanisms, such as radiation pressure, jets, and winds. The main questions that arise are: which is the driver for the observed outflows? and how does the energy released by the central BH couple to the interstellar medium of the host galaxy?

One way of driving outflow is via radiation pressure on dust (Fabian 1999, 2002; Ishibashi & Fabian 2012, 2015). In this case, the main interaction is due to the absorption of the central radiation by dust grains. Most of AGN luminosity is emitted at UV wavelengths whose photons are efficiently absorbed by dust and re-emitted in the IR domain. The emitted radiation accelerates the dust grains on scales larger than the BLR ($\sim$ few pc), where the typical temperatures are below the sublimation temperature (see equation 1.2). Meanwhile, the AGN radiation partially charges the dust grains and the particle of gas (Murray et al. 2005; Fabian et al. 2008), ensuring that the gas is efficiently dragged out with the dust. The absorption and scattering of UV photons couple the L/c momentum to the interstellar medium. We note that the critical luminosity to start this mechanism of outflow is lower than that assumed in the equation 1.3. Indeed, the dust cross section is $\sim$ 1000 times larger than the Thompson cross section (Fabian et al. 2008), so the critical luminosity $L'_{\rm Edd}$ is three orders of magnitude smaller than the critical luminosity $L_{\rm Edd}$ estimated for electron scattering (equation 1.3). Therefore an AGN with bolometric luminosity close to Eddigton luminosity, it has already overtaken the effective luminosity limit for dusty gas. The results by Ishibashi & Fabian (2012, 2015) show that radiation pressure on dust grains drives gas out to large radii, i.e. $\sim$ kpc and with outflow mass rates consistent with those observed in the local and high-z Universe.

Another possible physical mechanism to explain fast outflows on galactic scales invokes high-velocity winds from the central nucleus. The first to propose this idea were Silk & Rees (1998) who suggested an intense wind from the immediate vicinity of the BH, able to sweep up the gas into a shell, and push it outwards at constant velocity. This model assumes that the energy wind is completely transferred to the interstellar medium (energy-driven outflows) and that the shock pattern is moving with the escape velocity. These two hypothesis lead to $M_{\rm BH} \propto \sigma^5$. (see Section 1.3). In the last years, King (2010); King & Pounds (2015) proposed a new wind-mode model, able to reproduce the observed M_{BH}-σ_e correlation (see Figure 1.10). The (ultra) fast wind is generated in proximity of the BH with outflow momentum rate of the same order of the Eddington limited photon momentum

$$\dot{M}_w v_w \approx L_{\rm Edd}/c,$$

where $\dot{M}_w$ is the wind mass flow rate and v_w is the speed of the outflow wind. Assuming that the wind mass flow rate is equal to the Eddington mass accretion rate ($\dot{M}_w \sim \dot{M}_{\rm Edd}$), we find that the wind speed is close to light speed:

$$\dot{M}_w v_w \approx L_{\rm Edd}/c \approx \eta \dot{M}_{\rm Edd} c \Rightarrow v_w \approx \eta c \sim 0.1c.$$

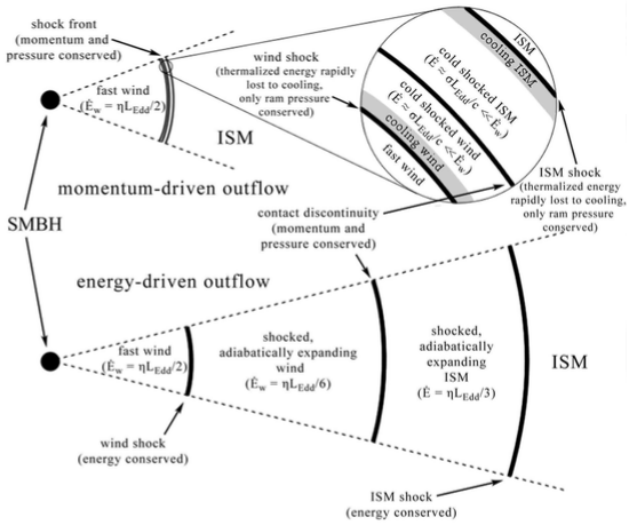

Figure 1.10: Schematic picture of momentum-driven (top) and energy-driven (bottom) outflow. In both cases a fast wind ($v_w \sim 0.1c$) impacts the interstellar gas of host galaxy, producing an inner revers shock slowing the inner wind, and an outer forward shock accelerating the swept-up gas. In the momentum-drive case, the shocks regions are very narrow and rapidly become effectively isothermal. Only the ram pressure is communicated to the outflow. In a energy-driven case, the shocked regions are much wider and do not cool. The shocked regions expand adiabatically communicating most of the kinetic energy of the wind to the outflow. King (2010); King & Pounds (2015) proposed the shocked region to be, at first, confined within $\sim$ 1 kpc of the AGN, and the momentum-driven mode to establish the M_{BH}-$\sigma_e$relation. Once the BH mass attains a critical mass, the shocks move further from the AGN and the outflow becomes energy-driven. This produces the observed large scale molecular outflow, quenching star formation in the host galaxy.

and the kinetic power $\dot{E}_w$ of the fast wind is about 5% of Eddington luminosity:

$$\dot{E}_w = \frac{\dot{M}_w v_w^2}{2} \simeq \frac{L_{\rm Edd}}{c}\frac{v_w}{2} \simeq \frac{\eta c L_{\rm Edd}}{2c} \simeq 0.05 L_{\rm Edd}$$

These ultra-fast wind, also called Ultra-Fast Outflow (UFO), with velocity up to 0.2-0.4c have been recently observed (Pounds et al. 2003b,a; Reeves et al. 2009; Tombesi et al. 2010a,b, 2015; Feruglio et al. 2015) in X-ray iron absorption lines, supporting the idea that the majority of QSOs produce such winds. When ultra-fast winds encounter the cold interstellar medium, a strong hot ($\sim 10^{11}$ K) shock occurs and the shocked wind gas sweeps up the host ISM (upper panel Figure 1.10). In the inner region ($\lesssim$ 1kpc) where the AGN's radiation field is strong the shocked gas loses its thermal energy via inverse Compton effect (Ciotti & Ostriker 1997) and the momentum of wind is completely transferred to the ISM (momentum-driven regime). The cooled shocked wind gas is compressed to high density, retaining and communicating only its pressure, which is equal to the pre-shock ram pressure, to the host ISM:

$$\dot{M}_o v_o = \dot{M}_w v_w \simeq L_{\rm edd}/c, \tag{1.5}$$

where $\dot{M}_o$ and v_o are the outflow mass rate and outflow velocity of the gas of the ISM, respectively. This momentum-driven regime is shown in the upper schematic picture of Figure 1.10. Assuming an isothermal ISM density distribution with velocity dispersion σ and gas fraction f_c, the model leads to:

$$M_{\rm BH} = \frac{f_c \sigma_T}{\pi G^2}\sigma_e^4 \simeq 4\times 10^8 M_\odot \sigma_{200}^4,$$

where $f_c = 0.16$ and $\sigma_{200} = \sigma_e/(200$ km/s) (King 2003, 2005, 2010). The calculated mass is consistent with that obtained from the observed $M_{\rm BH} - \sigma_e$ relation. A large scale ($\gtrsim$ 1 kpc), when the AGN's radiation field is weak and inverse Compton effect is not efficient, outflow becomes energy-driven. In

this regime, most of the wind kinetic power goes into mechanical energy of the outflow:

$$\dot{E}_o = \frac{\dot{M}_o v_o^2}{2} = \frac{\dot{M}_w v_w^2}{2} = 0.05 \frac{L_{\rm Edd}}{c} \tag{1.6}$$

The strong thermal pressure expands the outflows on kpc large-scale, with velocity v_o of a few thousand km/s. On the other hand, the scalar momentum rate of the outflow is greater than the Eddington value. Indeed Zubovas & King (2012) derive an expression for the momentum outflow rate $\dot{M}_o$ of:

$$\dot{M}_o v_o \sim 20 L_{\rm Edd}/c \tag{1.7}$$

Recent observations of molecular outflows (e.g., Feruglio et al. 2010; Rupke & Veilleux 2011; Sturm et al. 2011; Cicone et al. 2014; Feruglio et al. 2014) have revealed that they are extended ($\sim$ kpc), with v_o exceeding 1000 km/s, and $\dot{M}_o$ and $\dot{E}_o$ in agreement with the energy-driven outflow model. In conclusion, when the BH achieves the M_{BH}-σ_e relation, the energy-driven outflows move into the momentum-driven regime cleaning up the host galaxy.

Although, observations support the mode wind model we are still studying the main properties of outflows and their interaction with the surrounding ISM of host galaxy.

1.4.2 Evolutionary Sequence

In the last few years, astronomical observations have established that SMBHs reside in the centre of all galaxies (Kormendy & Richstone 1995; Richstone et al. 1998; Kormendy 2001) and the properties of the two populations are somehow correlated. In particular, the energy emitted by matter accretion onto the central BH affects the surrounding environment out to large kpc scales leading to the M_{BH} - σ_e relation observed for nearby galaxies. This observed correlation lead to the paradigm of BH-galaxy coevolution.

In addition to BH-galaxy mass correlation, models and theories of coevolution paradigm have been also proposed to explain the typical galaxy LF, the existence of blue (late-type) and red-and-dead (early-type) galaxies observed in the Local Universe.

The first evolutionary sequence proposed by Sanders et al. (1988) (top panel of Figure 1.11), later rearranged by others (e.g Hopkins et al. 2009) is summarised in Figure 1.11 where the main phases of a star-forming galaxy evolving from the blue cloud population to the red sequence are shown. In this simple picture, galaxy evolution begins in the early Universe ($z \sim 4-6$), when galaxies are formed as gas-rich, rotation-dominated systems with a BH in their centre (Figure 1.11 panels (a) and (b)). The BH mass is below the critical mass required to activate any type of feedback mechanism so the galaxy grows through the accretion of cold gas or through minor merges with other system (Hopkins et al. 2009). At the same time, the surrounding dark matter halo increases as well in mass via the hierarchical growth of structure.

When dark halo matter reaches a critical mass of $10^{12} - 10^{13}$ $M_\odot$ (Croton 2009), a dramatic event occurs that triggers lower-luminosity AGN with BH accretion rates up to $\sim$ 10 – 100 $M_\odot$/yr. We note that this high accretion rate values cannot be produce by secular process, but it has to be driven by a "powerful" mechanism such as the major-merger of two gas-rich galaxies. The asymmetric and evolving gravitational potential of a major merger exerts torques on gas originally in circular rotation, depleting its angular momentum and driving inflows toward the nucleus of the remnant. Large simulations of major mergers well reproduce many observed properties of QSOs and the resulting spheroidal remnants, as well as their abundance and redshift evolution (Kauffmann & Haehnelt 2000; Springel et al. 2005; Hopkins 2006; Hopkins et al. 2008). Moreover there are also observations of merger remnants hosting individual QSOs supporting major-merger model as driven of most luminous QSOs (Riechers et al. 2008; Aravena et al. 2008). An other way to trigger luminous AGN may also be large-scale disk instability and accretion of pristine gas from halo within the massive gaseous disks (Mo et al. 1998; Bower et al. 2006; Genzel et al. 2008; Dekel et al. 2009; Bouché et al. 2010; Cresci et al. 2010). In conclusion major-merger, inflows and disk instability modify the gravitational

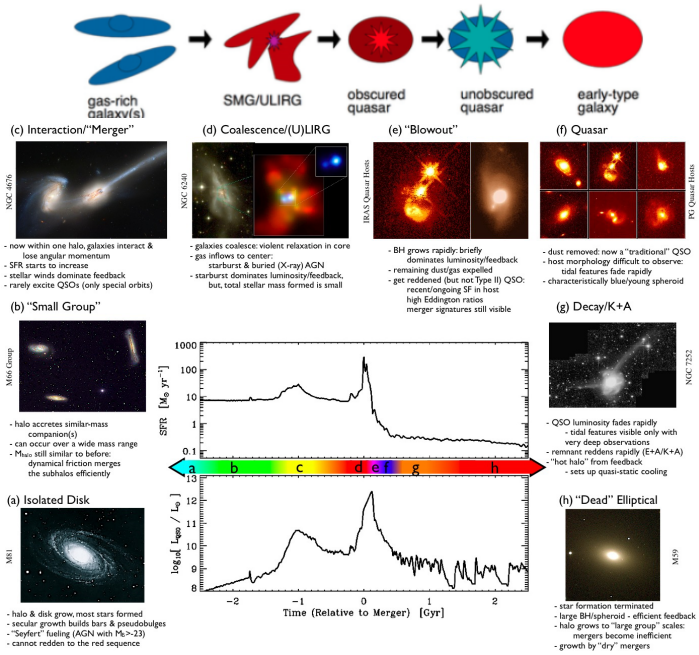

Figure 1.11: Top panel: Main components in the major-merger evolutionary scenario proposed for the first time by Sanders et al. (1988). Bottom panel: Schematic outline of the phases of growth in a galaxy undergoing a gas-rich major merger proposed by Hopkins et al. (2008). The panels from (a) to (h) represent the different phase of the evolutionary track (see the text). The picture are real images of different type of galaxies, which have been observed with sky-based and ground-based telescopes. The central plot shows the SFR and AGN luminosity as a function of the time from the merger phase.

potential so the gas is driven into the central region through a series of gravitational instabilities that help overcoming the angular momentum of the gas.

The flow of cold gas fuels a rapid starburst in the host galaxy (SFR > 100 $M_\odot$/yr; Di Matteo et al. 2005; Sijacki et al. 2011; Valiante et al. 2011) and, at the same time, the large masses of gas and dust surrounding the central BH obscure the electromagnetic emission of AGN (Tran et al. 2001; Yuan et al. 2010; Iwasawa et al. 2011; Petric et al. 2011). Most of the UV radiation emitted by AGN and young stars is absorbed by the surrounding dust that re-emitted at Far-InfraRed (hereafter FIR) wavelengths (8-1000 μm). The FIR luminosity is as high as that emitted by ULIRG and SMG galaxies. During this phase (panels (c) and (d) of Figure 1.11) the star-forming galaxy reaches its peak of star-formation activity, i.e. most of the mass in stars forms in this period. Although most of observed ULIRIGs and SMGs, at both low and high redshift, show a major-merger (Tacconi et al. 2008; Engel et al. 2010) driving the star formation and BH accretion, high-redshift observations revealed the presence of unperturbed rotating discs in strongly star-forming galaxies (e.g. Epinat et al. 2009; Cresci et al. 2009; Gnerucci et al. 2011a; Carniani et al. 2013), suggesting other possibilities for mass accretion, such as strong inflows of pristine gas from the halo. In fact, a key question is whether a starburst scenario is a dominant process at high redshift since the fraction of major-merger system is small (Rodighiero et al. 2011). The belief that ULIRG/SMGs is a phase of the evolutionary path toward the red-and-dead population is supported by millimetre and X-rays observations, which are able to probe the dusty obscured nuclei, that individuate the presence of AGN in some of these sources (Alexander et al. 2003, 2005; Laird et al. 2010). BH mass estimates in SMGs hosting an AGN in their centre indicate that a BH is less massive with respect to the host galaxy and may, therefore, be in an early stage (heavily obscured) preceding the bright unobscured phase.

The BH grows until the energy released by mass accretion is large enough to unbind the gas not only from its host galaxy, but from the entire surrounding halo. This negative feedback mechanism, which shuts down the growth of both the BH and its host bulge/galaxy (panel (e) of Figure 1.11), determines the observed BH-galaxy observations. Most of gas and dust is swept away by AGN emis-

sion observationally translating into emission from molecular and ionised gas moving away from the nucleus. When most of the host galaxy has been cleaned up along the line of sight, the AGN emission becomes detectable and different types of AGN, i.e. I and II, could be defined on the basis of the inclination of the dust torus. As shown in panel (f) of Figure 1.11, this is the unobscured AGN phase. Models (see Figure 1.11) and observations (Sturm et al. 2011; Cicone et al. 2014) require AGN-driven outflows to remove the whole gas in the host galaxy over short-time scales. They infer a depletion time scale of few Myr ($\sim 10^6$ years), roughly anti-correlated with the AGN luminosity and supporting the merger scenario where the highest outflow rates are a short-lived, late, AGN-dominated stage in the merger evolution. The released energy impacts on the diffuse gas in the host DM halo and prevents cooling from getting new stars, as required in order to produced the observed stellar mass and luminosity function of galaxy (see Section 1.1.3; Bower et al. 2006, 2008; Croton 2006) Finally, as the remnant relaxes, star formation and quasar activity decline as the gas is consumed and dispersed, and the remaining galaxy resembles an elliptical with a quiescent BH satisfying the observed correlations between central BH and spheroid properties (panels (g) and (h) of Figure 1.11). During this intermediate ~Gyr decay, depending on the details of the merger and the exact viewing time, the remnant may be classified as a low-luminosity (decaying) AGN in a massive (and relatively young) spheroid, or as a post-starburst galaxy. The merger exhausts gas and star formation very efficiently, so the remnant reddens rapidly onto the red sequence. Later on, the quiescent remnant galaxy could increase its stellar mass only through minor-merger or interaction with closer gas clumps or galaxy satellite.

1.4.3 Is AGN Feedback really needed?

The presence of tight empirical correlations between the mass of BHs and the velocity dispersion, mass, and binding energy or potential well depth of their hosts demonstrate a fundamental link between the growth of BHs and galaxy formation. Understanding the physical origin and consequences of these correlations is critical for models of co-formation of BHs and bulges, as well as theories relating the evolution and statistics of BH formation and quasar activity to the remnant spheroid population.

It is puzzling not only that the M_{BH}-bulge correlations exist, but also that they have a small intrinsic scatter of 0.3 dex in M_{BH} and that the correlation with the bulge mass is practically linear. In contrast, a separate class of models has been proposed to explain the BH-host correlations (or a subset of them) without feedback. The analysis of these models do not concern this thesis, but for sake of clarity we briefly present these other predictions able to explain BH and galaxy properties.

The linear relation between BH mass and stellar mass in the host bulge might be originated from hierarchical assembly of BH and stellar mass through galaxy merging without any causal origin (Peng 2007; Jahnke & Macciò 2011; Fanidakis et al. 2011). The M_{BH}-M_{bulge} correlation appears to emerge when galaxies have undergone five or more major and minor mergers, regardless of the initial M_{BH}-M_{bulge} and of how primordial BHs were seeded inside galaxies.

Although it is possible for these models to explain the mean correlation between BH and host mass, a more stringent constraint comes from the surprisingly small observed scatter in that correlation, with observations suggesting it be at most $\sim 0.25 - 0.3$ dex. Such a small scatter can be explained only using a self-regulated BH growth model: the BH does not interact with whole galaxy quenching star formation, but it operates only with the ISM in its surroundings, shutting off its supply of gas.

Whether or not AGN/stellar feedback is responsible for the bulk of the gas removal nowadays is still an open question. Recent observations have revealed that starburst galaxies can drive molecular gas outflows through stellar radiation pressure (Bolatto et al. 2013; Cicone et al. 2014; Geach et al. 2014). The stellar feedback produced by multiple supernovae explosion pushes gas away over large scale of galaxy ($\sim$ 10 kpc) with velocities comparable to those typical of AGN-driven outflows ($\sim$ 1000 km/s). These observation are also supported by recent model prediction (Hopkins et al. 2012) claiming that radiative stellar feedback disrupts even the most massive clumps over a short timescale of $\sim 10 - 100$ Myr, ejecting material into a super-wind and recycling the rest of the gas into the diffuse ISM. Therefore these outflows can remove gas at a high rate compared to the SFR. Feedback from massive stars seems to play a critical role in driving galactic super-winds that enrich the IGM

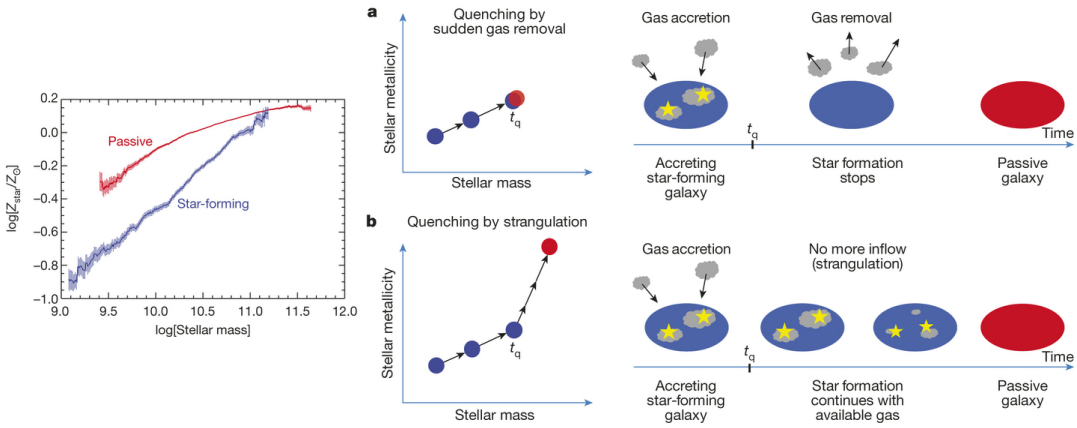

Figure 1.12: Left panel: Average stellar metallicities estimated for a subsample of 3905 star-forming (blue line) and 22618 quiescent (red line) local ($z \lesssim 0.1$) galaxies from the SDSS catalogue. At a given stellar mass ($\leq 10^{11}$ $M_\odot$), the stellar metallicity of passive galaxies is higher than the star-forming galaxies one. Right panels: Evolution of stellar metallicity for two different quenching scenarios. The top panels assume that the rapid quenching (i.e. AGN-driven feedback) transforms a star-forming galaxy into a quiescent galaxy and stellar metallicity does not increase. In the lower panels, a "strangulation" process halts inflow of cold gas but the star formation activity goes on until all the available gas is used up. The stellar metallicity increase steeply (see text for details). Image from Peng et al. (2015).

and shape the galaxy mass function, mass-metallicity relation, and other global properties of a galaxy. However, AGN feedback seems to be necessary in most massive objects ($M_{halo} > 10^{12}$ $M_\odot$) where stellar feedback is not able to overcome the gravitational potential (Hopkins et al. 2014). But also AGN-driven outflows in massive object are not a proof of "negative feedback". As a matter of fact, simulations claim that AGN-driven outflows remove a substantial amount of gas from the host galaxy, but the impact of AGN feedback on the star formation efficiency in the interstellar gas is just marginal.

An alternative mechanism to halt the supply of cold gas is the "strangulation" process (Larson et al. 1980; Balogh & Morris 2000; Keres et al. 2005; Dekel & Birnboim 2006). This theory assumes a galaxy is accreted onto a massive dark halo. Once the massive dark halo reaches a critical mass ($> 10^{12}$ $M_\odot$), the gas is heated by virial shocks that halt the inflow of cold gas to the galaxy. The star formation slowly declines until the whole reservoir of gas is exhausted. Recent results by Peng et al. (2015) claim that the "strangulation" process could explain the different metallicity in passive and star-forming galaxies with stellar mass $\leq 10^{11}$ $M_\odot$ (left panel of Figure 1.12). Before quenching process, the star formation increases the gas metallicity but, at the same time, inflowing gas dilutes the new metal content in the interstellar medium, so the overall metallicity increment is modest. In the case of "negative feedback", SF is rapidly quenched and the galaxy evolves in a quiescent system where the metallicity does not increase any longer and it is the same as of the progenitor before quenching (top-right panel of Figure 1.12).

In the "strangulation" scenario, the metal content of the galaxy keeps rising and eventually stop, because star formation continues until the existing gas gets completely used up. Once the gas in the galaxy is exhausted, the stellar metallicity in a passive galaxy is higher than that measured in a star-forming galaxy (lower-left panel of Figure 1.12).

In conclusion, Peng et al. (2015) suggest that galaxies with stellar masses $\leq 10^{11}$ $M_\odot$ evolve via "strangulation" mechanism. On the other hand, passive galaxies with stellar masses $\sim 10^{11}$ $M_\odot$ have stellar metallicity similar to the star-forming ones, and the quenching process can be well described by fast "negative feedback". Anyway, this last result cannot shed light on the quenching mechanism at stellar mass $\geq 10^{11}$ $M_\odot$. Understanding the mechanism of quenching at high redshift is, therefore, still an open question that deserves further investigation. The negative feedback would be an important key to understand the BH-galaxy co-evolution, but there are still no clear evidences on the properties of ionised and molecular outflows and, even, whether or not this mechanism is the only process able to remove gas and to quench SF in all star-forming galaxies.

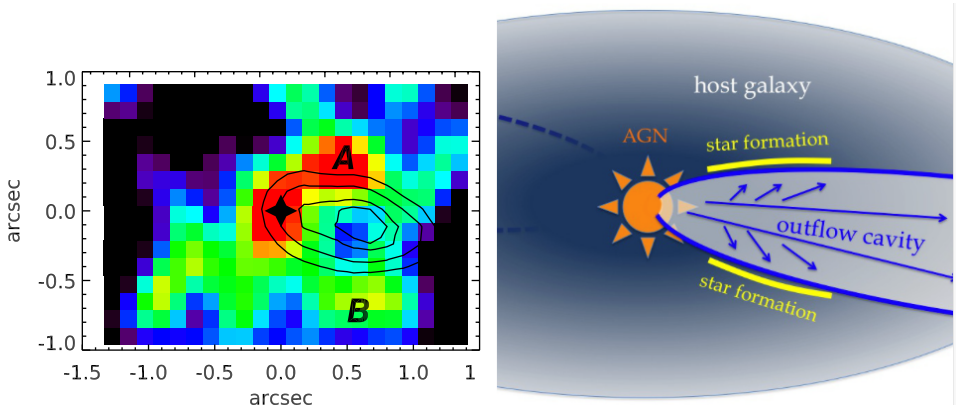

Figure 1.13: *Left panel:* Narrow Hα flux map tracing star formation in the host galaxy. The black contours represent the region affected by ionised outflows, which is traced by [OIII]λ5006 emission line. The star formation is located at the edges of outflows. *Right panel*: Schematic view of the geometry of the system. The high velocity material is sweeping the gas suppressing star formation in a cavity along the core of the outflow (negative feedback), but also triggering star formation by outflow induced pressure at the edges (positive feedback). Figures by Cresci et al. (2015).

1.4.4 Positive Feedback

In the previous Sections, we described how the AGN interacts with the host galaxy, in particular quenching the star formation activity and influencing the BH growth. However, observations and simulations have proposed a new scenario regarding AGN and star-formation activity.

Studies of AGNs with low- and high-luminosity in the local Universe revealed a positive correlation between AGNs and starburst activity in the nuclear region (< few kpc) of the host galaxy (Imanishi 2002; Rodríguez-Ardila & Viegas 2003; Imanishi & Wada 2004; Imanishi et al. 2011). The first theoretical prediction proposed that the BH growth would be controlled by a starburst-induced turbulence (Kawakatu & Wada 2008, e.g.).

Later on, AGN observations have shown that clumps of molecular gas are aligned with the AGN radio jets triggering star formation in these regions (e.g. Croft et al. 2006; Rodriguez et al. 2007; Elbaz et al. 2009; Crockett et al. 2012; Salomé et al. 2015). These observations revolutionised the idea that starburst activity influences the BH growth. The new paradigm supposed that AGNs trigger the star formation in their host galaxy (Silk & Norman 2009). The emission due to BH accretion inflates a huge hot bubble into that ISM that sweeps up galactic gas into a shell, which is driven out at velocities faster than the escape velocity of the host gas. In the regions where the gas cools rapidly by inverse Compton effect, the shocked gas is compressed into this cold dense shells, filaments, and clumps. These cold dense regions are gravitationally unstable due to over-pressuring and start forming stars (Nayakshin & Zubovas 2012; Zubovas et al. 2013). Under these conditions the BH actually accelerates the star formation in the host galaxy, determining a positive rather than a negative effect ("positive" feedback). Note that this does not rule out the QSO's negative feedback mechanism: at late, gas poor epochs, when the gas does not cool rapidly, the QSO shock is very effective in driving the gas outward and thus halting further star formation in the host galaxy.

Cresci et al. (2015) show an example of positive feedback analysing the direction of the AGN-driven ionised outflow and the distribution of star formation regions in a QSO at $z = 1.59$. The left panel of Figure 1.13 is a flux map of Hα tracing the star-forming regions. The pattern of Hα is elongated on the left of the central AGN (marked with a star) with two clump labelled A and B. The black contours trace the ionised outflow position inferred by [OIII]λ5006 kinematics. In the region affected by the outflow, Hα emission is suppressed suggesting that the outflowing material is sweeping the gas out from the outflow core. On the other hand, star formation seems to be triggered in the regions surrounding the bulk of outflows. The interpretation of this observations is shown in the right panel of Figure 1.13. The collimate high velocity makes a cavity on the galaxy along the direction of the outflow, while compresses the gas at the edges of the outflow cone. This source represents the

first example of a host galaxy showing both types of feedback simultaneously at work, as predicted by positive feedback model. So far, this is the only source that exhibit positive and negative feedback, so more galaxies are needed to confirm this feedback scenario.

Chapter 2

Thesis Aims

Over cosmic time the evolution of galaxies and BHs is surprisingly similar. Both the star formation activity in galaxies and the AGN activity show a peak at $z \sim 2-3$ (Figure 2.1). Moreover, the histories of the two classes have a similar slope both at low-z $(0 < z < 3)$ and in the early stages of cosmic history ($z > 3$). Up to now, the reason why a connection between these two classes of objects should exist is still unclear, as well as the nature of the physical mechanisms connecting such different kinds of astronomical objects.

Many processes have been invoked to forge a direct connection between the growth of BHs and red-and-dead galaxies, including major mergers, star-formation winds, and AGN-driven outflows. However, different observational results obtained with current telescopes seem to disagree with recent model predictions, leaving this debate open.

In the previous Chapters we showed how AGN-driven outflows regulate the BH growth and star formation activity in host galaxies, by blowing away the gas. This devastating mechanism may be the key to explain the steep bright-end slope of the stellar mass function, and to account for the existence of the red sequence where massive passive galaxies live. Moreover, negative feedback may give rise to the tight correlations observed between BH masses and masses, stellar velocity dispersions, and luminosities of the hosting bulges. However, we are still looking for the "smoking gun", i.e. a clear evidence that AGN-driven outflows quench the star formation out to large scales and strongly affect the evolution of the host galaxies. In addition to this, the origin of the BH-galaxy scaling relations may be explained without a physical coupling, but as the result of a statistical convergence process or other galaxy mechanism, e.g. strangulation.

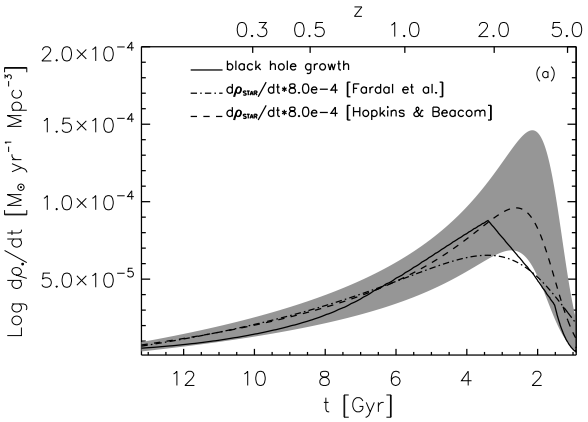

Figure 2.1: The cosmic history of black hole growth and stellar mass growth. The average black hole accretion rate is compared to the SFR as a function of redshift, where the latter is given by Hopkins et al. (2006) and Fardal et al. (2007), scaled by the factor 0.8×10^{-3}. The shaded grey area shows the uncertainty region from Hopkins et al. (2006). Figure from Shankar et al. (2009).

On the basis of above, a comprehensive study on AGNs is fundamental to finally solve the dichotomy of BH-galaxy coevolution.

This PhD thesis is intended to address the following key questions on BH-galaxy coevolution:

- What fuels the rapid growth of most BHs?
- What are the main proprieties of the outflowing gas?
- What are the links between AGN feedback and the large-scale environment?
- What is the detailed nature of AGN feedback?

Following the evolutionary track shown in the top panel of Figure 1.11, we analyse the evolution of the bright and massive galaxies over cosmic time: from the gas-rich galaxies to unobscured QSOs. We make use of new data obtained in several wavelength ranges and, in detail, we analyse the spectral lines emitted by both molecular and atomic gas existing in the active galaxy with the aim of solving the feedback puzzle.

Most of data were obtained with the new millimetre facility, the Atacama Large Millimetre Array (ALMA). In Chapter 3 we describe ALMA in details and we explain how millimetre observations can help in studying galaxy evolution.

ALMA broad band continuum observations are exploited to analyse the millimetre properties of high-redshift (z >1) gas-rich galaxies. Although most of studies over the past years have focused on the luminosity function in the optical wavelength range, the luminosity distribution of millimetre sources is still largely unknown. In fact, the poor sensitivity and low angular resolution of previous single-dish millimetre and sub-millimetre observations have only allowed us to determine the bright-end distribution, while the faint-end profile is still debated. We are interested in analysing the distribution of faint millimetre sources in order to understand their main properties and how much they contributed to the background radiation at millimetre wavelengths. Furthermore, we investigate whether this population could be the progenitor of the observed local galaxies or not by comparing our observations with different models of galaxy evolution which include or not AGN negative feedback (Chapter 4)

The thermal continuum emission at submillimetre wavelengths is not the only goal of ALMA observations carried out during our PhD studies. Some of the strongest lines emitted by the ISM, such as the [CII]λ158μm and the [OI]λ63μm fine structure lines (the two main coolants of the ISM), are redshifted into the ALMA bands at z >2-4. These lines are mainly emitted by star-formation region in galaxies. To test the coevolution paradigm we analyse the [CII] emission lines in a major-merger system at $z \sim 4.7$ composed by a QSO and a ULIRIG/SMG (Chapter 5). The two objects are separated by a project distance of about $\sim$ 24 kpc and are characterised by high SFR ($\sim$1000 $M_{\odot}$/yr). This is one of few system where we can study whether a major-merger mechanism can induce high SFR in a galaxy and seed the BH in host galaxy of a QSO. Since in this framework the SMG and QSO are at the same redshift and in the same environment we are interested in testing whether the two objects have similar properties supporting the fact that SMG is a early phase of QSO.

The last part of this thesis (Chapter 6) concerns AGN-driven outflows and their interaction with host galaxy. Outflow signatures are observed in many QSOs and nearby Seyfert nuclei, in particular in the ionised gas. The observed prominent blue and red wing components in the profile of ionised emission lines suggest the presence of outflowing material at high velocity receding from the nuclear centre. Although the observed outflows are potentially able to provide the negative feedback required by models, we are still missing the evidence that they are effectively quenching star formation, especially during luminous quasar phases. Since feedback is expected to be particularly important in luminous QSOs at $z \sim 2-3$, when we observe the peak of QSO activity, we select a sample of six type-1 QSOs at $z \sim 2.5$ and thus we study the main properties of ionised outflows and their effects on the host galaxy. For this goal we use the spectra obtained with the Spectrograph for INtegral Field Observations in the Near Infrared (SINFONI; see Sec. 3.2) in the H (1.45 - 1.85 μm) and K-bands

(1.95-2.45 μm). At $z \sim 2.5$, the H-band covers the rest frame spectral ranges including the Hβ and [OIII]λ5006lines, while the K-band covers the Hα and [OIII]λ5006 lines location. The [OIII]λ5006 is a good tracer of fast ionised gas and permits a study on the main properties of the ionised outflows, i.e. loss mass rate, energy, morphology, size. On the other hand Hα traces the star formation activity allowing us to test whether the AGN-driven outflows is able to quench star formation in the host galaxy or not.

Finally, in Appendix A we summarise four side projects carried out in parallel. Part of the work used in these projects are developed in this thesis and reused for other goal connected to galaxy evolution.

Summarising, the goal of this thesis is a comprehensive investigation of the BH-galaxy co-evolution over cosmic time through multi-wavelengths observations. In particular, we focus on the main mechanisms (e.g. "negative feedback") connecting the central BH to its host galaxy.

Chapter 3

An Overview On the Instruments

In the last few years ALMA has made remarkable progress on the galaxy evolution investigation in the local and distant Universe. Therefore in this Chapter we briefly introduce the readers to the millimetre extragalactic astronomy and we summarise what are advantages of using millimetre observations. In particular, since most of this thesis is based on data from the interferometer Atacama Large Millimetre/Submillimetre Array, we describe in Section 3.1 the main properties of this facility and go through the basic concept of interferometry. Additionally, we dedicate the Section 3.2 to illustrate the characteristic of the other instrument whose data are used in this PhD thesis: the spectrograph SINFONI mounted ad the ESO VLT. Finally, the last Section 3.3 is dedicated to explaining the properties of a 3D datacubes which are the science outputs from both ALMA and SINFONI observations.

3.1 ALMA: Millimetre Observations

The last few years have seen remarkable progresses in the study of cool, molecular, and atomic gas in the Universe, thanks to millimetre and submillimetre observations. In order to simplify the text, we use the term millimetre to refer wavelength range between 0.1 and 10 mm.

In millimetre (and radio) astronomy the flux density associated with an electromagnetic emission is usually expressed in units of one Jansky[1] or Jy, that is equal to:

$$1\ \mathrm{Jy} = 10^{-26}\ \frac{\mathrm{W}}{\mathrm{m^2\ Hz}} = 10^{-23}\frac{\mathrm{erg}}{\mathrm{cm^2\ Hz}}.$$

Millimetre images usually have intensities (hereafter S) in units of Jy/beam because the flux density of a point source equals its brightness in this units and because the rms of the image does not depend on the synthesised beam on the instrument. Additionally, at high redshift, the line luminosity can be expressed in the following two ways:

- L_{line}, defined in unit of $\mathrm{L_\odot}$ or $\mathrm{erg/s^{-1}}$;
- L'_{line}, expressed via the integrated source brightness temperature, in units of $\mathrm{K\ km\ s^{-1}\ pc^2}$.

The relation between the two expressions is

$$L_{line} = 3 \times 10^{-11} \nu_{rest}^3 L'_{line}$$

where ν_{rest}^3 is the rest frame frequency of the line. L'_{line} is directly proportional to the brightness temperature $\mathrm{T_B}$ assuming that the source emits like a black body $B(\nu)$. In the low frequency regime

[1] It was named in honour of Karl Jansky, the first radio astronomer

($\frac{kT}{h\nu} \gg 1$) $B(\nu)$ can be approximated as

$$B(\nu) \sim \frac{2\mathrm{kT_B}\nu^2}{c^2}$$

where k and c are the Boltzmann constant and the speed of light, respectively.

3.1.1 Observing in the Millimetre Wavelength Range

Millimetre observations are fundamental for understanding galaxy formation and evolution.

The warm dust emitting at FIR wavelengths is mostly heated by UV radiation produced by young massive stars located in star forming regions. Consequently, the FIR luminosity L_{FIR} and its millimetre Rayleigh-Jeans counter-parts are considered good tracers of star formation activity within galaxies. Moreover since this emission is not affected by dust extinction, FIR and millimetre observations allow us to detect obscured SF regions, totally missing in the optical bands.

Beside permitting to study dust emission, millimetre observations are fundamental for detecting emission and absorption molecular lines. The majority of molecules known to populate the cold ISM emit in the millimetre wavelength range due to rotational transitions, with a density of $\sim$ 70 lines/GHz. These transitions are good diagnostics of chemistry, physics, and dynamics of the ISM from which stars forms.

The most abundant molecule, the hydrogen H_2, can not be directly detected due to the lack of electric dipole moment. The first rotational level ($\lambda \sim 0.03$ mm), accessible only through a quadrupolar transition, is more than 500 K above the fundamental one, while the bulk of molecular hydrogen in a galaxy is around 10-20 K. This implies that only a very small fraction of the cool molecular gas in a galaxy can be studies through H_2 emission in the FIR. However, the second most abundant molecule, the carbon monoxide CO, has low excitation ($\sim$ 5 K for the first excited state) and can be observed in the millimetre wavelength range: CO emission is due to rotational transitions with $\Delta J = 1$ whose levels are excited by collision with H_2. CO(1-0) emission line is usually used as tracers of the molecular gas mass through the linear relation:

$$\mathrm{M(H_2)} = \alpha \mathrm{L_{CO}}.$$

Unfortunately, the conversion factor α is not a constant, but depends on the physical conditions of the gas, i.e. temperature and density. Recent results have found that $\alpha \sim 4$ $\mathrm{M_\odot/(K\ km/s\ pc^2)}$ for Giant Molecular Clouds[2] in the Milky Way and for nearby spirals galaxies (Bolatto et al. 2013). In local starburst galaxies, molecular observations have revealed a conversion factor of $\alpha \sim 0.8$ $\mathrm{M_\odot/(K\ km/s\ pc^2)}$ (Downes & Solomon 1998). It is still debated whether these conversion factors are valid for active galaxies and for astronomical sources at high redshift.

In addition to the $L_{CO} - M(H_2)$ relation, a correlation between the FIR luminosity and L_{CO} has been found. According to Daddi et al. (2010) and Genzel et al. (2010) star-forming galaxies follow:

$$Log(L_{FIR}) = 0.53 + 1.13 \times Log(L'_{\mathrm{CO}})$$

with L_{FIR} in units of $L_\odot$ and L'_{CO} in units of K km/s pc^2. At the highest luminosities, i.e. ULIRGs, SMGs and QSO, Carilli & Walter (2013) derived:

$$Log(L_{FIR}) = -1.74 + 1.37 \times Log(L'_{\mathrm{CO}}).$$

Since L_{FIR} is proportional to the SFR, L_{CO} can be also used as tracer of star formation activity in galaxies. Furthermore the non linear relation between L_{FIR} and L_{CO} implies that the star formation efficiency (hereafter SFE) increases with the galaxy luminosity:

[2]Giant Molecular Clouds are dense ($\sim$ 100 particles/cm^3) regions where the gas is primarily molecular. Their masses range from 10^4 $M_\odot$ to 6×10^6 $M_\odot$ diameters are up to 200 pc, and the typical temperature is $\sim$ 10 K.

$$SFE = \frac{SFR}{M_{H_2}} = \frac{L_{FIR}}{L_{CO}} \propto L_{FIR}^{1+\gamma}$$

where γ is equal to 1.13 and 1.38 for star-forming galaxies and starburst, respectively. The inverse of SFE is the gas depletion timescale $\tau = 1/SFE = M_{H_2}/SFR$ that indicates the time required to convert all molecular gas into stars. The non-linear relation existing between L_{FIR} and L_{CO} translates into a short life ($\sim 10^7$ yr) for the most powerful starbursts. This is consistent with the coevolution paradigm according to which ULIRGs and SMG, which have high $L_{FIR}(> 10^{12}$ $L_\odot$), are a fast evolutionary phase between star-forming galaxies and read-and-dead ellipticals. Recent CO surveys claim that the depletion time in SMG and ULIRGs decreases with redshift. It is of the order of $\sim$ 1 Gyr for ULIRIGs at $z \sim$ 0 and becomes al low as $\sim$ 100 Myr from SMG at $z \sim 2$ (Greve et al. 2005; Combes et al. 2011).

In high angular resolution observations, where the CO emission is spatially resolved, we are also able to trace the kinematics of the molecular gas. In typical star-forming galaxies gas kinematics is generally dominated by (nearly) regular rotation since this population is mainly dominated by secular processes, while outflows, inflows, or a merging scenario perturb the morphology and kinematics of the gas in the disk. A clear signature of massive, energetics outflows extending on kpc scale has been observed in CO(1-0) kinematics in local ULIRGs and QSOs (e.g. Feruglio et al. 2010; Cicone et al. 2012, 2014). These studies show that CO(1-0) profiles are characterised by broad wings with velocity grater than 300 km/s, which deviate from the typical rotation pattern in the Position-Velocity diagram. In these sources the gas depletion time scales due to molecular outflows, ranging from a few hundred million years in starburst galaxies down to just a few million years in galaxies hosting powerful AGNs, are anti-correlated with the presence and luminosity of the AGN itself. Extended emission and kinematic signatures in the CO line profiles indicates that the properties of molecular outflows and are fundamental to probe the nature of AGN - or SF - feedback.

At high redshift ($z > 1$), the ionised ISM can be also studied through FIR atomic fine structure lines (e.g. [CII]158 μm , [NII]205 μm , [OI]63 μm, [OIII]88 μm) that are redshifted in the millimetre wavelength range. The fine atomic structure lines are the major coolants of the cool interstellar gas with $T < 10^4$ K. The ionised carbon [CII] at $\lambda = 158$ μm, emitted by Photo-Dissociation Regions, is the strongest line in the FIR domain, and it could be even 10^3 times stronger than CO(1-0) in star forming galaxies. The ratio $L_{[CII]}/L_{FIR}$ observed in QSO and ULIRGs/SMGs ranges usually around 10^{-4}, reaching up to $\sim 10^{-3}$ in the Milky Way and local star forming galaxies. The ratio $L_{[CII]}/L_{FIR}$ significantly drops at $L_{FIR} > 10^{12}$ $L_\odot$. Even though the reason for this drop is yet to be found, one possible explanation is a reduction in the heating efficiency by photoelectric emission from dust grains in high radiation environments due to highly charged grains. This hypothesis is supported by the $L_{[CII}/L_{FIR}$ ratio decreasing as the dust temperature increases.

The ionised carbon [CII] is a good tracer of both the ionised gas and the cold neutral medium due to a lower ionisation level potential compared to the HI. In particular the detection of [CII] in high-z galaxies indicates a cold neutral medium enriched by heavy metals. Maiolino et al. (2005) was the first to detect [CII] in a QSO at $z \sim 6.4$ revealing a vigorous star formation (SFR$\sim$ 3000 $M_\odot$/yr) in the host galaxy. Later on, high resolution maps of the [CII] line revealed the presence of an ionised outflow extending over 30 kpc from the nuclear centre with an inferred outflow rate > 3000 $M_\odot$/yr, the highest ever found up to now (Maiolino et al. 2012; Cicone et al. 2015).

3.1.2 ALMA

As described in detail above, millimetre observations can be powerful tools in the study of galaxies up to the early phases in cosmic history. The main issue regarding currently existing millimetre instruments is tracing molecular and atomic gas in external galaxies with a limited sensitivity and poor angular resolution.

The majority of astronomical objects in the sky cannot be spatially resolved at millimetre wavelengths with single-dish telescopes. The smallest detail that can be resolved on the image is indirectly

proportional to the size of the primary disc of the telescope:

$$\theta \simeq \frac{\lambda}{D}$$

where θ is the angular resolution in arcsec, D the diameter of the primary disc, and λ the wavelength at which the observations are carried out. The angular resolution is consequently limited by the size of the telescope and typical values for millimetre single-dish telescopes are $\sim 10''$-$20''$.

Interferometry permits to achieve a higher angular resolution thanks to an array of telescopes or antennae acting together so as

$$\theta \simeq \frac{\lambda}{b_{\max}}$$

where $b_{\max}$ is the maximum distance between the antennae.

The Atacama Large Millimetre/submillimetre Array (ALMA) is a millimetre interferometer located on Chajnantor Plateau, in the Atacama desert (Chile) at an altitude of 5000 m. Upon completion, it will consist of 54 antennae with a primary disc of 12 m and 12 antenna of 7 m, for a total collecting area of $\sim$ 6500 m^2. The antennae configuration will cover baselines ranging from 200 m to 18 km, achieving an angular resolution down to $0.005''$at λ ~0.4 mm. The field of view is limited by the primary beam of each individual antenna and is $\sim 10'$. The 7 m antennae and 4 of the 12 m ones will be clustered into the Atacama Compact Array (ACA), with a compact configuration aimed at covering the *uv*-plane (see Section 3.1.3) on short spacings. The goal of ACA is to recover diffuse emission extending on scales larger than few arcsec. Each antenna in ALMA is designed to accommodate up to 10 receiver basebands of 4-16 GHz bandwidth covering most of the wavelength range between 0.3 and 10 mm. Sky images can only be taken in one baseband at a time and in each baseband the astronomical target can be observed in four sub-basebands, the so spectral windows, with bandwidths up to 1.875 GHz and with a spectral resolution down to 3.8 KHz ($\sim$ 0.01 km/s at λ ~3 mm). ALMA is designed for three main scientific cases:

- detecting CO and [CII] emission line in star-forming galaxies at $z \sim 3$ in less than 24 h
- mapping gas kinematics in protostars and protoplanetary discs around young Sun-like stars at a distance of 150 pc
- providing high quality images at angular resolution of at least $0.1''$

Before the completion of the project, ALMA operates with a reduced number of antennae, frequency bands, array configurations, and observing modes. For reference, during ALMA Cycle 3, scheduled from October 2015 to September 2016, at least 36 12-m antennas in the main array will be available, as well as 7 basebands (3,4,6,7,8,9 and 10), and baselines up to 10 km.

ALMA have already shown its capabilities in the very first observations (Science Verification Cycle, Cycle 0, Cycle 1 and Cycle 2). Although the configuration is not yet completed, in the following we present some crucial results regarding galaxy and BH evolution that have been achieved thanks to ALMA millimetre observations.

In the optical domain, cosmological dimming acts reducing the flux of a galaxy (see Calvi et al. 2014, and references therein):

$$I_0 = \frac{I_e}{(1+z)^4},$$

where I_0 and I_e are the observed and intrinsic surface brightness of the object, respectively. Differently, in the millimetre range the intrinsic observed luminosity increases as a consequence of the steeply rising submillimetre continuum which more than compensate cosmological dimming. The left panel of Figure 3.1 shows the observed flux distribution for a star-forming galaxy at different redshifts, in particular the flux observed at 1 mm is unchanged within the redshift range $z = 1 - 10$, while at ~2 mm the flux for the $z \sim 10$ galaxy is higher than than at $z \sim 1$. This effect counteracts completely cosmological dimming, so that detecting a source at $z \sim 10$ is as easy as detecting a source a $z = 1$

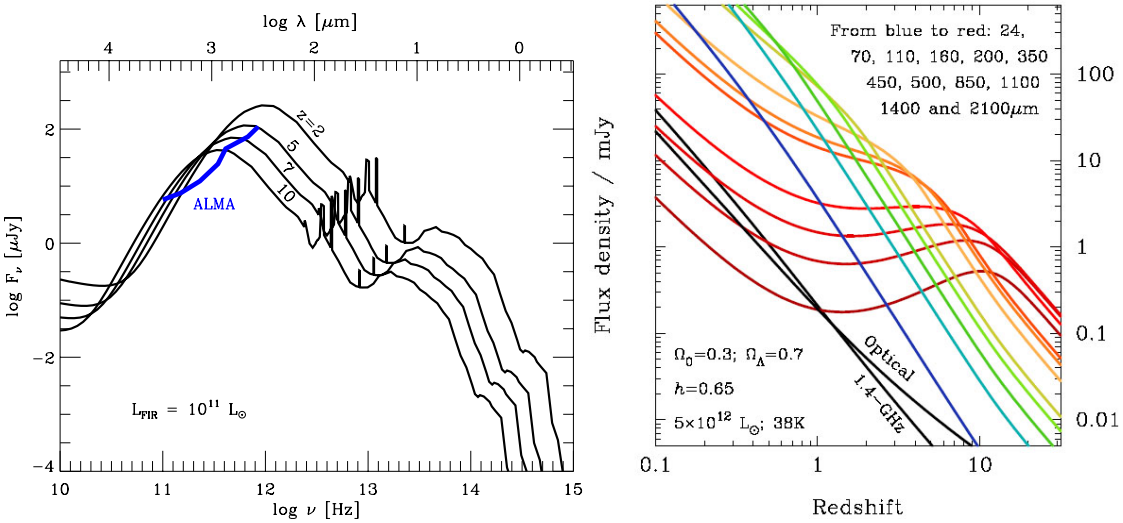

Figure 3.1: *Left Panel*: Observed SED of a star-forming galaxy with $L_{FIR} = 10^{11}$ $L_{\odot}$(scaled from the SED of M82) at different redshifts (z =2, 5, 7 and 10, as labeled). Note that the observed flux at $\lambda_{obs} \sim 1$ mm changes very little. The thick blue shows the ALMA sensitivities for continuum detection at 5σ with an integration of 105 sec. Maiolino et al. (2005). *Right panel*: Predicted flux density for a dusty star-forming galaxy as a function of redshift in various wavelength ranges. The predicted flux densities in the optical (λ_{obs} = 5500 Å) and radio (ν_{obs} = 1.4 GHz) domain are shown for comparison.

with similar intrinsic luminosity. The right panel of Figure 3.1 shows the same effect by plotting the observed flux in several ALMA bands as a function of redshift for a given starburst template. As mentioned above, the trend in ALMA band 7 (~0.85 mm) is nearly flat for $1 < z < 10$, while the optical predicted flux density at $z \sim 1$ is about two orders of magnitude fainter than in millimetre observations. However a high sensitivity is not sufficient to observe primeval faint galaxies, since as described in Section 1.1.3, the density of faint sources is higher than the bright ones and the poor angular resolution of a single dish telescopes ($\sim$ 10 $''$) is not sufficient to resolve into individual sources. Thanks to ALMA high sensitivity and angular resolution, the study of the faint end of the LF is no longer a challenge: Hatsukade et al. (2013) detected 15 faint millimetre sources at 1.3 mm. ALMA band 6 observations can thus constrain the faint millimetre source number counts one order of magnitude deeper than previous studies based on single-dish and interferometer telescopes (Figure 3.2).

ALMA's capabilities are also fundamental to detect emission lines from molecular and atomic gas, e.g. CO, [CII]. Figure 3.3 shows the observed frequency of the CO rotational transitions and atomic fine structure lines as a function of redshift overlaid on the ALMA frequency bands. At $z > 3$ at least two CO transitions are observable within band 3, the most sensitive one, providing a very good determination of the redshift of the source. Weiß et al. (2013) conducted a blind redshift survey in the 3 mm range (band 3) for 26 strongly lensed dusty star-forming galaxies with ($S_{1.4mm} > 20$ mJy): in 12 of these sources multiple lines were detected, while 11 sources show only a single line. The redshift distribution for this sample of galaxies is almost flat between $z = 2 - 4$, with a mean redshift of $z = 3.5$. This result suggests that bright dusty star-formation activity lead to formation of massive galaxies at high redshift. However, at such "high" fluxes the population of millimetre/submillimetre sources is associated with galaxies characterised by extreme SFR ($\sim$ 100-1000 $M_{\odot}$/yr) certainly not representative of the bulk of the galaxy population at any redshift (see Figure 3.2). Future deeper ALMA observations will aim at determining the redshift distribution of the faint millimetre population (SFR < 100 $M_{\odot}$/yr) in order to provide solid constraints on the evolution of galaxies across cosmic times.

The distribution and the properties of cold gas allow the analysis of the complex interplay between accretion (e.g from major/minor merger and inflow of pristine gas) and mass loss (e.g. from stellar and AGN outflows) within galaxies. The [CII] and other fine structure lines are observed with ALMA to

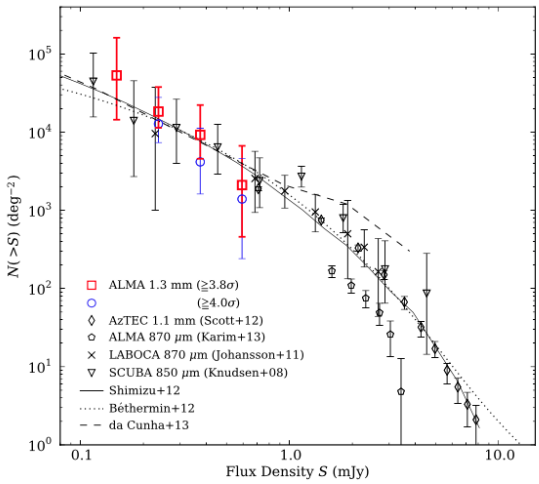

Figure 3.2: Cumulative number counts (see definition in the Chapter 4) at 1.3 mm in the ALMA band 6 (red and blue squares). Other symbols refer to ALMA 870 μm (Karim et al. 2013), AzTEC 1.1 mm (Scott et al. 2012), LABOCA 870 μm (Johansson et al. 2011) and SCUBA 850 μm counts (Knudsen et al. 2008), i.e. data from sub-millimetre single-dish telescopes. The solid, dashed, and dotted lines show the model predictions by Shimizu et al. (2012), da Cunha et al. (2013), and Béthermin et al. (2012), respectively.

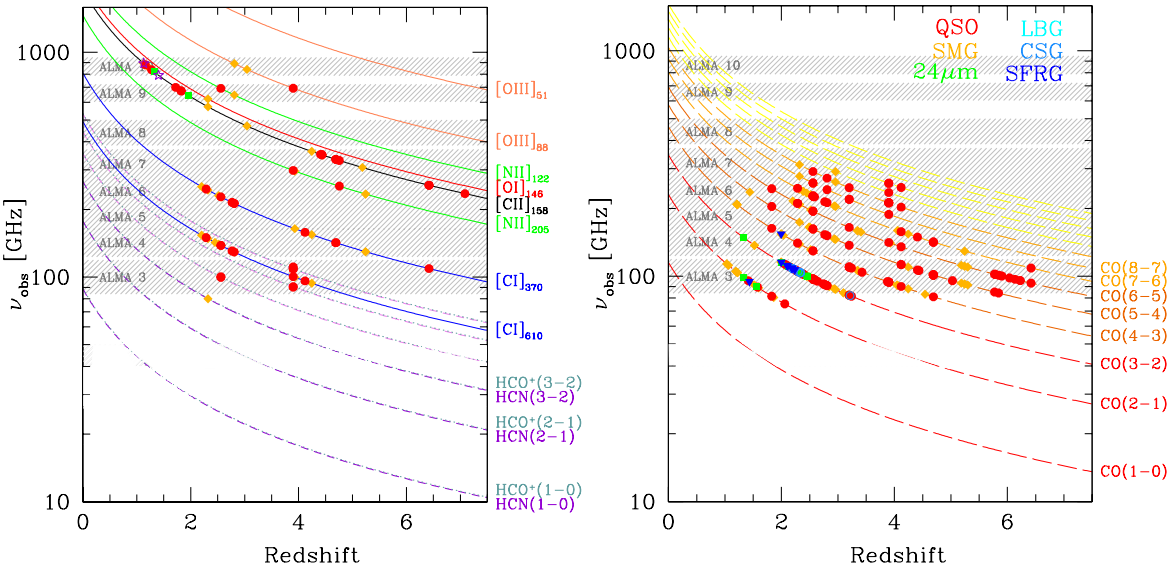

Figure 3.3: Spectral coverage of the molecular lines (left),i.e. CO(J - J-1), and atomic fine structure lines (right) as a function of the redshift, following $\nu_{obs} = \nu_{rest}/(1+z)$. The shaded areas indicate the frequency bands covered by ALMA. The coloured points indicate detection of all high-z lines. The colour code refers to different source types, as explained in the left panel.

resolve the kinematics gas of starburst galaxies at $z \sim 4.7$ (e.g. Wagg et al. 2012; Carilli & Walter 2013; De Breuck et al. 2014). These galaxies with high SFR (> 1000 $M_\odot$/yr) exhibits with clear kinematics signature of rotation, which is unexpected for starburst source. The distribution of the ionised gas suggests that matter accretion may be induced by minor interactions with close satellite galaxies or by inflow of pristine gas from the cosmic web. Furthermore, the study of the interstellar medium in these systems, performed via [NII] and [CII] line emissions, reveals that in bright millimetre sources most of the [CII] emission is associated with the neutral medium rather than ionised one (HII region). Further observations of other fine-structure line (e.g. [OIII], [OI]) will allow us to constrain other galaxies main parameters (e.g. metallicity) in the early Universe.

The atomic and molecular line emission are also fundamental to detect the presence of AGN-driven outflows and for understanding their main mechanisms. During the ALMA-era, a lot of projects proposed during the first Cycles aimed at observing the kinematic of gas in active galaxy. An example is given by the works of García-Burillo et al. (2014) and Sun et al. (2014) who map molecular outflows in local active galaxies by using ALMA CO observations.

Finally, the detection of [CII] at high-z have revealed the main properties of the first star forming galaxies, which are important in understanding the galaxy formation and evolution over cosmic history. Recently, ALMA observations of [CII] at z$\sim$ 7 suggested that molecular clouds in the central part of primordial galaxies are rapidly disrupted by stellar feedback. As a result, [CII] emission mostly arises from more external satellite clumps of neutral gas (Maiolino et al. 2015).

3.1.3 Principles of Interferometry

The response of an astronomical interferometer is the complex visibility $V(u, v)$ that is the Fourier transform of the sky brightness distribution in the sky plane $I(x, y)$:

$$V(u, v) = \int\int I(x, y) e^{2\pi i(ux+vy)} dxdy,$$

where x, y and u, v are the coordinate in the sky and the Fourier plane (also known as uv-plane), respectively. The sky brightness distribution is, consequently, the inverse Fourier transform of the complex visibility:

$$I(x, y) = \int\int V(u, v) e^{-2\pi i(ux+vy)} dudv.$$

Therefore, by measuring the distribution of $V(u, v)$, we are able to recover the sky brightness distribution.

Starting from the theory of interference fringes by Thomas Young, we identify u and v as the projected lengths in the E-W and N-S directions of the antenna separations (baseline) measured in unit of the wavelength at the time of observations. Therefore, for each pair of antenna we measure the complex visibility $V(u_{ij}, v_{ij})$, where i, j indicate the baseline composed by antenna i and antenna j. Since the number of baselines is limited by the number of antennas, the uv-plane is not totally covered and the inverse Fourier transform is no longer the original sky surface brightness $I(x, y)$, but represents the so called "dirty image":

$$I_D(x, y) = \int\int V(u, v) S(u, v) e^{-2\pi i(ux+vy)} dudv$$

where $S(u, v)$ is the sampling function, which is 1 in parts of u, v-plane where we have sampled and 0 we have not. By using the convolution problem, the dirty image can be rewritten as :

$$I_D(x, y) = I(x, y) * B(x, y),$$

with

$$B(x, y) = \int\int S(u, v) e^{2\pi i(ux+vy)} dudv$$

where $B(x, y)$ is the "dirty beam" and it corresponds to the Fourier transform of the sampling function. Since the antenna configuration is known, we can recovering the image $I(x, y)$ with a classical deconvolution process.

In radio and millimetre astronomy the algorithm of deconvolution is called "CLEAN" and it is usually implemented into the data reduction pipeline. All ALMA datasets presented in this thesis have been processed by using the software CASA (Common Astronomy Software Application) that includes the CLEAN algorithm by Clark (1980) needed to obtain the surface brightness images of our target. An important parameter in the CLEANing process is the weight to apply to the data in order to reduce noise fluctuations and the presence of spurious features in the final image. The CASA software comes with three different types of weighting:

- Natural weighting, i.e. all visibility are treated equally, provides the best signal-to-noise in the final images, but minimising the angular resolution.
- Uniform weighting, depending on the density of visibility in *uv*-plane, allows the highest angular resolution at the expense of sensitivity.
- Briggs weighting (Briggs et al. 1999), depends on the parameter ROBUST (R) ranging from −2.0 to 2.0. The result obtained assuming R=-2.0 is similar to the one coming from the uniform scheme, while assuming R=2.0 is similar to using normal weighting. R = 0.5 is a good compromise between sensitivity and angular resolution.

3.2 SINFONI at VLT

The Spectrograph for INtegral Field Observations in the Near Infrared (SINFONI) is a near-infrared (1.1 μm - 2.45 μm) integral field spectrograph mounted in the Cassegrain focus of the 8.2-m Very Large Telescope (VLT) telescope in Chile. The spectrograph operates with 4 gratings (J, H, K, H+K) providing a spectral resolution around 2000, 3000, 4000 in J, H, K, respectively, and 1500 in H+K.

SINFONI uses an "image slicer" technique as shown in Figure 3.4. A two-dimensional image (panel (a)) is chopped into smaller components (32 slices) and re-positioned by special segmented mirrors so that they lie in a line end-to-end instead of on top of each other (panel (b)). This essentially forms a very long virtual slit. The light from the virtual slit is split into separate wavelengths (panel (c)), and the image is then reconstructed from the individual slices at each wavelength, i.e. the image is reconstructed from all slices at the red end of the spectrum, then the green, etc. They are then combined to give us the final 3D information (panel (d)), the so-called datacube.

Pre-optics allow to chose the angular size of the slices on the sky. The choices are 0.″250, 0.″100 and 0.″025 mas, leading to field of views on the sky of 8″×8″, 3″×3″and 0.″8×0.″8 respectively. Each one of the 32 slitlets is imaged onto 64 pixels of the detector. Thus, one obtains $32 \times 64 = 2048$ spectra of the imaged region of the sky. Typical limiting magnitudes (S/N = 10 in 1h on source) are around 17-18 mag in J, H, K.

SINFONI can be used with or without an adaptive optics (AO) module. The observations presented in this thesis have been taken without the AO module, so the spatial resolution is dictated by the natural seeing.

3.3 Datacube

The data-reduction procedures of both ALMA and SINFONI provide in output a so-called datacube, a 3D image with spatial coordinates as the first two axes (x,y) and the wavelength (or frequency or velocity) as third axis (z). In the following we will either refer to spaxels or (spatial) pixels as the bins in the spatial coordinates plane, while the wavelength bins will be named either channels or spectral channels. The size of the spatial pixels and spectral channels depends on the instrument and the data reduction pipeline.

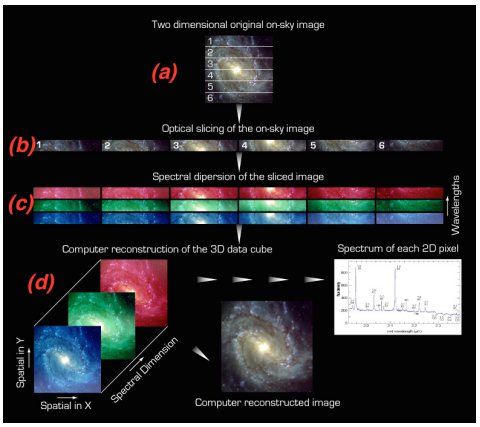

Figure 3.4: The principle of a integral field spectrograph, like SINFONI. See the text for details.

Figure 3.5 shows a schematic diagram of a datacube. Extracting a plane in the z-axis, we obtain a image of the astronomical source at fixed wavelength (or frequency). When we extract an array from a fixed x,y coordinate, we are looking at a spectrum at a fixed position in the sky plane.

Broad continuum observations refer to an image obtained collapsing (summing) over all the spectral channels of the datacube. This image, also called continuum image (or continuum observation), is obtained from free-line channel. In other words, when we generate the continuum we exclude channels that contain both emission and absorption lines.

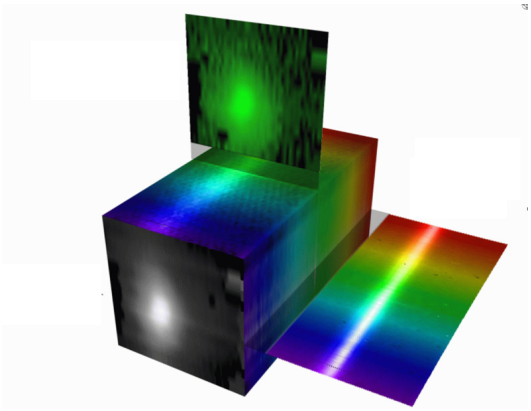

Figure 3.5: Schematic diagram of a datacube showing how it provides information in three dimensions: two spatial dimensions x,y and a third dimension of wavelength. It is possible to obtain an image of the target at a single wavelength or collapsed over wavelength slices. Furthermore, at every spatial pixel of the datacube a spectrum can be extracted.

Chapter 4

The Early Star-Forming Galaxies

Based on:
Carniani, S. et al. 2015: ALMA constraints on the faint millimetre source number counts and their contribution to the cosmic infrared background; A&A, 584, A78.

Millimetre wavelength surveys have now established the important role of dusty, star-forming galaxies in the assembly of stellar mass and the evolution of massive galaxies in the Universe. In fact, dust-obscured star formation is known to be a major contributor to the cosmic star formation history. Galaxies selected by thermal dust emission at submillimetre wavelengths are therefore thought to play an important role in the rapid build-up of the stellar population within massive systems.

High-z observations have found a median redshift of $z = 2 - 3$, which corresponds to peak of cosmic QSO activity, for millimetre sources at fluxes S > 1.0 mJy. However, at such "high" fluxes the population of millimetre/submillimetre sources is associated with galaxies characterised by extreme star formation rates of $\sim 100 - 1000$ $M_{\odot}$/yr, certainly not representative of the bulk of the galaxy population at any redshift (see Figure 3.2). Since the "old" definition of SMG is a galaxy emitting at millimetre wavelengths with high SFR (> 100 $M_{\odot}$/yr), in this work we call millimetric sources the whole population of galaxy that emits mainly at millimetre wavelengths, regardless of their relative SFR.

The density distribution of millimetric sources as a function of the flux density provides strong constraints for modelling the formation and evolution of galaxies. The issue of reliable millimetric sources density distribution measurement, needed to robustly constrain the theoretical models, is obviously an area where the ALMA will have significant impact. Having its capability of high angular resolution and sensitivity, ALMA enables us to investigate the faint submillimetric and millimetric sources with the negligibly small uncertainties of the source confusion and blending, which are not observable so far with previous millimetric single-dish telescopes.

Our goal is to compare density distributions of SMGs, based on ALMA observations, with predictions from recent models. Previous blank surveys of submillimetre sources have provided strong constraints on models of galaxy formation, but observations of fainter sources are needed to understand the evolution and coevolution of BHs and galaxies.

The following analysis is based on ALMA observations carried out during the 2012 and 2013 campaigns, so far the highest sensitivity observations in the submillimetre wavelength range. These observations enables us to explore faint (down to 60 μJy) sources, twice deeper than previous millimetric observations. The source counts presented here thus provide constraints on models of galaxy evolution and predictions for future ALMA follow-up surveys.

This chapter is organised as follows. In Section 4.1, we briefly discuss which is the contribute of millimetric sources to the Extragalactic Infrared Background and the results achieved so far at this wavelength. Then we present our sample of observations in Section 4.2 and we focus on the source

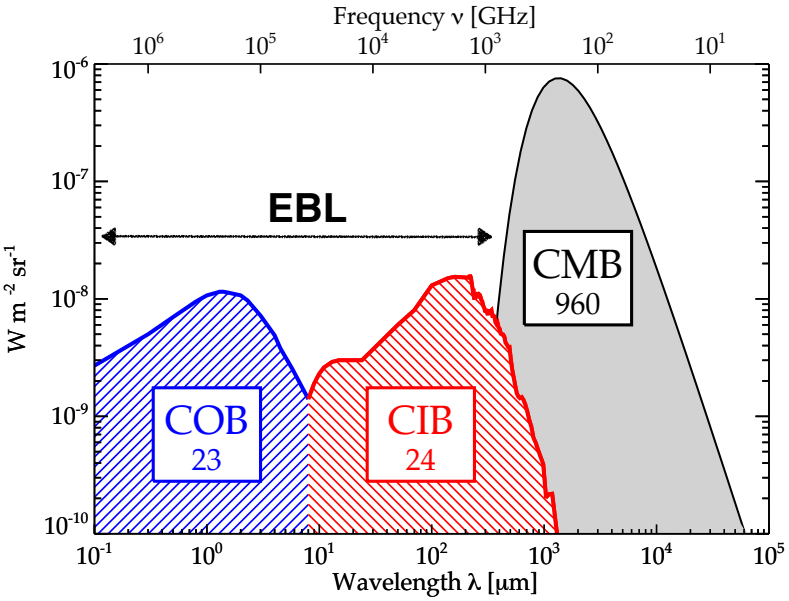

Figure 4.1: Illustration of the EBL intensity, with the COB in blue and the CIB in red. The CMB is shown as well. The numbers indicate approximate the total intensity of each single component in unit of nW m^{-2} sr^{-1}; note the total intensity of COB is comparable with that of CIB. Image from Dole et al. (2006)

extraction technique in Section 4.3. Section 4.4 presents the number counts[1] we derived and the comparison between our results and recent galaxy formation models. In Section 4.5, we discuss and summarise our results.

4.1 Radiation Background

The extragalactic background light (EBL) is a diffuse and isotropic radiation in the Universe, covering the range between ultraviolet and far-infrared wavelengths (Fixsen et al. 1998). After the Cosmic Macrowave Background (CMB), the EBL represents the second-most energetic background. The IR/mm spectrum of the EBL was first estimated by Puget et al. (1996) using data from Far Infrared Absolute Spectrometer on the Cosmic Background Explorer (COBE) satellite. The EBL spectral energy distribution is composed of two peaks: the cosmic optical background (COB) and the cosmic infrared background (CIB). The former is caused by the radiation from stars, while the latter is due to UV/optical light absorbed by dust and re-radiated in the infrared wavelength range. By measuring the integrated flux of the two components, the ratio between the COB and CIB is of the order of unity (Dole et al. 2006), suggesting that half of the star light emission is absorbed by dust in galaxies (Figure 4.1). Therefore, the EBL contains information about star formation processes and galaxy evolution in the Universe. The study of this emission helps us to understand the star formation evolution over the history of the Universe.

The mixture of source populations contributing to the CIB depends strongly on the specific wavelength (e.g. Viero et al. 2013; Cai et al. 2013). At millimetre wavelengths ($\lambda \sim 1.1 - 1.3\ \mu m$), a significant percentage ($\sim 30\%$) of the CIB is emitted by submillimetre galaxies (e.g. Viero et al. 2013; Cai et al. 2013). Recent studies have shown that massive red-and-dead galaxies share the same clustering properties as bright SMG. Thus, SMGs may be the progenitors of local massive elliptical galaxies (Simpson et al. 2014; Toft et al. 2014).

[1] Galaxy number count is defined as the number of galaxies per magnitude (or flux density) interval and square degree in the sky, as a function of the apparent magnitude (or flux density) in a certain photometric band.

As already mentioned, SMGs represent an extreme class of objects, not representative of the bulk of the galaxy population at high-z ($z \gtrsim 1$). Most high-z galaxies show a much lower SFR and are likely associated with systems that evolve through secular processes (e.g. Rodighiero et al. 2011). For the bulk of the high-z population, the rest-frame far-IR/submm properties (which provide information on obscured star formation and dust content), are still poorly known at mm/submm fluxes below 1 mJy.

In the past decades the SCUBA and LABOCA single-dish surveys resolved 20% to 40% of the CIB at 850 μm (e.g. Eales et al. 1999; Coppin et al. 2006; Weiß et al. 2009) and 10% to 20% of the CIB at 1.1 mm with deep single-dish surveys using the AzTEC camera (e.g. Scott et al. 2010). Until recently, the number counts of fainter sources ($S < 1$ mJy) were not well constrained because of the limited sensitivity. However, the observation of lensed galaxies, hence reaching somewhat deeper flux limits (e.g. Cowie et al. 2002; Knudsen et al. 2008; Johansson et al. 2011; Chen et al. 2013b,a) suggests that more than 50% of the CIB is emitted by faint sources with flux densities < 2 mJy.

Recently, the number counts of faint mm sources, at fluxes fainter than 1 mJy, have been inferred thanks to high-sensitivity and high-resolution observations obtained with ALMA. Hatsukade et al. (2013) claim to have resolved $\sim$ 80% ($\sim$ 13 Jy deg^{-2}) of the CIB at 1.3 mm exploring faint (0.1 - 1 mJy) sources with signal-to-noise (S/N) $\geq$ 4 extracted from ALMA data. A similar result has been obtained at 1.2 mm by Ono et al. (2014), who suggest that the main contribution to the CIB comes from faint star-forming galaxies with SFR < 30 $M_\odot$/yr. However, as we discuss later, the uncertainties on the CIB spectrum are large, and once these are taken into account, the fraction of resolved background at these fluxes, as well as the identification of the sources contributing to the bulk of the CIB, are much more uncertain than is given in these papers. Source number counts with deep millimetre observations can provide a tight lower limit on the CIB intensity. Moreover, the slope of the faint counts constrains contributions to the CIB from still fainter sources.

4.2 Data

Our source extraction is applied to 18 continuum maps with high sensitivities, which were obtained in ALMA cycle 0[2] and cycle 1[3]. For our analysis we focused on observations in band 6 (λ = 1.1 − 1.4 mm) and 7 (λ = 0.8 − 1.1 mm), since these are some of the deepest observations available.

The faintest sources are detected in three ALMA datasets taken by Maiolino et al. (2015) who targeted three Lyα emitters[4] at z~6-7: BDF-3299, BDF-521 and SDF-46975 (Vanzella et al. 2011; Ono et al. 2012). The BDF-3299 data (field *a* in Tab. 4.1) were observed during two different epochs: a first observation in October-November 2013 and a second one in April 2014. The target was observed with 27 12m antennae array in 2013 and 36 12m antennae array in 2014, with a maximum baseline of 1270 m. The flux densities were calibrated with the observation data of J223-3137 and J2247-3657. The total on source integration time was ~5.2 hrs. The other two sources, BDF-521 and SDF-46975, were observed in November 2013 and March 2014, respectively (field *c* and *e* in Tab. 4.1). 29 12m antennae were used in the extended configuration of 17-1284 m baseline for BDF-521 and 40 12m antennae with maximum baseline of 422 m for SDF-46975. We used the observations of J223-3137 to calibrate the flux density. The total on source observing time was about 83 min and 121 min, respectively for the two targets.

We analysed 9 continuum maps (fields *j-r* in Tab. 4.1) taken by Capak et al. (2015), who targeted [CII] emission line from sources at high-redshift ($z \geq 5$). The data were taken in November 2013 using 20 antennae in band 7. The total on source integration was about 20 min for each.

We also used ALMA data (field *b* in Tab. 4.1) for the Lyα emitter at z = 7.215, SXDF-NB1006-2 (PI K. Ota; Shibuya et al. 2012). The target was observed on May 3-4 2014, with a maximum baseline

[2]Cycle 0 observations started on September 30, 2011 and ended on August 31, 2012

[3]Cycle 1 observations extended from the end of October 2013 to the end of May 2014

[4]Lyα emitters are galaxy at high redshift (z>1) that have been decide through their strong emission of Lyα radiation. The Lyα is usually caused by an ongoing outburst of star-formation.

Table 4.1: ALMA Survey fields used in this paper, sorted by sensitivity.

Project code	ν_{obs} [GHz] (1)	σ [μJy beam^{-1}] (2)	λ [mm] (3)	area [10^{-4} deg^2] (4)	field
2012.A.00040.S	230	7.8	1.28	1.17	a
2012.1.00374.S	225	14.5	1.31	1.17	b
2012.1.00719.S	230	17.7	1.30	1.17	c
2011.1.00115.S	260	18.6	1.16	0.87	d
2012.1.00719.S	244	19.5	1.23	1.06	e
2011.1.00243.S	250	20.9	1.2	0.97	f
2011.0.00767.S	230	20.9	1.30	1.17	g
2012.1.00142.S	230	26.3	1.28	1.07	h
2011.1.00243.S	249	28.9	1.2	0.97	i
2012.1.00523.S	286	29.9	1.05	0.72	j
2012.1.00523.S	295	30.0	1.02	0.71	k
2012.1.00523.S	286	30.3	1.05	0.72	l
2012.1.00523.S	289	33.1	1.05	0.72	m
2012.1.00523.S	290	36.3	1.03	0.71	n
2012.1.00523.S	289	38.1	1.05	0.72	o
2012.1.00523.S	289	41.8	1.05	0.72	p
2012.1.00523.S	292	49.1	1.02	0.71	q
2012.1.00523.S	292	52.1	1.02	0.71	r

of $\sim$ 558 m. The total on source observing time of the 37 12 m antennae was 106 min. The flux densities were scaled with the observation data of J0215-0222.

In addition to these maps, we analysed public archival ALMA data to increase the number of detections at intermediate flux densities. We selected only continuum maps in band 6 and 7 with sensitivity $\leq$ 50 μJy/beam, since we were interested in analysing the number count at flux densities $<$ 1 mJy that contribute to $>$ 60% of the CIB (Ono et al. 2014). Therefore, we analysed the data with the highest sensitivity taken by Willott et al. (2013) (fields *f* and *i* in Tab. 4.1) , Ota et al. (2014)(fields *g* in Tab. 4.1) , MacGregor et al. (2013) (fields *h* in Tab. 4.1) and Ouchi et al. (2013) (fields *d* in Tab. 4.1). Further details on the ALMA observations are summarised in those papers.

All ALMA datasets were data processed by using the CASA v4.2.1 package. The parameters of clean are set up in order to obtain final images with sensitivity as high as possible (see Section 3.1.3). In the case of our data, BDF-3299, BDF-521 and SDF-46975, we were able to achieve a sensitivity in the range between 7.8 μJy/beam (which is the deepest ALMA observation at this wavelength, three times deeper than data used in previous studies) and 52.1 μJy/beam. The correlator of each observations was configured to provide four independent spectral windows, so the central frequency ν_{obs} in Table 4.1 is equivalent to the mean frequency of the four bands. The continuum map sensitivity and the area mapped in each observation are summarised in Table 4.1. The source extraction was performed out to two primary beams, after masking the targeted source of each observation, so as to not bias the final counts determination. Around all of these sources we placed 1″ diameter mask ($\sim$ ALMA beam) since most of the main targets were non spatially resolved. In the particular case where the main target is extended (e.g. MacGregor et al. 2013) the dimension of the mask is as large as the size of the target, where the size of the target is estimated from its surface brightness emission down to 3σ. In the worst case we masked about 5% of the field of view. The combined fields result in a total area of $\sim 9.5 \times 10^{-4}$ deg^2 at 1.1 mm and $\sim 6.6 \times 10^{-4}$ deg^2 at 1.3 mm (which is globally two times larger than previous studies).

4.3 Source Extraction

In total we analysed 18 ALMA continuum maps to derive the number counts of sources at millimetre wavelengths. Since we do not yet know either the SEDs or the redshifts of our faint mm sources, we estimated the number counts at two different wavelengths, 1.1 mm and 1.3 mm, to minimise the effects of wavelength extrapolation. The flux densities, S, of sources detected at wavelengths less than 1.2 mm were scaled to the 1.1 mm flux density while counts at $\lambda >$ 1.2 mm were scaled to 1.3 mm using a modified blackbody (see Section 4.3.4) with values typical of SMGs at z=2. We adopted a spectral index β = 2.0 and dust temperature T = 35 K from Greve et al. (2012), who measured the spectral energy distribution from a sample of SMGs at the same wavelength range of our data. Recent works (Hatsukade et al. 2013; Ono et al. 2014; Fujimoto et al. 2015) have combined ALMA observations at 1 mm and at 1.3 to extrapolate the number counts a 1.2 mm to reduce Poisson error. However, the merging of the two bands introduce larger error in the flux density as well explained in the s Section 4.3.4. In the following we describe in detail the source extraction method and the statistical assessment.

4.3.1 Source Catalogue

The source extraction was performed within an area as large as two primary beams, which has a diameter of about 20", before correcting for the primary beam attenuation[5]. We first extract the sources fulfilling the following requirement: 1) the source should be above the 3σ threshold in its continuum map (we will then take a more conservative threshold of 3.5σ, as discussed later on); 2) the size of the 2D Gaussian fitting the putative source must be consistent, within the errors, with the beam size of the selected map (or at most marginally resolved, within 1.5 times the beam size). Indeed, most faint sources are not expected to be spatially resolved at the resolution of our maps. Detections with dimensions smaller than the beam must be associated with noise fluctuation of individual antennae or a group of antennae, or due to sidelobes of bright sources.This additional source detection criterion enables us to greatly reduce (by a factor of 3) the number of spurious sources hence making the final catalogue much less plagued by false detections than previous studies.

Figure 4.2 shows an example of an ALMA map in which the source extraction was performed down to 3σ with the above requirements. At this low significance level ($> 3\sigma$), some of these source candidates are likely to be spurious, due to noise fluctuations. To define a more solid detection threshold, we estimated the number of spurious sources expected in the maps by applying the source extraction method to the continuum maps multiplied by -1, so as to estimate the number of negative sources as a function of the signal-to-noise ratio (S/N). Top panel of Figure 4.3 shows the number of positive and negative sources as a function of S/N. The number of the negative sources is almost always less than that of the positive at S/N > 3, suggesting that down to 3σ some fraction of the positive detections are real (most of the negative sources and false positive sources are removed from the second requirement in the source extraction process). This is also clear from the fact that the cumulative number of positive sources is larger than that of the negative ones down to S/N =3 (bottom panel of Figure 4.3). Moreover, simulations of blank fields, with exactly the same observing conditions as our data (Section 4.4.2), show that the number of positive and negative sources due to noise fluctuations are equal for any S/N level. Since in previous works from Hatsukade et al. (2013) and Ono et al. (2014) the number of positive sources was found to be larger than the number of negative ones at S/N > 3.5, we decided to be conservative and include in our catalogue only those objects satisfying the S/N > 3.5 criterion.

In the 18 continuum maps we detected 50 sources with S/N in the range 3.5-38.4 and none of them appear to be marginally resolved. Such statistics is a factor of four higher than previous studies (Ono et al. 2014).

[5]The final image obtained by clean process is a representation of the sky multiplied by the primary beam response of the antennas. Thus, the rms in the final image is spatially uniform in the whole field of view.The primary beam response is typically similar to a 2D-Gaussian function, although it also has sidelobes.

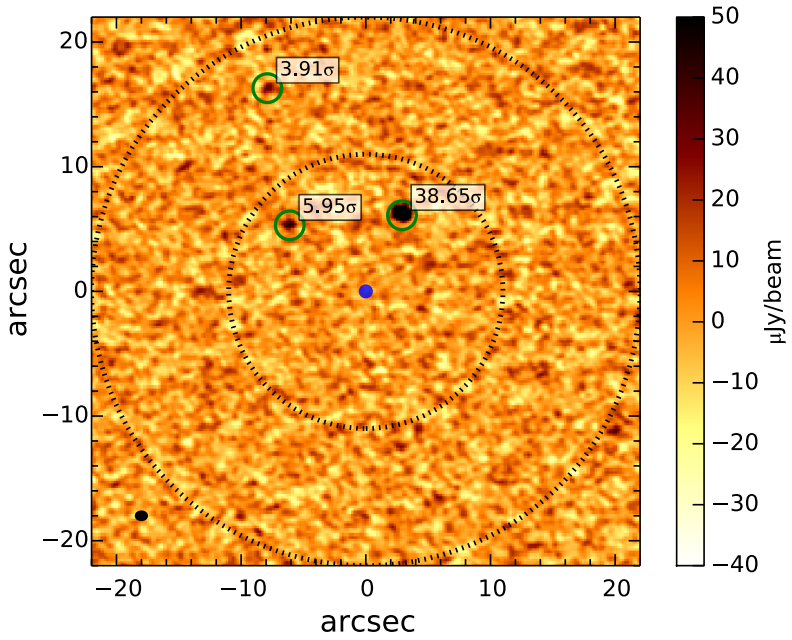

Figure 4.2: Example of a band 6 continuum map obtained with ALMA (field *a* Table 4.1). The green circles represent the sources detected with S/N > 3.5σ that also fulfil the requirement of having a size consistent with the beam (or marginally resolved). The inner black dotted circle indicates the primary beam and outer circle shows twice the primary beam. The blue filled circle shows the masked region. The synthesised beam is indicated by a filled black ellipse in the lower left corner of the plot.

4.3.2 Completeness and Survey Area

For each ALMA map i, we estimated the completeness, $C_i(S)$, that is the expected probability at which a real source with flux S can be detected, within the entire field of view considered by us (i.e. two primary beams). $C_i(S)$ is calculated in each ALMA map corrected for primary beam attenuation. To estimate the completeness we inserted artificial sources with a given flux density S (at which we want to estimate the completeness). The positions of these artificial sources are randomly distributed within the 2-primary beams. The input source is considered to be recovered when it is extracted with S/N≥ 3.5σ. Within the selected flux densities range (0.05 to 1 mJy) we iterated the procedure of inserting artificial sources for each continuum map 1000 times, using 4-8 artificial sources in each simulation for each field. The completeness calculated in each map, $C_i(S)$, is equal to the ratio between the number of recovered sources and the number of input sources, for each flux S. Figure 4.4 shows $C_i(S)$ as a function of the intrinsic flux density S, estimated on the deepest ALMA continuum map (field *a* in Table 4.1).

The beam response is not uniform and decreases with increasing distance from the map centre. Therefore the effective area sensitive to a given flux S decreases rapidly with the flux itself. As a consequence, the effective area of the survey depends on the considered flux, i.e. $A_{\rm survey}(S)$. Since the completeness $C_i(S)$ is estimated on the continuum maps corrected for primary beam attenuation, the completeness function already automatically includes the effect of variation of sensitivity as a function of distance from the map center. Therefore, the effective survey area of each map at a given flux S is given by $C_i(S)A_i(S)$, where $A_i(S)$ is the 2-primary beam area of the ALMA map i. Therefore, the total effective survey area is given by

$$A_{\rm survey}(S) = \sum_i C_i(S)A_i(S)\,.$$

We obtained $A_{\rm survey}(S)$ both at 1.1 mm and at 1.3 mm, as shown in Figure 4.5.

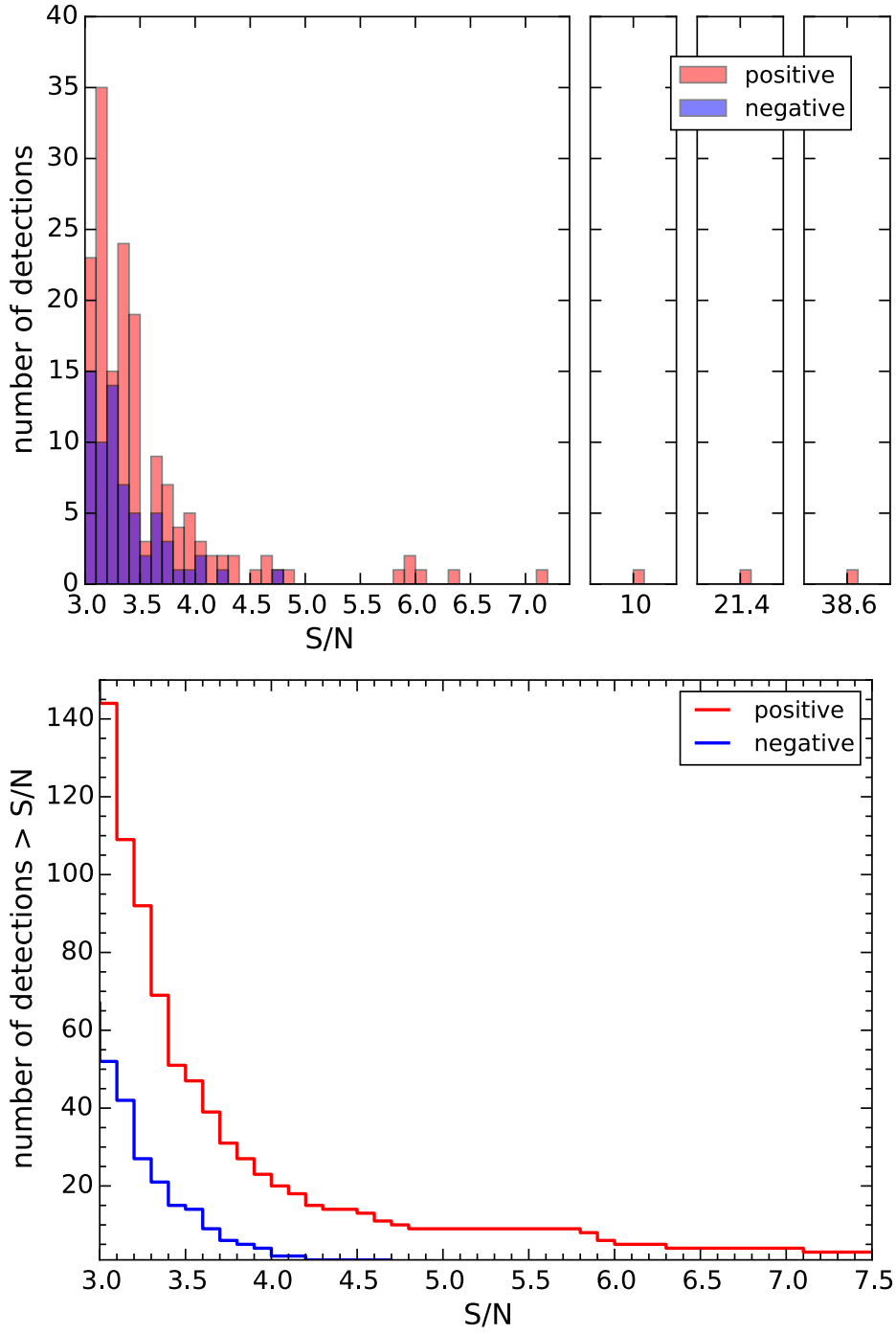

Figure 4.3: *Top:* number of positive (red) and negative (blue) sources, detected in the 18 continuum maps, as a function of signal-to-noise ratio (S/N). *Bottom:* cumulative distribution of positive (red) and negative (blue) detections.

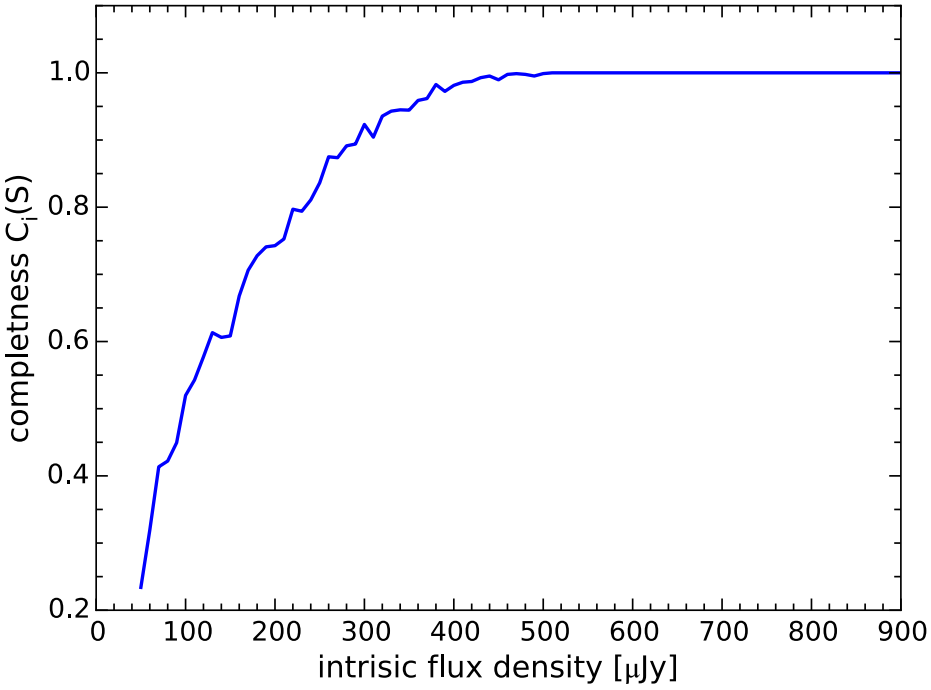

Figure 4.4: Completeness $C_i(S)$ as a function of the flux density S estimated from simulations. The solid curve is the result for field a with rms = 7.8 μJy/beam.

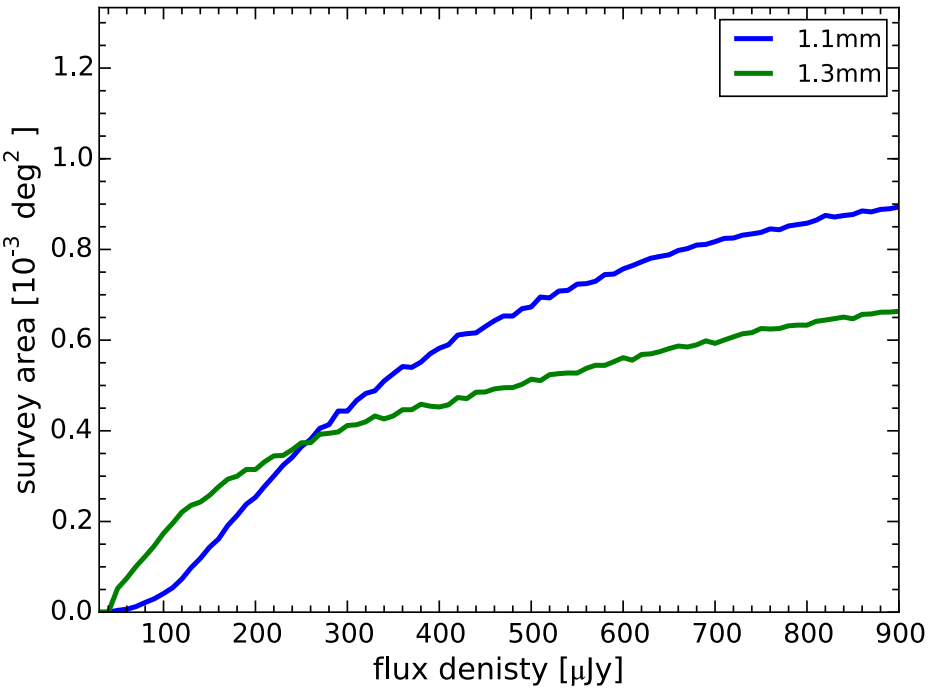

Figure 4.5: Effective survey area as a function of intrinsic flux density. This is the area over which a source with an intrinsic flux density S can be detected with $S/N > 3.5\sigma$. The blue and green curves are the survey areas for the maps at 1.1 mm and 1.3 mm, respectively.

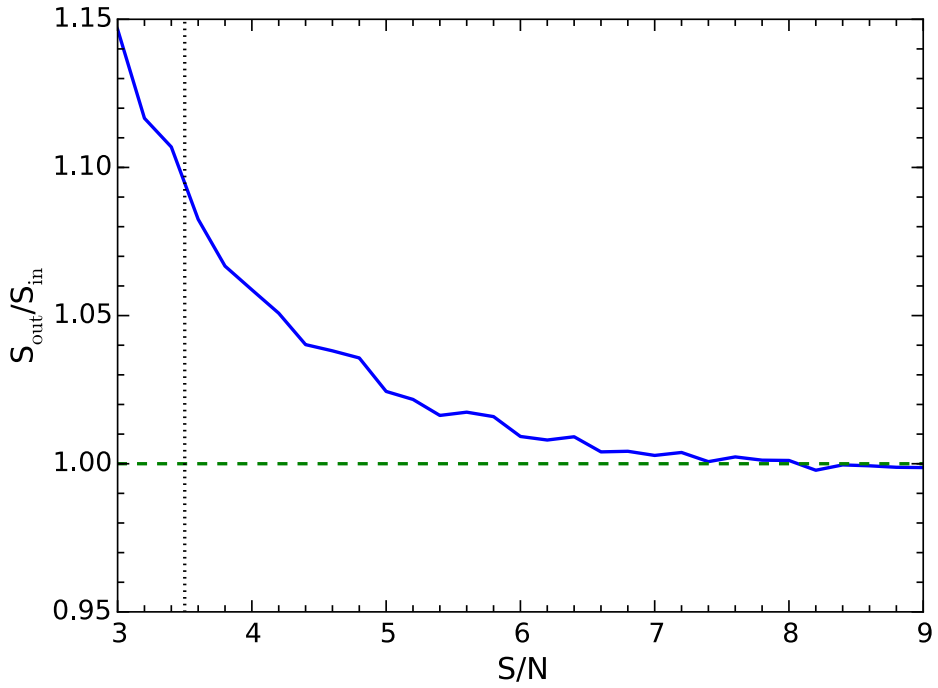

Figure 4.6: Flux boosting factor as a function of S/N estimated from simulations. The horizontal dashed line corresponds to $S_{out} = S_{in}$. The vertical dashed line corresponds to the detection threshold, S/N = 3.5.

4.3.3 Flux Boosting

The noise fluctuations in continuum maps may influence photometric measurements of the extracted sources. Since the counts of faint sources increase with decreasing flux density (see Section 1.1.3; e.g Scott et al. 2012; Hatsukade et al. 2013; Ono et al. 2014), there should be a 'sea' of faint source below the noise level that may influence photometric extraction. There is, indeed, a greater probability that intrinsically faint sources are detected at higher flux than that bright ones are de-boosted to a lower flux. See Hogg & Turner (1998) and Coppin et al. (2005) for a full description of this effect. This effect, called "flux boosting", is extremely important at low S/N (< 5) where flux measurement can be overestimated. Since we do not know the priori distribution of flux densities in the range 0.001-1 mJy, we performed a simple simulation to estimate the boost factor as a function of S/N detection.

The simulation was carried out in the map uncorrected for primary beam attenuation. We inserted into the maps flux-scaled artificial sources (4-8), whose S/N are in the range of 3-8. Then, we extracted the flux densities at the same position where the sources have been located. The *a priori* knowledge of the source position in this process may lead to underestimate the flux boosting correction as the noise in the maps may lead to an offset in the recovered position of mock (or real) sources. However this effect is maximum when sources are near a noise peak. Since the number of mock (or real) sources in each continuum map is low (<10), the probability that a artificial (or real) source is near to a noise peak is lower than 5%. In conclusion, the error on the flux boosting factor due to the *a priori* knowledge of artificial source position is small (< 5%). The flux boosting is calculated as the ratio of the measured flux density (S_{out}) to the input flux density (S_{in}). We repeated this simulation for each ALMA continuum map 10^4 times. Figure 4.6 shows the average ratio of the extracted flux densities S_{out} to the input flux densities S_{in} as a function of S/N. At S/N = 3.5, the boost fraction is ≃1.09, so the difference between extracted flux and input flux is less than 10%. The boosting factor correction (Figure 4.6) was then applied to the measured detection fluxes.

4.3.4 Flux Error

None of the detected sources in this work has a spectroscopic redshifts, which prevents us from determining their SED and their flux densities at different wavelengths. In Section 4.4.1, we scaled the flux density of the sources observed at $\lambda < 1.2$ mm to the flux density at 1.1 mm and the sources observed at $\lambda > 1.2$ mm are scaled to the flux density at 1.3 mm, by assuming a SED given by a black body law modified with a spectral emissivity that varies physically such that the dust opacity reaches unity at frequency ν_0 (Blain et al. 2003):

$$f(\nu) \propto (1 - e^{-(\nu/\nu_0)^\beta}) B(\nu, T)$$

where ν is the frequency a rest frame, T is the dust temperature, β is the dust emissivity index, and $B(\nu, T)$ is the Planck function. Following Draine (2006) who studied properties of interstellar dust of protoplanetary disk, we assume a $\nu_0 = 3000$ GHz and $\beta = 2$. Then we fix $z = 2$ and $T = 35$ K from recent observations of a sample of bright ($S_{1.4mm} > 15$ mJy) millimetre sources (Greve et al. 2012). However, we are aware of the fact that only one photometric value for each source is not enough to constrain the properties of SEDs of our sample. Therefore, we estimate how the assumed SED properties affect the outcomes of the flux scaling procedure. To this aim, we vary the SED properties in the following ranges: $1 < z < 6$, $20 < T < 60$ K, $1.5 < \beta < 2$.

The errors are estimated as the maximum scatter obtained by varying these parameters with respect to the typical SED used in our observations. Figure 4.7 shows the flux error (red error bars) associated with each continuum map resulting from scaling the flux density of the sources observed at $\lambda \leq 1.2$ mm to the flux density at 1.1 mm and those at $\lambda > 1.2$ mm to the flux density at 1.3 mm. At 1.3 mm, the flux errors are smaller than those at 1.1 mm since the wavelength range of observations is smaller ($\Delta\lambda \sim 0.15$ mm) than at 1.1 mm ($\Delta\lambda \sim 0.20$ mm). The blue error bars show the flux error resulting from scaling all observations to a common average wavelength of 1.15 mm. The latter show that by rescaling all our ALMA observations to a single common wavelength there is, in most cases, a significant increase of the flux errors. Indeed, at 1.1 mm the flux errors approach 30%, while at 1.3 mm the flux errors are at least twice as large as those resulting from splitting the number counts in two different wavelength ranges. Since we aim at minimising the flux errors as much as possible (and keeping them lower than the size of our flux bins), we split the number counts into two different wavelength ranges so as to reduce the flux errors associated to each detected source, at the sacrifice of having slightly worse statistics.

4.4 Results

Summarising the previous sections: we detected 50 sources with S/N > 3.5 in 18 continuum maps in the ALMA bands 6 and 7. Then, we corrected the flux densities for the "flux boosting" effect. In the following we discuss the additional steps required to infer the sources number counts and the comparison with the CIB.

4.4.1 Differential Number Counts

We scaled the flux density of the sources observed at $\lambda < 1.2$ mm to the flux density at 1.1 mm and those at $\lambda > 1.2$ mm to the flux density at 1.3 mm. The reason for splitting the sources in these two wavelength ranges is that this significantly reduces the uncertainties on the flux obtained from the extrapolation, as described in Section 4.3.4. With this strategy the error on the flux associated to each source is always less than 18%. Following the prescription of Hatsukade et al. (2013) and Ono et al. (2014) we estimated the number counts at two different wavelengths: 1.1 mm and 1.3 mm. We then estimated the effective survey area associated with the flux of each source. To estimate the number counts, we corrected for the contamination of "spurious" sources, i.e. the fraction of sources due to noise fluctuations above the 3.5σ level (and meeting the additional requirements given in sect 3.1).

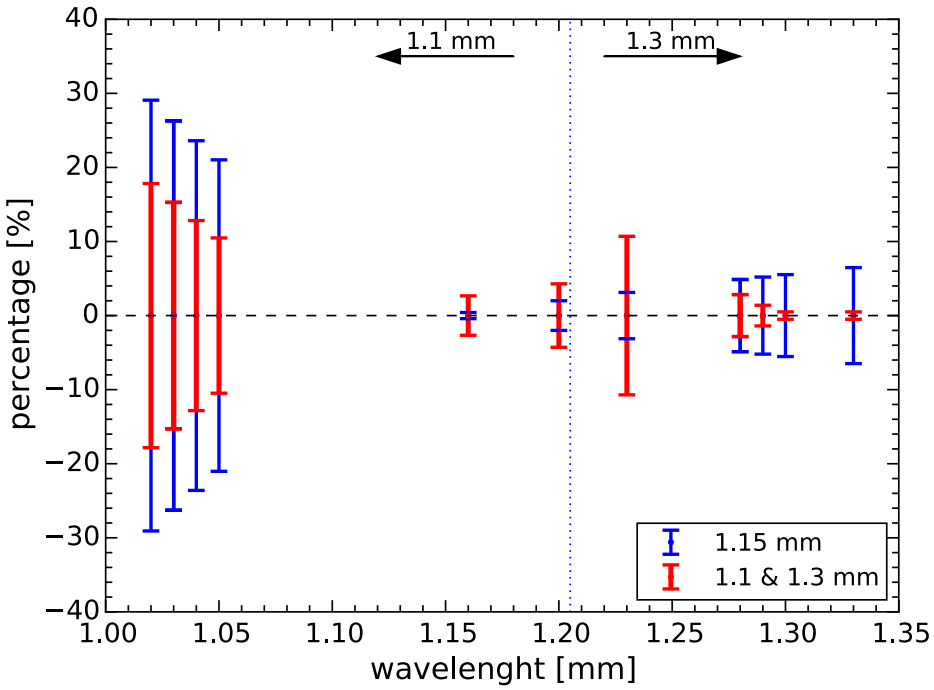

Figure 4.7: Flux error at different wavelength. The red error bars show the flux error scaling the flux density of the sources observed at $\lambda \leq 1.2$ mm to the flux density at 1.1 mm and those at $\lambda > 1.2$ mm to the flux density at 1.3 mm. The blue error bars indicate the flux error combining all observations to 1.15 mm.

The contamination fraction f_c was inferred from the fraction of negative sources at each S/N level, as inferred from Figure 4.3. For each source f_c is the ratio between negative and positive detections at its S/N. Therefore, the contribution of each source to the number counts is (1-f_c) divided by its respective effective survey area $A_{\rm survey}(S)$. We carried out the logarithmic differential number counts $dN(S)/d\mathrm{Log}S$ in logarithmic flux density bins with size $\Delta\mathrm{Log}S = 0.2$. So the logarithmic differential number counts for a selected bin is given by:

$$\left.\frac{dN(S)}{d\mathrm{Log}S}\right|_{S\pm1/2\Delta\mathrm{Log}S} = \sum_j \frac{1-f_{cj}}{A_{\rm survey}(S)}$$

where j are all sources with flux density between $\mathrm{Log}S$-1/2$\Delta\mathrm{Log}S$ and $\mathrm{Log}S$+1/2$\Delta\mathrm{Log}S$. The resulting differential number counts are scaled to $\Delta\mathrm{Log}S = 1$.

The total uncertainty on the logarithmic differential number counts is computed by combining the contribution from Poisson noise, from the cosmic variance[6] and from errors due to completeness and flux boosting corrections. In the following we evaluate each single contribution:

- The observational uncertainty related to the actual number of detected sources is calculated from Poisson confidence limits of 84.13% (Gehrels 1986) by using the number of sources detected in each bin.

- The error due to the cosmic variance is estimated by using a software tool provided by Moster et al. (2011). This procedure uses predictions of the underlying structure of cold dark matter and the expected bias for a galaxy population. The estimate depends on the angular dimension of the field, the mean redshift, the redshift bin size, stellar mass of the galaxy population in question and also by the number of independent fields sampled in different regions of the sky. We assume a mean redshift of $z = 3.5$, a redshift bin size of $dz = 3$ and a stellar mass of $10^{10.5}$ $M_\odot$ from

[6]The cosmic variance is a statistical uncertainty due to large-scale density fluctuations. It may lead to uncertainties in excess of naive Poisson errors. Cosmic variance error is irrelevant for sampling volume much larger that the typical clustering scale of the observed object.

Table 4.2: Differential number counts.

λ = 1.1 mm		
S [mJy]	$dN/d\mathrm{Log}(S)$ [10^4]	$N_{\mathrm{detections}}$
0.13	10^{+7}_{-4}	5
0.20	11^{+3}_{-3}	14
0.30	2^{+2}_{-1}	3
0.63	$0.7^{+0.9}_{-0.4}$	2

λ = 1.3 mm		
S [mJy]	$dN/d\mathrm{Log}(S)$ [10^4]	$N_{\mathrm{detections}}$
0.03	<70	-
0.04	<30	-
0.06	11^{+14}_{-7}	2
0.08	10^{+7}_{-4}	5
0.12	7^{+4}_{-3}	7
0.22	3^{+2}_{-2}	5
0.34	4^{+2}_{-2}	7

Yun et al. (2012) and Weiß et al. (2013) who measured and analysed SEDs and redshifts of bright (S>1mJy) sub-millimeter galaxies through spectroscopic and photometric observations. Considering that for widely separated fields the cosmic variance goes as $1/\sqrt{N_{\mathrm{field}}}$, the relative error is < 18% in the deepest logarithmic differential number count bin.

- The relative uncertainties relating to completeness and flux boosting corrections are on order of 5%.

Because the cosmic variance and errors induced by count estimations (completeness, flux boosting) are less than 20%, the uncertainty on logarithmic differential number counts is completely dominated by the Poisson errors.

The resulting differential number counts are summarised in Table 4.2 and shown in Figure 4.8 (blue solid symbols). Number counts could be derived down to 60μJy at 1.3mm and down to 100μJy at 1.1mm. Moreover, since we do not detect any faint sources with flux densities $30 \lesssim S \lesssim 50\,\mu$Jy in the deepest ALMA map (field *a* in table 4.1) with sensitivity of $\sim 7.8\,\mu$Jy, we can set a tight upper limit on the number counts at S = 30 μJy and at S = 40 μJy. We note that with the latter we constrain the number counts at flux levels that are a factor of four deeper than previous studies (Ono et al. 2014). We also show separately (hollow symbols) the number counts inferred by only using the sources detected within the primary beam (i.e. 7 sources at 1.1 mm and 6 sources at 1.3 mm). In the latter case the statistical errorbars are obviously larger, but fully consistent (within errors) with the number counts inferred over two beams.

We also show the number counts of bright (S > 1 mJy) SMGs obtained by Scott et al. (2012) at 1.1 mm with AzTEC. However, the two faintest bins in the latter data will not be considered when comparing models or to fit analytic functions, since the completeness at these flux densities is too low and the number counts are underestimated. Since there are no number counts of bright sources at 1.3 mm, we used the number counts at 1.1 mm by scaling the flux density to 1.3 mm flux density. Figure 4.8 shows that the differential number counts increase with decreasing flux density. A flux density cutoff at $S \gtrsim 1$ mJy suggests an upper limit on SFR of millimetric sources (Karim et al. 2013; Hayward et al. 2013) that may be a consequence of star-formation or/and AGN feedback, but may also be simply a consequence of limited gas supply.

At 1.3 mm, the differential number counts of Hatsukade et al. (2013) (orange symbols), which

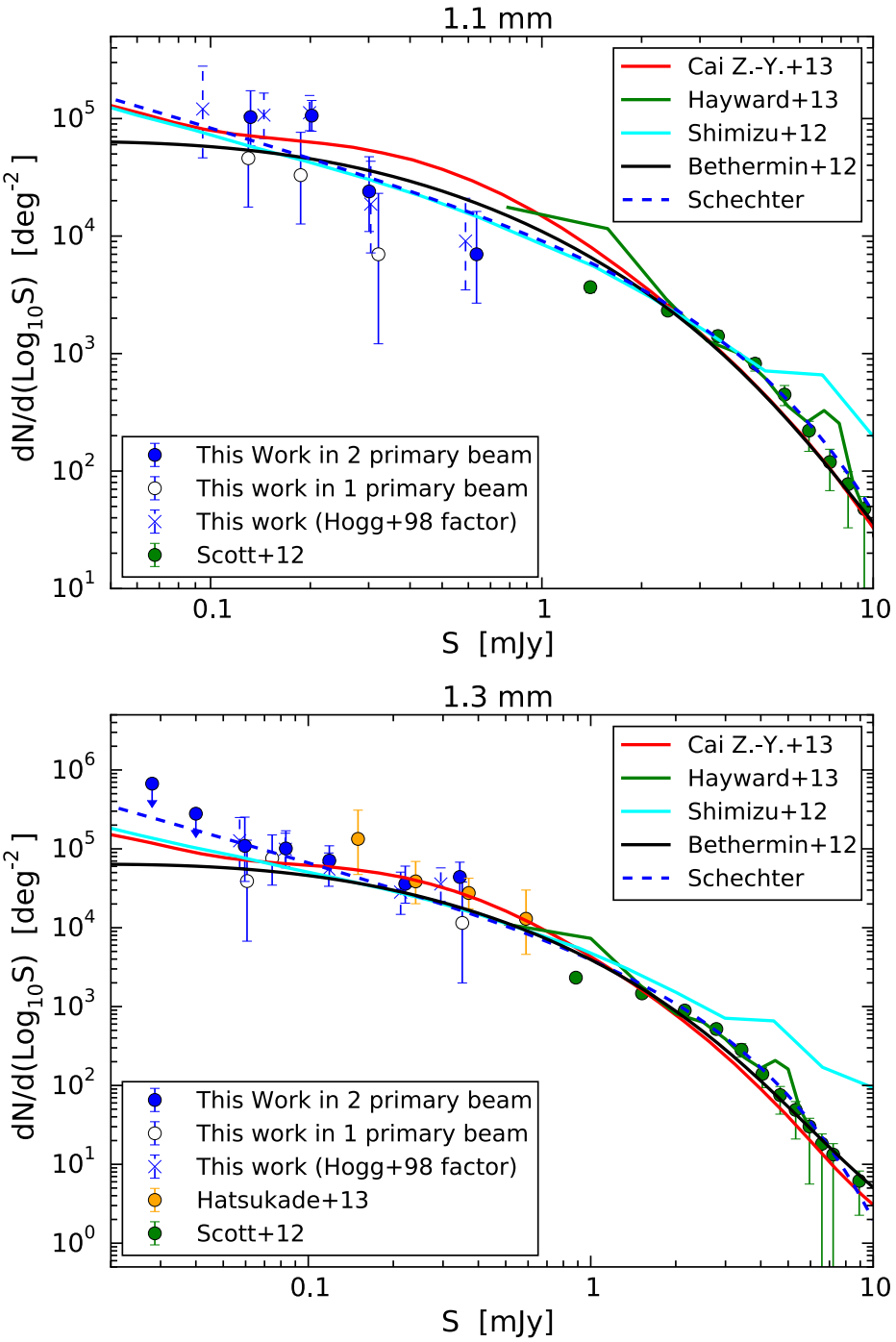

Figure 4.8: Logarithmic differential number counts as a function of flux density at λ =1.1 mm and λ =1.3 mm. The blue solid and upper limit symbols are the results of this work. The hollow symbols are the results obtained by using only the sources within one primary beam. The blue crosses with dashed error-bars are the differential number counts corrected for "flux boosting" by using equation 4 in Hogg & Turner (1998). The green symbols are estimated from Scott et al. (2012). The orange symbols are the number counts estimated by Hatsukade et al. (2013). The red, green, cyan and black solid curves are the model predictions obtained by Cai et al. (2013), Hayward et al. (2013), Shimizu et al. (2012), and Béthermin et al. (2012), respectively. The blue dashed curve shows the best-fit Schechter function.

are obtained from sources with S/N≥ 4, are consistent with our results within the uncertainties, but our slope of the logarithmic number counts at sub-mJy flux densities is flatter than those obtained by Hatsukade et al. (2013). We do not plot the number counts of Ono et al. (2014) as they were estimated at 1.2 mm using continuum maps over the whole 1.04-1.22 mm wavelength range, i.e they were not extracted with the same procedure we used to define our sample. Given that there is no information yet on the SED or on the redshift of the sources contributing to the number counts, our approach of dividing sources into two wavelength ranges, hence minimising the extrapolation assumptions, provides more solid results, as discussed more in detail in the Section 4.3.4.

Since some previous works assessed the boosting factor correction by using a Bayesian estimation (e.g. Coppin et al. 2005) instead of that shown in Section 4.3.3, we verified that final results do not depend on method used to correct for flux boosting effect. Therefore, we show (with crosses and dashed error-bars) the differential number counts by correcting for a boost factor estimated from equation (4) of Hogg & Turner (1998) (note that the correction was on the data *not* corrected for flux boosting as described in Section 4.3.3, else this would result in a double correction). In order to apply the prescription of Hogg & Turner (1998) we used the best-fit Schechter function (Section 4.4.4) as a conservative a priori distribution of flux densities at faint fluxes (we shall see that a Schechter function tends to give an extrapolation of the number counts that is steeper than expected by models and tend to overproduce the CIB). It should however be noted that the prescription given by Hogg & Turner (1998) may not apply to these data, since the noise is not uniformly distributed over the field of view as a consequence of the primary beam attenuation. However, as seen in Figure 4.8, the slopes obtained with this correction factor are consistent with those obtained using a boost factor estimated in Section 4.3.3. Our result are recently confirmed by a new studies by Fujimoto et al. (2015) who estimate the differential number counts down to 20 μJy by exploiting data on a lensing cluster. There is a slightly discrepancy between their results and ours at 20-40μJy: their number counts are higher then the upper limits estimated by us. We tentatively ascribe the discrepancy to uncertainties associated with the calculation of the lensing factor for sources of unknown redshift and to uncertainties associated with the complex calculation of the effective survey area in the presence of strong lensing. However, new forthcoming deep ALMA observation will enable us to further clarify these discrepancies.

4.4.2 Reliability of our Catalogue

In Section 4.4.1, we have defined f_c as the ratio between negative and positive detections and we have estimated how f_c depends on the S/N of our observations. Since this study shows that some of the real sources can be spurious due to noise fluctuations, in this Section we further verify the reliability of our catalogue by estimating the f_c value expected in blank fields observed with ALMA. In a pure blank field the positive and negative sources are only caused by noise fluctuation, so we expect $f_c \sim 1$ at any S/N level.

We used the 'simobserve' CASA v.4.2.1 task to produce synthetic interferometric observations of a blank field placed at the RA = 22:28:12.28 and DEC = -35:089:59.6, which are the coordinates of the deepest continuum map (field *a* Table 4.1). The 'simobserve' task simulates interferometric ALMA measurement sets. It depends on different input parameters, i.e. target, frequency, thermal noise, atmospheric condition, antenna configuration and spectral resolution. As for the CASA input, we required that antenna configuration would be the same as those used during the observations. Furthermore, we added a thermal noise component by setting the parameter 'thermal noise' to *tsys-atm* with a precipitable water vapour of 1.1 mm and ambient temperature of 269 K which are typical values of our observations. We simulated 300 continuum maps changing each time the parameter 'seed' with a random value, which allows us to generate a random thermal noise for each observation.

We then applied the source extraction technique, mentioned in Section 4.3, on each mock continuum map. Figure 4.9 shows the number of positive and negative sources as a function of S/N normalised to 18 continuum fields. The number of negative sources is equal to those of positive ones at any S/N, indicating that the number of positive and negative spurious sources due to noise fluctuations

is equal ($f_c \sim 1$ for each S/N).

Since the number of spurious positive sources is almost equal to negative ones in a blank field, most of the positive sources detected in our observations with S/N> 3 (Fig. 4.3) are likely to be real.

4.4.3 Comparison with Models

We compared the differential and integrated number counts to the theoretical results obtained by recent simulations and semianalytical models. In Figure 4.8, the differential number counts by Hayward et al. (2013) are shown with a green line. Their results were obtained by combining a semi-analytical model with 3-D hydrodynamical simulations and 3-D dust radiative transfer calculations. The main contributions to the millimetric counts is from isolated-disc, galaxy pairs, and late-stage merger induced starbursts. The simulations also include model for feedback from AGN. However there result do not depend crucially on AGN feedback. In fact their simulation the SFR decreases sharply after the starburst phase simply because the majority of the cold gas is consumed in the starburst. Figure 4.8 shows that their model predictions are able to reproduce the observational results at flux densities > 2 mJy,

We also compared our results with the model by Shimizu et al. (2012), who performed cosmological hydrodynamics simulations using an updated version of the Tree-PM smoothed particle hydrodynamics code GADGET-3. They assumed feedback mechanisms to be triggered by supernovae and the SED of galaxies at mm-FIR wavelengths to be described by a modified black body emission. This model predicts that the bright SMGs reside in greater massive halos ($> 10^{12}$ $M_\odot$) and that their typical stellar masses are greater than 10^{11} $M_\odot$. Their results are broadly consistent with the ALMA results up to 1–5 mJy. However, their estimated number counts of bright SMGs ($> 1-5$ mJy) are significantly higher than the observed number counts both at 1.1 and 1.3 mm. According to this model, approximately 90% of millimeter sources in the flux range of 0.1-1 mJy are at $z > 2$. Therefore most of the observed sources are high-z galaxies, and the contribution from low-z is small.

Béthermin et al. (2012) developed an empirical model in which they start from mid-IR and radio number counts and, by using a library of SEDs, they predict the number counts at far-IR and millimeter wavelengths. This model is based on a redshift evolution of the SEDs associated with the two star formation modes: main-sequence and starburst. The predictions of their empirical model are plotted as solid black curves in both panels of Figure 4.8. Their corresponding SEDs are derived from Herschel observations. The predictions are slightly below the observed faint-end both at 1.1 mm and 1.3 mm. However, the generally good matching of the model with the observations suggests that the faint millimeter sources (S < 1mJy) are more likely associated with normal (main sequence) star-forming galaxies, since the starburst emission dominates at higher flux densities at these wavelengths.

Finally, Figure 4.8 shows the theoretical predictions of Cai et al. (2013)[7]. The Cai et al. (2013) model starts from considering the observed dichotomy in the ages of stellar populations of massive spheroidal (components of) galaxies on one side and late-type galaxies on the other. Spheroidal galaxies and massive bulges of Sa's must have formed most of their stars at $z \gtrsim 1$, while the disc components of spirals and the irregular galaxies are characterised by significantly younger stellar populations and star formation activity continuing up to the present time. The energy feedback from supernovae and AGN regulate the star-formation and the growth of the central BH. The AGN feedback is relevant especially in the most massive galaxies and is responsible for their shorter duration ($\sim 10^8$ yr) of the active star-forming phase. In less massive proto-spheroidal galaxies, the SFR is mostly regulated by SN feedback and continues for a few Gyr. Only a minor fraction of the gas initially associated with the dark matter halo is converted into stars. The rest is ejected by feedback processes. The model includes a self consistent treatment of the chemical evolution of the ISM, calculated using the standard equations and stellar nucleosynthesis prescriptions. The chemical evolution controls the evolution of the dust abundance, hence the dust absorption and re-emission. On the other hand, the evolution of Late-type galaxies was described using a phenomenological approach, considering two populations with

[7]The models predictions are available in electronic format at the Web site http://staff.ustc.edu.cn/~zcai/

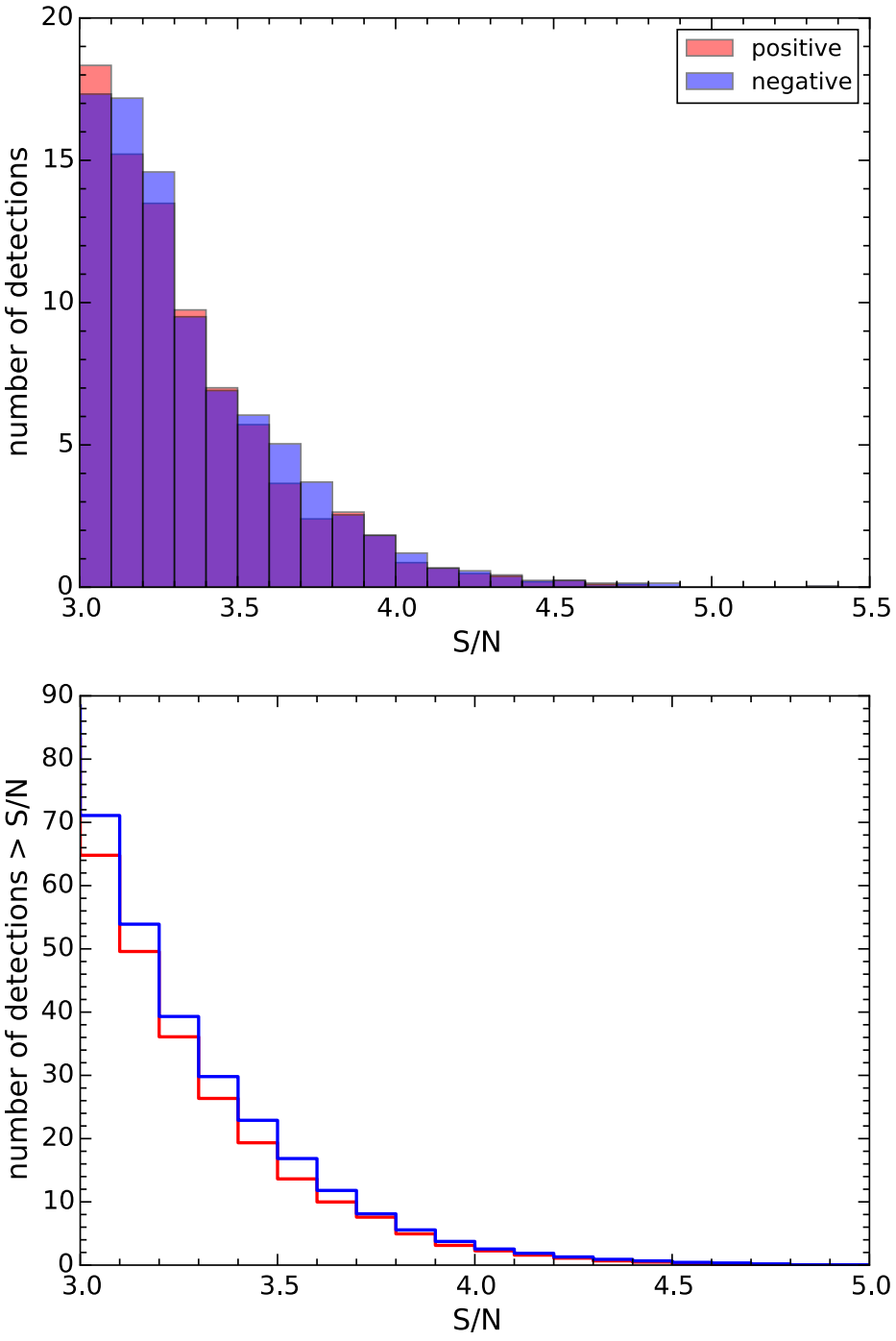

Figure 4.9: *Top:* number of positive (red) and negative (blue) sources detected in 300 continuum pure noise maps and normalised for 18 continuum maps. *Bottom:* cumulative distribution of positive (red) and negative (blue) detections.

Table 4.3: Best fit parameters of the Schechter function at λ =1.1,, and λ =1.3mm.

λ	$\phi_\star$ [deg^{-2}]	$S_\star$ [mJy]	α
1.1 mm	$(2.7 \pm 0.9) \times 10^3$	2.6 ± 0.4	-1.81 ± 0.14
1.3 mm	$(1.8 \pm 0.4) \times 10^3$	1.7 ± 0.2	-2.08 ± 0.11

different spectral energy distributions (SEDs) and different evolutionary properties: "normal" late-type galaxies, with low evolution and low dust temperatures ("cold" population) and rapidly evolving starburst galaxies, with warmer dust temperatures ("warm" population). Their results are in good agreement with our differential number counts from faint to bright flux densities at 1.3 mm and also 1.1 mm (although with some deviations). According to this model the steep slope of the bright counts is accounted for by the sudden appearance of star-forming proto-spheriodal galaxies at $z \gtrsim 1.5$, whose counts already begin to flatten at flux densities of a few to several mJy's. The counts of starburst galaxies have a somewhat flatter slope and come up at levels similar to those of proto-spheroids at the flux densities of the (new) faint counts, while the contribution of "normal" late-type galaxies is always minor in the considered flux density range but increases with decreasing flux density. The redshift distribution at the flux densities of the present counts is bimodal, with starburst galaxies peaking at $z \simeq 1.5$ and proto-spheroids peaking at $z \simeq 2$. At bright flux densities ($S \sim 10$ mJy) the starburst galaxy peak shifts to $z \ll 1$ (since the brightest, in flux terms, starburst galaxies are mostly local) while the proto-spheroid one remains at $z \simeq 2$.

4.4.4 Source Counts Parametrisation with a Schechter Function

We also parametrised the differential number counts using a Schechter function:

$$\frac{dN}{dS}dS = \phi_\star \left(\frac{S}{S_\star}\right)^\alpha \exp\left(-\frac{S}{S_\star}\right) d\left(\frac{S}{S_\star}\right)$$

with $\phi_\star$ being the normalisation, $S_\star$ the characteristic flux density, and α the faint-end slope of the number counts. We fitted separately the Schechter function at 1.1 mm and 1.3 mm by using the number counts estimated in this work and from the literature (e.g Scott et al. 2012, Hatsukade et al. 2013). We did not use the two faintest data points from Scott et al. (2012) because they may suffer from completeness problems. The three free parameters were then derived by χ^2 minimisation. Table 4.3 reports the best-fit parameters and Figure 4.8 and 4.10 show the results of the Schechter function fitting.

The reduced χ^2 are 0.9 and 1.1 at 1.1 mm and 1.3 mm, respectively, meaning that the differential number counts can be properly described by a Schechter function down to the flux levels observed by us. The two faint-end slopes are similar within the errors, suggesting that the two number counts can be described by the same function. The bright-end shape also matches perfectly well with a pure Schechter function at both wavelengths, which has recently been observed in Dayal et al. (2014).

However, we note that the slope of the Schechter function is significantly steeper than expected by models (especially at 1.3 mm) and would overproduce the CIB at faint fluxes, even taking the upper boundary of the CIB, which will be discussed in the next section. Therefore, we warn that the Schechter function fitted to the current data is probably not suitable for describing the number counts at fluxes fainter than those observed by us.

4.4.5 Cosmic Infrared Background

We calculated the 1.1 mm and 1.3 number counts down to 60 μJy using Cycle 0 and 1 ALMA observations. Using the improved number counts estimated in this works, we estimated the integrated flux densities from resolved sources and we derived the fraction of the CIB resolved by ALMA at 1.1 mm and 1.3 mm. The integrated flux densities are given by

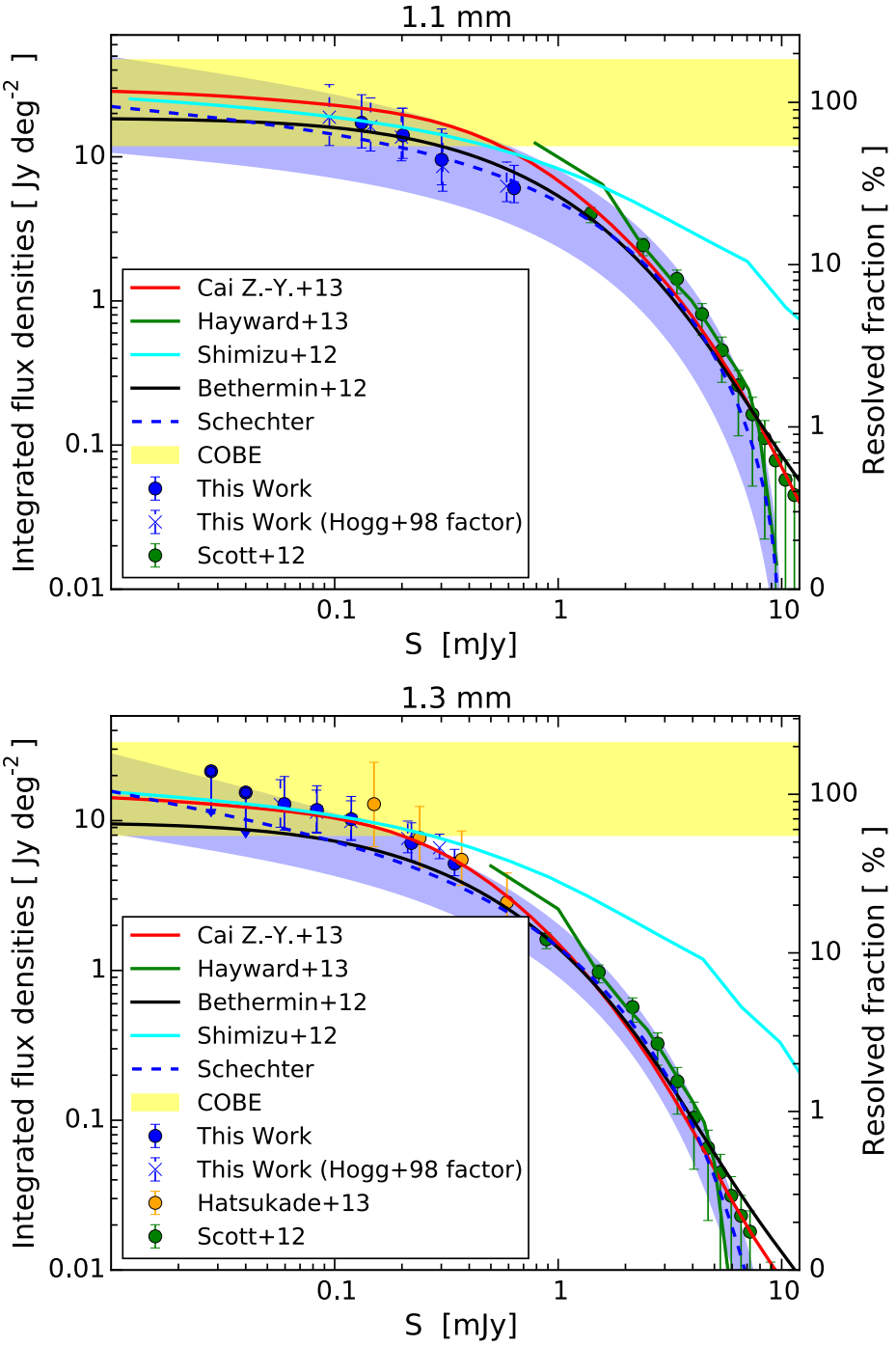

Figure 4.10: Integrated flux density at λ =1.1 mm and λ =1.3 mm. The right axis shows the fraction of resolved CIB. The yellow shaded region is the CIB measured by COBE (Puget et al. 1996; Fixsen et al. 1998). The blue symbols are the results from this work (we used the differential number counts by Scott et al. (2012), green symbols, for $S > 1$mJy). The blue crosses with dashed error-bars are the results from this work corrected for the "flux boosting" by using equation 4 in Hogg & Turner (1998). The orange symbols are from the number counts estimated by Hatsukade et al. (2013). The red, green, cyan and black solid curves are the model predictions by Cai et al. (2013), Hayward et al. (2013), Shimizu et al. (2012), and Béthermin et al. (2012), respectively. The blue dashed curve shows the integrated flux densities estimated from the best-fit Schechter function and the blue shaded region indicates its statistical uncertainty.

$$I(S > S_{lim}) = \int_{S_{\rm limit}}^{\infty} \frac{dN(S)}{dS} S\, dS$$

where

$$\frac{dN(S)}{dS} = \frac{dN(S)}{dLogS} \frac{1}{S\ \ln(10)}$$

Figure 4.10 shows the integrated flux densities at 1.1 mm and 1.3 mm as a function of $S_{\rm limit}$. Note that we used the results of Scott et al. (2012) at bright flux ($S > 1$mJy), but excluding the two point at faintest fluxes, because of incompleteness issues. The integrated counts down to $S_{\rm limit} = 0.1$ mJy at 1.1 mm and to $S_{\rm limit} = 0.06$ mJy at 1.3 mm are 17^{+10}_{-5} Jy deg^{-2} and 13^{+6}_{-3} Jy deg^{-2} respectively. We compared these results with the analytical fit obtained by Fixsen et al. (1998) from the COBE measurement: 25^{+22}_{-13} Jy deg^{-2} at 1.1 mm and 17^{+16}_{-9} Jy deg^{-2} at 1.3 mm (see also Lagache et al. 1999 and Schmidt et al. 2015). Since these measurements suffer from large uncertainties (especially due to the uncertainties on the Galactic contribution), we are not able to determine exactly the fraction of CIB resolved. Certainly, even by taking the highest value of the CIB consistent with the uncertainties given by Fixsen et al. (1998) we can say that at 60μJy more than 50% (probably much more) of the CIB is resolved. Thus our results provide a lower limit on the CIB intensity at 1.1 mm and 1.3 mm. Moreover, the flatness of the faint end-slopes, in particular that at 1.3 mm, suggests that the integrated flux densities estimated in this work are likely close to the CIB intensity.

The blue curve gives the integrated number counts inferred from the Schechter function fitting the differential number counts, and the shaded blue area gives the associated uncertainty. The uncertainty of the latter is large enough to be consistent with any value of the CIB within the range given by Fixsen et al. (1998), however the slope would indicate that this functional form would saturate even the highest boundary at the CIB at faint fluxes, as discussed above.

We note that the integrated number counts show a clear flattening at lowest flux bins populated by our detections. The flattening of the number counts is supported also by the tight upper limits at the faintest fluxes sampled by us. Such flattening of the number counts, fully consistent with models, suggests that at our faint fluxes we are actually resolving most of the CIB.

It will be of great interest to investigate, with followup observations, what is the redshift distribution of these sources which produce most of the background, especially to the faint end. In the meantime we can infer what the properties are of these galaxies in terms of SFR. Indeed, because of the negative K-correction, at 1.3mm a given observed flux density corresponds to an IR-luminosity (hence a SFR) nearly independent of redshift, across the entire redshift range 0.5< z <15 (by adopting the conversion factor and IMF given in Blain et al. 1999; Maiolino et al. 2008). In particular, the minimum flux density sampled by us, 60 μJy at 1.3mm, corresponds to a total IR luminosity L(8 – 1000μm) = 6 $\times 10^{44}$ erg s^{-1}, corresponding to a SFR = 40 M$_\odot$ yr^{-1} (Kennicutt & Evans 2012), nearly independent of redshift. This is consistent with the predictions of Béthermin et al. (2012) and Cai et al. (2013) as they expect that faint sources are associated with "normal" star-forming galaxies. We can therefore state that galaxies with SFR < 40 M$_\odot$ yr^{-1} certainly contribute less than 50% of the CIB at 1.3 mm, and probably a much lower fraction. Viceversa, the bulk of the CIB (50% and probably much more) must be due to galaxies with SFR > 40 M$_\odot$ yr^{-1}.

4.5 Summary And Conclusions

We have used 18 deep ALMA maps in band 6 and 7 to investigate the number counts of sources at millimetre wavelengths. The sensitivity (rms) of these ALMA maps range from 7.8 μJy/beam to 52 μJy/beam.

Sources were detected down to 3.5σ. We applied, as a requirement for detection, that the size of the sources should be equal to the beam size (or slightly larger) within the uncertainties. Since the noise due to bad uv-visibilities, or to sidelobes emissions from bright sources, or thermal noise

associated with individual antennae or group of antennae, should introduce fluctuations that have a spatial shape completely different from the coherent beam, this criterion enables us to remove most of the spurious detections associated with noise fluctuations.

We searched for sources out to a distance equal to diameter of two primary beams. However, we have checked that the final number counts do not change, within errors, by restricting the source search to within the primary beam (although the statistics are obviously lower).

A total of 50 sources were detected matching these criteria. We explored counts at these two different wavelengths, 1.1mm and 1.3mm (hence the ALMA maps were divided into two groups depending on their central wavelength). This approach avoids large flux extrapolation from observations obtained at different wavelengths. Since we do not yet know the intrinsic SED and redshift distribution of the detected sources (which would be required for a proper extrapolation of the fluxes from different wavelengths), our approach provides safer results, although at the expense of lower statistics.

Number counts were obtained by taking into account completeness, flux boosting effects, correction for spurious sources and effective survey area at different flux limits. We extracted differential number counts down to 60 μJy and 100 μJy at 1.3mm and 1.1mm, respectively, inferring sources number densities of $dN/d(\mathrm{Log}S) \sim 10^5\ deg^{-2}$ at these faint limits. Using the deepest ALMA field, we inferred tight upper limits on the number counts at 30 μJy and at 40 μJy.

The differential number counts at 1.1mm (1.3mm), across the entire range from 60 μJy to 10 mJy, can be fitted with a Schechter function with a faint end slope $\alpha \approx -1.8$ ($\alpha \approx -2.0$), a characteristic flux density $S_* \approx 2.6$ mJy ($S_* \approx 1.7$ mJy) and a normalisation at S_* of $\phi_* = 2.7 \times 10^3$ deg^{-2} ($\phi_* = 1.8 \times 10^3$ deg^{-2}). We note that such Schechter functions describe the number counts down to 60–100 μJy, but their extrapolation to fainter fluxes is not trustworthy.

The good agreement between the observations and the model predictions by Cai et al. (2013) suggests that AGN feedback regulate star formation in massive galaxy. However, the model by Cai et al. (2013) relies on different contribution by several classes of galaxies (normal star- forming discs, proto-spheroid, merging systems) and predict a significantly different distribution in redshift for normal galaxies, so it will be fundamental compare the properties of our sample to the one predicted by model through future spectroscopic observations.

The large uncertainties plaguing our knowledge of the CIB level prevents us from setting tight limits on the fraction that is resolved by our data. Clearly, at least 50% of the CIB is resolved by our data (and probably much more). However, our results set a lower limit to the CIB intensity at 1.1-1.3 mm, significantly above the one coming from direct measurements. The flatness of the faint counts implies that this lower limit is likely close to the CIB intensity.

The SFR of the sources contributing to the CIB at such faint fluxes is about 40 $M_\odot$ yr^{-1}, independent of their redshift. We therefore infer that sources with SFR $< 40\ M_\odot$ yr^{-1} contribute less than half of the CIB at 1.3 mm, and probably much less. Viceversa, the bulk of the CIB must be produced by galaxies with SFR $> 40\ M_\odot$ yr^{-1}.

Chapter 5

QSO and SMG: Two Different Phase?

Based on:
Carniani, S. et al. 2013: Strongly star-forming rotating disks in a complex merging system at z = 4.7 as revealed by ALMA; A&A, 559A, 29C

The growth of galaxies is closely traced by star formation, and the cosmological evolution of the global SFR density is thus a fundamental element for understanding galaxy evolution from high to low redshift. It has been estimated that more than $\sim$ 50% of the stars in the Universe have formed at z=1$\sim$3, where the cosmic SFR density peaks (Lilly et al. 1996; Madau et al. 1996; Haarsma et al. 2000; Hopkins et al. 2001). Until recently, galaxy evolutionary models usually associated this peak with the increased rate of galaxy mergers and interactions in that redshift range. In particular, the merger process is at the base of the formation of massive galaxies: the majority of the stars are formed following major-merger episodes that induce high SFRs (from several hundreds to over a thousand $M_\odot$/yr; Di Matteo et al. 2005; Guyon et al. 2006; Sijacki et al. 2011; Valiante et al. 2011). But a different point of view has emerged very recently, according to which the peak of the cosmic SFR density is expected to follow the evolution of the cosmic gas inflow rate. This is suggested by the existence of a main-sequence of star-forming galaxies at any redshift , which is most likely fuelled by continuous gas accretion (Keres et al. 2005; Genel et al. 2008; Conselice et al. 2013).

Strongly starbursting outliers of such a main sequence do exist and represent an increasingly important phase at higher redshifts: these outliers are thought to be mostly merger-induced star-forming objects, such as SMG and ULIRG galaxies (Tacconi et al. 2010), even if some authors have found that the fraction of merger systems is small (Rodighiero et al. 2010). Whatever the origin of the evolution of the cosmic SFR density, bright ($S > 1$ mJy) SMGs appear to fit well within a merger-induced star formation scenario. They are dust-obscured strongly star-forming galaxies whose number density peaks around z$\sim$2 (Chapman et al. 2003, 2005), although recent ALMA surveys have shown that the SMG redshift distribution probably peaks at even higher redshift (z$\sim$3.5, Weiß et al. 2013). Their luminosities are in excess of $10^{12}\,L_\odot$, their SFRs are of about $\sim 10^2 - 10^3$ $M_\odot$/yr, and their stellar masses are around $10^{11} M_\odot$, although recent estimates made by different authors vary by a factor ~ 6 (Magnelli et al. 2010; Chapman et al. 2010; Hainline et al. 2011; Michałowski et al. 2010; Magnelli et al. 2012). When combining these properties with typical gas fractions of 40% (Narayanan et al. 2012), it is natural to assume that SMGs are the late stages of major-merger events.

However, in contrast with the major-merger scenario, a large portion of the strongly star-forming galaxies at z$\sim$1-3, especially among Lyman-break galaxies[1] does not show the expected disturbed kinematics but is characterised by regularly rotating disks (Förster Schreiber et al. 2009; Epinat et al.

[1] A Lyman-break galaxies are a star-forming galaxies at high redshift ($2.5 < z < 5$) that are selected by the colours of their far-UV SED around the 912 Å Lyman continuum discontinuity (see review by Giavalisco (2002).

2009; Cresci et al. 2009; Gnerucci et al. 2011b). This observational result has prompted the suggestion that even stronger star formation may be fueled by the accretion of pristine gas from the halo and dynamical instabilities within the massive gaseous disks (Genel et al. 2008; Dekel et al. 2009; Bouché et al. 2010; Cresci et al. 2010). Another evidence of this smooth accretion is provided by the so-called fundamental metallicity relation, a tight relation for star-forming galaxies that connects gas metallicity, SFR and stellar mass, and which does not evolve with redshift up to $z \sim 3$ (Mannucci et al. 2010; Dayal et al. 2013; Bothwell et al. 2013).

Star formation is not the only ingredient in the formation of galaxies. The discovery of the correlations between the masses of BHs and the properties of their host spheroids (see Section 1.3; e.g. Ferrarese & Merritt 2000; Gebhardt et al. 2000; Marconi & Hunt 2003; Gültekin et al. 2009; McConnell & Ma 2013) and the observed cosmological evolution of the AGN number density, which follows that of the cosmic SFR density (Marconi et al. 2004; Merloni & Heinz 2008; Shankar et al. 2010), have suggested that the growth of BHs is intimately linked with that of their host galaxies: this so-called co-evolution is also based on the merger paradigm (e.g. Hopkins et al. 2007). In particular, in the most luminous AGN, major-merger episodes destabilise large amounts of gas, which forms stars and eventually accretes onto the central BHs. The luminous AGN that are then activated have feedback onto their host galaxies. This is the beginning the observed BH galaxy correlations and explains the decrease of the cosmic SFR and AGN densities below $z \sim 1$. The co-evolution scenario then implies that there should be a population of active, clustered star-forming galaxies at high redshift ($z > 3$).

Observations of the morphology and kinematics of molecular gas in high-redshift galaxies may help to understand the main mechanism that caused the peak of the cosmic SFR density. In particular, the kinematics of gas in merging systems might indicate whether star formation activity is indeed associated with disturbed kinematics. Moreover, the distribution of ionised and molecular gas in active high-redshift sources such as quasars might reveal outflows, as expected from the feedback model.

Here we perform a kinematical analysis of the [CII] line emission in BR 1202-0725, a major-merger system at $z \sim 4.7$ composed by a QSO and SMG. We show that, at variance with a simple major-merger scenario, the high SFRs in both the QSO host galaxy and the SMG are associated with apparently regularly rotating disks, suggesting that the high SFRs are probably induced by minor mergers, interactions, or gas inflows that do not strongly affect the large-scale disk kinematics. We determine the dynamical masses of the two galaxies and study the relation between black hole and host galaxy for the QSO.

The target BR1202 is presented in Section 5.1, data reduction is described in Section 5.2 and results from the data analysis are discussed in Section 5.3. In Section 5.4 we present our kinematical analysis and the dynamical mass measurements of the QSO host galaxy and SMG. We discuss our findings in Section 5.6 and finally draw our conclusions in Section 5.7.

Throughout this project we adopt the standard cosmological parameters $H_0 = 70$ km s^{-1}Mpc^{-1}, $\Omega_M = 0.30$ and $\Omega_\Lambda = 0.70$, according to which 1 arcsec at $z = 4.7$ corresponds to a proper distance of 6.48 kpc.

5.1 BR 1202-0725

BR 1202-0725 is an ideal system to test coevolution scenario as it is composed of strongly star forming interacting galaxies at redshift z~4.7. The most prominent sources are a QSO at the southeast and a SMG at the northwest. The SMG has been observed for the first time at 1.4 GHz (Carilli et al. 2002) and is located about ~24 kpc from the QSO (Wagg et al. 2012). The observed flux level at 850 μm (Iono et al. 2006) places the SMG at the bright end of the submillimetre galaxy population (S[850 μm] > 5 mJy), which represents only 20-30% of the submillimetre sources responsible for the 850 μm extragalactic background radiation (see Chapter 4, e.g. Coppin et al. 2006). Both sources have a high FIR luminosity, $L_{FIR} > 10^{13}$ $L_\odot$ (Iono et al. 2006; Omont et al. 1996; Carilli et al. 2002) that likely indicates very strong star formation activity (SFR > 10^3 $M_\odot$/yr). Assuming that warm dust is heated by star formation activity and re-emits in the FIR, it is possible to derive an SFR~4500 $M_\odot$/yr for the

QSO and an SFR~2000 $M_\odot$/yr for the SMG (Iono et al. 2006).

The system BR 1202-0725 has been recently observed with ALMA during the science demonstration phase (Wagg et al. 2012; Carilli et al. 2013) and with the IRAM PdB Interferometer as reported by Salomé et al. (2012). These authors derived SFRs of about 1000 $M_\odot$/yr and molecular gas masses of $\sim 5\times10^{10}\,M_\odot$. Moreover, the system has been found to be more complex than previously thought (left panel of Figure 5.1). The bright QSO (M_B=-28.5) presents broad Lyα emission extended toward the northwest, which suggests interaction with the SMG (Hu et al. 1996). This emission, labelled Lyα-1 by Salomé et al. (2012), was confirmed spectroscopically to be a Lyα emitter at the same redshift of the system (Omont et al. 1996; Ohyama et al. 2004; Williams et al. 2014). A second Lyα source, labelled Lyα-2 by Salomé et al. (2012), is also observed at similar distance to the south-west of the QSO (Hu et al. 1996). The two Lyα emissions are produced by in situ star formation (Williams et al. 2014) likely triggered by QSO outflows as proposed by several recent models of positive feedback. [CII] counterparts of Lyα emitters were detected by Wagg et al. (2012) and Carilli et al. (2013) thanks to ALMA capabilities. In addition to [CII] and Lyα detections, the CO line analysis by Salomé et al. (2012) indicate a close companion also for the SMG. Although the complex of the system, the CO position-velocity diagrams for both the QSO and the SMG suggest that the two galaxies have regularly rotating disks, which is not expected in a interacting system.

5.2 Observations and Data Reduction

BR1202-0725 was observed at 0.9 mm (334 GHz) using the millimetre interferometer ALMA , with 18 12-m and 3 7-m diameter antennas on 2012 January 16; for this work we took advantage of all the available data. The total on-source observing time was about 25 minutes with a maximum baseline length ~ 280 m. The weather conditions were generally very good with a precipitable water vapour of 0.7 mm, and the continuum sensitivity of ALMA was one order of magnitude higher than previous submillimetre observations of the system.

The receivers were tuned to a [CII] redshifted frequency of about 333 GHz (the rest frequency of [CII] is 1900.539 GHz). The ALMA correlator has a total bandwidth of 7.5 GHz and was divided in to four spectral windows of ~ 1.8 GHz with a channel width of 15.6 MHz (~ 14 km s^{-1}). The data were calibrated by using the CASA software. The amplitude and phase fluctuations were calibrated by observations of 3C279, for which we took the flux of 15 Jy obtained from SMA observation at 850 μm. Afterwards we used observations of Titan to rescale the flux, assuming a total value of 2.5 Jy. The QSO 3C 279 was also used to calibrate the time-dependent gain and the bandpass. Overall, we estimate a 15% uncertainty on the measured absolute fluxes.

The continuum image was extracted using all the line-free channels in the last three spectral windows; the image was then cleaned using the CASA task "CLEAN". During the cleaning we set the weight of each visibility sample in order to the fidelity of the final image. This weighting can be used to account for differences in the density of sampling in different parts of the u-v planes, or to account for different noise variances in different samples, or to improve sensitivity to extend objects. For this target we selected the algorithm by Briggs et al. (1999) with parameter ROBUST = 1.5. This weighting provides a good compromises between angular resolution and sensitivity. The final image has an angular resolution of 0.8″×0.7″with the beam oriented at P.A. = 8°. The achieved sensitivity in the continuum image is 0.2 mJy (*rms*/beam).

A UV plane model of the continuum emission was made from the line-free channels of the last three spectral windows and was subtracted from the first and second spectral windows after linear extrapolation. Following the same deconvolution procedure as for the continuum image, we then obtained the final line data cube with the first two spectral windows rebinned to channels of ~28 km/s . The spatial scale is 0.15″ per pixel (~ 0.97 kpc per pixel). The rms noise was estimated to be 2.0 mJy per beam per channel, from several line-free channels.

The continuum and line maps obtained by us are similar to those provided with the data release. Continuum and line fluxes are consistent within the errors and the main difference consists in our

Table 5.1: Summary of the physical properties of the BR1202-0725 system from the literature and from this PhD thesis.

	Sources		
	BR1202 N	BR1202 S	References
RA	12:05:22.98	12:05:23.13	
Dec	-07.42.29,56	-07.42.32,68	
Integrated continuum flux at 900 μm [mJy]	15.8±2.4	14.8±2.2	
Distance from S source [kpc]	23.5±0.3	-	
FWHM from Gaussian fitting of continuum	0.84″×0.75″	0.81″×0.78″	
Integrated [CII] flux [Jy/km s^{-1}]	9.06	8.45	
FHWM of [CII] line [km s^{-1}]	500± 20	300±20	
Redshift	4.6891	4.6943	
L_{FIR} [$L_\odot$]	1.5×10^{13}	1.8×10^{13}	
SFR from continuum [$M_\odot$/yr]	2600	3200	
SFR from [CII] [$M_\odot$/yr]	6800±1000	5000±1000	
L'_{CO} [10^{10} K km/s pc^2]	7.8 ± 1.2	5.3 ± 0.8	1
α_{CO}	0.6 ± 0.2	0.6 ± 0.2	2
Molecular mass [$10^{10} M_\odot$]	4.6 ± 1.7	3.2 ± 1.2	
Disk inclination [°]	25±15	15 ± 10	
P.A. of line of nodes [°]	180±5	230±10	
Scale radius [kpc]	2.8±0.2	2.4±0.2	
$\log_{10}(M_{dyn}/M_\odot)$	10.8±0.6	$10.6^{+0.8}_{-0.4}$	
$\log_{10}(M_{BH}/M_\odot)$	-	9.1±0.3	
M_{BH} [10^9 $M_\odot$]	-	$1.5^{+1.5}_{-0.8}$	
Σ_{SFR} [$M_\odot$/yr kpc^{-2}]	80	180	
Σ_{gas} [$M_\odot$ pc^{-2}]	1900	1800	
Dark halo mass [$M_\odot$]	$> 3.2 \times 10^{11}$		

(1) -Salomé et al. (2012) ; (2)-Bolatto et al. (2013)

choice of pixel scale and ROBUST values, which improved the spatial resolution by a factor ∼ 2.

5.3 Results

Table 5.1 summarises the physical properties of the BR1202-0275 system as measured in this PhD thesis or collected from the literature. Here we identified the two brightest sources with the labels N and S (north and south). The north source is the SMG and the south source is the QSO .

Right panel of Figure 5.1 presents the [CII] intensity map of the BR1202-0275 system with the surface brightness contours of the 900 μm continuum emission overlaid. The integrated fluxes of the N and S sources at 334 GHz and in the [CII] line and their centroid coordinates (Table 5.1) are consistent with those found by Iono et al. (2006) and the previous analysis of these data by Wagg et al. (2012) and Carilli et al. (2013). The projected distance between the two continuum sources is 23.5±0.3 kpc. The fainter continuum source discovered by Wagg et al. (2012) southwest of the QSO (Fig. 5.1) is detected in the continuum at the ∼8σ level (σ= 0.2 mJy beam^{-1}). This source is not observed in the integrated line map of Figure 5.1 because of the large velocity range used in integration.

The continuum emission of the N and S sources is not spatially resolved because their FWHM are similar, within the errors, to that of the synthesised beam (Tab. 5.1). The line emission of both sources, however, is spatially resolved compared to the continuum, as shown by the FWHM in Table 5.1 and

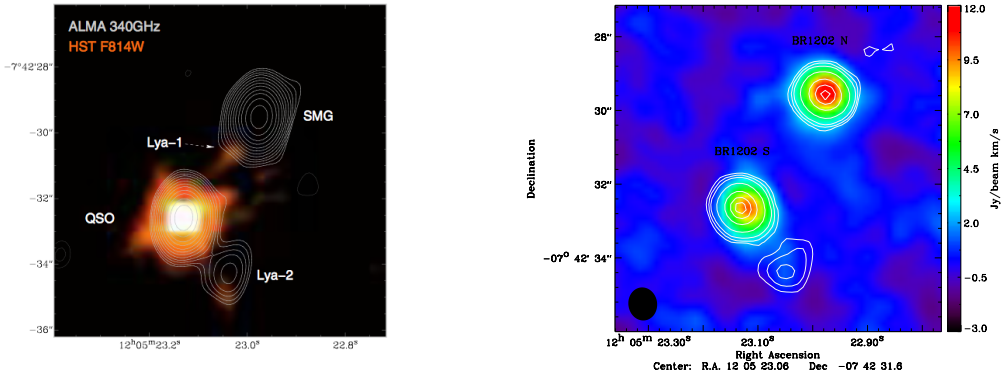

Figure 5.1: *Left*: white contours show the submillimetre continuum emission from BRI 1202-0725 at 340 GHz. Contour levels are a geometric progression in square root two, starting at 0.25 mJy beam^{-1}. Negative contours are dashed. The rms noise on the image is 0.1 mJy beam^{-1}. The colour shows the HST F 814W image of Hu et al. (1996). The SMG, QSO, Lyα-1, and Lyα-2 are indicated. *Right*: [CII] integrated intensity map in BR 1202-0725 with identification of the north and south sources. The rms noise is 0.6 Jy km s^{-1}. The synthesized beam (0.8″×0.7″) is indicated by a filled black ellipse in the lower left corner of the plot. The continuum emission of BR1202-0725 a 334 GHz is overplotted as white contours. The contour levels are logarithmic [-3.4, -3.2, -3.0, -2.6, 2.2, 2.0, 1.9] of σ with σ=0.2 mJy. The rms noise is 0.2 mJy beam^{-1}.

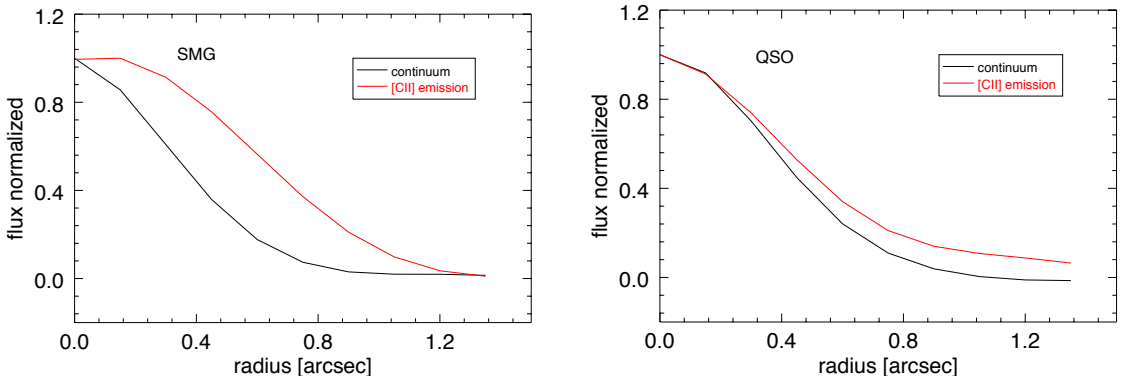

Figure 5.2: Radial surface brightness profiles of the submm galaxy (N source, left panel) and of the QSO (S source, right panel). The continuum and [CII] line emissions are denoted by the black and red lines, respectively.

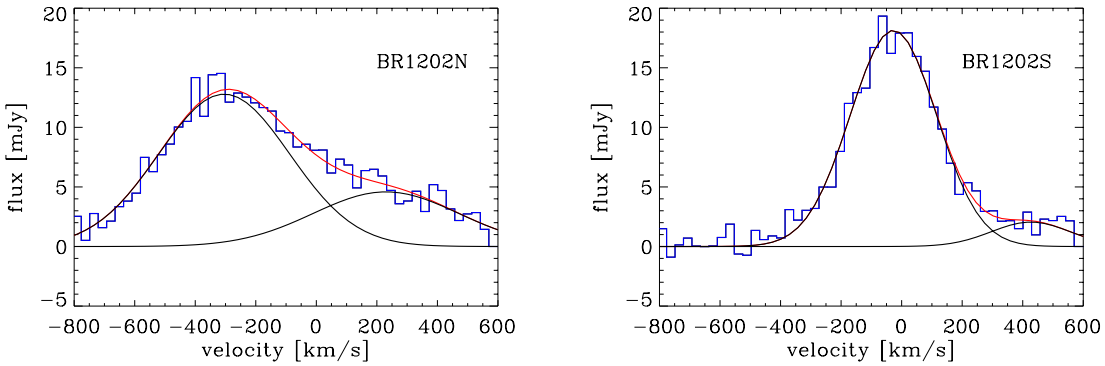

Figure 5.3: Integrated spectra of the N and S sources (left and right panels, respectively), targeting the [CII] line with a spectral resolution of 28 km s^{-1} per channel. The spectra have been extracted from the ALMA data cubes using beam-sized apertures centered on the sources. All velocities are referred to a redshift z=4.6949. The red curves denote the best fits, which are obtained with a double Gaussian function for both sources. For the QSO the width of the second component is fixed to that of the main component. For the SMG, the velocity of the fainter component is fixed at 250 km/s (Salomé et al. 2012).

by the radial surface brightness profiles presented in Figure 5.2. As shown in the Figure for both the N and S sources, the radially averaged FWHM of the [CII] emission along the x-axis (E-W) is $\sim$ 1.2 times higher than that of the synthesised beam and of the continuum. Moreover, it is clear from Figure 5.1 that the peak of [CII] emission in the QSO (S source) is shifted by 0.2″ ($\sim$ 1.3 kpc) with respect to the continuum.

The integrated spectra of the N and S sources are shown in Figure 5.3. The line profile of the QSO is generally symmetric, except for a "red wing" at $\sim$ 500 km/s that is probably associated with a faint companion or with an outflowing wind, as suggested by Carilli et al. (2013). To take into account the red wing, the spectrum was fit with two Gaussian functions with the same FWHM because the red wing is at the edge of the band and not fully constrainable. As discussed below, this choice does not affect the kinematics of the QSO host galaxy. Conversely, the line profile of the SMG is asymmetric and broader than that of the quasar. It was fit with a combination of two Gaussians with the fainter component fixed at 250 km/s, as suggested by Salomé et al. (2012) and explained in more detail below. The results, including average velocities and velocity dispersions, are presented in Table 5.1. The redshifts of the two sources are determined from a Gaussian fit to the [CII] lines and corresponds to z= 4.6891 ± 0.0004 for the SMG and z= 4.6943 ± 0.0005 for the QSO. In all cases [CII] velocities are referred to the systemic redshift of z=4.6949 adopted by Salomé et al. (2012); our velocity and the velocity dispersion measurements for [CII] are consistent with the measurements by Carilli et al. (2013), Wagg et al. (2012), Iono et al. (2006), and with the corresponding CO values by Salomé et al. (2012).

5.3.1 Star Formation Rate and Gas Mass

We first estimated the SFR from the FIR continuum emission. To this aim, we fit the spectral energy distributions (SEDs) of the two sources in the FIR-radio range using the model of Yun & Carilli (2002) and assuming typical values for the dust temperatures (T_d) and opacities (k_ν) of SMGs and quasars (T_d = 65 K for the SMG and T_d = 50 K for the QSO; $k_\nu \sim \nu^{1.5}$; see Iono et al. 2006; Beelen et al. 2006; Kovács et al. 2006 for more details). Fluxes for BR 1202N and BR 1202S were compiled from Carilli et al. (2002, 1.4 GHz), Omont et al. (1996, 4.8 GHz), Benford et al. (1999, 1000 GHz) and from our own ALMA measurement (334 GHz). The adopted SED model is composed of thermal bremsstrahlung, nonthermal synchrotron and dust continuum emission; the latter depends on the SFR, which is the only free parameter of our SED fit. From this we estimate a star formation ratio (SFR) of $\sim$ 4000 $M_\odot$/yr for the N galaxy and $\sim$ 5000 $M_\odot$/yr for the S source.

Using the SED fitting only for estimating the FIR luminosity and applying the well-known SFR-FIR relation

$$SFR = 1.73 \times 10^{-10} (L_{FIR}/L_{\odot})\, M_{\odot}/yr \tag{5.1}$$

by Kennicutt (1998), one obtains $\sim$ 2600 and $\sim$ 3200 $M_{\odot}$/yr for the SMG and QSO, respectively. These values are similar to the previous ones and to those found by Iono et al. (2006) with the same relation. The adopted SFR-FIR relation was calibrated with a Salpeter IMF[2]; the use of a top-heavy Kroupa IMF would lower the SFRs by a factor $\sim$ 1.6 (see Salomé et al. 2012 and Mor et al. 2012 for more details).

The SFR can also be estimated from the luminosity of the [CII] emission line, since it has been shown to be a tracer of star formation activity in different types of galaxies (Genzel & Cesarsky 2000; Malhotra et al. 2001; Luhman et al. 2003). Using the calibration of Maiolino et al. (2005), we estimate an SFR of $\sim$ 6800 $M_{\odot}$/yr for the SMG and of $\sim$ 5000 $M_{\odot}$/yr for the QSO. The calibration of Sargsyan et al. (2012) would provide much lower SFRs of less than 900 $M_{\odot}$/yr for both sources, but this calibration may not be applicable since it is obtained from galaxies at lower redshifts ($z \sim 1-2$) and with lower star formation rates (SFR < 500 $M_{\odot}$/yr). Given the uncertainties on the use of [CII] as an SFR indicator and the possibility that [CII] could trace the cold neutral interstellar medium, in the following we used only SFRs based on the FIR luminosity and considered the values based on [CII] just as a confirmation of the very high SFR.

We estimated the molecular gas masses from $L'_{\rm CO}$(5-4) (Salomé et al. 2012) using the conversion factor $\alpha_{\rm CO} = 0.6 \pm 0.2$ $M_{\odot}$ (K km/s pc^2)$^{-1}$ derived by Papadopoulos et al. (2012) from a large sample of starburst galaxies. For comparison, Salomé et al. (2012) used the classical value of $\alpha_{\rm CO} = 0.8$. $M_{\odot}$ (K km/s pc^2)$^{-1}$ from Downes & Solomon (1998). As discussed in detail by Bolatto et al. (2013), the $\alpha_{\rm CO}$ conversion factor is still very uncertain especially at high redshift and, for this reason, we adopted a factor 2 (0.3 dex) systematic uncertainty on $\alpha_{\rm CO}$. The molecular masses are therefore $M_{CO} = (4.6 \pm 1.7) \times 10^{10} M_{\odot}$ and $M_{CO} = (3.2 \pm 1.2) \times 10^{10} M_{\odot}$ for the SMG and the QSO host galaxy, respectively. These measurements are also affected by the factor 2 systematic uncertainty on $\alpha_{\rm CO}$.

Summarizing, the FIR and [CII] based indicators provide SFRs between $\sim 1000 - 5000$ $M_{\odot}$/yr for the two sources, which are associated with very large masses of molecular gas ($M_{mol} \sim 4 \times 10^{10}\, M_{\odot}$). Overall, these results suggest extreme star formation activity, like that associated with major-merger events, and place the two sources at the higher end of the SFR distribution for star-forming galaxies. To verify this scenario and determine whether the two galaxies show the disturbed kinematics typical of a major merging event, we performed a detailed kinematical analysis.

5.4 Kinematical Analysis

In this section we perform a detailed kinematical analysis of the N and S sources, trying to assess whether they show the disturbances typical of a major-merger system, or are regularly rotating disks.

The QSO and the SMG probably identify two massive galaxies that undergo an interaction or are in the early stages of a major-merger It is therefore possible to estimate the total mass of the system using a simple virial relation such as

$$M_{\rm tot} = d\, \Delta V^2 / G = 3.2 \times 10^{11} M_{\odot}, \tag{5.2}$$

[2]IMF: Initial Mass function is an empirical function that describes the distribution of initial masses for a population of stars. The IMF is often given as probability distribution function for the mass at which a stars enters the main sequence. The IMF determines the baryonic content, the chemical enrichment and the evolution of galaxies, and thus the Universe's light and baryonic matter evolution. The most famous IMF are that of Salpeter (1955) and Kroupa (2001). Salpeter IMF shows that the number of star in each mass range decreases rapidly with increasing mass assuming a power law with an exponent of -2.35. Kroupa IMF is similar to Salpeter one, but it assumes different exponent at different masses: -2.35 for 0.5$M_{\odot}$< M, -1.3 for 0.08$M_{\odot}$<M<0.5, and -0.3 for M < 0.08

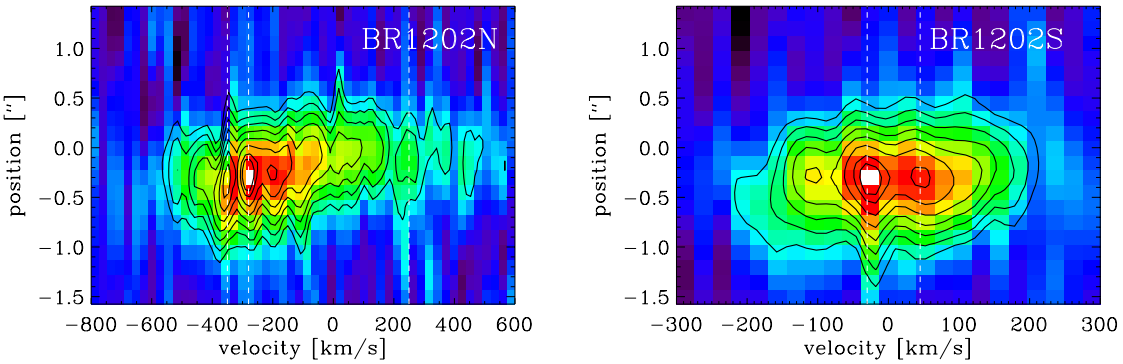

Figure 5.4: Left panel: the position-velocity diagram extracted from a three-pixel-wide E-W slit centered on the N source (SMG). The right panel is the PV diagram for a slit oriented N-S and centered on the S source (QSO). The white dashed lines identify the components discussed in the text.

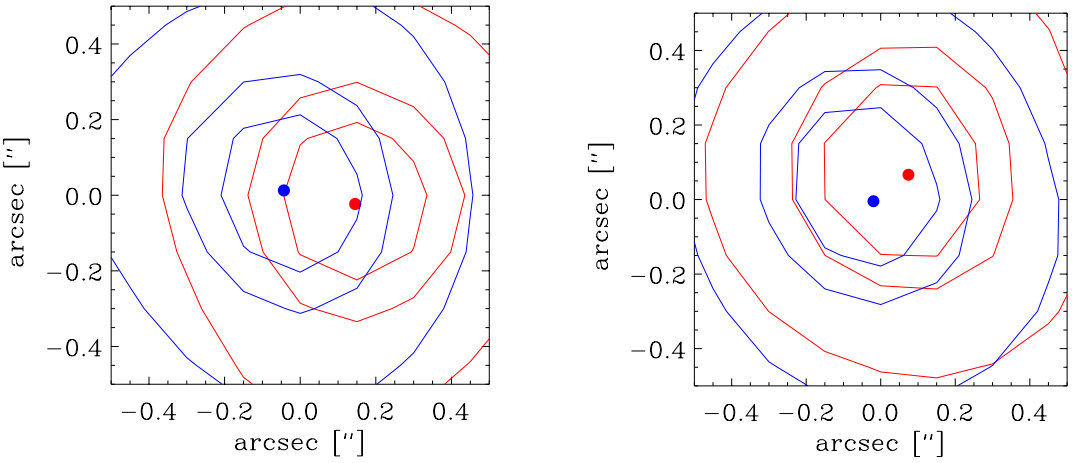

Figure 5.5: Surface brightness contours obtained by collapsing the red and blue channels in the submm galaxy (N source, left panel) and QSO (S source, right panel). Contours are at 90%, 80%, and 50% of the peak values.

where d is the observed projected distance (d = 23.5 kpc) and ΔV is the relative velocity (ΔV = 240 km/s). The dynamical mass was estimated assuming that the binary system is observed edge-on and that the galaxies are moving along the line of sight. This estimate is therefore a lower limit for the mass contained within the volume delimited by the location of two sources; obviously, this is also the lower limit of the mass of the dark matter halo hosting the system.

The extended [CII] emission detected in the two sources (Fig. 5.2) makes a spatially resolved kinematical analysis, which is now described for each source separately. Following Salomé et al. (2012), we first analyzed the position-velocity (PV) diagrams of the [CII] line and performed a full modeling of the observed kinematics.

5.4.1 The Submillimetre Galaxy BR1202 North

The left panel of Figure 5.4 shows the [CII] position-velocity diagram for the submillimetre galaxy. It has been obtained by extracting the spectrum from a three-pixel-wide (0.45″) slit centered on the [CII] surface brightness peak and oriented E-W, as in Salomé et al. (2012). The absolute velocity scale is referred to z = 4.6949. This diagram presents at least three main [CII] components at ∼-350 km s^{-1}, ∼-280 km s^{-1}, and ∼250 km s^{-1}. As suggested by Salomé et al. (2012) based on the CO PV diagram, the component at about ∼250 km s^{-1} probably indicates another weak galaxy east of the SMG, which

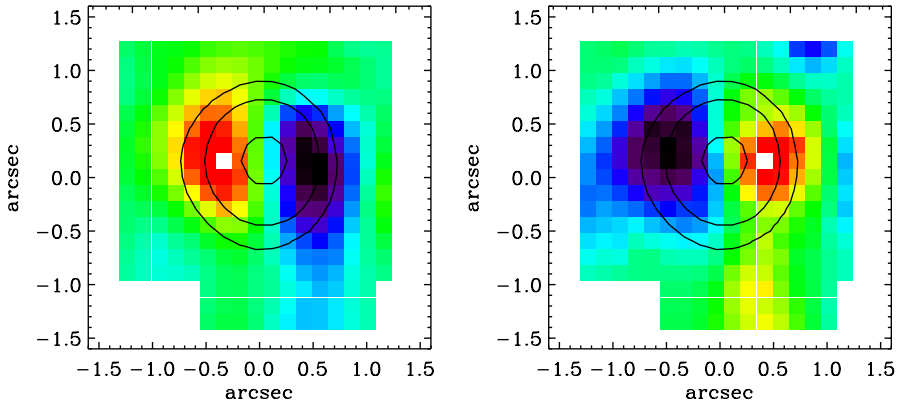

Figure 5.6: Blue and red residual maps of the submillimetre galaxy obtained assuming spatially unresolved kinematics (left and right panels, respectively). Contours represent the total line surface brightness at 90%, 50%, and 30% of the peak value.

might be undergoing an interaction or a merger. This component is responsible for the asymmetric line profile of the SMG compared with that of the QSO (Fig. 5.3). The two main components are separated by Δv=70 km s^{-1}, resulting in a double-peaked line profile which, in some cases, can be the signature of a rotating disk. These separate peaks are not seen in the CO PV diagram by Salomé et al. (2012).

Before performing a spatially resolved kinematical analysis, we tested whether the kinematics is indeed spatially resolved and consistent with a rotating disk.

The first test was to perform a spectroastrometric analysis by collapsing all the velocity channels blueward of the line peak and the redward ones in two separate images. If the SMG has a rotating disk and the rotation is resolved, the blue and red channel maps should have offset surface brightness centroids since they map the approaching and receding halves of the disk, respectively. This is indeed shown in the left panel of Figure 5.5 where the surface brightness peaks of the blue and red maps are separated by $\sim 0.2''$ (1.3 pixels corresponding to 1.2 kpc) along the E-W direction. Following (Gnerucci et al. 2011a), we can therefore use spectroastrometry to obtain a first estimate of the dynamical mass of the SMG as

$$M_{\rm dyn} \sin^2 i = (2.3 \pm 0.2) \times 10^9 {\rm M}_\odot \left(\frac{FWHM}{100 \text{ km s}^{-1}}\right)^2 \left(\frac{r}{1{\rm kpc}}\right) \tag{5.3}$$

where i is the disk inclination with respect to the line of sight, $FWHM$ is the full width at half maximum of the [CII] emission line emission, and r is the half distance between the "red" and "blue" luminosity centroids. On top of the measurement errors, one should consider a 10% systematic *rms* error, deriving from the calibration of Gnerucci et al. (2011a), which was based on a sample of $z \sim 2-3$ Lyman-break galaxies with spatially resolved kinematics. Using $FWHM = 500\pm40$ km/s, $r = 0.6\pm0.2$ kpc, the spectroastrometric mass estimate is then $M_{\rm dyn} \sin^2 i = (3.5 \pm 0.4) \times 10^{10} {\rm M}_\odot$, with a systematic error of 10% *rms*. We stress that this value is valid only under the assumption of a virialized rotating disk. Indeed, the results from the spectroastrometric analysis are consistent with the expectations from a virialized rotating disk, but it could also be possible to reproduce them with outflowing gas in a particular configuration and therefore the more accurate analysis described below is required.

The second test consists of analyzing velocity residual map obtained with a pixel-by-pixel kinematical fitting after assuming that the sources are spatially unresolved. In this case, the line profile of the integrated [CII] emission plotted in Fig. 5.2 is expected to be equal to any line profile regardless of the spatial pixel from where they have been extracted. We therefore performed a pixel-by-pixel fit of the emission line with two Gaussian functions, only allowing for a variation of the total line flux, as expected from unresolved emission. We then obtained the residuals maps by collapsing the blue and red spectral channels, as we did for spectroastrometry. The results of this exercise are shown in

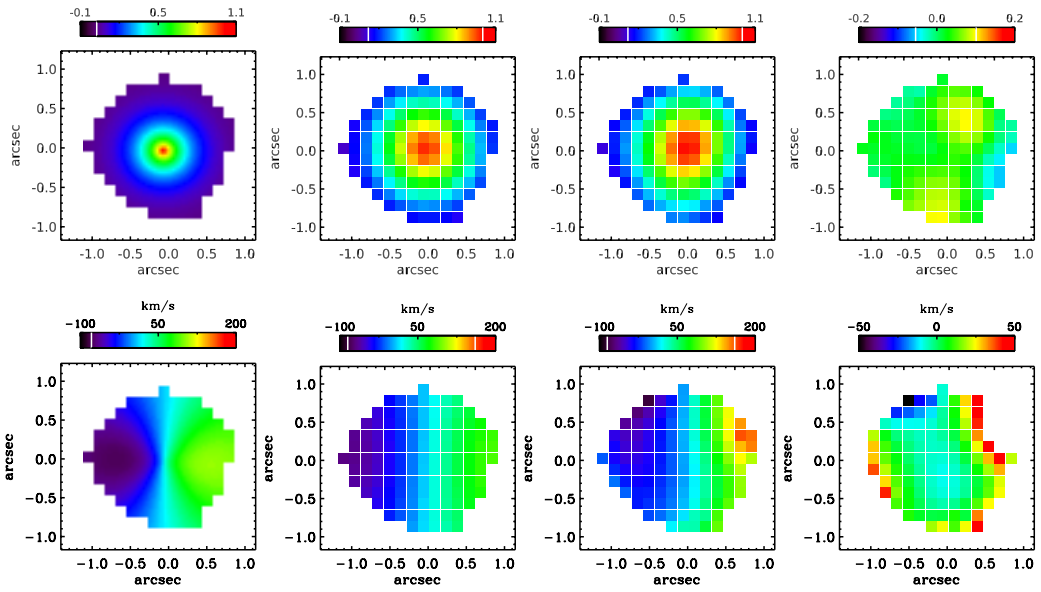

Figure 5.7: Analysis of the SMG surface brightness and kinematics. Upper panels: surface brightness fitting with an exponential disk. Lower panels: velocity field fitting with a circularly rotating disk. From right to left: model, model convoluted for PSF, data and residual map.

Figure 6.2, where we show the blue and red residuals (left and right panels, respectively) with the contours of the total line surface brightness superimposed. The structure of the residuals is clearly what we would expect for a rotating disk after a line fit that does not allow for a variation of the line average velocity. Indeed, the residual map from the blue channels shows positive residuals on the left side and negative residuals on the right side, while the opposite takes place in the residual map from the red channels. Therefore the line velocity is bluer than the average one on the left side, and redder on the right side, as already suggested by the spectroastrometry. This is expected for a rotating disk with the line of nodes oriented E-W with the eastern half approaching the observer.

The observed radial profile of the [CII] surface brightness and the two tests performed above strongly suggest that the [CII] kinematics has been spatially resolved. When extracting the line kinematics we took into account that the [CII] line profile is the result of the combined emission of the SMG and of its faint companion observed in the PV diagram at a velocity of ~250 km s^{-1}. Since the emission of the companion is probably too weak to resolve its kinematics, we performed a pixel-by-pixel fit with the two Gaussian components, but allowing only the stronger one to vary its average velocity and velocity dispersion. Therefore we obtained the velocity field only for the SMG galaxy, cleaning out the distortions due to the faint component. The velocity and flux maps, shown in Figure 5.7, were obtained after selecting only those spatial pixels for which the signal-to-noise ratio of the emission line is equal to or higher than 3; we defined the signal-to-noise ratio of the emission line as the ratio between the peak of the main Gaussian component and the rms of the residuals.

We then fit the velocity map of the SMG using the kinematical disk model used for $z \sim 3$ Lyman-break galaxies by Gnerucci et al. (2011b). We assumed that the gas is circularly rotating in a thin disk, that the gravitational potential depends only on disk mass, and that the disk surface mass density distribution is exponential $\Sigma(r) = \Sigma_0 e^{-r/r_0}$, where r is the distance from the disk center and r_0 is the scale radius. Following Cresci et al. (2009) and Gnerucci et al. (2011b), we also assumed that the mass density distribution is traced by gas emission, and therefore that the center of rotation and scale radius are set by the peak and scale radius of the [CII] surface brightness distribution parameterized by $I(r) = I_0 e^{-r/r_0}$ (Cresci et al. 2009). Rotation center and r_0 were then derived by χ^2 minimization following the comparison of observed and model surface brightness distributions after convoluting the latter with the spatial PSF of the data. The circular velocity field was projected along the line of sight, weighted by the intrinsic line surface brightness, and then convolved with the spatial resolution of the

data to be directly compared with the observed velocity field.

The free parameters of the kinematical model are i, the inclination of the disk along the line of sight, θ, the position angle of the disk line of nodes, V_{sys}, the systemic velocity of the galaxy, and $M_{\rm dyn}$, the total dynamical mass of the disk. $M_{\rm dyn}$ is actually the disk mass enclosed within a radius of 5 kpc. Since this radius is much larger than the disk scale radius, this corresponds to the total mass of the disk. The value of 5 kpc was chosen because the proper distance at $z \sim 5$ corresponds to a proper distance of 10 kpc at $z \sim 2$, which is the value used in the work of Cresci et al. (2009).

The best-fit parameter values for the kinematical model were found using the MPFIT (Markwardt 2009) and AMOEBA algorithms in the IDL environment. The χ^2 space was explored using Monte Carlo Markov chains (MCMC), which allow one to sample a target density distribution, or, in other words, allow one to estimate the posterior probability distribution for the i-dimensional parameter space that defines our disk models. We used the IDL routines developed for the EXOFAST IDL package (Eastman et al. 2013).

Since the disk inclination is not well constrained from the data and since the dynamical mass could be larger than the molecular gas mass, we considered two cases, one with a totally free $M_{\rm dyn}$ and the other with a prior on $M_{\rm dyn}$ based on the molecular gas mass. The prior is given by a lognormal Gaussian step function, that is a lognormal Gaussian on the left side of the peak and a constant value on the right. The peak of the Gaussian is given by the molecular gas mass presented in Table 5.1, and the dispersion is 0.3 dex, corresponding to a factor 2 and compatible with the uncertainties on the conversion factor (e.g. Bolatto et al. 2013).

Figure 5.7 shows the results of the kinematical model fitting and Table 5.1 reports the best-fit parameters. Figure 5.8 show the confidence contours for the $\rm M_{dyn}$ and inclination i values obtained from the MCMC with 10^5 trials with (red) and without (green) the dynamical mass prior.

The scale radius here is $r_0 = 2.8$ kpc, similar to the maximum distance with measured velocity from the disk center, indicating that the observed velocity field traces only the inner regions of the galaxy where dark matter is very likely negligible. It also shows that deviations from the exponential mass density profile due to dark matter are very likely negligible and that $M_{\rm dyn}$ is indeed close to the total disk mass because $2r_0 \sim 5$ kpc.

It is clear from Figure 5.8 that without the prior the best fitting dynamical mass would be smaller than the gas molecular mass by ~ 0.5 dex. However, the velocity map of the SMG is limited to the central parts of the disks and, given the spatial resolution, it lacks a clearly defined spider diagram: only the central velocity gradient is well detected. Therefore, the inclination cannot be well constrained from the data: given the well-known degeneracy of mass and inclination, the mass is poorly constrained, too. The use of the prior therefore provides a physically motivated lower limit to the dynamical mass, which helps constraining its value.

We also performed a fit without the proxy on mass and in which the disk inclination was constrained by assuming that the [CII] flux distribution was radially symmetric on the disk: the resulting disk inclination is in the range $i = 6° \pm 3°$ (90% confidence), which additionally supports the low disk inclination.

To verify whether the rotating disk is really rotationally supported, we compared the intrinsic velocity dispersion with the rotational velocity. By intrinsic velocity dispersion we mean the one that is not accounted for by unresolved rotation and which might be due to turbulent motions. From the dynamical modeling we can estimate the maximum rotational velocity ($\rm V_{max}$) and the intrinsic gas velocity dispersion $\sigma_{\rm int}$

$$\langle \sigma^2_{\rm int} \rangle = \langle \sigma^2_{\rm obs} - \sigma^2_{\rm model} \rangle$$

where $\sigma_{\rm obs}$ is the observed velocity dispersion and $\sigma_{\rm model}$ is that expected from the model that best fits the velocity map. $\sigma_{\rm obs}$ is directly obtained from the main Gaussian line component without any correction for the spectral resolution; $\sigma_{\rm model}$ is computed by assuming a cold rotating disk, that is with no intrinsic velocity dispersion, and by taking into account the spectral and spatial resolutions of the observations. In particular, the main contribution to $\sigma_{\rm model}$ is given by beam smearing, while the effect of the spectral resolution is negligible since line widths are large. $\sigma_{\rm int}$ is therefore the intrinsic

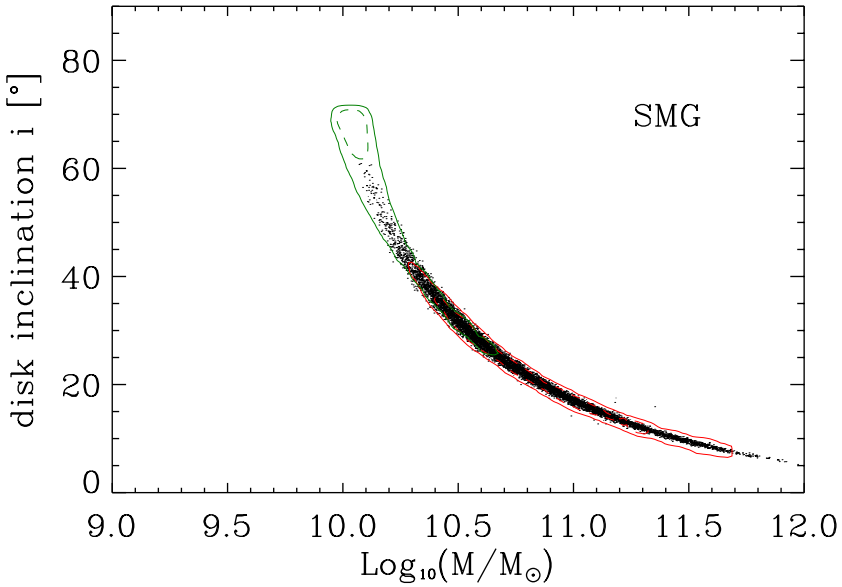

Figure 5.8: Confidence contours for the dynamical mass and inclination values of the SMG obtained with the MCMC and 10^5 trials. The solid and dashed lines identify the 95% and 60% confidence limits, respectively. The red and green contours denote the cases with and without the prior on the dynamical mass, respectively.

velocity dispersion of the emitting material.

The ratio V_{max}/σ_{int} was used to indicate whether the kinematic of the galaxy is rotation dominated ($V_{max} > \sigma_{int}$) or dispersion dominated ($V_{max} < \sigma_{int}$). For the SMG we obtained $V_{max}/\sigma_{int} \sim 1.3$ with $V_{max} \sim 270$ km/s and $< \sigma_{int} >\sim 200$ km/s. This indicates that the submillimetre galaxy has a dynamically hot disk compared with local galaxies for which $V_{max}/\sigma_{int} \sim 10$, but comparable with LBGs at redshift $z \sim 2-3$ (Cresci et al. 2009; Gnerucci et al. 2011b).

Summarizing, the mass and inclination of the SMG disk were derived from the posterior distributions of the parameters by considering the median values and the 5 and 95 percentiles and result in $Log_{10}(M_{SMG}/M_\odot) = 10.8 \pm 0.6$ ($M_{SMG} = 6^{+18}_{-5} \times 10^{10}\,M_\odot$) and $i = 25° \pm 15°$.

The spectroastrometric estimate performed at the beginning of this section $M_{SMG,vir} = (4.7 \pm 1.5) \times 10^{10}\ M_\odot$ (for an average inclination value of $i = 60$ deg, taking into account the 0.15 *dex* systematic error) is perfectly consistent with the dynamical mass measured from the spatially resolved kinematics, confirming the reliability of the spectroastrometric method of Gnerucci et al. (2011a).

We conclude this section by roughly estimating the amount of mass that could be supported by the disk velocity dispersion, because M_{SMG} is only the amount of mass that is supported against gravity by disk rotation. If the velocity dispersion indeed provides support against gravity, the dispersion-supported mass would not be negligible since $\sigma_{int} \sim V_{rot}$. In this case, unfortunately, it is not possible to apply simple recipes such as the asymmetric drift correction (see, e.g., Barth et al. 2001), and we therefore rely only on a virial estimate. With $\sigma_{int} \simeq 200$ km/s and $r_0 = 2.8$ kpc the dispersion-supported mass is $M_{SMG,disp} \simeq \sigma^2_{int} r_0/G = 2.6 \times 10^{10} M_\odot$, similar to the rotation-supported mass, as expected.

5.4.2 The Quasar BR1202 South

The [CII] position-velocity diagram for the QSO (fig. 5.4, right panel) was obtained by extracting a spectrum from a three-pixel-wide (0.45″) slit centered on the surface brightness peak and oriented N-S to compare with Salomé et al. (2012). Similarly to what was found in the PV diagram of the CO(5-4) line by Salomé et al. (2012), the two main components at $v = -30$ and 40 km/s a rotating gas disk.

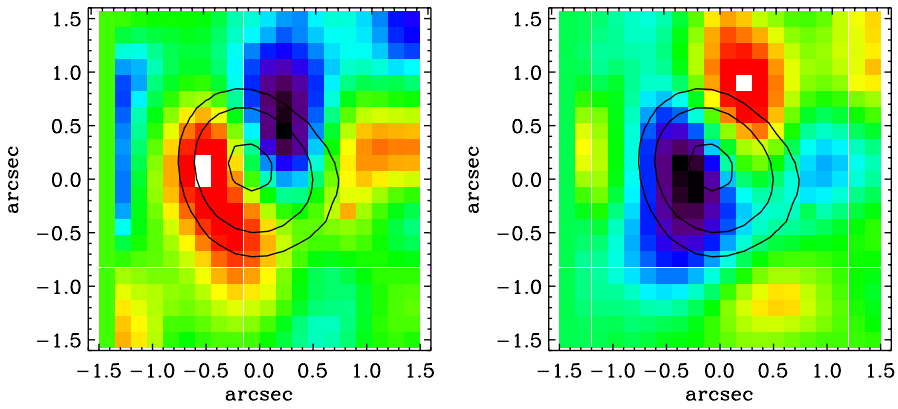

Figure 5.9: Blue and red residual maps of the QSO host galaxy obtained assuming spatially unresolved kinematics (left and right panels, respectively). Contours represent the total line surface brightness at 90%, 50%, and 30% of the peak value.

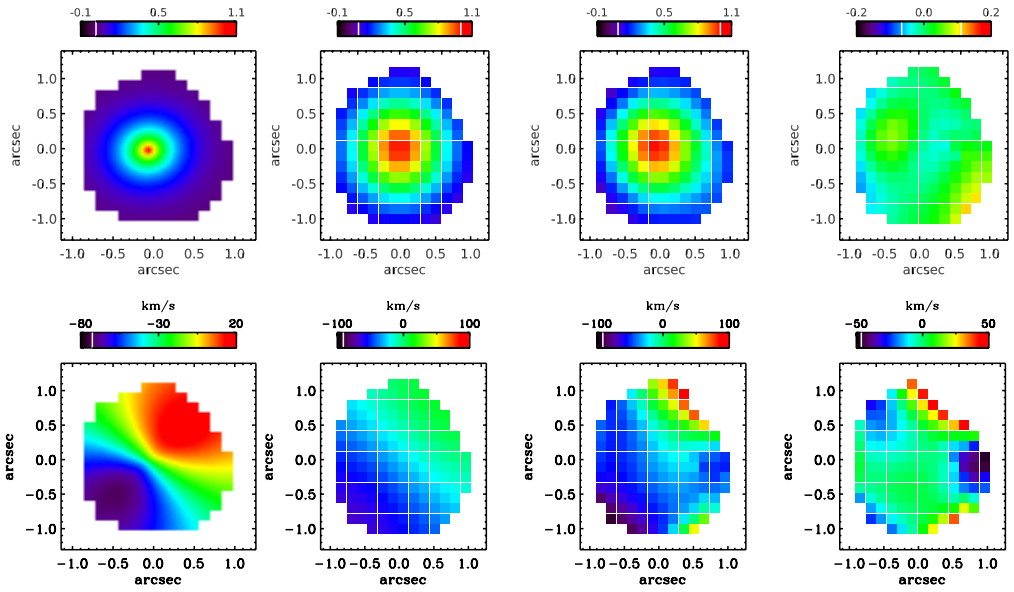

Figure 5.10: Analysis of the QSO surface brightness and kinematics. Upper panels: surface brightness fitting with an exponential disk. Lower panels: velocity field fitting with a circularly rotating disk. From right to left: model, model convoluted for PSF, data and residual map.

The results of the spectroastrometric test, performed in the same way as for the SMG, are shown in Figure 5.5 and confirm the possibility of a rotating disk. The dynamical mass estimated from spectroastrometry following Gnerucci et al. (2011b) is $M_{\rm dyn} \sin^2 i = (8.3 \pm 1.0) \times 10^9$ M$_\odot$for measured values of $FWHM = 300 \pm 20$ km/s and $r = (0.4 \pm 0.1)$ kpc, the half distance between the blue and red surface brightness centroids.

The results of the residuals tests are shown in figure 5.9 and, as for the SMG, they confirm that the kinematics is spatially resolved and that the disk is probably rotating.

The [CII] kinematical map for the QSO host galaxy has been obtained with a pixel-by-pixel fitting of two Gaussian functions, as suggested by the presence of the red wing shown in Figure 5.3. As for the SMG galaxy, we first fit the spectrum obtained from the integrated QSO emission with two Gaussian components, constrained to have the same line width. The fainter component, which reproduces the red wing, was then kept fixed in the pixel-by-pixel fitting except for its flux. The resulting surface brightness and velocity maps are shown in Figure 5.10. As for the SMG galaxy, the QSO velocity field shows a velocity gradient oriented in the same direction as the shift between the red and blue centroids. To ensure that the kinematics of the QSO host galaxy is not affected by our decomposition method, we furthermore assumed that the red wing was caused by outflows or tidal interactions and therefore is emitted by gas with a high velocity dispersion (Carilli et al. 2013). After constraining the width of the fainter Gaussian function to $\sim$ 400 km/s (Carilli et al. 2013), we repeated the previous procedure and obtained a kinematical map that is consistent with the former, within the errors.

We then repeated the analysis performed for the SMG galaxy and fit the QSO kinematics with a rotating disk. We computed an MCMC with 10^5 trials with and without the molecular gas mass prior; the results are shown in Figure 5.11, where, as before, the red and green contours denote the cases with and without the prior on the mass. At variance with the case of the SMG, the confidence contours on the two cases overlap at $\log M/M_\odot \sim 10.6$, indicating that even without the prior, the dynamical mass is consistent with the molecular gas mass. All the relevant best-fit parameter values are also shown in Table 5.1.

In this case we also performed a fit without the proxy on mass and with the disk inclination constrained by assuming that the [CII] flux distribution is radially symmetric on the disk: the resulting disk inclination is in the range $i = 2^\circ \pm 2^\circ$ (90% confidence), which also supports the low disk inclination, as for the SMG.

As in the case of the SMG, by using the rotating disk model we estimated $V_{\rm max} \sim 230$ km/s and a $\langle \sigma_{\rm int} \rangle \sim 150$ km/s and corresponding ratio $V_{\rm max}/\sigma_{\rm int} \sim 1.5$. This indicates a dynamically hot disk compared to local galaxies, but still marginally colder than that of the SMG.

Summarizing, the mass and inclination of the QSO disk derived from the posterior distributions of the parameters by considering the median values and the 5 and 95 percentiles result in $Log_{10}(M_{QSO}/M_\odot) = 10.6^{+0.8}_{-0.4}$ ($M_{QSO} = 4^{+20}_{-3} \times 10^{10}\, M_\odot$)) and $i = 15^\circ \pm 10^\circ$. This is consistent within the error with the mass estimated from spectroastrometry.

Finally, using $\sigma_{int} \simeq 150$ and $r_0 = 2.4$ kpc, the dispersion-supported mass is $M_{QSO,disp} \simeq \sigma^2_{int} r_0/G = 1.2 \times 10^{10} M_\odot$, a significant contribution to the rotation-supported mass, as expected.

Overall, the total SMG and QSO mass is smaller than the lower limit we estimated for the dark halo mass.

Intriguingly, the QSO and SMG have similar SFRs (between 1000 and 5000 M$_\odot$ for both), molecular gas masses ($\sim 4 \times 10^{10}$ M$_\odot$) and moderately similar dynamical masses when the different inclinations of the gas disks are considered.

5.4.3 Spectroscopically Detected Faint Companions

In Figure 5.12 we show the surface brightness maps of the sources identified as faint Gaussian components in the spectra plotted in Figure 5.3. These components have velocities of 570 km/s (SMG) and 500 km/s (QSO) with respect to the main components, and velocity dispersions of 220 km/s and 150 km/s. These values where kept fixed during the pixel-by-pixel fit. The surface brightness centroids of these components have a distance of 0.24″ and 0.15″ from the SMG and QSO, respectively, which

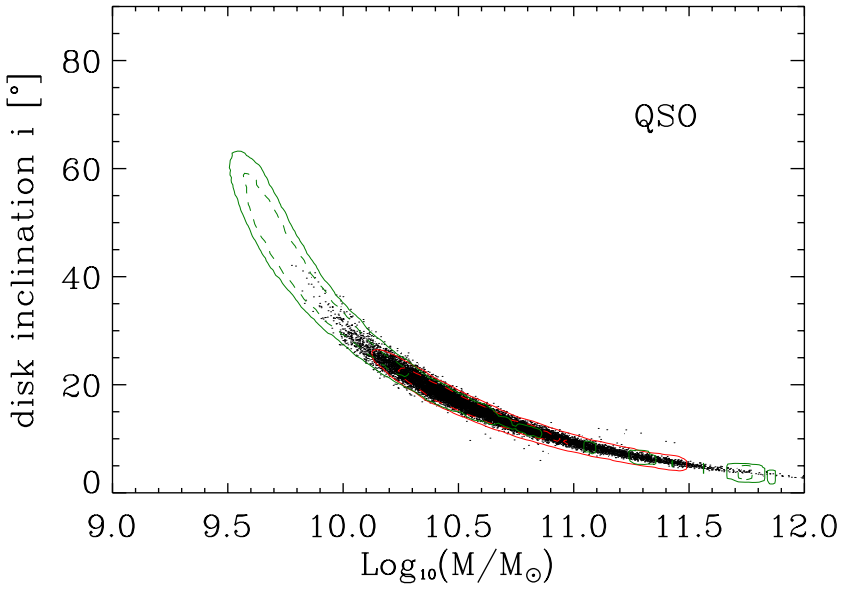

Figure 5.11: Confidence contours for the dynamical mass and inclination values of the QSO obtained with the MCMC and 10^5 trials. The solid and dashed lines identify the 95% and 60% confidence limits, respectively. The red and green contours denote the cases with and without the prior on the dynamical mass, respectively.

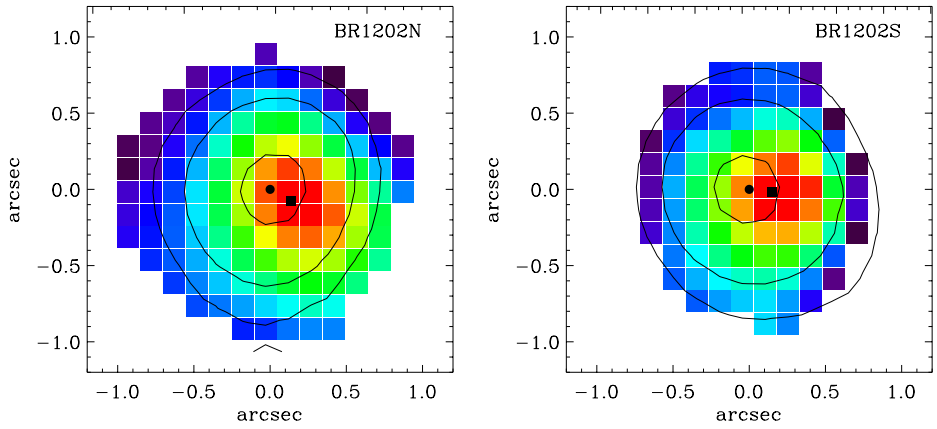

Figure 5.12: Surface brightness maps of the sources identified as faint components in the spectral fits: the left and right panels show the SMG and QSO, respectively. The black contours denote the surface brightnesses of the main spectral components; the filled circles and squares denote the centroids of the main and faint components, respectively.

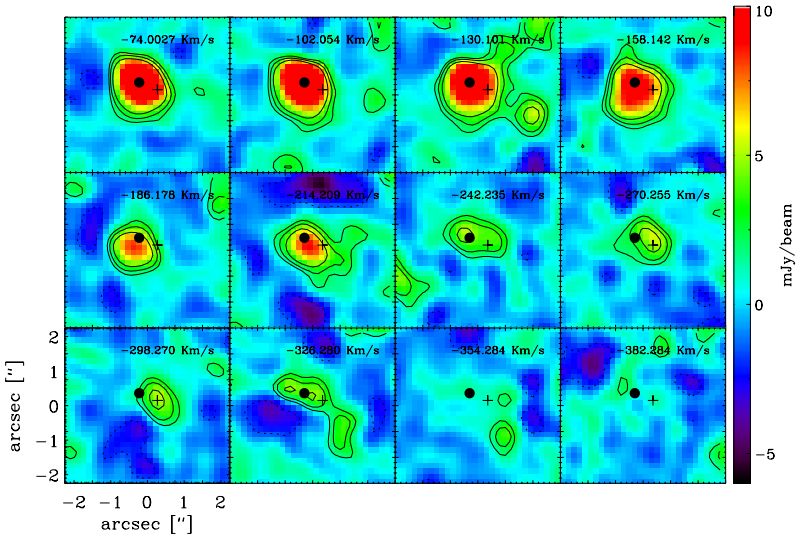

Figure 5.13: Brightness per velocity channel in the QSO. Color-coded values and contours at [2,3,5] σ levels are shown. The numbers in the upper right corners of the panels denote the central velocity of the channel. The filled circle represents the peak of the integrated surface brightness of the QSO, while the cross represents the peak of the surface brightness of the faint companion, which is detected in channels $\sim -362 : -242$ km/s.

at the redshift of the BR1202-0725 system corresponds to $\sim$ 1.6 and $\sim$ 0.9 kpc. These components are only detected spectroscopically, and because of their faintness and distance from the main components cannot be seen in direct images obtained by collapsing a given velocity range in the datacube. Therefore these are sources additional to those identified by Wagg et al. 2012 and Carilli et al. 2013.

Figure 5.13 shows the [CII] channel map for the QSO where, in the channels at velocities from -326 to -242 km/s, we observe a small weak component whose integrated surface brightness peak is indicated by a cross. For comparison, the filled circle indicates the centroid of the QSO main emission. Its relative velocity with respect to the QSO is ~ -250 km/s for a projected distance of $r = 3.4$ kpc.

Overall, we have spectroscopically identified three new components at distances less than 3.5 kpc from the SMG and QSO host galaxy. Considering also the two components identified by Wagg et al. (2012) and Carilli et al. (2013) which correspond to the Ly-α emitters visible in the HST images, we have a total of at least five faint components on top of the two main components, which are the SMG and QSO host galaxy. The BR1202 system clearly represents a complex system, probably a dense group or protocluster in the early Universe with intense ongoing star formation. However, it is not possible to assess whether these components represent small galaxies, or gas clouds in tidal tails, inflows or outflows. They are probably they are the same type of objects as Ly-α emitters.

However, assuming that they are subjected only to gravitational motions, it is possible to use these components for a rough estimate of the mass of the associated main component (SMG or QSO). Assuming that their orbital planes are seen edge-on and that their motions are entirely along the line of sight, we can combine their velocities and distances from the main components to obtain a virial mass estimate of the SMG or QSO host galaxy. Given our assumptions, these are clearly lower limits on the true mass values. The inferred masses are $\sim 1.2 \times 10^{11}$ $M_\odot$ for the SMG and $\sim 5.2 \times 10^{10}$ $M_\odot$, $\sim 5.9 \times 10^{10}$ $M_\odot$ from the redshfited and blueshifted components of the QSO. These lower limits should be compared with the measurements performed in the previous sections, which are $0.6^{+1.9}_{-0.4} \times 10^{11}$ $M_\odot$ for the SMG and $0.4^{+2.1}_{-0.2} \times 10^{11}$ $M_\odot$ for the QSO. These values are evidently agree in remarkably with the measurements from the spatially resolved kinematics supporting the hypothesis of gravitational motions for the spectroscopically detected components. However, it should be noted that (i) any correction for the unknown geometrical projection effects will increase the mass estimate, (ii) the SMG and QSO host galaxy masses enclosed within the measured distances from the faint components are smaller than the total dynamical estimates, and (iii) the above estimates are based on the assumption of

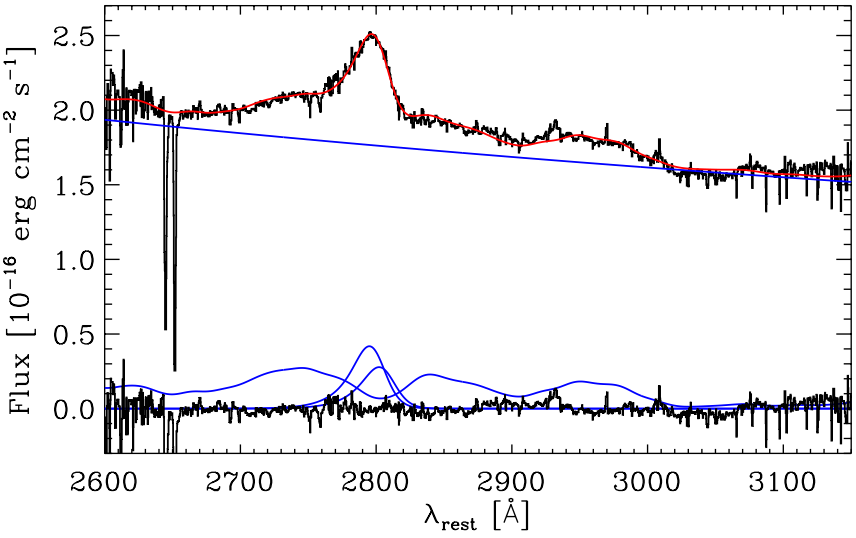

Figure 5.14: X-Shooter spectrum of the QSO (S source) and model fit (red line) in the good atmospheric regions. The MgII doublet, FeII spectrum and power law continuum are shown with blue lines. Below is the residual spectrum.

circular orbits while, higher velocities could be found with other, more general, types of orbits. Both (i) and (ii) will undoubtedly worsen the agreement with the dynamical masses at an unknown level, while (iii) would improve it.

It is also possible that these faint components represent quasar- or star formation-driven outflows. This interpretation has been proposed by Carilli et al. (2013) for the red wing of the QSO. However, outflows detected from emission lines at submm wavelengths are seen on both blue and red sides of the emission line profiles (e.g., Feruglio et al. 2010; Maiolino et al. 2012). Moreover, it would be very peculiar that we are seeing almost face-on galactic disks for the SMG and QSO while detecting only outflows on the far sides.

Summarizing, although it is not possible to assess the physical origin of the faint spectral components, the relative velocities and positions of the faint components detected spectroscopically suggest that they are orbiting in the gravitational wells of the SMG and QSO host galaxy, favoring their identification as small galaxies, or gas clouds in an accretion flow or in tidal stream. The relative velocities and positions provide no support either for their identification as gas clouds in QSO or star formation driven outflows. ALMA observations with higher sensitivity and spatial resolution are needed to establish the physical origin of these faint spectroscopic components.

5.5 Black Hole Mass of the QSO

To estimate the black hole mass in the QSO and compare it with the mass of the host galaxy, the only possibility is to use a virial estimate based on broad emission lines such as Hβ, MgII λ2800 Å, and CIV λ1546 Å. Hβ and MgII are currently believed to be the most accurate BH mass estimators with systematic uncertainties of up to $\sim$ 0.5 dex, while CIV is very likely affected by outflows or nonvirial motions (see Shen 2013 for a review).

An intermediate-resolution spectrum of the QSO has been obtained with X-shooter (Vernet et al. 2011) at the ESO VLT (P.ID. 084.A-0780B) with the main aim of studying galactic and intergalactic absorption lines. A total of 2.5 hours of exposure time was obtained using a slit set of 0.8″/0.7″/0.6″ for the blue, visual (VIS), and near-infrared (NIR) arms, resulting in spectral resolutions of 6000, 11000, and 7950, respectively. The data were reduced with the public X-shooter pipeline (Modigliani et al. 2010) using the default parameters. The pipeline rebins the spectra to 0.4 Å/pixel in the blue and VIS arm and to 1 Å/pixel in the NIR arm. Telluric absorption was removed using the spectrum

of the B5V star Hip 073345 after removing the prominent H absorption lines. The NIR portion of the spectrum (extending from 1 to 2.5 mum) includes the broad MgII emission line doublet at 2800 Å rest frame, which is considered a good estimator for the mass of the supermassive black hole. The region of the spectrum around the MgII emission is shown in Figure 5.14.

The spectrum was fit with a combination of power-law continuum, FeII emission and broad line. For the FeII emission we used a combination of model templates generated with CLOUDY (version 10.00; Ferland et al. 2013) at the conditions typical of the BLR and allowing for Doppler broadening with a Gaussian of given velocity dispersion. For each of the MgII lines we used a broken power-law profile (Nagao et al. 2006) convolved with a Gaussian with unknown velocity dispersion. The two MgII lines were forced to have the same line profile in velocity, with a flux ratio $\lambda 2796/\lambda 2803$ limited in the 1.0-2.0 range (Laor et al. 1997). The red line in Figure 5.14 shows the best model fit, which results in the following line width and continuum luminosity for the MgII lines: $FWHM = 3400 \pm 100$ km/s and $\lambda L_\lambda(3000\text{Å}) = (1.1 \pm 0.1) \times 10^{47}$ erg/s. Extrapolating the power-law continuum, we obtain $\lambda L_\lambda(1450\text{Å}) = 1.3 \times 10^{47}$ erg/s and $\lambda L_\lambda(5100\text{Å}) = 9.5 \times 10^{46}$ erg/s.

The black hole mass was estimated using the virial relation $M_{BH} = fV^2R/G$, where V is the line width (FWHM or σ) and R is the broad line region radius derived from the well-known radius luminosity relation (Kaspi et al. 2000; Bentz et al. 2009). The scaling factor f was calibrated by imposing that viral masses agree with the relations between BH mass and host galaxy properties observed in the local Universe (see, e.g., Peterson 2011). Here we adopted the very recent calibration by Marconi et al. (2013, in preparation), obtained by matching the virial BH masses of the AGN with reverberation-mapping data with the BH masses estimated from the velocity dispersions and luminosities of the host galaxy spheroids, using the $M_{BH} - \sigma$ and $M_{BH} - L$ relations by McConnell & Ma (2013): the adopted virial relation is then $M_{BH}/M_\odot = 10^{6.7} FWHM^2_{1000}[\lambda L_\lambda(3000\text{Å})]^{0.5}_{44}$ where the subscripts 1000 and 44 indicate units of 1000 km/s and 10^{44} erg/s, respectively. The zero point of this relations has a ~ 0.3 dex systematic uncertainty and is lower by 0.15 dex with respect to the zero point of the calibration by Vestergaard & Osmer (2009). Finally, the estimated black hole mass is $M_{BH} = 1.9 \times 10^9$ $M_\odot$ (± 0.3 dex, systematic). The QSO bolometric luminosity was estimated from the UV and optical luminosities. Using the relation by Mor et al. (2012), we derived $L_{AGN} \sim 3.8 \times 10^{47}$erg/s from $\lambda L_\lambda(1450\text{Å})$, while we derived $L_{AGN} \sim 5.7 \times 10^{47}$erg/s adopting $L_{AGN} \sim 6\lambda L_\lambda(5100\text{Å})$ from Marconi et al. (2004). The Eddington ratio is therefore $L/L_{Edd} \sim 1.5$. Finally, combining the BH with the dynamical mass for the host galaxy of $\sim 4 \times 10^{10}$ $M_\odot$, the ratio between the black hole and dynamical galaxy mass is ~ 0.05; if we also consider the contribution from the velocity dispersion to the host galaxy mass, this ration drops to 0.04. These values are consistent with the upper envelope of the local $M_{BH} - M_{gal}$ relation (see, e.g, Figure 3 of Sani et al. (2011) and fig. 5.15 below).

5.6 Discussion

According to the paradigm of co-evolution between BHs and their host galaxies, large bursts of star formation and AGN activity should be induced by mergers or interactions, at least at large galaxy masses: gravitational torques cause gas inflows that fuel star formation and accrete onto supermassive black holes in galaxy nuclei. In this framework it is predicted that an SMG and a QSO represent two distinct phases (see, e.g., Alexander & Hickox 2012 for a recent review). The SMG represents the early phases after a major merging of gas-rich galaxies when star formation and BH accretion proceed at very high rates in a dust-obscured environment. When the active galactic nucleus is powerful enough, it can expel the gas from the host galaxy, quenching both star formation and black hole accretion, and we are left with a QSO shining in an otherwise passive galaxy (e.g. Di Matteo et al. 2005; Hopkins et al. 2010, 2006).

The BR 1202-0725 system, composed of a submm galaxy (SMG, N Source) and of a quasar (QSO, S Source) at $z \sim 4.7$, is an ideal test bench for this paradigm. The physical properties of the submm galaxy and of the QSO are summarised in Table 5.1. Overall, the two galaxies have remarkably similar FIR continuum, [CII] and CO line luminosities, which can be translated into similar SFRs and

molecular gas masses. Moreover, they also have similar dynamical masses.

These two galaxies are highly gas rich ($M_{mol} \sim 4 \times 10^{10}\,M_\odot$) and strongly star forming ($SFR \sim 3000\,M_\odot/yr$) with dynamical masses within the inner 5 kpc of about $M_{dyn} \sim 5 \times 10^{10}\,M_\odot$ which suggests high gas fractions. Taking into account the uncertainties on the disk inclinations and on the conversion factor, the corresponding gas fractions are constrained in the ranges 0.1-1.0 (0.7 average) for the QSO and 0.2-1 (0.8 average) for the SMG. The average values in parenthesis are for the average disk inclinations of i=25° for the SMG and i=15° for the QSO. Although weakly constrained, the data suggest moderately high to high gas fraction values.

The relative proximity of the SMG and QSO (projected distance of $\sim$ 24 kpc) suggests that the two galaxies might be in the early phases of a major merger that is taking place within a relatively massive halo: the relative velocities of the two galaxies combined with the projected distance allow one to obtain a lower limit to the mass of the host halo, which is $> 3.2 \times 10^{11} M_\odot$, compared with a total mass of $1.0^{+3.8}_{-0.8} \times 10^{11} M_\odot$ for the QSO and SMG.

Summarising, the SMG and QSO have very similar characteristics, and the only real difference is that the S source is a QSO, although it is not possible to exclude the presence of a luminous obscured AGN even in the SMG. The intriguing results are that these high SFRs are apparently not triggered by major mergers and that there are no evident signs of feedback in action.

5.6.1 Rotating Disks and the Origin of the High Star Formation Rates

At variance with the major-merger scenario, the kinematical analysis we have performed indicates that both galaxies have velocity fields that are consistent with regular rotation, without indications of significant distortions like those expected from major mergers, strong interactions, or AGN feedback. For the merger scenario, this fact confirms that the two galaxies are still far enough away from each other not to be affected by significant tidal forces.

Both galaxies are experiencing star formation at rates that will exhaust the gas on very short timescales. The observed molecular gas masses and SFRs imply gas depletion time scales of $\tau_{\rm dep} = M_{\rm gas}/{\rm SFR} \sim 10^7$ yr, similar with those of ULIRGs (e.g Tacconi et al. 2006; Bouché et al. 2007). If the SMG and QSO are in an early merger phase, their gas might be entirely converted into stars before they actually do merge. In fact, the relative velocity between the two sources is about 240 km/s which, combined with a projected distance of 23.5 kpc, suggests a merger timescale of $\sim 10^8$ yr, longer than the gas depletion timescale. Overall, there are no signs of major-merger induced star formation, and the stars in the galaxies might be already formed when the two galaxies are close enough to merge.

The question that naturally arises is what triggered the burst of star formation in the SMG and the QSO since, apparently, it is not a major merger.

Both the SMG and QSO in the BR 1202-0725 system are experiencing high star formation rates (SFR>1000 $M_\odot$/yr) in rotating disks, apparently excluding major mergers. However, both galaxies show fainter companions that are revealed spectroscopically and whose emission lines have been deblended when measuring the kinematics (see also Salomé et al. 2012). The velocities and positions of these companions relative to the SMG and the QSO are consistent with gravitational motions within the gravitational potential wells of the two largest sources. Furthermore, Carilli et al. (2013) and Wagg et al. (2012) find evidence for the emission of a faint southwest source which is probably interacting with the S source, and also an additional companion between the two galaxies. Therefore the BR 1202-0725 system might be a massive proto-cluster where the high star formation activity is probably triggered by minor mergers or interactions that destabilise the gaseous disks, but that do not significantly affect the kinematics of the SMG and QSO galaxies. Alternatively, the high star formation rate might be triggered by cold gas inflows from the halo, which, again, destabilise the gas disks gravitationally. Intriguingly the trigger of star formation from minor mergers, interactions or disk instabilities might be consistent with the dynamically hot disks, indicated by the observed ratios $V_{\rm max}/\sigma_{\rm int} \sim 1.3$ and 1.5 for the SMG and for the QSO respectively. Moreover, both velocity maps show residuals at the positions of the possible faint companions after subtracting the rotating disk models. However, the sensitivity and spatial resolution of the data do not allow us to quantify this result.

Evidence that processes such as accretion of pristine gas might induce star formation is starting to accumulate. For instance, Cresci et al. (2010) found evidence that gas accretion might be the origin of metallicity gradients in high-redshift star-forming galaxies. In a recent study, Kaviraj et al. (2013) estimated that only ∼27 percent of the total star formation budget in a sample of 80 massive galaxies a z≃2 is due to major mergers. This suggests that other contributions to star formation activity such as cold flows and minor merger might be operating. The dynamically hot rotating disks are also found in LBGs at $z \sim$ 1-2 (e.g. Genzel et al. 2006; Förster Schreiber et al. 2006) and at $z \sim 3$ (Gnerucci et al. 2011), associated with the very high gas fractions that can destabilise the disk gravitationally (Tacconi et al. 2010; Daddi et al. 2010a). Future observations with ALMA at higher spatial resolution and sensitivity might help to reveal the trigger of the strong star formation activity in BR1202 and in other systems.

To explore the origin of the star formation activity in more detail, we located the two galaxies on the Schmidt-Kennicutt relation at high redshift. With the disk scale radii estimated during the kinematic analysis, we estimated the SFR and gas surface densities, $\Sigma_{\rm SFR}$ and $\Sigma_{\rm gas}$ in the two sources. The values obtained for the SMG ($\Sigma_{\rm SFR}$ = 80 $M_\odot$/yr kpc^{-2}, $\Sigma_{\rm gas}$ = 1900 $M_\odot$ pc^{-2}) and QSO ($\Sigma_{\rm SFR}$ = 180 $M_\odot$/yr kpc^{-2}, $\Sigma_{\rm gas}$ = 1800 $M_\odot$ pc^{-2}) are perfectly consistent with the relation found by Daddi et al. (2010) for starburst galaxies (SMGs and ULIRGs, see their Figure 2), which form a different relation from that of local star-forming galaxies.

Summarising, the lack of major-merger-induced features combined with the high SFR per unit mass suggest that star formation in the BR 1202-0725 system is probably triggered by interactions, minor mergers, or inflow of gas from the halo that increase the concentration of the gas and dust in the galaxy and destabilise the disks gravitationally.

5.6.2 Relation between the Accreting BH and its Host Galaxy

First of all, we compared the AGN and star formation luminosities in the QSO with the active sources at similar redshifts observed by Mor et al. (2012). Using the λL_λ(1450Å) value estimated from the XShooter spectrum and combining it with the bolometric correction by Mor et al. (2012), we derive $L_{\rm AGN} \sim 3.8 \times 10^{47}$erg/s. When combining this with $L_{\rm SF} \sim 7 \times 10^{46}$erg/s, the QSO is located above the $L_{\rm SF} \sim L_{\rm AGN}^{0.7}$ relation observed for lower luminosity sources (Netzer 2009), but close to the five z∼ 4.8 sources observed by (Mor et al. 2012): the location above the local $L_{\rm SF} - L_{\rm AGN}$ relation might suggests that the feedback mechanism is still not effective enough to reduce star formation activity (see the discussion in Netzer 2009; Mor et al. 2012). Indeed, the regular kinematics observed for the QSO host galaxy suggest that the feedback process might not yet be affecting star formation.

For the SMG, we did not find any evidence for an accreting BH, but the presence of an obscured AGN is supported by radio and X-ray observations. The radio continuum flux density of the N source at 1.4 GHz suggests the presence of a highly obscured AGN (Carilli et al. 2002; Iono et al. 2006). This presence is tentatively confirmed by the X-ray emission observed by Chandra at the SMG position (Iono et al. 2006). However, nothing more can be inferred, apart that from here we did not find any evidence for feedback, either.

Figure 5.15 shows the most up-to-date $M_{\rm BH}$-$M_{\rm bulge}$ relation in the local Universe obtained by McConnell & Ma (2013). The filled red dot with error bars marks the location of the QSO from the measurements presented above. The empty red circle marks the location of the QSO if the dynamical mass supported by the intrinsic velocity dispersion is taken into account. We recall that the QSO BH mass is a viral estimate, not from spatially resolved kinematical modelling as for the black points in the figure. Moreover, the mass of the QSO host galaxy is not the bulge mass, but the total dynamical mass enclosed within 5 kpc.

The present measurement agrees marginally with the upper envelope of the relation, where the uncertainties on the galaxy mass are taken into account. The best-fit relation by McConnell & Ma (2013), $\log(M_{BH}/M_\odot) = 8.46 + 1.05 \log(M_{bulge}/10^{11} M_\odot)$, would predict a BH mass of $\sim 1.2 \times 10^8 M_\odot$, which is a factor 10 smaller than observed, consistent with previous estimates for luminous quasars at high redshift (see, e.g., Willott et al. 2013; Wang et al. 2013; Venemans et al. 2012; Merloni et al.

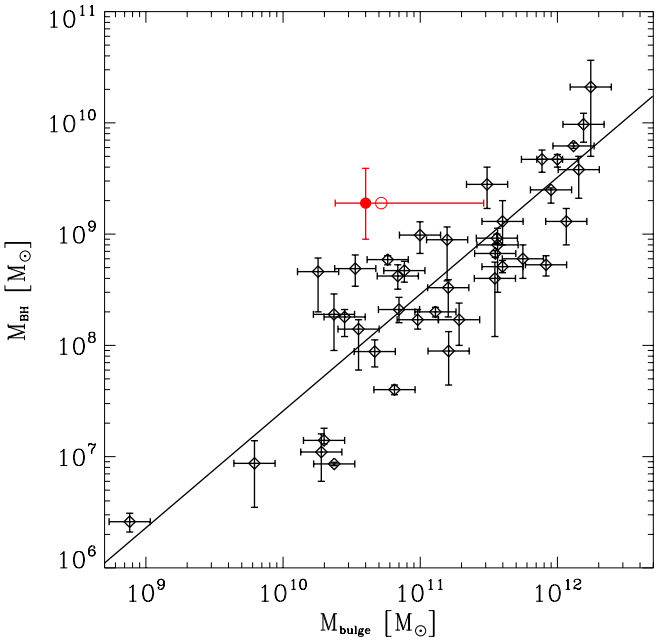

Figure 5.15: M_{BH}-M_{bulge} relation for 35 early-type galaxies in the local Universe (empty diamonds) and BR1202 S (red filled circle; the empty filled circle also considers the contribution from the dispersion-supported mass). The black line represents the best-fitting relation estimated by McConnell & Ma (2013): $\log(M_{BH}/M_\odot) = 8.46 + 1.05\log(M_{bulge}/10^{11}M_\odot)$.

2010; Decarli et al. 2010; Lamastra et al. 2010; Riechers et al. 2009; Peng et al. 2006). However, the uncertainties on the disk inclination of the QSO host galaxy are such that this measurement could be consistent with the upper envelope of the local relation and in particular with the most massive local galaxy like BCGs (McConnell et al. 2012).

This is the first dynamical mass estimate of a QSO host galaxy at high redshift based on the analysis of the spatially resolved kinematics, the only other one is that of a QSO host galaxy at $z \sim 1.3$ (Inskip et al. 2011). All other measurements are either stellar masses based on photometry (Merloni et al. 2010; Decarli et al. 2010; Peng et al. 2006) or dynamical masses based on simple virial estimates (Willott et al. 2013; Wang et al. 2013; Venemans et al. 2012). The former are subjected to large uncertainties and selection biases, which might account for the large M_{BH}/M_{bul} observed (Lamastra et al. 2010). The latter are subject to large uncertainties on the unknown geometry and kinematics of the host galaxy. In particular, the present work has shown that it is critical to properly take into account the disk inclination: if we were to assume an average inclination of 60 degrees, the dynamical masses so obtained would have been inconsistent with the molecular gas masses.

Therefore, the only possibility to avoid the large uncertainties and selection biases on stellar masses and the large uncertainties on virial mass estimates is to use dynamical host galaxy masses obtained from spatially resolved kinematics. Intriguingly, in the only other case in which the dynamical mass of a QSO host galaxy ($z \sim 1.3$) has been determined from a spatially resolved kinematical analysis, the BH mass and the galaxy mass agree with the local relation (Inskip et al. 2011). This suggests that dynamical mass determinations from submm spectroscopy such as presented here might be much better probes of the cosmological evolution of the $M_{BH} - M_{gal}$ relation.

5.7 Conclusions

We performed a kinematical analysis of the [CII] line emission in the BR 1202-0725 system at $z \sim 4.7$ from ALMA Science Verification observations. The QSO and the submillimetre galaxy are separated by ~24 kpc and are characterised by very high star-formation rates, larger than $\sim 1000\,M_\odot\,yr^{-1}$. Our

kinematical analysis reveals that these galaxies apparently have regularly rotating disks, that are seen almost face-on and that indicate dynamical masses of 6×10^{10} $M_\odot$, and 4×10^{10} $M_\odot$ for the SMG and QSO host galaxy, respectively. These disks are hotter than the disks of nearby galaxies, since the maximum rotational velocity is similar to the intrinsic velocity dispersion, but they are very similar to the disks of $z \sim 2 - 3$ Lyman-break galaxies. If the intrinsic velocity dispersion of the gas disks provides support against gravity, these masses could increase up to $\sim 9 \times 10^{10}$ $M_\odot$ and $\sim 5 \times 10^{10}$ $M_\odot$. Overall, the SMG and the QSO host galaxy are characterised by very similar physical properties in terms of SFRs, molecular gas mass, and dynamical mass.

The existence of these rotating disks suggest the the high star formation and black hole accretion rates are not induced by a major-merger event, at variance with the commonly accepted scenario for very massive galaxies and very high SFRs. We also detected faint components which, after a spectral deblending, were spatially resolved from the main QSO and SMG emissions. The relative velocities and positions of these components are consistent with orbital motions within the gravitational potentials generated by the QSO host galaxy and SMG, suggesting that they are smaller galaxies in interaction or gas clouds in accretion flows of tidal streams. Moreover, we did not find any clear spectral evidence for outflows caused by AGN or stellar feedback.

The rotating disks and the spectroscopically detected faint components suggest that the high SFRs might be induced by interactions or minor mergers with these companions which, however, do not affect the large-scale kinematics of the disks. Alternatively, the strong star formation may be fuelled by the accretion of pristine gas from the host halo. Both these processes could explain the relative high intrinsic velocity dispersion.

Finally, the ratio between the black hole mass of the QSO, obtained from new XShooter spectroscopy, and the dynamical mass of the host galaxy might be comparable with the similarly high value found in very massive local galaxies, suggesting that the evolution of black hole galaxy relations is probably better studied with dynamical than with stellar host galaxy masses.

New ALMA observations with higher sensitivity and spatial resolution are required to confirm the findings presented here.

Chapter 6

Ionised Outflows in z ~ 2.4 QSO Host Galaxies

Based on:
Carniani, S; et al. 2015: Ionised outflows in z ~ 2.4 quasar host galaxies; A&A, 580A.102C
Carniani, S; et al. 2015: Fast outflows quenching star formation in quasar host galaxies; submitted.

Feedback mechanisms from QSOs are considered to be crucial for galaxy evolution (see Section 1.4; King 2010, Fabian 2012 and King & Pounds 2015). During the bright active phase, AGN are believed to drive energetic outflows that expel gas at large scales from their host galaxies (e.g. Granato et al. 2004; Di Matteo et al. 2005; Menci et al. 2008; King 2010; Zubovas & King 2012; Fabian 2012; Faucher-Giguère & Quataert 2012; Zubovas & King 2014; Nayakshin 2014; Costa et al. 2014, 2015), hence removing the supply of cold gas required for star formation (SF) activity.

Quasar-driven outflows extending to kpc-scales have been resolved both locally (e.g. Feruglio et al. 2010; Rupke & Veilleux 2011; Cicone et al. 2012; Rupke & Veilleux 2013; Rodríguez Zaurín et al. 2013; Feruglio et al. 2013; Cicone et al. 2014; Rodríguez Zaurín et al. 2014; Aalto et al. 2015; Feruglio et al. 2015) and at high redshift (e.g. Alexander et al. 2010; Nesvadba et al. 2011; Harrison et al. 2012; Maiolino et al. 2012; Cano-Díaz et al. 2012; Harrison et al. 2014; Cresci et al. 2015; Cicone et al. 2015) in ionised, atomic, and molecular gas. Despite impressive advances in data quality and analysis in the past decade, the main properties of these energetic outflows remain largely unknown. The exact outflow morphologies and driving mechanisms are still poorly known: it is debated whether their morphology is conical or shell-like, and the physical process responsible for the coupling of the energy or momentum released by the central AGN with the galaxy interstellar medium is likewise unclear (e.g. inner winds and shocks, radiation pressure on dust). Recent observations of kpc-scale outflows in local AGNs support the momentum-driven model (Cicone et al. 2014; Feruglio et al. 2015; Tombesi et al. 2015). Moreover, it is unclear whether molecular and ionised outflows are accelerated by the same mechanism, if they have the same spatial distribution, or if they occur on similar timescales. So far, there are only a few observations of both molecular and ionised AGN-driven outflows in the same galaxy: SDSS J1356+1026 is an example of an obscured QSO where molecular and ionised outflows have different properties, i.e. outflow rates, velocities, radii, morphologies, and time scales (Greene et al. 2012; Sun et al. 2014).

The forbidden emission line doublet [OIII] at $\lambda = 5007, 4959$Å is a good tracer of ionised outflows on large scales since it cannot be produced at high densities and so cannot trace the sub-parsec scales of the BLR. In the presence of outflows, the spectral profile of the [OIII]λ5006 emission line can be highly asymmetric, with a broad, blue-shifted wing that is rarely observed in star-forming regions. For this reason, the [OIII]λ5006 emission line has been used to identify outflowing ionised gas in low-redshift and high-z AGNs. Recent integral field observations of the [OIII]λ5006 emission have

provided quantitative measurements of the outflowing gas properties in AGN at low redshifts $z < 0.5$ (e.g. Greene et al. 2011; Harrison et al. 2014). At higher redshift, $z \sim 2$, Alexander et al. (2010) found evidence for galactic-scale ionised outflows by mapping the [OIII]λ5006 emission line in ultra-luminous IR galaxies (ULIRGs) hosting type 1 AGNs. Cano-Díaz et al. (2012) observed an ionised outflow that extended up to ~8 kpc in a QSO at $z \sim 2.4$. Finally, Brusa et al. (2015) and Perna et al. (2015) detected broad [OIII]λ5006 blue wings in a sample of obscured AGN that revealed outflows extended over several kiloparsecs. In one case of the latter sample, the ionised outflow extended up to ~ 12 kpc and is anti-correlated with the presence of star formation in the host galaxy (Cresci et al. 2015, see Section 1.4.4;), similarly to what was found by Cano-Díaz et al. (2012). However given the low S/N of the star-formation powered Hα detected by Cano-Díaz et al. (2012) and by Cresci et al. (2015), we need to confirm these findings with higher S/N and in a larger sample of objects. Moreover, the Hα emission in the two host galaxies of these two QSOs indicates remarkable SFR of ~ 100 $M_\odot$/yr. Therefore, it still unclear whether these AGN-driven outflows are able to completely quench SF in the host galaxy, as required by models.

In this Chapter, we present a kinematical analysis of the [OIII]λ5006 emission line observed in six high-luminosity ($L_{bol} > 10^{47}$ erg/s) QSOs at $z \sim 2.4$. The line profiles and the velocity maps obtained by the kinematical analysis show ionised outflows extended on scales larger than $2 - 3$ kpc from the nucleus. This is one of the first observations of extended ionised outflows in QSO or type 1 AGN; most AGN-driven outflows have so far been observed in type 2 AGN. We present a new method for measuring outflow properties from datacube images when the source is only marginally spatially resolved. We show that the typical signature of outflows, that is, asymmetric line profiles and blue-shifted components in the velocity maps, can be described by two point sources (the central AGN source and the outflowing material) separated by a distance of a few kpc. We find that the ionised gas most likely traces only a fraction of the total outflowing gas, unless ionised outflows have a different origin than the molecular ones. In addition to [OIII]λ5006 observations, we discuss the Hα emission of two out of six QSOs belonging to the sample. The aim of this further analysis is to compare the outflow location to the star-formation region distribution in the host galaxies that are traced by Hα surface brightness. This comparison aims to test negative feedback paradigm.

The Chapter is organised as follows: in Section 6.1 we present the sample selection and in Section 6.2 we describe the SINFONI observations. Section 6.3 shows data analysis and spectral fitting. The results of our data analysis are presented in Section 6.4. Finally, in Section 6.5 we discuss the main results, that is, the nature of ionised outflows and the comparison with other observations.

A $H_0 = 67.3$ km s^{-1} Mpc^{-1}, $\Omega_M = 0.315$, $\Omega_\Lambda = 0.685$ cosmology is adopted throughout this work (Planck Collaboration et al. 2014).

6.1 Sample Selection

We selected six QSOs at z ~2.4 with large [OIII]λ5006 equivalent widths (> 10Å in the rest frame) and bright H-band magnitude (< 16.5 mag) from the samples of Shemmer et al. (2004), Netzer et al. (2004), and Marziani et al. (2009). The luminosities of the objects in our sample are in the range $L = 10^{47} - 10^{48}$ erg/s, making them the highest luminosity sources where outflows have been spatially mapped. These characteristics are chosen to maximise our chances of detecting signatures of feedback on the host galaxy. As explained in Chapter 1, the cosmic epoch corresponding to $z \simeq 2$ is crucial for the growth of the most massive galaxies and black holes, and shows the highest activity both in star formation and in BH accretion (e.g. Madau & Dickinson 2014). The selected objects at the high end of the QSO luminosity function are those where we expect to detect feedback in action, at least according to current galaxy evolutionary models (e.g. Hopkins et al. 2006). Moreover, the targets were selected depending on their particular [OIII] profile. The large [OIII]λ5006 equivalent width is expected to allow us to easily recover the kinematical maps of the ionised gas, a challenging task in luminous QSOs where narrow emission lines are usually weak (e.g. Netzer et al. 2004). Finally, the bright ionised line profile can be easily de-blended from the broad Hβ and FeII emission, which are

Table 6.1: Properties of our quasar sample

ID	Target Name	λ_0 [μm]	$\Delta\lambda_{rest}$ [Å]	Redshift	λL_{5100} [10^{46} erg/s]
LBQS0109	LBQS 0109+0213	1.68 ± 0.04	28.5 ± 0.2	2.35 ± 0.08	4.9 ± 0.8
2QZJ0028	2QZ J0028-2830[(a)]	1.70 ± 0.04	27.9 ± 0.2	2.40 ± 0.09	3.1 ± 0.6
HB8905	HB89 0504+030	1.75 ± 0.05	22.7 ± 0.2	2.48 ± 0.09	2.9 ± 0.6
HE0109	HE 0109-3518	1.706 ± 0.003	17.342 ± 0.011	2.407 ± 0.007	7.4 ± 1.5
HB8903	HB89 0329-385	1.720 ± 0.013	19.31 ± 0.06	2.44 ± 0.03	5 ± 2
HE0251	HE 0251-5550	1.68 ± 0.03	31.81 ± 0.17	2.35 ± 0.05	6.8 ± 1.4

(a): this is the same target of Cano-Díaz et al. (2012) which has been re-observed.

associated with the BLR. Based on near-IR spectra available from the literature (Shemmer et al. 2004; Netzer et al. 2004; Marziani et al. 2009), we also chose our objects such that the contamination from broad FeII emission is expected to be weak.

The basic properties of the observed objects are given in Table 6.1. One of our sources, 2QZJ0028, has previously been studied by Cano-Díaz et al. (2012) and was reobserved with a much longer integration time. Their results are confirmed.

6.2 Observations and Data Reduction

The targets, whose properties are described in Table 6.1, were observed in February and September 2012 using SINFONI (see details in Section 3.2) at the Very Large Telescope (VLT). The observations were obtained in H band ($\lambda \sim 1.45 - 1.85$ μm, where [OIII]λ5006, [OIII]4959 and Hβ are detected), in seeing-limited mode with a spatial scale of 0.250″ and medium spectral resolution of R = 3000. The total on-source integration time is over 3h per target. The airmasses are different for each target and span a range between ~ 1.0 and ~ 1.4.

Two out of six QSOs, LBQS0109 and HB8903, were observed K band ($\lambda \sim 1.95 - 2.45\mu$m, where H$\alpha$ is redshifted) with SINFONI as well. The K-band observations were executed in seeing-limited mode (angular resolution of ~0.6″) with 0.250″ spatial scale and with spectral resolution of R = 4000. The observations of each target were divided in six 1h long observations block for a total on-source integration time of four hours (plus overheads).

In all observations, the object was moved across the 8″×8″ field of view to perform the sky subtraction. A standard star for telluric correction and flux calibration was observed shortly after or before the on-source exposures.

After removing cosmic rays[1] from the raw data using the L.A. cosmic procedure (van Dokkum 2001), we used the ESO-SINFONI pipeline to reduce the data. The final data cubes produced by the ESO-SINFONI pipeline have a spatial scale of 0.125″×0.125″ and a field of view of about 8″×8″. The estimated angular resolution is ~ 0.4 – 0.6″, based on a 2D-Gaussian fitting of the flux map of the spatially unresolved broad Hβ line (see Sect. 6.3.3).

6.3 Data Analysis

Figure 6.1 shows the H-band spectra extracted from the nuclear region of each QSO from an aperture of 0.25″×0.25″. The spectra clearly show the broad Hβ and the strong emission-line doublet [OIII]$\lambda\lambda$5007, 4959. In addition to these components, weak FeII emission lines are also visible in two out of the six QSOs (LBQS0109 and HE0251). The asymmetric [OIII]λ5006 profiles suggest the presence of ionised outflows in most of the targets (LBQS0109, 2QZJ0028, HB8905, HB8903, and HE0251). A prominent blue wing is the typical signature of high-velocity gas moving toward the line

[1]The presence of cosmic ray hits in astronomical images is frequently considered as a disturbing effect

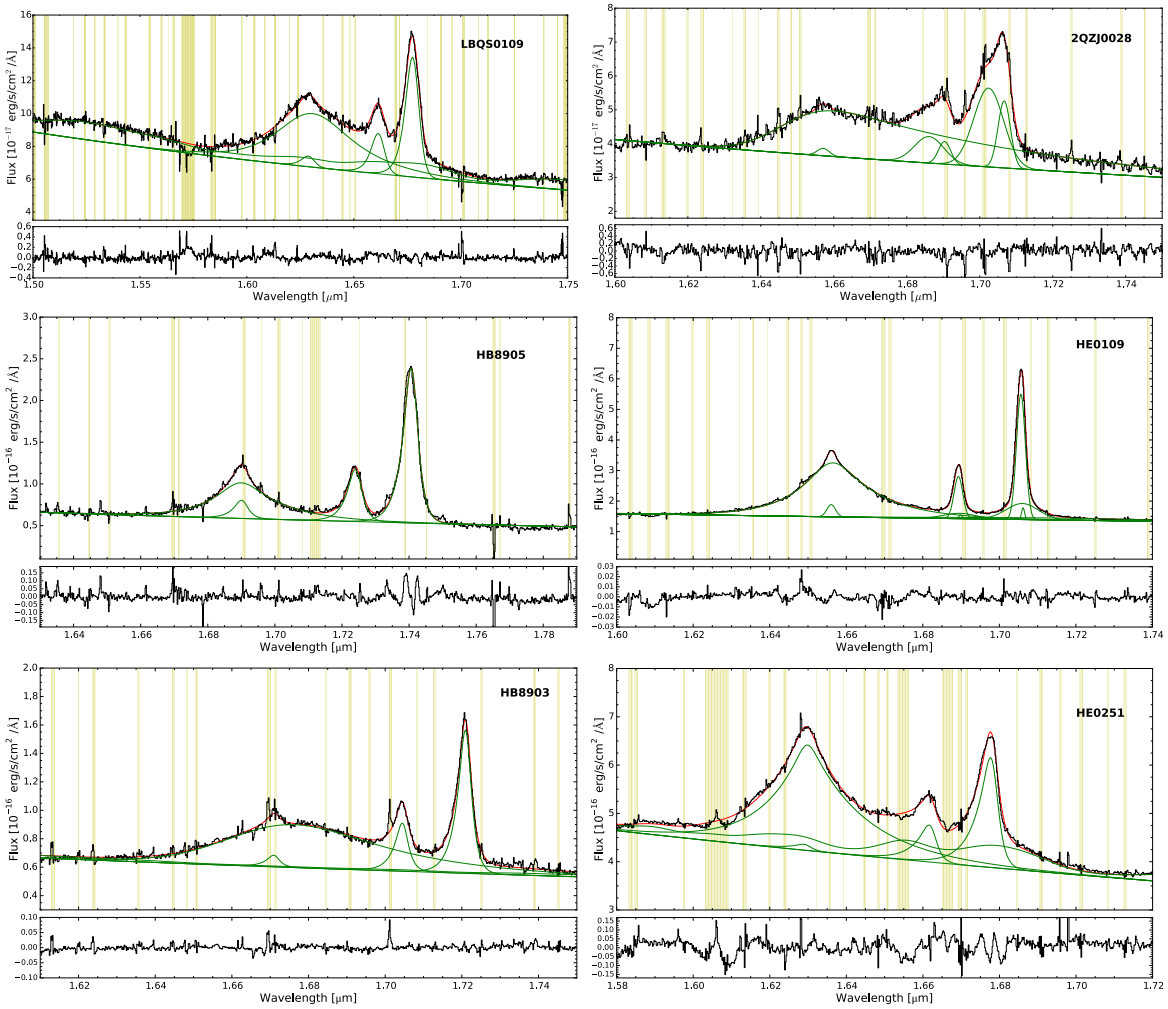

Figure 6.1: *Upper panel*: The spectra of the six QSOs if our sample. Each spectrum is extracted from a nuclear region of 0.25″×025″ (2 × 2 pixel). The different components in the fit for each line (Hβ,[OIII] and FeII) are shown in green, and the red line is the total fit. The shaded yellow regions indicate the zone affected by strong sky-line residuals that are excluded from the fit. *Lower panel*: Fit residuals, obtained as a difference between observed and model spectra.

of sight. The Hβ emission line shows asymmetric velocity profiles as well as, in some cases, two distinct emission peaks (i.e. HB8903). In all spectra the Hβ line is a sum of two different components: a very broad ($FWHM > 2000$ km/s) one that is associated to the BLR emission, and a fainter, narrower (FWHM~ 500-1200 km/s) component that is most likely associated with NLR emission.

6.3.1 Fitting Procedure

To understand the dynamics and the main properties of the ionised outflows, we performed a kinematical analysis of the forbidden lines.

First, we extracted the spectrum of each QSO from a nuclear region of 0.25″×0.25″ where the signal-to-noise ratio (S/N) is highest. We simultaneously fitted the continuum, Hβ and [OIII] emission lines by minimising χ^2 using the IDL routine MPFIT (Markwardt 2009).

The [OIII]λ5006 line profile is very complex in these objects, and a single Gaussian function is unable to reproduce the asymmetric velocity profiles, therefore we fitted the emission-line doublet using either multiple Gaussian components or a broken power-law convolved with a Gaussian distribution. Initially, we fitted the emission line using two Gaussian components, one broad (FWHM > 1000 km/s) and one narrow (FWHM < 1000 km/s), and, when necessary, added a third component to minimise the χ^2 value. Since in a few cases the [OIII]λ5006 emission line exhibits a very asymmetric line pro-

file with blue wings extended to $|v|$ >1000 km/s, we replaced the multi-Gaussian components with a broken power-law profile convolved with a Gaussian distribution. We did not add additional Gaussian components to avoid an unnecessary large number of free fitting parameters. We do not attribute any physical meaning to the individual fitting component, and we measured gas kinematics by analysing the total line profile. Therefore, using either multiple Gaussian components or a broken-power law does not change the results of this work, provided that the quality of the fit is similar. The two emission lines of the [OIII] doublet, originating from the same upper level, were fitted by imposing the same central velocity and velocity dispersion, with the intensity ratio $I(5007)/I(4959)$ fixed at ~3.

Hβ is well described by a broad (BLR) and a narrow component (NLR). We used a broken power-law profile for the very broad component (FWHM > 2000 km/s) since it usually provides a good fit to QSO broad emission lines (Nagao et al. 2006). The model used for the Hβ profile of 2QZJ0028 shows a broad red wing that is probably caused by continuum or FeII emission, so we do not attribute any physical meaning to this red-shifted emission. A similar profile is visible in Figure 1 of Cano-Díaz et al. (2012). Since the narrower Hβ is weak and sometimes only marginally detected, it is not possible to reliably constrain its profile and kinematics. We therefore assume that it has the same average velocity and velocity profile as [OIII]λ5006.

Finally, we used a power law for the continuum, and for the spectra showing FeII emission, we used the FeII template from Tsuzuki et al. (2006). These best-fitting solutions are used as first guesses in the pixel-to-pixel fitting of the kinematical analysis described in the following.

Before performing a spatially resolved kinematical analysis, we tested whether the kinematics of the ionised gas is spatially resolved. Following the method described in Section 5.4, we analysed the flux residual maps obtained with a pixel-by-pixel kinematical fitting with the components just described, after assuming that the targets are spatially unresolved. In this case, the H-band spectrum is expected to be the same in any spaxel apart for a different normalisation. The residual maps (Figure 6.2) at the wavelength range of [OIII]λ5006 indicate that the forbidden line emission is kinematically resolved in all but one of the quasars, that is, HE0251. In fact, if the emission were unresolved, we would expect to observe both a spectral profile and a residual map consistent with the noise, as in the case of HE0251. The flat residual at the wavelength range of Hβ indicates that the broad component of Hβ is spatially unresolved, consistently with an Hβ origin in the BLR.

After testing that the [OIII]λ5006 line emission is kinematically resolved in five of the six sampled QSOs, we performed a pixel-by-pixel fitting of the data cubes by allowing the spectral components to vary, except for the broad Hβ, which is not spatially resolved. Figure 6.3 shows the kinematical properties of the ionised gas as obtained from the fit of the [OIII]λ5006 line:

- zeroth-moment map (i.e., line flux map; first panel);
- first-moment map (i.e., median velocity map; second panel);
- blueshifted velocity map, v_{10}, the velocity at the tenth percentile of the overall emission-line profile (third panel); fitted in each spatial pixel;
- line width map , W_{80}, the velocity width of the line that contains 80% of the emission-line flux (fourth panel); this is defined as $W_{80} = v_{90} - v_{10}$, where v_{10} and v_{90} are the velocities at tenth and ninetieth percentiles, respectively. For a Gaussian profile, W_{80} is approximately the full width at half maximum (FWHM).

The observed kinematical maps are the results of the convolution of the intrinsic ones with the PSF of the observations. Where the [OIII]λ5006 emission line was fitted with multiple Gaussians, line profiles are based on the sum of all Gaussian components. The maps were obtained by selecting only those spatial pixels with a S/N equal to or higher than 2. We defined the S/N as the ratio between the peak of the [OIII]λ5006 line and the rms of the residuals. Zero velocities correspond to the peak position either of the narrow (FWHM < 1000 km/s) and strongest Gaussian component or of the broken power-law one of the [OIII]λ5006 profile estimated in the preliminary spectral fitting. The

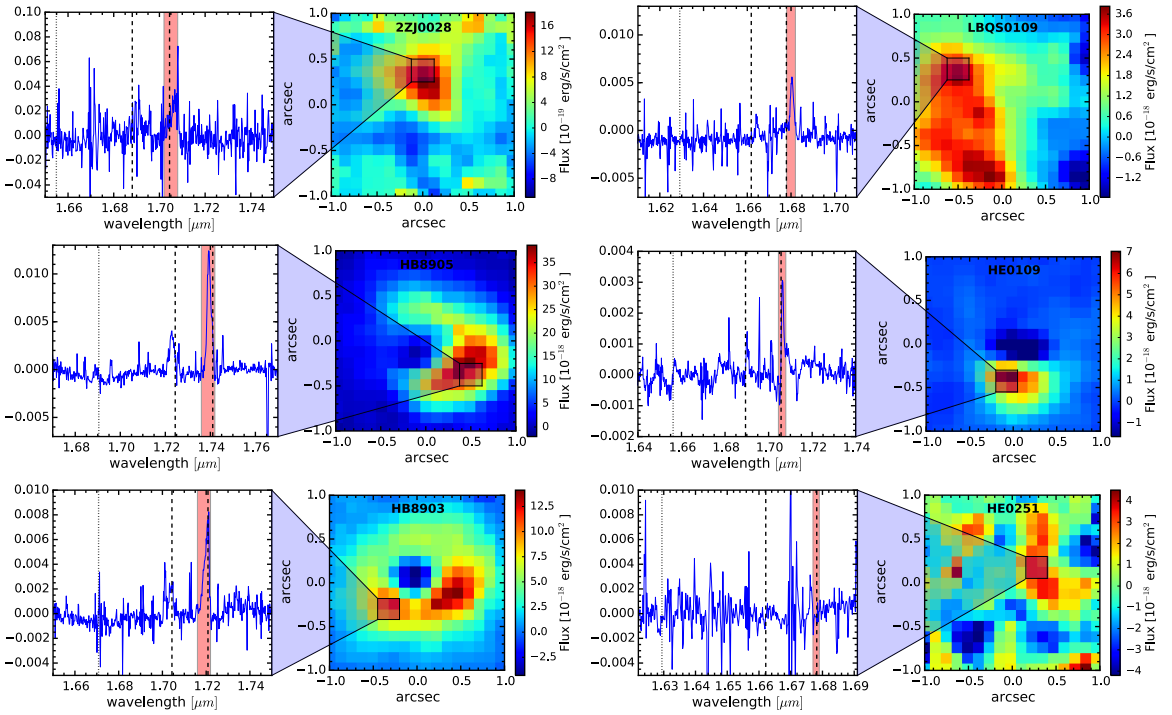

Figure 6.2: Residuals from the pixel-per-pixel fitting assuming that the QSO emission is not spatially resolved. Left panels: Residual spectra extracted from a region of 0.25″×0.25″, where the residual map, obtained by collapsing the [OIII]λ5006 spectral channel, probably shows a spatially resolved emission. Dashed lines indicate the wavelength of the doublet [OIII]λ5006, and the dotted line shows the Hβ position. The red shaded region denotes the wavelength range over which the residual [OIII]λ5006 emission has been integrated to produce the maps shown on the right. Right panels: Residual maps obtained by collapsing the spectral channels corresponding to the residual [OIII]λ5006 emission, as shown by the red region in the left panels. In the first five maps the clear [OIII]λ5006 residual emission suggests that the emitting region is spatially resolved. The "noise" residual map of HE0251 indicates that the sources are not resolved.

Table 6.2: Central wavelengths and line widths of the two narrow components of [OIII]$_{nar}$ and H$\alpha_{\rm nar}$.

	[OIII]$_{nar}$		H$\alpha_{\rm nar}$	
	λ_0 [μm]	FWHM [km/s]	λ_0 [μm]	FWHM [km/s]
LBQS0109	1.6802±0.0004	490±90	2.203±0.001	250±200
HB8903	1.7214±0.0002	480±70	2.2560±0.0006	500±150

zero-velocity wavelength was also used to refine the redshift of each QSO (Table 6.1) providing the velocity of the host galaxy. The inferred redshift and [OIII]λ5006 line width are consistent, within the errors, with those estimated by Shemmer et al. (2004) and Marziani et al. (2009).

The v_{10} maps (Figure 6.3, third panel) show strongly blue-shifted regions that are spatially associated with high-velocity dispersion (> 400 km/s, Figure 6.3, forth panels). The broad [OIII]λ5006 profile cannot be explained by a rotating gas component, which in local star-forming galaxies has typical FHWM values of about ~250 km/s. Moreover, the morpholgy of the velocity maps, suggesting the presence of a conical blue-shifted region, is completely different from the typical "spider" diagram of a disc. Consequently, both the [OIII]λ5006 profile and the velocity maps suggest that in at least five out of six QSOs we detect ionised outflowing gas with velocities > 300 km/s.

We only detect the blue-side outflows because the red side is probably obscured by dust in the host galaxy along the line of sight. For this reason, the [OIII]λ5006 line emission is asymmetric, with a prominent blue-shifted wing. While this is what commonly happens, in some cases the particular orientation of the line of sight with respect to the source can result in red-shifted outflows (e.g. Rodríguez Zaurín et al. 2013; Bae & Woo 2014; Perna et al. 2015).

The next step is to understand the physical mechanisms that expel the ionised gas out to a distance of a few kpc from the centre of the host galaxy.

6.3.2 The Narrow [OIII]λ5006 Components

In two out of six QSO, LBQS0109 and HB8903, we detect a weak, narrow (FWHM < 500 km/s) component of the [OIII]λ5006 emission that is only visible in some parts of the field of view. The narrow components are in the red side of the [OIII]λ5006 profile. In Figure 6.4 we compare, for both galaxies, the spectrum extracted from a region of 4″×4″ centred on the AGN position (red profiles) with the spectra extracted from external regions of the galaxy (blue profiles). The regions from which we extracted the spectra are shown in the left panels of Figure 6.4. The narrow [OIII]λ5006 component (hereafter [OIII]$_{nar}$), identified in the figure by a dashed green line, is clearly visible in the Eastern (E) side for LBQS0109 and in the Western (W) one for HB8903, showing that in these regions the [OIII]λ5006 profile is different from the one extracted from the nuclear region. Note that the blue-shifted emission shown in the lower-left boxes of HB8903 is due to outflow emission since the velocity dispersion in this region (FWHM ~ 800 km/s) is larger than that observed in the other external regions (FWHM ~ 500 km/s); Figure 6.3. In Section 6.3.1 we showed that a broken-power-law parametric profile represents a good fit to the main [OIII]λ5006 component. The data presented here suggest that a more complex line profile should be used in the external regions where [OIII]$_{nar}$ is visible. For this reason we re-analysed the H band spectra and we have performed a fit by adding an additional fixed [OIII]λ5006 component. Velocity and width of this narrow component are pre-determined from a Gaussian fit of the line profile (Figure 6.5) obtained by subtracting the spectrum extracted from a ring-shaped region (0.5″< r < 1″) from the nuclear spectrum (r < 0.5″), after scaling the two spectra to match the intensity of the broad Hβ and [OIII]λ5006 lines. The best-fit results are listed in Table 6.2 for both the targets.

The flux maps of the [OIII]$_{nar}$ components are shown in Fig. 6.6. The narrow emission is not symmetrically distributed around the QSO. This property was already evident from Figure 6.4: the peak emission of [OIII]$_{nar}$ for LBQS0109 is visible W of the AGN location (at 0,0 position that is

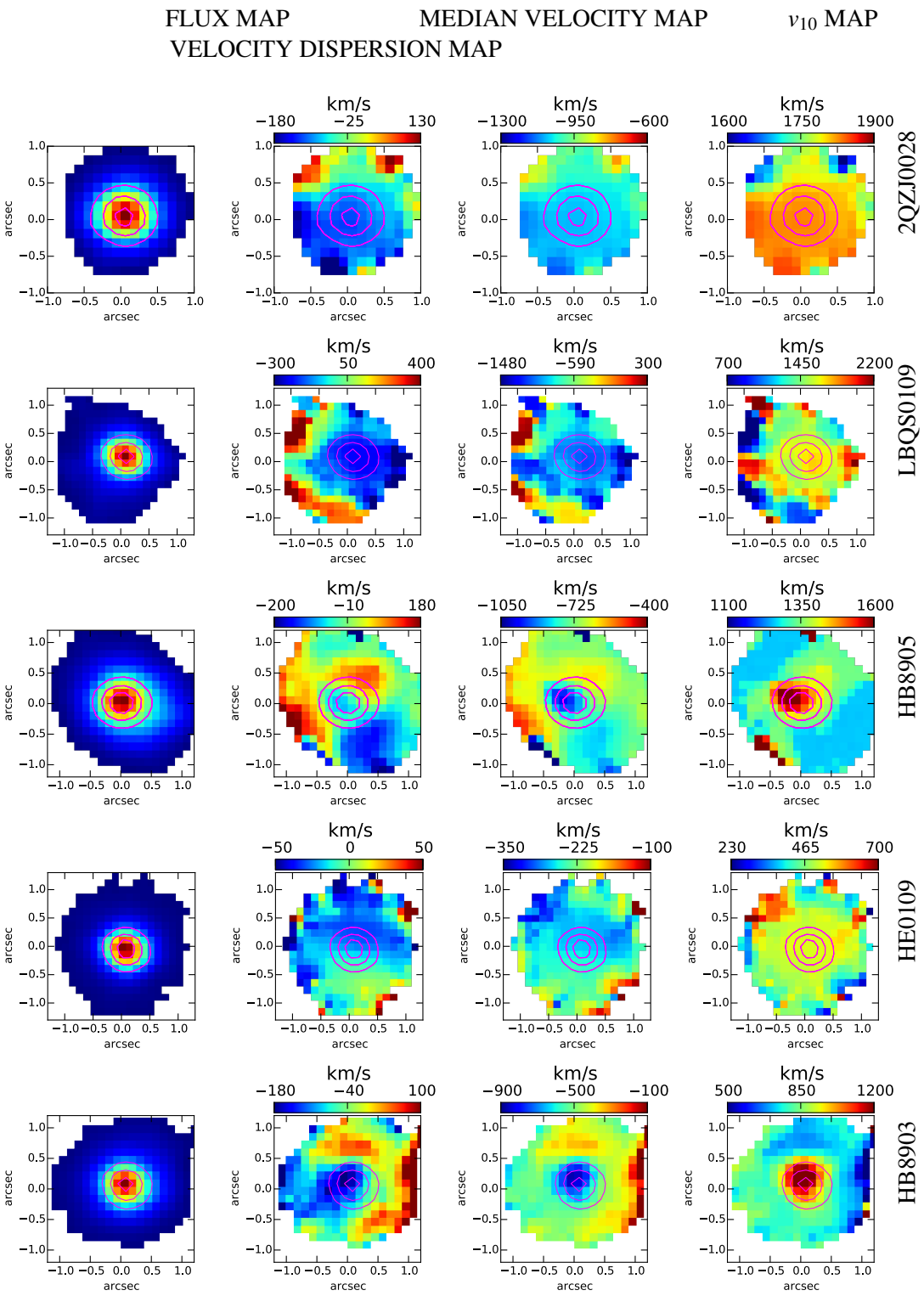

Figure 6.3: [OIII]λ5006 flux, median velocity, v_{10}, and velocity dispersion map. The maps are obtained by selecting pixels with a S/N>2. The velocity maps are characterised by blue-shifted regions with a high velocity dispersion. Contours represent the total Hβ line surface brightness at 90%, 50%, and 30% of the peak value.

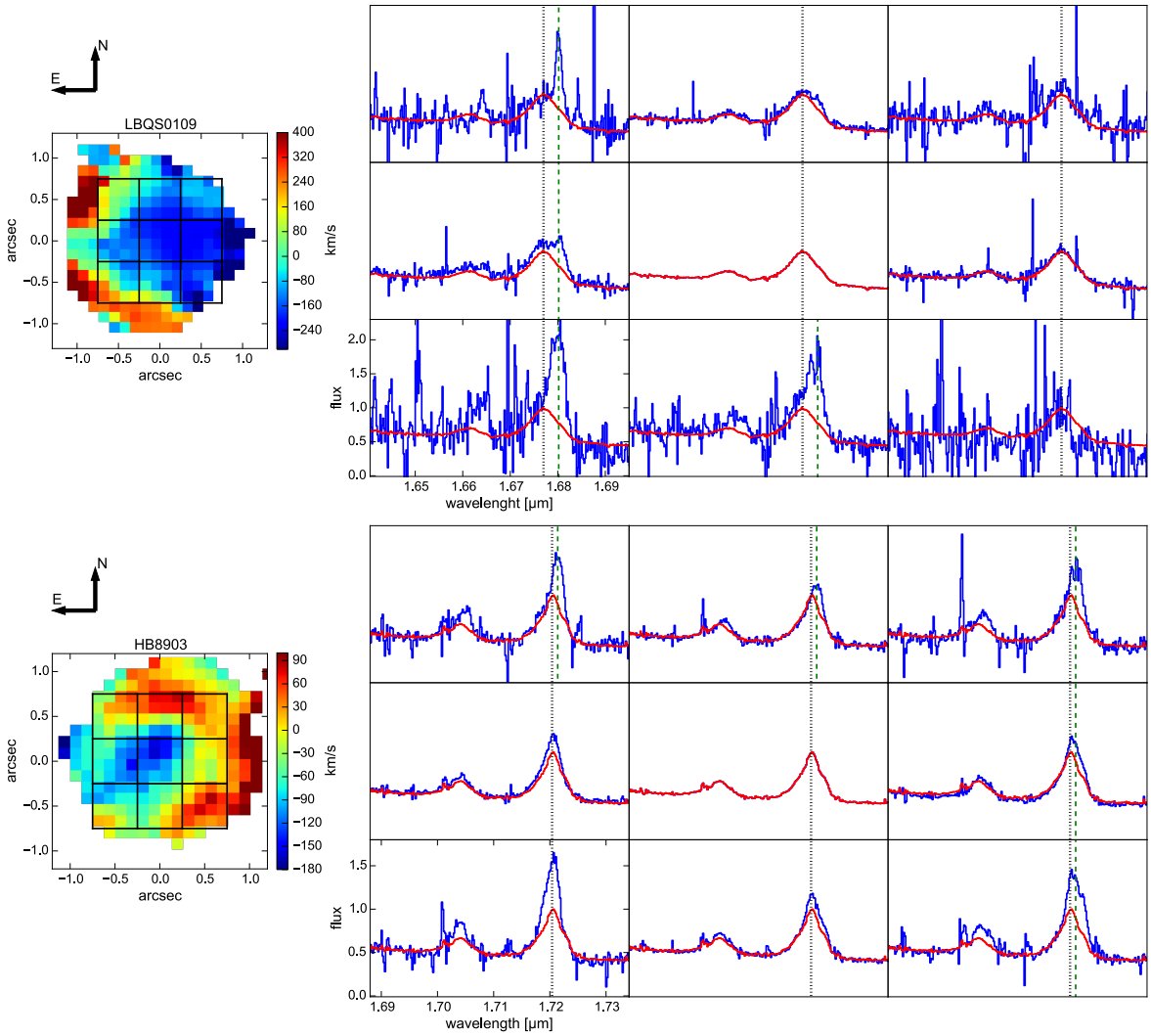

Figure 6.4: *Left panels*: the [OIII]λ5006 velocity maps of LBQS0109 (top) and HB8903 (bottom) presented in Figure 6.3. Black squares indicate the nine regions where we extracted the corresponding spectra shown in the right panels. *Right panels*: comparison between the nuclear [OIII]λ5006 profiles (red) and those from the external regions (blue) of LBQS0109 (top) and HB8903 (bottom). The regions from which the [OIII]λ5006 profiles were extracted are identified by the black squares drawn on the velocity maps (right panels). The black dotted line corresponds to the [OIII]λ5006 central wavelength. Narrow (FWHM∼490 km/s for LBQS0109 and FWHM∼480 km/s for HB8903) components of the [OIII]λ5006 emission, identified by the green dashed line, are clearly detected.

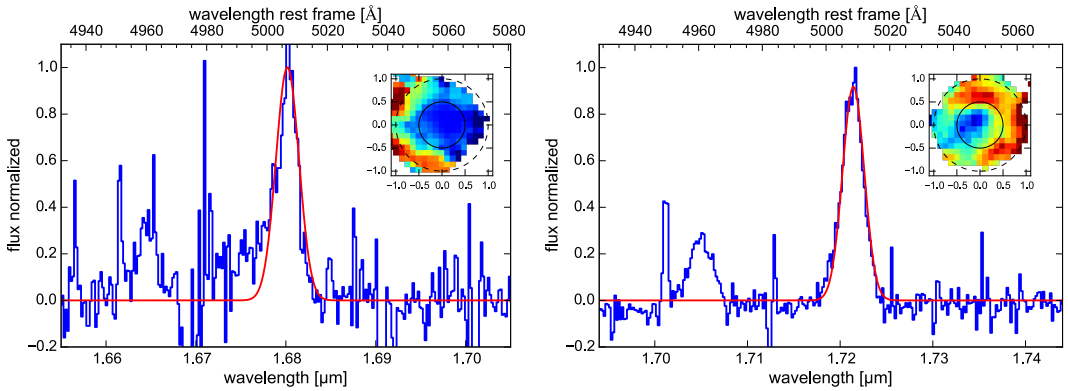

Figure 6.5: The H-band SINFONI spectra of LBQS0109 (top) and HB8903 (bottom). The observed spectra (blue lines) are the result of the subtraction between the spectra extracted from the ring-shaped regions ($0.5'' < r < 1''$) and from the nuclear regions ($r < 0.5''$). The narrow doublet [OIII]λ5006 is evident in both sources. The red curves denote the Gaussian fits whose parameters are shown in Table 6.2. In the smaller inset, the nuclear region (solid black line) and the shape-ring region (dashed black line) are drawn in the [OIII]λ5006 velocity maps.

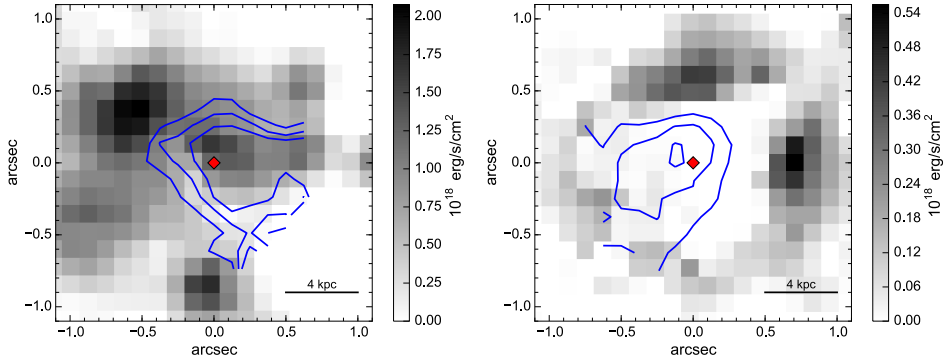

Figure 6.6: Flux maps of $[OIII]_{nar}$ component for LBQS0109 (top) and for HB8903 (bottom). The map is obtained integrating the single broad Gaussian Hα fit residuals on the spectral channels $1.679 < \lambda < 1.681$ μm for LBQS0109 and $1.721 < \lambda < 1.722$ μm for HB8903.The AGN position is identified with a red diamond symbol. The blue contours trace the [OIII]λ5006 velocity blue shifted shown in the left panels of Figure **??**. The contours represent the velocity -200, -180 and -150 km/s for LBQS0109 , and -150, -100 and -50 km/s for HB8903. The $[OIII]_{nar}$ emissions are not symmetrically distributed and are anti-correlated with the outflow region.

identified with a red diamond symbol) and that of HB8903 is N and E of the AGN. These narrow components are not detected in Hβ likely because the lower S/N of the data. Note that the kinematic of the broad [OIII]λ5006 of LBQS0109 and HB8903 shown in the left panels of Figure 6.4 and in Figure 6.3 remain unchanged even if we add the weak narrow $[OIII]_{nar}$ component.

The comparison of the $[OIII]_{nar}$ flux maps with the velocity maps of the broad [OIII]λ5006, whose negative velocity are shown in blue contour in Figure 6.6, ,reveals that the emission of the narrow components is not spatially correlated with the ionised outflows. The surface brightness of $[OIII]_{nar}$ seems to be attenuated in the S-W region of LBQS0109 and in the S-E region of HB8903: both regions are characterised by high blue-shifted velocity associated to the ionised outflow gas.

The $[OIII]_{nar}$ spatial extension well over 4 kpc excludes that this line is emitted by NLR, which is usually extended from hundreds to thousand pc. Both the line widths (FWHM~ 480 km/s) and the line strengths of $[OIII]_{nar}$ compared to the main broad [OIII]λ5006 component suggest that these narrow components could be associated to star forming regions in the turbulent galactic disks.

6.3.3 K-band Spectral Fitting and the Narrow Hα Component

Figure 6.7 shows the K-band spectra of LBQS0109 and HB8903, which are extracted from a nuclear region ($0.25'' \times 0.25''$). By comparing the Hα profile with the [OIII]λ5006 and Hβ profiles analysed

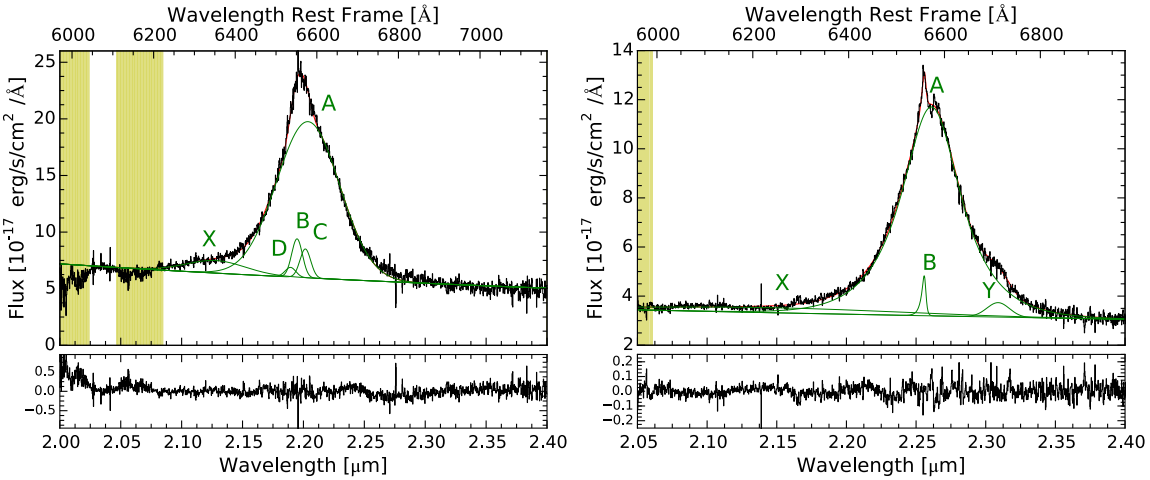

Figure 6.7: The K-band SINFONI spectra of LBQS0109 (left panel) and HB8903 (right panel) in the spectral region of Hα integrated in a region of 0.25″×0.25″ (2 × 2 pixel) around the QSO. *Upper panels*: the observed spectra are shown in black line. The different components in the fit for each line (Hα [NII] and continuum) are shown in green and the red line is the total fit. The shaded yellow regions indicate the zone affected by strong sky line residuals which are excluded from the fit. *Bottom panels*: fit residuals, obtained as a difference between observed and model spectra.

in Section 6.3.1, we expect a broad (FWHM > 4000 km/s) component originating from the BLR and a narrower component (500 km/s < FWHM < 2000 km/s) emitted from the NLR and tracing the [OIII]λ5006 outflow.

In order to set up the spaxel-by-spaxel fit for both targets, we initially consider the spectrum extracted from the nuclear aperture. Continuum emission is fitted with a single power law while the Hα line is fitted with broken power-law profiles for the BLR component and for the narrower (500 km/s < FWHM < 2000 km/s) NLR component associated with the outflow. The [NII] doublet associated with component B is fitted with two Gaussian components (labelled as C and D in Figure 6.7) and their velocities and widths are fixed to those of component B. Since the two [NII] emission lines ($\lambda\lambda$6584, 6548 Å) originate from the same upper level, their intensity ratio was fixed at the value of 3, given by the ratio of the Einstein coefficients. The fitting procedure does not require the addition of the [NII] components to reproduce the Hα profile of HB8903. In addition to the previously mentioned components (A, B, C, D for LBQS0109 and A, B for HB8903), we added one additional Gaussian component for LBQS0109 (component X in the left panel of Figure 6.7) and two additional Gaussian components for HB8903 (X and Y in the right panel of Figure 6.7) . The Y component may be associated either to the broad HeI line at λ = 6679.99Å or the doublet [SII]$\lambda\lambda$6717, 6731Å. The wavelength of X component in both sources can not be associated to any known emission lines, but it was added to reduce the χ^2 of our fit. The fit residuals shown in Figure 6.7 indicate that the adopted components well describe the nuclear spectrum of each target.

We performed the spectral fitting on evert individual spaxel keeping the broad components A fixed except for their normalisation (flux). Figure 6.8 shows the residual spectra correspond to a ring-shaped region (0.5″< r< 0.8″) of the galaxy. These residual spectra reveal a weak but significant, narrow (FWHM ~ 250 km/s for LBQS0109 and FWHM~500 km/s for HB8903; see Tab. 6.2) component of Hα. The redshift of this narrow component (hereafter H$\alpha_{\rm nar}$) is consistent, within the error, with the redshift of the narrow [OIII]$_{nar}$ detected in the H-band spectra (Section 6.3.2): the red arrow in Figure 6.8 denotes the expected position of H$\alpha_{\rm nar}$ based on the observed position of [OIII]λ5006. The red dashed lines denote the expected position of the [NII] component associated to H$\alpha_{\rm nar}$. The [NII] lines are clearly not detected in any objects resulting in an upper limit of $\log_{10}$([NII]/Hα) < -0.85 for LBQS0109 and of $\log_{10}$([NII]/Hα) < -1.32 for HB8903. By studying the line ratios using the "Baldwin, Phillips & Terlevich" (BPT) method (Baldwin et al. 1981) we find that the narrow emission is consistent with gas excited by star formation excited region (Kauffmann et al. 2003b). Moreover,

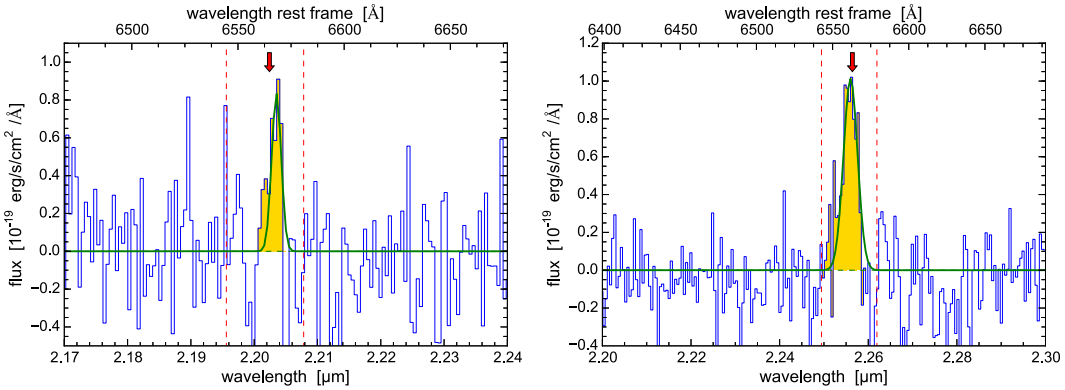

Figure 6.8: Narrow Hα emission from the residual K-band fitting, extracted from a ring-shaped region ($0.5'' < r < 0.8''$) of LBQS0109 (top) and HB8903 (bottom). The red arrows indicate the expected position at the redshift of the [OIII]$_{nar}$ component. The dashed red line mark the expected positions for doublet [NII]: the lines are not detected, confirming that star formation is the excitation mechanism for the narrow Hαline (See text).

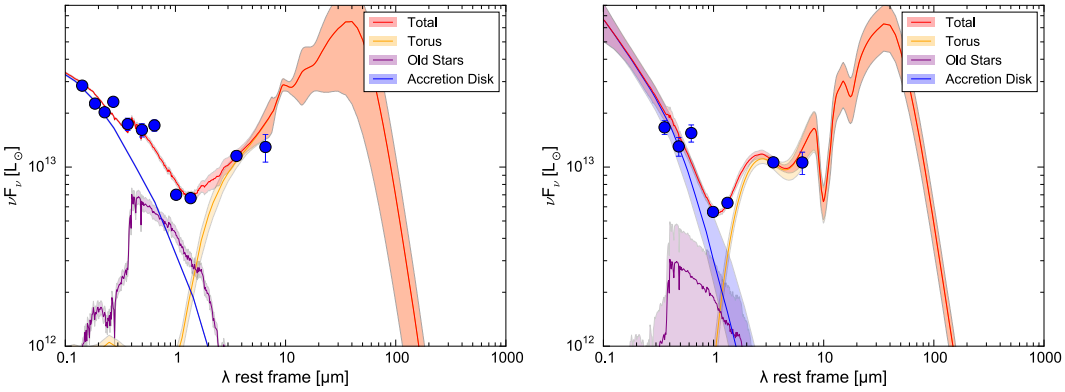

Figure 6.9: SED fitting of LBQS0109 on the left and of HB8903 on the right panel. The blue points are the QSO emission fluxes from SDSS, 2MASS, and WISE photometry. The total best fit models are plotted in red while accretion disk, old star and torus components are plotted in blue, purple and orange, respectively. The filled areas denote the uncertainties estimated with a Montecarlo procedure, see Balmaverde et al. (2015) for more details.

the FWHM$\lesssim$ 500 km/s of the H$\alpha_{\rm nar}$ component is consistent with the typical line widths observed in star-forming galaxies at z~2.5 (Förster Schreiber et al. 2009).

6.3.4 SED Fitting

Figure 6.9 shows the rest-frame Spectral Energy Distribution (SED) of the two QSOs obtained by combining SDSS (when available), 2MASS and WISE photometry. We have not included photometric points at rest-frame wavelength < 1215.67 Å since such emission is affected by intergalactic medium absorption. We take in advantage of Two Micron All Sky Survey (2MASS) data in the the J (1.24 μm), H (1.66 μm) and K (2.16 μm) bands. The photometric points are extracted from All Sky Point Source Catalogue. In the range between 3.4 μm and 22 μm, we use the data observed with the infrared telescope Wide-field Infrared Survey Explorer (WISE) in the W1 (3.4 μm), W2 (4.6 μm), W3 (12 μm) and W4 (22 μm) bands. The continuum fluxes for both targets in all four bands can be found in the WISE All-Sky Source Catalogue. For LBQS0109, we extract the continuum flux from four out of five SDSS colour bands (g, r, i and z), selecting the parameter *psfMag* that measured the total flux of the object by fitting a PSF model in the position of the target.

The SED fitting decomposition, shown as red solid line in Figure 6.9, is performed by using the SED fitting code by Balmaverde et al. (2015), who assume that the best fit is the combination of different components: accretion disk emission, unabsorbed (old) stellar population, emission of dust heated by the AGN (black body at ~ 1500 K and torus template) and by a starburst emission (starburst

template). See Balmaverde et al. (2015) for a detailed description of the adopted templates and fitting procedure. The lack of photometric points in the rest frame 8-1000 μm do not allow us to constrain the starburst component, which, indeed is not required to reproduce the observed SEDs.

The colour-filled areas indicate the uncertainties on the best fit which are estimated through a Montecarlo procedure. Clearly, the lack of photometric points beyond 10 μm rest-frame does not allow to well constrain the emission from the AGN torus in both sources. The luminosity at short wavelength around 2 μm is correlated with the emission of a unobscured population of old stars in the host galaxy (Meidt et al. 2012). From the SED fitting, we derive a stellar mass (hereafter $M_\star$) of 1.5×10^{12} $M_\odot$ for LBQS0109 and of 0.6×10^{12} $M_\odot$ for HB8903, the latter with a large uncertainty. However, since, the old star components contribute less than 25% to the total luminosity in the range between 1 μm and 3 μm, so the inferred $M_\star$ are considered as upper limits.

6.4 Outflow Properties

In the following, we estimate the mass, average velocity, and radius of the high-velocity winds. We then infer the mass outflow rate, momentum rate, and kinetic power and compare them with previous works (Greene et al. 2012; Cicone et al. 2014; Harrison et al. 2014; Sun et al. 2014; Brusa et al. 2015; Cresci et al. 2015; Feruglio et al. 2015).

6.4.1 Outflow and Radius

Given the uncertainties on the driving mechanism, we used a simple model to estimate the physical properties of the outflow. In this model, the outflow is represented by a shell-like cloud ejected from the nucleus within a cone and with a filling factor equal to 100%. We assumed that the physical size of the outflowing material is smaller than the spatial resolution typical of our datasets. This model is defined by the mass of the cloud, M_o, the distance between the cloud and the location of the AGN, R_o, and the averaged cloud velocity, v_o. The outflow mass rate is given by

$$\dot{M}_o = \frac{M_o}{\tau_{dyn}} = \frac{M_o v_o}{R_o}, \tag{6.1}$$

where τ_{dyn} is the dynamical time, that is, the time taken by the ionised gas to reach a distance R_o with an average velocity v_o. We note that assuming either a shell or a uniformly filled cone with a filling factor equal to 1 (e.g. Maiolino et al. 2012) changes the $\dot{M}_o$ estimate by a factor of 3. Since this factor is constant, it does not affect the main conclusions of this work, but we take it into account when comparing our results with previous ones.

The extension of an outflow (R_o) is usually trivially estimated from the observed flux or velocity maps (e.g. Harrison et al. 2014; Cresci et al. 2015). However, in our cases, the [OIII]λ5006 emission is only marginally spatially resolved in each QSO, therefore the kinematical maps in Figure 6.3 are affected by PSF smearing, and the sizes of the regions showing blue-shifted emission (Figure 6.3) do not directly provide the parameter R_o to be used in Eq. 6.1. Furthermore, the sizes of the outflowing regions are affected by the choice of S/N threshold adopted in plotting the maps. In particular, assuming a S/N threshold larger than 2, the blue regions would be smaller than those shown in Fig. 6.3. For these reasons, we cannot estimate R_o from our observations by using the flux or velocity maps as in previous works, where emission lines are clearly spatially resolved. Therefore, we decided to estimate R_o by using spectroastrometry,

which allows position measurements on scales smaller than the spatial resolution of the observations. Spectroastrometry consists of measuring the photo-centroid in each velocity channel. If outflowing ionised gas is moving away at a distance R from the QSO, we expect that the centroid of light emission extracted from blue-shifted velocities channels of [OIII]λ5006 will be displaced by the same amount R with respect to the QSO position, identified by the BLR and/or continuum emission. By means of a simple simulation, we show in Sect. 5.3 that spectroastrometry can, indeed, provide

Table 6.3: Outflow properties

QSO	v_o [km/s]	R_o [kpc]	Log($L_{[OIII]}$)	Log($L_{H\beta}$	$M_{[OIII]}$ [10^7 $M_\odot$]	$M_{H\beta}$ [10^7 $M_\odot$]	$\dot{M}_{[OIII]}$ [$M_\odot$/yr]	$\dot{M}_{H\beta}$ [$M_\odot$/yr]
LBQS0109	1850	0.4	43.17	42.10	1.2	2.2	60	110
2QZJ0028	2300	0.7	43.68	43.07	3.8	20	140	700
HB8905	500	1.3	43.95	42.99	7.1	16.8	30	75
HE0109	900	0.4	43.75	42.71	4.5	8.6	110	210
HB8903	1450	1.9	42.95	41.8	0.7	1.2	6	10
HE0251	-	-	43.82	42.55	5.3	6.1	-	-

Notes: The outflow masses are estimated assuming a $T_e \sim 10^4$ K and a $n_e \sim 500 cm^{-3}$.

information on the outflow position at scales that are significantly smaller than the limit imposed by the spatial resolution of the observations.

We applied the spectroastrometry technique to the [OIII]λ5006 line emission after subtracting the best-fit model of the continuum, broad Hβ and FeII emission. To maximise the signal-to-noise ratio for our measurements and minimise the uncertainty due the spectral resolution, we rebinned the spectra by three velocity channels (~ 105 km/s). The centroid of the [OIII]λ5006 emission in each rebinned velocity channels was, then, estimated by a 2D Gaussian fitting. The QSO position was estimated by applying the same spectroastrometry technique to the the continuum and the broad Hβ emission.

The results of the spectroastrometric analysis are displayed in Figure 6.10. In the left panels, we plot the distance R of the emission line photocentre from the continuum one as a function of velocity v. The right panels show the photocentre position on the sky in each velocity channel. The reliable spectroastrometric measurements for the [OIII]λ5006 emission line were selected to satisfy the following criteria:

- signal-to-noise ratio higher than 1.5 for the line flux in each spectral channel of the rebinned spectra extracted from a $0.25'' \times 0.25''$
- FWHM of the 2D Gaussian equal or larger than that of the PSF of the observations.

In all targets, the [OIII]λ5006 blue-wing centroids are displaced at least 0.05″, that is, 0.4 kpc, from the continuum position and, in some cases, we observe an offset in the red wavelengths as well. This latter offset may be caused by three reasons: (i) the continuum is not well subtracted during the kinematic analysis; (ii) the [OIII]λ5006 emission line associated to outflows is so large that the displacement is also slightly observable in the red wings; (iii) the red wings are emitted by the receding outflows that are not completely obscured by dust in the disc; (iv) the presence of a narrow [OIII]λ5006 component (see Section 6.3.2), which may be associated to star-forming region, causing a displacement from the continuum centre.

Since the position of the photocentre at high blue velocities reveals an extended ionised outflow, we adopted R_o equal to the largest distance measured for the approaching gas, and $v_o = v(R_0)$ as measured from our maps (see arrows in Fig. 6.10). Since the spectra were rebinned by three velocity channels, the error on v_0 due to the spectral resolution typical of our datasets is negligible. R_o and v_o for each quasar are listed in Table 2.

6.4.2 Outflow Mass

A great challenge in estimating the mass of the wind is caused by its multiphase nature. Only a fraction of the mass of the outflows is in the warm ionised phase traced by [OIII]λ5006. Recent works estimated the mass of ionised outflows either using Hβ emission line (e.g. Liu et al. 2013; Harrison et al. 2014) or using the [OIII]λ5006 line (e.g. Cano-Díaz et al. 2012). So far, it is unclear which is the best tracer of ionised gas powered by AGN feedback. To compare two different measurements carried

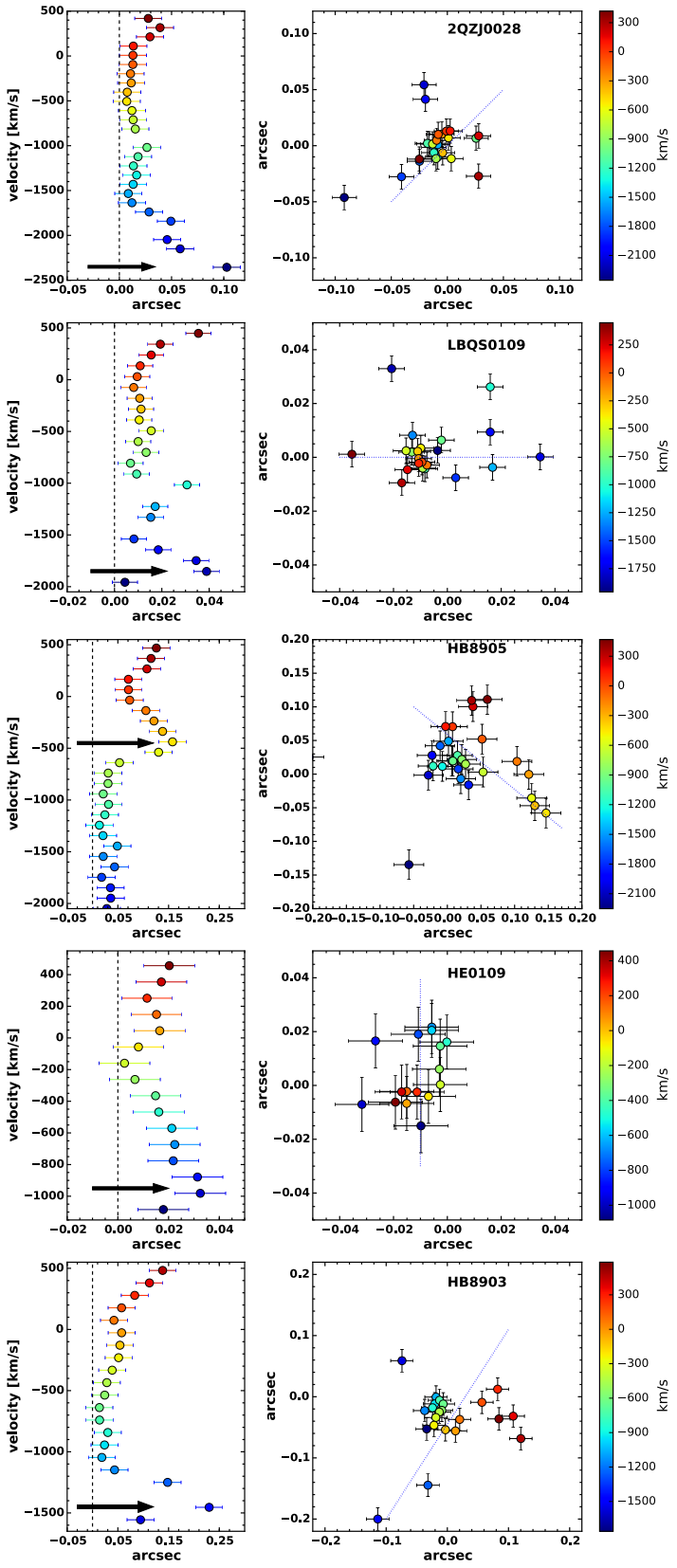

Figure 6.10: Left panels: The points show the [OIII]λ5006 velocity v versus the distance R of the [OIII]λ5006 photocentre from the continuum (indicated by the dashed line). The arrows indicate the velocity $v_o = v(R_o)$ corresponding to the distance R_0. Right panels: The [OIII]λ5006 photocentre position in the field of view. Symbols are coloured according to their velocity (the velocity scale is reported in the colour bar). The dotted line indicates the project direction of the outflow as inferred by comparing the spectroastrometry results with velocity maps (Figure 6.3).

out with these two different tracers, we discuss how the mass of ionised outflows can be constrained through the observations of [OIII]λ5006 and Hβ.

The [OIII]λ5006 luminosity is given by

$$L_{[\mathrm{OIII}]} = \int_V f n_e n(O^{2+}) j_{[\mathrm{OIII}]}(n_e, T_e) dV, \tag{6.2}$$

where f is the filling factor, n_e the electron density, $n(O^{2+})$ the density of O^{2+} ions, and $j_{[OIII]}(n_e, T_e)$ the line emissivity. $n(O^{2+})$ can be written as

$$n(O^{2+}) = \left[\frac{n(O^{2+})}{n(O)}\right]\left[\frac{n(O)}{n(H)}\right]\left[\frac{n(H)}{n_e}\right] n_e$$

and, with a reasonable assumption, $n(O^{2+}) = n(O)$,

$$n(O^{2+}) \simeq (6.04 \times 10^{-4} 10^{[O/H]-[O/H]_\odot}) \times (1.2)^{-1} \times n_e,$$

where $[O/H] - [O/H]_\odot$ is the metallicity relative to solar with a solar oxygen abundance of $[O/H]_\odot \sim 8.86$ (Centeno & Socas-Navarro 2008). The factor $(1.2)^{-1}$ takes into account a 10% number density of He atoms with respect to H atoms:

$$n_e \approx n(H) + 2n(H_e) = n(H) + 2 \times 0.1 \times n(H) = 1.2n(H).$$

Assuming a typical temperature ($T_e \simeq 10^4 K$) and electron density ($n_e \simeq 500$ cm^{-3}) for the NLR, the line emissivity is

$$j_{[\mathrm{OIII}]} = 3.4 \times 10^{-21} \text{ erg s}^{-1}\text{cm}^{-3}.$$

This line emissivity was estimated making use of PyNeb (Luridiana et al. 2015). Based on this, Eq. (6.2) can be rewritten as

$$L_{[\mathrm{OIII}]} = 6.0 \times 10^{-4} f 10^{[O/H]-[O/H]_\odot} j_{[\mathrm{OIII}]} < n_e^2 > V, \tag{6.3}$$

where $< n_e^2 >$ is the volume-averaged squared density. The gas mass can be expressed as

$$M \simeq \int_V f \overline{m} n(H) dV \simeq f m_p < n_e > V, \tag{6.4}$$

where $\overline{m}$ is the average molecular weight, m_p is the proton mass, and we have taken into count that a 10% number density of He atoms with respect to H atoms:

$$\overline{m} n(H) \approx \frac{m_p n(H) + 4 m_p n(He)}{n(H) + n(He)} \frac{n(H)}{n_e} n_e$$

$$\approx \frac{n(H) + 0.4n(H)}{n(H) + 0.1n(H)} m_p (1.2)^{-1} n_e \approx 1.2 m_p (1.2)^{-1} n_e = m_p n_e.$$

Finally, from combining Eqs. (6.3) and (6.4), we obtain

$$M_{[\mathrm{OIII}]} = 1.7 \times 10^3 \frac{m_p C L_{[OIII]}}{10^{[O/H]-[O/H]_\odot} j_{[OIII]} < n_e >}, \tag{6.5}$$

where $C = < n_e >^2 / < n_e^2 >$. For $T_e = 10^4$ K and $n_e = 500$ cm^{-3} we obtain a mass of

$$M_{[\mathrm{OIII}]} = 0.8 \times 10^8 \mathrm{M}_\odot \left(\frac{C}{10^{[O/H]-[O/H]_\odot}}\right)\left(\frac{L_{[OIII]}}{10^{44} erg/s}\right)\left(\frac{< n_e >}{500 cm^{-3}}\right)^{-1}.$$

We note that the gas mass is sensitive to temperature and density of the clouds.

Now we similarly derive M from Hβ. The Hβ luminosity can be expressed as

$$L_{H\beta} = \int_V f n_e n_p j_{H\beta}(n_e, T_e) dV \simeq 1.2^{-1} f j_{H\beta}(n_e, T_e) < n_e^2 > V, \tag{6.6}$$

where $j_{H\beta}$ is line emissivity and n_p is the proton density that can be written as

$$n_p = \left[\frac{n(H)}{n_e}\right] n_e = (1.2)^{-1} n_e.$$

At the typical temperature and density of the NLR, the line emissivity of Hβ also estimated with PyNeb is

$$j_{H\beta} = 1.2 \times 10^{-25} \text{ erg s}^{-1}\text{cm}^{-3}.$$

By combining Eqs. (6.4) with (6.6) of $L_{H\beta}$, we derive

$$M_{H\beta} \simeq 0.8 \frac{m_p C L_{H\beta}}{j_{H\beta} < n_e >}. \tag{6.7}$$

For $T_e \sim 10^4$ K and $n_e \sim 500$ cm^{-3} we obtain a mass of

$$M_{H\beta} = 1.7 \times 10^9 \text{M}_\odot \, C \left(\frac{L_{H\beta}}{10^{44} erg/s}\right) \left(\frac{< n_e >}{500 cm^{-3}}\right)^{-1}.$$

From comparing the two masses at the same temperature and density, we derive

$$\frac{M_{[OIII]}}{M_{H\beta}} \simeq 0.05 \frac{L_{[OIII]}}{L_{H\beta}}, \tag{6.8}$$

with [O/H] = [O/H]$_\odot$, T$_e$ ~ 10^4 K and n$_e$ ~ 500 cm^{-3}, the same values as assumed in the following analysis. The [OIII]λ5006/Hβ ratio measured in Seyfert galaxies typically is ~ 10, providing $M_{[OIII]}/M_{H\beta} \sim 0.5$. This apparent discrepancy is the consequence of the different volumes from which [OIII]λ5006 and Hβ are emitted: in the above example the volume of Hβ emitting gas is ~ 2 higher than that of [OIII]λ5006. Therefore, Hβ emission traces a higher ionised gas mass than [OIII]λ5006. The mass estimated from [OIII]λ5006 is therefore considered as a lower limit on the ionised gas mass.

6.4.3 Simulations of Spectroastrometric Observations of Outflows

In Section 6.4.1 we have described our method for estimating R_o, which is not affected by the spatial resolution of the data and by the S/N threshold used to map velocities.

In the following, we present results of simple simulations of outflowing gas that validate the spectroastrometric method. We note that the purpose of this work is not to build an outflow model to fit our observations, but the only purpose of this simulation is to show that the extension of the flux or velocity maps when the source is marginally resolved can provide incorrect estimates of the outflow extension due to PSF smearing. We also show that an ionised clump with a given velocity that is located a few kpc away from the AGN can appear as a blue-shifted region extended over ~ 5-10 kpc in velocity maps, which is larger than the real outflow extension.

We considered a simple model of an outflow (Figure 6.11) based on the following assumptions.

1. The outflow has a biconical geometry with the axis approximately more or less perpendicular to the host galaxy disk; indeed, the AGN wind, although roughly isotropic, cannot propagate through the galaxy disk because of its high density.

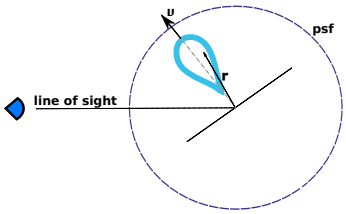

Figure 6.11: Cartoon showing the basic structure of our model. The outflow (solid blue curve) is perpendicular to the galaxy plane. $\vec{v}$ indicates the direction of the outflow and $\vec{r}$ is the distance from the QSO. This model assumes that the outflow is marginally resolved but it is not larger than the PSF dimension (dashed purple line).

2. The receding half-cone is not observed because its emission is absorbed by the dust in the host galaxy. This geometry best explains the asymmetric [OIII]λ5006 profile with a prominent blue wing over 1000 km/s.

3. The surface brightness distribution of the outflow is parameterised by

$$I(\vec{r}) = I_0 e^{-\tilde{r}/R_o^{model}},$$

where the vector $\vec{r}$ is the distance from the QSO. We note that the surface brightness distribution and the opening angle of the cone are not fundamental for these simulations, since the spatial resolution of our data is not high enough to resolve the surface brightness profile. We assume an opening angle of 30 degrees. R_o^{model} identifies the photocentre of the surface brightness of the ionised cloud. I_0 is proportional to the outflow mass M_o^{model} defined in Eq. (4).

4. The ionised gas in the outflow has an average velocity v_o^{model} and a velocity dispersion σ_o^{model}.

Therefore the input parameters are the outflow mass M_o^{model}, the distance R_o^{model} of the ionised clouds from the centre of the QSO, the average velocity v_o^{model} , and the velocity dispersion σ_o^{model} of the ionised gas.

To reproduce the [OIII]λ5006 line profile of LBQS0109, we simulated a QSO with an outflow characterised by $M_o^{model} = 1.0 \times 10^7$ $M_\odot$ (Eq. 5), $R_o^{model} = 0.05$ arcsec (i.e. ~0.4 kpc), $v_o^{model} = 1500$ km/s and $\sigma_o^{model} = 500$ km/s. We also considered a point source at the location of the AGN describing the gas at the systemic velocity with a velocity dispersion ~ 400 km/s and an amplitude scaled so as to reproduce the observed line profile. The total [OIII]λ5006 emission was then projected onto the sky plane, assuming a galaxy disc inclination of 10 degrees, that is, almost face-on, as is typical of QSOs. Finally, we convolved the surface brightness maps in each spectral channel with the PSF and added Gaussian noise to match the sensitivity of our observations.

The comparison between the [OIII]λ5006 line profile extracted from the simulated data and that from the observations is shown in Figure 6.12. Both spectra were extracted from a nuclear region of $0.25'' \times 0.25''$. The simulated emission line presents prominent blue wings similarly to the real spectrum of LBQS0109. We then performed the kinematic analysis on the simulated data as described in Sect. 6.3.3. The flux, velocity, and velocity dispersion maps (Figure 6.12) obtained from the simulations are similar to those shown in Figure 6.3 extracted from observations. Indeed, the velocity map shows blue-shifted velocities in the outflow region extended over 0.5 ″(i.e ~4.2 kpc). This means that the simulation confirms that the blue-shifted region suffers from beam smearing, and its size does not match the real radius of the outflow.

Since the simulated outflow well describes the asymmetric [OIII]λ5006 profile and the velocity gradient observed in our datasets, we carried out the spectroastrometry analysis on the simulated data to estimate the average velocity and radius of the ionised gas to compare these derived values with the input parameters. The offset of the photocentroids at different velocities are shown in Figure 6.13. The radius R_o (~ 0.05 ″) and the average velocity $v(R_o)$ (~ 1450 km/s) estimated from spectroastrometry are consistent with the initial input parameters. Clearly, provided that the S/N is high enough, the

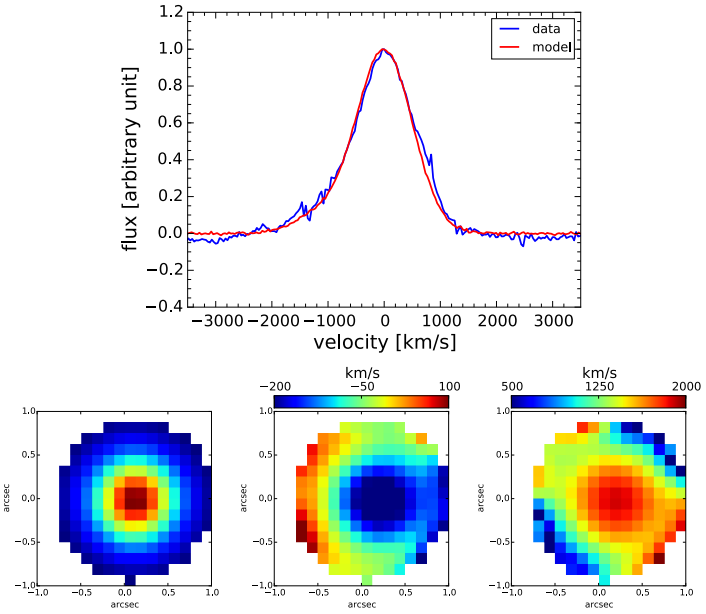

Figure 6.12: *Top panel:*[OIII]λ5007 emission lines extracted from a nuclear region of 0.25″× 0.25″ . The blue line is the [OIII]λ5006 emission line of LBQS0109 after subtracting all the other best-fit components. The red line is the ionised emission line obtained from the simulated data. *Bottom panel:* [OIII] flux, velocity, and velocity dispersion map obtained from the simulated [OIII]λ5006 data. The regions with S/N < 2 are masked out.

spectroastrometry method can provide the position and the velocity of outflows with an accuracy well below the seeing limit. Moreover, since the integral flux of [OIII]λ5006 at high blue-shifted velocity (-2500km/s $< v < v(R_o)$) is consistent with about half of the total flux emitted from the ionised outflowing gas, the outflow luminosity can be inferred from

$$L_o = 2 \int_{-\infty}^{\lambda_0} L_\lambda(\lambda) d\lambda, \tag{6.9}$$

where λ_0 is the wavelength corresponding to v_0. When the [OIII]λ5006 emission line was well described by a multi-Gaussian fit, the luminosity value calculated with Eq. (6.9) and the one estimated from the broad Gaussian component, as typically done in the literature, are consistent within the errors. In the multi-Gaussian fit we therefore estimated L_o from the broad component, and in the other case we measured the luminosity of the gas using Eq. (6.9).

Since the narrow Hβ component has the same profile as [OIII], we can measure the outflow luminosity for both the emission lines using the same equation. From the luminosity we derive the mass of the ionised outflows by using Eqs (6.4) and (6.7). As the [OIII]λ5006/Hβ ratio measured in each QSO is ~ 10, the mass inferred by Hβ is twice higher than that estimated by [OIII]λ5006 (see Eq. 6.8). The luminosity and mass of the outflow are listed in Tables 6.1 and 6.3, respectively. Since HE0251 is not spatially resolved, we cannot estimate the outflow luminosity using the method described above. In this case, we fitted the [OIII]λ5006 with two Gaussian components and inferred the outflow luminosity from the broad Gaussian component.

6.5 Results

6.5.1 The Nature Of Ionised Outflows

To investigate the nature of the ionised wind, we need to estimate the main quantities of the outflows: mass outflow rate, momentum rate, and kinetic power. Theoretical models (e.g. Zubovas & King 2012; Faucher-Giguère & Quataert 2012) predict tight relations between these quantities and the AGN bolometric luminosity, $L_{\rm AGN}$. In particular, the correlation between the momentum rate and

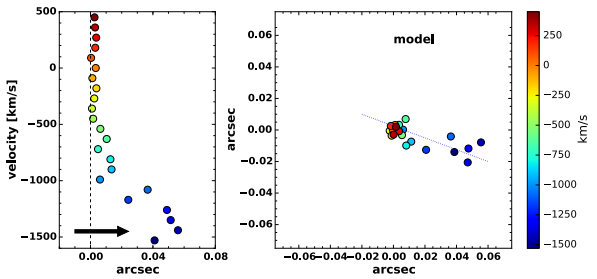

Figure 6.13: Spectroastrometry results obtained from the simulated data. On the left, centroid offset of [OIII]λ5006 emission respect to continuum emission (dashed line) at different wavelengths. On the right, the photocentroid position in each velocity. Colour-coding corresponds to velocity offset.

$L_{\rm AGN}$ provides an indicator of the nature of the feedback mechanism. In this section we derive the main properties of the AGNs in our sample and compare them with the prediction of the models. As explained in Sect. 6.4.3, the low spatial resolution of our observations does not allow us to discern whether our outflows are single explosive events or refilled with clouds ejected from the galactic disc. Hence, we assumed a simple model where a single ionised cloud is ejected outward of the nuclear region and the mass outflow rate is equal to the mass of the outflow divided by the dynamical timescale (see Eq. 1). The dynamic time is the time that it takes a clump of ionised gas in outflow to reach a fixed distance from the QSO. We derived $\dot{M}_o$ values in the range 6 − 700 $M_\odot$/yr. We assumed an average outflow mass rate error of ±50%, which takes in account the uncertainties associated with the gas physical properties (i.e. density and temperature), flux calibrations, and R_0 and v_0 estimates due to projection effects. For each source we estimated two value of $\dot{M}_o$ that were calculated by using Hβ and [OIII]λ5006, respectively. Since the [OIII]λ5006 outflow luminosities are about ten times higher than those from Hβ, the outflow masses inferred from the hydrogen emission line are about twice higher than those estimated by [OIII]λ5006.

In Fig. 6.14 we plot the outflow velocity and mass rate as a function of the AGN luminosity. $L_{\rm AGN}$ is derived by using the relation $L_{\rm AGN} \sim 6\lambda L(\lambda 5100\text{Å})$ from Marconi et al. (2004). The solid and empty blue points are the $\dot{M}_o$ estimated for five out of six QSOs; we were unable to infer the value of HE0251 since we were unable to measure the size of the outflow. The red points represent the ionised outflows observed in type 2 AGN at redshift $0.08 \lesssim z \lesssim 0.2$ (Harrison et al. 2014); the orange and purple points are adopted from Brusa et al. (2015) and Cresci et al. (2015), who mapped ionised outflows in six X-ray selected obscured QSOs at $z \sim 1.5$; and the black circle corresponds to the the ionised outflow in an obscured radio-quiet QSO at z ~0.123 (Greene et al. 2012). For consistency with our work, we re-calculated the outflows properties using an electronic density of n_e =500 cm^{-3} and a temperature of $T_e = 10^4$ K. We note that the outflow masses from literature may be overestimated since we used the luminosities from the total [OIII]λ5006 and Hβ profiles.

In addition to ionised outflows, we compared our results with those obtained from molecular outflows (green, black, and brown solid squares; Cicone et al. 2014, Sun et al. 2014, and Feruglio et al. 2015, respectively). The molecular outflow properties were re-estimated assuming a shell-like cloud model (Eq. 6.1).

In Figure 6.14 we show that the outflow velocity v_0 and outflow rate are correlated with the AGN luminosity, although with a large scatter. The increase in velocity and outflow rate with increasing AGN luminosity is consistent with the idea that a luminous AGN pushes away the surrounding gas through a radiatively driven fast wind whose kinetic power is a fraction of the AGN luminosity. However, it is difficult to establish a direct relation between AGN luminosity, velocity, and outflow rate. The acceleration process of the outflow by the fast wind and the fraction of the kinetic power injected might vary from object to object; moreover, the observed AGN luminosity may not represent the long-term average luminosity that in the end is responsible for driving the outflow. For these reasons, we do not expect tight correlations between velocity, outflow rate, and AGN luminosity, as observed. Indeed, previous studies on more heterogenous samples, but smaller luminosity ranges,

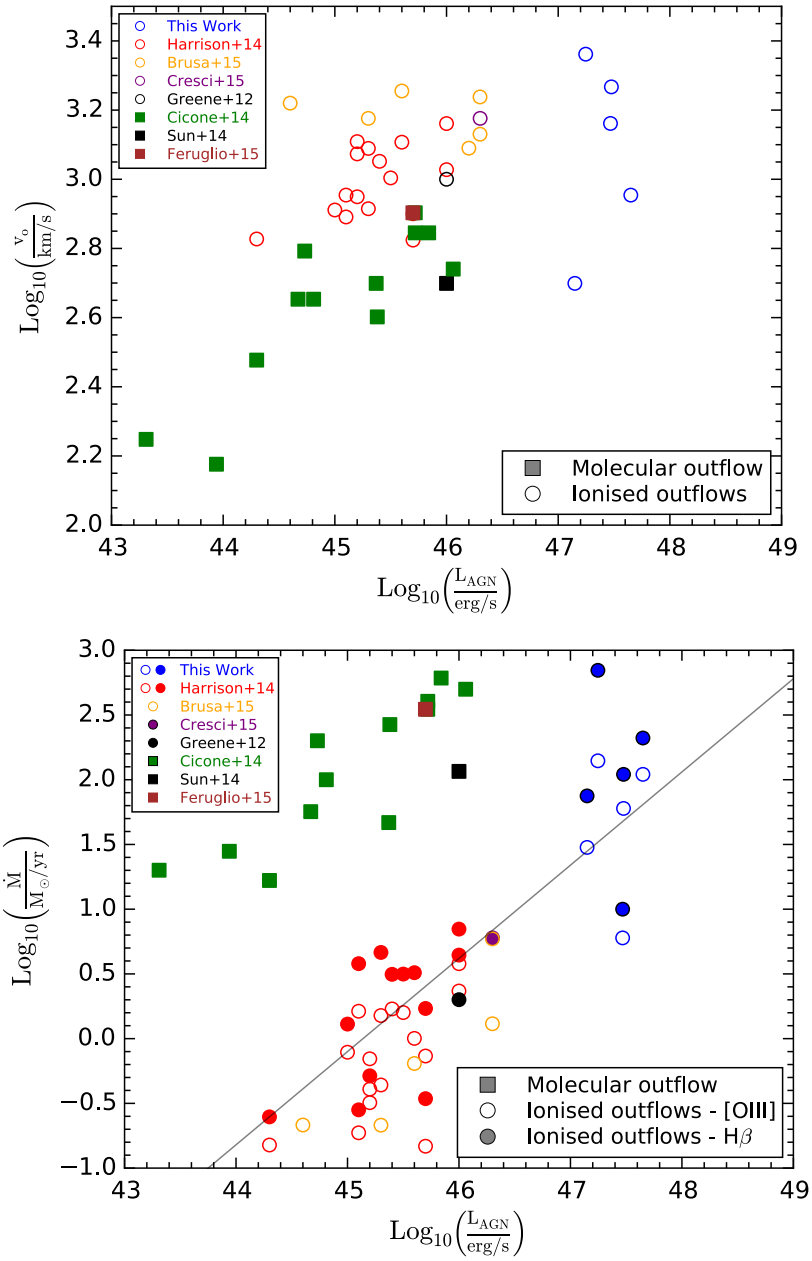

Figure 6.14: Top panel: Outflow velocity as a function of the AGN bolometric luminosity. The blue circles denote the results from this work; the open circles mark the velocities of ionised gas (mainly [OIII]λ5006): the red, orange, purple, and black circles are the estimates obtained from Harrison et al. (2014), Brusa et al. (2015), Cresci et al. (2015), and Greene et al. (2012), respectively. The green, black, and brown squares denote the velocities of the molecular outflows from Cicone et al. (2014), Sun et al. (2014), and Feruglio et al. (2015). Bottom panel: Outflow rates as a function of the AGN bolometric luminosity. Notation is the same as in the top panel, expect that open circles represent the estimates obtained with [OIII]-inferred masses, while the filled ones denote the estimates based on Hβ. We recalculated the outflow properties inferred by previous works to make them consistent with our estimates (see text). The solid line is the best-fit relation to the averages of filled and empty circles.

did not find any significant correlation between the outflow velocities and the AGN luminosities (e.g. Veilleux et al. 2013; Brusa et al. 2015). In the luminosity range where we have data from both CO and [OIII] ($10^{44.5}$ erg/s $\lesssim$ L_{AGN} $\lesssim$ $10^{46.5}$ erg/s), the velocities of the ionised outflows are a factor ~2 higher than those of the molecular gas, which is consistent with higher masses of molecular gas in both momentum- and energy-driven scenarios, but also with different acceleration and deceleration processes. However, given the heterogeneous nature of the sample and the non-uniform measurements of outflow velocities, we cannot draw any firm conclusions. Moreover, there is only one galaxy (black circle and square in Figure 6.14) where both molecular and ionised outflows are detected. This discrepancy is even more evident when comparing molecular with ionised outflow rates. Cicone et al. (2014) fitted a a log-linear relation between $\dot{M}$ and L_{AGN} for their molecular outflows and found $Log_{10}(\dot{M}) = 2.84 + 0.720 \times Log_{10}(L_{AGN}/10^{46}\mathrm{erg/s})$, where we have corrected for the factor 3 discrepancy described in Section 6.4.1. Here, we fitted the same relation between $\dot{M}$ and L_{AGN} by fixing the slope to that of Cicone et al. (2014),

$$Log_{10}(\dot{M}) = (0.6 \pm 0.2) + 0.720 \times Log_{10}(L_{AGN}/10^{46}\mathrm{erg/s}). \quad (6.10)$$

Since the velocities and the radii of ionised outflows are similar to those of molecular outflows, we interpret the offset between the two L_{AGN}- $\dot{M}$ correlations as an indication that the ionised gas only traces a small fraction of the total gas mass. Comparing the normalisation of the L_{AGN}- $\dot{M}$ relation inferred from our data with that obtained from molecular outflows, we can infer that the outflow rate of the ionised gas is a small fraction (< 10%) of the molecular outflow, suggesting that outflow masses are dominated by molecular gas. However, since molecular and ionised outflow rates are not estimated in the same objects and the relations have quite a large scatter, it is not possible to estimate the exact fraction of ionised gas in the outflows. On the other hand, the different normalisation could indicate that two different acceleration mechanisms are at work. Future ALMA observations of the molecular gas in these objects are essential to distinguish between these two different scenarios.

Figure 6.15 shows the kinetic power of outflowing gas as a function of AGN luminosity where the outflow kinetic energy rate is given by

$$\dot{E}_o = \frac{1}{2}\dot{M}_o v_o^2 = \frac{1}{2}\frac{M_o}{R_o}v_o^3.$$

We indicate with solid, dashed, and dotted lines the locus of points that have an outflow kinetic power that is 100%, 5%, and 0.1% of the AGN luminosity, respectively. Recent AGN feedback models (e.g. King 2010; Zubovas & King 2012; Lapi et al. 2014) predict a coupling efficiency between AGN-driven outflows and AGN power of about ~5%, which is needed to explain the M_{BH} - σ relation observed in local galaxies. Although the molecular outflow observations are consistent with the models within the errors, the kinematic power estimated from ionised outflows is only < 0.1% of the L_{AGN}. This percentage is too low to explain the M_{BH} - σ relation. Since the kinetic energy is proportional to the outflow mass, we cannot discern whether the nature of ionised outflows is different from that of molecular ones or, as discussed above, the [OIII]λ5006 (and Hβ) line emission only traces a small fraction (< 10%) of the total outflowing gas.

The last fundamental parameter of the outflows is the outflow momentum rate defined as $v_o\dot{M}_o$. Energy-driven outflow models predict that the momentum of the large-scale outflow is boosted compared to the nuclear wind (or AGN radiation pressure momentum), that is, $v_o\dot{M}_o \sim 20L_{AGN}/$ c (Zubovas & King 2012). In Figure 6.15 we observe that molecular outflows follow the relation predicted by models (see Cicone et al. 2014 for more details), while ionised outflows are below the 1:1 relation. This could simply be the consequence of the discrepancy between the outflow masses of ionised and molecular gas.

Finally, we may conclude that the main difference between molecular and ionised outflows is the fraction of total gas mass pushed away from the AGN-driven wind. This is confirmed by the higher outflow rates (right panel of Figure 6.14) and kinetic power (Figure 6.15) of molecular outflows and by their lower outflow velocities (Top panel of Figure 6.14).

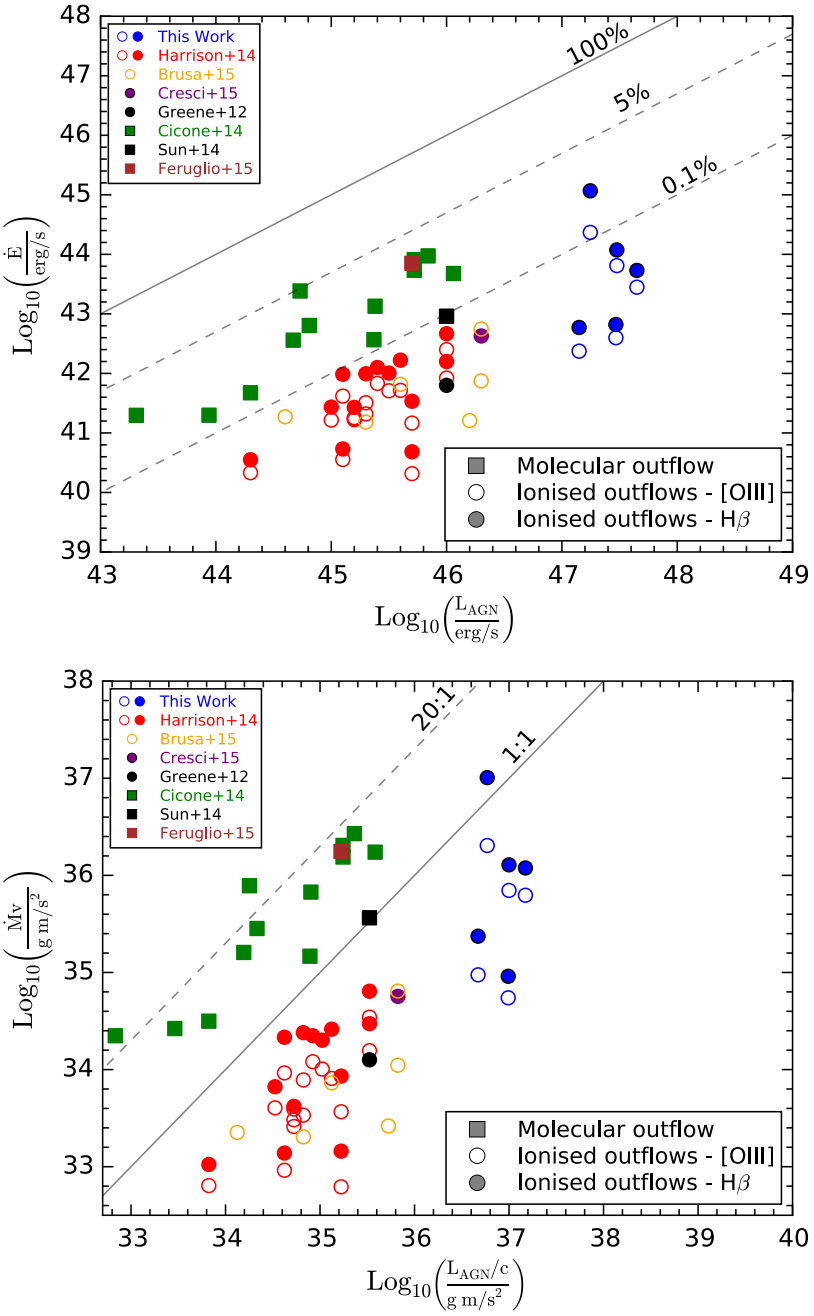

Figure 6.15: *Top:*Kinetic power as a function of the AGN bolometric luminosity. The blue circles denote the results from this work; the open circles mark the velocities of ionised gas (mainly [OIII]λ5006): the red, orange, purple, and black circles are the estimates obtained from Harrison et al. (2014), Brusa et al. (2015), Cresci et al. (2015), and Greene et al. (2012), respectively. The green, black, and brown squares denote the velocities of the molecular outflows from Cicone et al. (2014), Sun et al. (2014), and Feruglio et al. (2015). The solid, dashed, and dotted lines correspond to P_k = 100%, 5%, and 0.1%L_{AGN} , respectively. *Bottom:* outflow momentum rate as a function of photon momentum of the AGN. Notation is the same as in the top panel.The dotted and dashed line correspond to $\dot{P}\sim 20L_{\mathrm{AGN}}/$ c and $\dot{P}\sim L_{\mathrm{AGN}}/$ c, respectively.

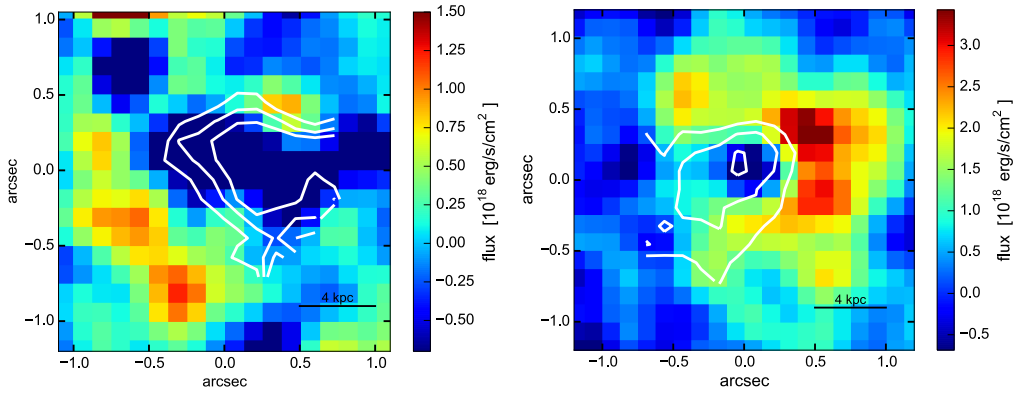

Figure 6.16: Maps of the narrow component of Hα for LBQS0109 (on the top) and HB8903 (on the bottom); the white contours trace the [OIII]λ5006 velocity blue shift shown in Figure 6.3. The contours represent the velocity -200, -180 and -150 km/s for LBQS0109 , and -150, -100 and -50 km/s for HB8903. Star formation, traced by H$\alpha_{\rm nar}$ is heavily suppressed in the S-W and S-E for region for LBQS0109 and HB8903, respectively, where the outflow traced by [OIII]λ5006 is fastest.

6.5.2 The Negative Feedback Scenario

Figure 6.16 shows the flux maps of the H$\alpha_{\rm nar}$ component obtained by collapsing the residual data cubes of LBQS0109 and for HB8903 over the wavelength bins where H$\alpha_{\rm nar}$ is detected. The H$\alpha_{\rm nar}$ emission is extended up to ∼1″ (∼ 8 kpc) from the AGN in both sources. Moreover, the H$\alpha_{\rm nar}$ surface brightness is asymmetrically distributed around the nucleus, similarly to [OIII]λ5006. The H$\alpha_{\rm nar}$ emission in LBQS0109 is primarily distributed toward N-E while that of HB8903 is concentrated in three different clumps located N-W and S-W of the AGN position. The H$\alpha_{\rm nar}$ surface brightness maps are clearly similar to those obtained for [OIII]$_{nar}$ shown in Fig. 6.6. By using the Kennicutt & Evans (2012) relation Log(SFR/M$_\odot$/yr) = Log(L$_{\rm H\alpha}$/erg s^{-1}) - 41.27, we derive a total star formation rate from H$\alpha_{\rm nar}$ of SFR∼ 50 M$_\odot$/yr for LBQS0109 and SFR∼ 90 M$_\odot$/yr for HB8903, which are not unusual in high-z QSOs (e.g. Lutz et al. 2008, Cano-Diaz et al. 2012, Cresci et al. 2015) and star forming galaxies at similar redshifts.

We compare the inferred SFRs of our targets with the star formation rates of to main-sequence galaxies with similar stellar masses, SFR$_{\rm MS}$. The stellar masses of LBQS0109 and HB8903 are 1.5 × 10^{12} M$_\odot$ and 6.0 × 10^{11} M$_\odot$, respectively. A MS star-forming galaxy with M$_\star$= 10^{12} M$_\odot$ at $z \sim 2$ has a SFR$_{\rm MS}$ ∼2000 M$_\odot$/yr (Rodighiero et al. 2011). Hence the SFR from H$\alpha_{\rm nar}$ is about one order of magnitude smaller than the corresponding SFR$_{\rm MS}$ at $z \sim 2$. However, the SFRs inferred for the two QSO may be lower limits since the H$\alpha_{\rm nar}$ emission is not corrected for dust extinction. In fact, by using the correlation between the infrared luminosity $L_{\rm IR}$ and $L_{\rm AGN}$ by Netzer (2009) and Hickox et al. (2014) at $z = 2$, we estimate a SFR∼1000-2000 M$_\odot$/yr, which is consistent with SFR$_{\rm MS}$. In addition to dust extinction, the M$_\star$ inferred for the two targets are upper limits as well as the SFR$_{\rm MS}$ derived from the main sequence. In conclusion we can only estimate that the SFRs of the two QSOs are in the range $\sim 100 - 1000$ M$_\odot$ which does not allow us assess whether AGN-driven outflows are indeed quenching the star formation of the *whole* galaxy. Future photometric measurements at 8-1000 μm rest frame will allow us to estimate the SFR from the L_{IR} . The comparison between the SFR from L_{IR} to the instantaneous one derived from H$\alpha_{\rm nar}$, will quantify the influence of AGN-driven outflow on the star formation history of the host galaxy.

The white contours in Figure 6.16 show the most blueshifted [OIII]λ5006 projected velocities (-200, -180 and -150 km/s for LBQS0109 , and -150, -100 and -50 km/s for HB8903) and therefore correspond to the regions where the fastest [OIII]λ5006 outflows are located: these appear spatially anti-correlated with the presence of the H$\alpha_{\rm nar}$ emission. We interpret these observations as an evidence for "negative feedback" in action because they indicate that star formation is quenched in the regions where AGN-driven outflows interact with the host galaxy. The present data do not allow us to distinguish between the possibilities that, in the regions encompassed by the fast outflows, star forma-

tion is absent due to missing molecular gas or to the fact that molecular gas has been heated or made more turbulent. Our planned ALMA observations of the CO(3-2) line at a resolution similar to the SINFONI observations will address this question.

6.5.3 The Positive Feedback Interpretation

Our observations vaguely resemble the observations at a z=1.5 source (XID2028) by Cresci et al. (2015), where the ionised outflow was found to anti-correlate with the Hα emission and the rest-frame U-band surface brightness, which map the current star formation in the host galaxy. The two emission lie in both edges of the outflow cone. These observations were interpreted in terms of positive feedback, where the outflow triggers star formation in the host by compressing the gas clouds.

In our sources and in that of Cano-Díaz et al. (2012), star formation is distributed along both edges of the outflow cone (Figure 6.16) as shown in the schematic view in Figure 5 of Cresci et al. (2015). Therefore, it is also possible to interpret our results represent an example of "positive feedback", which is invoked by recent models to explain the correlation between AGN and star formation activity in the host galaxy (Silverman et al. 2009; Imanishi et al. 2011; Mullaney et al. 2012; Zinn et al. 2013; Zubovas et al. 2013). This scenario may be confirmed by the fact that Hα emission is mainly produced by massive stars that have a lifetime of < 10 Myr. This time is as long as typical AGN activity, suggesting that the star formation activity is connected with AGN-driven outflows. However we cannot exclude that the current SFR in the host galaxies is a residual of SF activity occurring before the negative feedback phase. Indeed, star formation rates in the host galaxies of bright QSOs can be as large as 1000 $M_\odot$/yr,hence a SFR$<$ 100 $M_\odot$/yr might already imply a significant reduction in the past. In this case the existing star formation regions would not be induced by positive feedback, but they would be are region of star formation not perturbed by AGN-driven outflows.

6.6 Conclusions

We performed seeing-limited, near-IR integral-field spectroscopic observations with SINFONI of a sample of six high-luminosity ($L_{bol} = 10^{13} - 10^{14}$ $L_\odot$) QSOs at redshift $z \sim 2.4$. [OIII]λ5006 emission lines, red-shifted into the H band, are characterised by large FWHMs ($>$ 1000 km/s) and prominent blue wings, indicative of fast outflows accelerated by the powerful AGN. We summarise our results below.

- The [OIII]λ5006 emission line is spatially resolved in five out of six sources and is extended over several kiloparsecs.
- The analysis of the [OIII]λ5006 kinematical maps suggests conical outflows associated with regions of high-velocity dispersions ($>$ 500 km/s). The physical properties of the outflows, that is, mass, outflow rate, kinetic energy, and momentum rate, were estimated with a new method based on spectroastrometry, which is not affected by PSF smearing, at variance with results from previous works. The reliability of this method was confirmed with a simple simulation, but more accurate modelling will be developed in future work.
- Both ionised and molecular outflow velocities are weakly correlated with the observed AGN luminosity, despite the large scatter, and at a given AGN luminosity the velocity of the ionised gas is roughly a factor 2 higher than that of the molecular one. However, given the heterogenous nature of the combined sample, we cannot draw any firm conclusions.
- Mass and momentum rates, as well as kinetic powers, increase with AGN bolometric luminosity in a similar way to what is observed in molecular outflows in the local Universe. The ionised gas properties define relations with AGN luminosity that are parallel with those of molecular gas. In particular, ionised outflow rates are $\sim$ 50 times lower than molecular ones. The kinetic power carried by ionised outflows is of $\sim 0.1-0.05\%$ of the AGN luminosity compared to $\sim 5\%$

for molecular outflows. Finally, momentum rates are of the order of $L_{\rm AGN}$/c, a factor $\sim 20-50$ smaller than for molecular outflows.

- These discrepancies between ionised and molecular outflows can be explained with the fact that ionised gas traces a smaller fraction of the total gas mass. Alternatively, they are an indication of different acceleration mechanisms for the molecular and the ionised gas. Observations with ALMA would allow us to measure the molecular gas mass in these objects and distinguish between these two scenarios.

- The [OIII]λ5006 emission line profiles of two out of six QSOs are characterised by faint, narrow (FWHM < 500 km/s), redshifted components; The narrow components, $[\mathrm{OIII}]_{nar}$, are spatially extended (> 1 kpc) and are spatially anti-correlated with the outflow location.

- After subtracting pixel-by-pixel all broad (FWHM > 500 km/s) components from K-band spectra in both targets, we detect faint, narrow (FWHM $\sim 250-500$ km/s) $\mathrm{H}\alpha_{\rm nar}$ emission at the same redshift of $[\mathrm{OIII}]_{nar}$ and co-spatially distributed with the $[\mathrm{OIII}]_{nar}$ in both the QSOs.

- The emitted flux is not symmetrically distributed around the location of the QSOs, but it is extended towards N-E and S-W in the two targets, respectively. Both line widths and surface brightness distributions of these components suggest that they are powered by SF in the host galaxies. Indeed the inferred upper limit on Log([NII]/Hα) (-0.85 for LBQS0109 and -1.32 for HB8903) is consistent with the typical value observed in star-forming regions, according to the standard BPT diagrams, even if we take into account of the cosmic evolution of the BPT boundary (Kewley et al. 2013)

- We doubled the sample of QSOs (from two to four) where the effect go AGN-driven feedback on star formation are clearly visible. We note that in all these cases the star formation rates inferred from the narrow Hα components are significant, $\sim$ 100 $M_\odot$/yr; moreover, these are likely lower limits on the global star formation rate, since a large part of the Hα emission might be hidden because of dust reddening (e.g. Brusa et al. 2015). Although the statistics is still low, the combined observations reinforce the idea that that quasar outflows do affect only a (small) part of the host galaxy; therefore either AGN feedback does not completely quench star formation or several AGN episodes are needed to do that.

Summary & Conclusions

Galaxies are observed to broadly exist in two populations, those that are passive (red sequence) and those that are actively forming stars (blue clouds). For each galaxy the SFR is correlated with intrinsic properties (i.e. mass), environment, and redshift , but the origin of these correlations and the passive/star-forming dichotomy in general is still not well understood. It appears that some processes could inhibit the star formation activity as a function of environment and mass, and feedback is often considered as an important regulatory mechanism. The tight BH-galaxy mass correlation observed in the local Universe lead to the widespread belief that BHs and host galaxies coevolve by regulating each other's growth, i.e. implying the BH-galaxy coevolution scenario.

According to this scenario, a star-forming galaxy evolves along the main sequence growing its stellar mass by secular processes. Interactions with the dark halo and with other galaxies introduce gravitational instabilities on the disk that determine an increasing SFR. Meanwhile disk instabilities feed the massive BH hosted in the centre of the galaxy entering a phase during which the galaxy is obscured by dust and not visible in the optical wavelengths range. The starburst activity heats the surrounding dust that emits in the FIR (ULIRGs/SMG phase). Once the BH reaches a critical mass, the energy released by the accretion mechanism overtakes the gravitational potential and sweeps gas and dust away from the galaxy. The radiation emitted by BH and host galaxy is now visible in the optical wavelength range as well (QSO phase). The lack of gas halts the BH growth and the star formation activity in the host, and the galaxy turns into a read-and-dead Elliptical.

Although the BH-galaxy coevolution paradigm is motivated by observed correlations, there are still open question regarding the coevolution theory: *What are the main properties of outflowing gas? What is the link between AGN feedback and large-scale environment? What is the detailed nature of AGN feedback? What is the fuel of the rapid growth of the most massive BHs?*

Most theories of galaxy evolution invoke AGN negative feedback to quench star formation in massive galaxies. More specifically, AGN-driven outflows are expected to clean massive galaxies from their gas content, hence removing the fuel needed to form stars. Such a scenario is invoked to explain the red-and-dead properties of local Ellipticals, the shortage of extremely massive galaxies (with respect to that expected from the dark halos mass function), and the M_{BH}-σ_e relation.

A view of the formation and evolution of a galaxy over its whole history requires observations taken at different times, from the Big Bang to the current epoch. Since our lookback time is limited by the currently available instrumentation and we are not able to track the evolution of a single galaxy from $z = \infty$ to $z = 0$, I aimed at understanding the properties of galaxies at different redshifts assuming that they evolve following the same evolutionary track.

Following the scheme proposed for the first time by Sanders et al. 1988, (see Figure 1.3), in this PhD thesis I investigated the BH-galaxy coevolution paradigm through observations of galaxies existing both in the high-z and local Universe and going through different phases of galaxy evolution.

Most of the results presented here are obtained exploiting the capability of the Atacama Large Millimetre Array (ALMA). In Chapter 3, we described the advantages of millimetre observations. In particular, we emphasised that ALMA is fundamental to understand the properties of high$-z$ galaxies thanks to its high angular resolution and sensitivity, way better than those of previous millimetric

telescopes. ALMA capabilities allowed us to study the properties and kinematic of gas in the first galaxies. Moreover, both millimetre and fine structure line emissions trace cold and dense regions which are not observable in the optical range.

In Chapter 4 we conducted a 1.1 mm and a 1.3 mm analysis using 18 deep ALMA datasets taken during the first cycles of observations. Before the ALMA-era, only a small percentage (∼30%) of the background radiation was resolved at millimetre wavelengths, with millimetric surveys being able to detected only the bright end (S> 1 mJy) of the millimetre population. It should be noted that this population, characterised by high SFR ($> 100 - 1000$ $M_\odot$/yr), is not representative of the bulk of the galaxy population since the steep faint-end slope of the galaxy luminosity function suggests most of galaxies to be faint, especially at higher z in the early Universe. By using the deepest datasets obtained with ALMA, we derived the differential number counts down to 60 μJy and 100 μJy at λ =1.3 mm and λ =1.1 mm, respectively. With respect to previous works, we improved the source extraction method by requiring the dimension of the detected sources to be consistent with the beam size. This method enabled us to remove spurious detections that used to plague the purity of the catalogues in all previous studies We detected 50 faint sources (fluxes < 1 mJy) with $S/N > 3.5$ down to 60 μJy, hence improving the statistics by a factor of four with respect to previous studies. The inferred differential number counts are $dN/d(Log_{10}S) = 1 \times 10^5$ deg^2 at a 1.1 mm flux $S_{\lambda=1.1\ mm} = 130$ μJy, and $dN/d(Log_{10}S) = 1.1 \times 10^5$ deg^2 at a 1.3 mm flux $S_{\lambda=1.3\ mm} = 60$ μJy. At the faintest flux limits probed by our data, i.e. 30 μJy and 40 μJy, we obtained upper limits on the differential number counts of $dN/d(Log_{10}S) < 7 \times 10^5$ deg^2 and $dN/d(Log_{10}S) < 3 \times 10^5$ deg^2, respectively. Determining the fraction of the CIB resolved by ALMA observations was hampered by the large uncertainties plaguing CIB measurements (a factor of four in flux). However, our results provide a new lower limit to the CIB intensity of 17.2 Jy deg^{-2} at 1.1 mm and of 12.9 Jy deg^{-2} at 1.3 mm. Moreover, the flattening of the integrated number counts towards faint fluxes strongly suggests that we are probably close to the total CIB intensity. Our data imply that galaxies with SFR< 40 $M_\odot$/yr certainly contribute to less than 50% to the CIB (and probably to a much lower percentage) while more than 50% of the CIB must be produced by galaxies with SFR > 40 $M_\odot$/yr. The differential number counts are in nice agreement with recent semi-analytical models of galaxy formation even towards low fluxes like ours. This evidence supports the galaxy evolutionary scenarios and all the assumptions made in these models.

As mentioned above, the bulk of the galaxy population is represented by star-forming galaxies with SFR< 100 $M_\odot$/yr. However bright SMGs represent a crucial phase in the galaxy evolution track. Such outliers of the main sequence galaxies are believed to have mostly merger-induced SFRs, as in the case of local ULIRGs. SMGs galaxies appear to fit well into this merger-induced star formation scenario, being outliers of the main-sequence at $z \sim 2 - 3$, and showing SFRs $\sim 100 - 1000$ $M_\odot$/yr and $M_\star$ of about 10^{11} $M_\odot$. The BH-galaxy coevolution theory expects this type of galaxies to the precursors of QSOs. In the QSO phase the starburst galaxy and the AGN are completely obscured by dust and gas, and their emissions are visible only at the millimetre wavelength. The system BR1202-0725 is a good target to test this scenario since it is a major-merger system at $z \sim 4.7$ composed of a SMG and a QSO, with a projected separation of ∼ 24 kpc. Both sources are forming stars at high rate (∼ 1000 $M_\odot$/yr) and, according to the commonly accepted paradigm, their star formation should be triggered and sustained by major-merger events. In Chapter 5 we illustrated the kinematic of the [CII] emission line in BR1202-0725, observed with ALMA during the Science Verification Cycle. We fitted pixel-by-pixel the [CII] emission line, deriving the flux, velocity, and velocity dispersion map for both the targets. The gradient observed in the velocity map suggests the presence of a rotating gas disk in both the sources. We developed a model for this rotating gas disk and, by comparing the mock velocity map to the real one, ALMA observations revealed that the two galaxies apparently have undisturbed rotating disks, which is at variance with the commonly accepted scenario in which strong star formation activity is induced by a major merger. The dataset also permitted the detection of faint components that, after spectral deblending, were spatially resolved from the main QSO and SMG emissions. Their relative velocities and positions are compatible with orbital motions within

the gravitational potentials generated by the QSO host galaxy and the SMG, suggesting that they are either smaller galaxies in interaction or gas clouds within accretion flows of tidal streams. Finally, no clear spectral evidence for outflows caused by AGN or stellar feedback was found, suggesting that the high star formation rates might be induced by interactions or minor mergers with these companions, which do not affect the large-scale kinematics of the disks. The SF trigger due to minor-merger events seems to be consistent with the observed ratios $V_{\rm max}/\sigma_{int}$ of 1.3 for SMG and 1.5 for QSO, which indicate that the disk is slightly disturbed. Alternatively, the strong SF may be fuelled by the accretion of pristine gas from the host halo. Our kinematical analysis also indicates that the QSO and the SMG have similar dynamical masses, mostly in the form of molecular gas, and that the QSO host galaxy and the SMG are almost face-on with slightly different disk inclinations: $i \sim 15°$ for the host, and $i \sim 25°$ for the SMG. This result may support the fact that SMG and QSO represent two phases in the galaxy evolution path, with the SMG being the precursor of the QSO. Finally, the ratio between the BH mass, obtained from XShooter spectroscopy, and the dynamical mass of the host galaxy is similar to values found in very massive local galaxies, suggesting that the evolution of BH-galaxy relations could be better understood if studied through dynamical rather than stellar masses.

Unveiling the nature of AGN outflows is one of the hot topics in current extragalactic astronomy. However, the "smoking gun" evidence of negative feedback required by coevolution model is still missing. In Chapter 6 we detected the presence of extended ionised outflows in luminous QSOs at $z \sim 2.5$. In detail, we analysed a sample of six luminous QSOs (L > 10^{47} erg/s) observed in the H and K band using the spectrograph SINFONI mounted at VLT (see Section 3.2) and we performed a kinematical analysis of the [OIII]λ5006 emission line, which is a good tracer of ionised outflows. All sources reveal a broad asymmetric [OIII]λ5006 profile with a blue prominent wing suggesting the presence of fast-moving gas along the line of sight. We performed a pixel-by-pixel fitting assuming that the QSO emission is not spatially resolved and the residual map at the wavelength of the [OIII]λ5006 indicated that this emission line is spatially resolved in five out of six QSO. [OIII]λ5006 shows a complex gas kinematic, with blue-shifted velocities of a few hundreds of km/s and line widths up to 1500 km/s, suggesting the presence of fast, spatially extended outflows with conical morphology in the five QSOs. The velocity and size of the ionised outflows were estimated by using a new method based on spectroastrometry at variance with results from previous works. We generated a mock ionised outflow to validate the spectroastrmetric method revealing that this is not affected by PSF smearing. By using the spectroastrometric method we inferred size of the ionised outflows of up to ~2 kpc. The properties of the ionised outflows, mass outflow rate, momentum rate and kinetic power, are correlated with the AGN luminosity. We derived a logarithmic relation between outflow mass rate of ionised outflow and AGN luminosity. The increase in outflow rate with increasing AGN luminosity is consistent with the idea that a luminous AGN pushes away the surrounding gas through fast outflows driven by radiation pressure, which depends on the emitted luminosity. We derived mass outflow rates of about 6-700 $M_\odot$/yr for our sample, which are lower than those observed in molecular outflows. Indeed physical properties of ionised outflows show dependences on AGN luminosity which are similar to those of molecular outflows but indicating that the mass of ionised gas is smaller than that of the molecular one. Alternatively, this discrepancy between ionised and molecular outflows could be explained with different acceleration mechanisms. In two out of six QSOs we also detected a faint narrow (FWHM < 500 km/s) and spatially extended components in [OIII]λ5006 and Hα lines associated with star formation in the host galaxy. Such star-formation powered emission is spatially anti-correlated with the fast outflows: Hα seems to be suppressed in the location of the ionised outflow. Our new observations are doubling the sample of AGN with strong evidence of negative feedback in action. Although these fast outflows can suppress star formation, the detection of narrow, spatially-extended Hα emission indicates star formation rates of at least $\sim 50 - 90$ $M_\odot$/yr , suggesting that either the AGN feedback does not affect the whole galaxy or that many feedback episodes are required before the star formation is completely quenched. On the other hand, the narrow Hα flux map extended along the edges of outflow cone lead to a positive feedback interpretation.

The results presented in this thesis support the BH-galaxy coevolution paradigm, leading to belief

that BHs and host galaxy are interlinked. An important conclusion derived from this work concern AGN-driven outflows:

- The model predictions used to describe the number counts at millimetre wavelength include AGN feedback, but this mechanism is relevant only in the most massive galaxies while, in less massive galaxies, the SFR is mostly regulated by SN feedback.
- The AGN feedback seems to be irrelevant in the major-merging system BR1202-0725. The [CII] profile does not revel clear evidence of ionised outflow and its velocity map suggests that the gas is not perturbed. Such scenario is not expected during the bright QSO phase, when expect to observe large amount of gas pushed away by AGN-driven outflows.
- Two of the most luminous QSOs known so far show ionised outflows quenching the star formation activity in the central region, while in rest of the galaxy the SFR is at least 50 $M_{\odot}$/yr.

All these observational evidences suggest that there may be another process (or multiply processes) regulating the BH and galaxy growth. However, the sample presented in this thesis is statistical small, and therefore this work should be intended as a pilot project for future spectroscopic observations. A larger sample will allow us to reach more robust results on the BH-galaxy coevolution, and, in particular, future surveys targeting AGNs will resolve the coevolution puzzle.

Future Works

Most of the work presented in this thesis can be considered as a pathfinder for projects aimed at fully eploiting the future capabilities of ALMA. In the following we will present our future perspectives:

- We will propose ALMA observations to recover the redshift of faint millimetre sources identified in the work illustrated in Chapter 4 with the aim of discerning between the evolutionary models that have been proposed so far. Moreover, ALMA will allow a detailed study on star formation rates and gas kinematics for our sample galaxies, providing the first complete investigation on the faint millimetre galaxy population and solid constraints on galaxy evolutionary models.
- We will propose new BR1202-0725 observations with ALMA at higher spatial resolution and sensitivity. Should rotation be confirmed, this system would not fit at all into the current paradigm on the formation of massive galaxies which does not expect such large SFRs in "normal" rotating disk. Additionally, we aim at detecting and imaging faint galaxy companions around the two brightest sources of the system, whose presence is suggested by our previous analysis of the [CII] gas kinematics. If confirmed, such minor galaxy interactions and minor merger events may provide a viable explanation for the large SFRs observed in BR 1202-0725. Finally, the analysis of this faint companions will help obtain a complete picture of galaxy/cluster formation.
- We have just obtained ALMA observations of the two QSO, LBQS0109 and HB8903, presented in the Chapter 6. With the analysis of this dataset we will map CO(3-2) to trace the distribution of the cold molecular gas in the host galaxies of the two QSOs, the only ones known so far showing evidence of outflows quenching star formation. The CO(3-2) maps will be compared with our [OIII] maps with similar spatial resolution: the molecular gas should be absent in the outflow dominated region, while surviving in the rest of the galaxy. This would be the first direct confirmation of star formation quenching by quasar outflows. Moreover, it will be possible compare ionised and molecular outflow in the same target.

In addition to millimetre observations, we will use optical images carried out with the Multi Unit Spectroscopic Explorer (MUSE) at VLT. MUSE will permits us to study the properties of ionised

outflows in the local and distant Universe. We have already got MUSE data for a local active galaxy observed during the Science Verification cycle (PI. Carniani S.). We expect to use MUSE to test "negative" and "positive" feedback scenarios by identifying quasar-driven ionised outflows and possible signatures of star formation within these outflows. This will be done by mapping the intensity ratios of the broad wings of the lines associated with quasar driven outflows. If the outer parts of the outflows are consistent with in- situ excitation by star formation, this would strongly support the new scenario ascribing to quasar-driven outflows the capability of forming stars and substantially contributing to the evolution of galaxies.

Bibliography

Aalto, S., Garcia-Burillo, S., Muller, S., et al. 2015, A&A, 574, A85
Alexander, D. M., Bauer, F. E., Brandt, W. N., et al. 2003, AJ, 125, 383
Alexander, D. M., Bauer, F. E., Chapman, S. C., et al. 2005, ApJ, 632, 736
Alexander, D. M. & Hickox, R. C. 2012, NewA. Rev., 56, 93
Alexander, D. M., Swinbank, A. M., Smail, I., McDermid, R., & Nesvadba, N. P. H. 2010, MNRAS, 402, 2211
Antonucci, R. 1993, ARA&A, 31, 473
Antonucci, R. 2012, Astronomical and Astrophysical Transactions, 27, 557
Aravena, M., Bertoldi, F., Schinnerer, E., et al. 2008, A&A, 491, 173
Bae, H.-J. & Woo, J.-H. 2014, ApJ, 795, 30
Baldry, I. K. 2008, Astronomy and Geophysics, 49, 25
Baldry, I. K., Glazebrook, K., Brinkmann, J., et al. 2004, ApJ, 600, 681
Baldwin, J. A., Phillips, M. M., & Terlevich, R. 1981, PASP, 93, 5
Balmaverde, B., Marconi, A., Brusa, M., et al. 2015, ArXiv e-prints
Balogh, M. L. & Morris, S. L. H. 2000, Mon. Not. R. Astron. Soc., 318, 703
Barger, A. J., Aragon-Salamanca, A., Ellis, R. S., et al. 1996, MNRAS, 279, 1
Barth, A. J., Sarzi, M., Rix, H.-W., et al. 2001, ApJ, 555, 685
Barvainis, R. 1987, ApJ, 320, 537
Beelen, A., Cox, P., Benford, D. J., et al. 2006, ApJ, 642, 694
Beifiori, A., Courteau, S., Corsini, E. M., & Zhu, Y. 2012, MNRAS, 419, 2497
Bell, E. F., McIntosh, D. H., Katz, N., & Weinberg, M. D. 2003, ApJS, 149, 289
Bell, E. F., Wolf, C., Meisenheimer, K., et al. 2004, ApJ, 608, 752
Benford, D. J., Cox, P., Omont, A., Phillips, T. G., & McMahon, R. G. 1999, ApJLett, 518, L65
Benson, A. J., Frenk, C. S., Lacey, C. G., Baugh, C. M., & Cole, S. 2002, MNRAS, 333, 177
Bentz, M. C., Peterson, B. M., Netzer, H., Pogge, R. W., & Vestergaard, M. 2009, ApJ, 697, 160
Best, P. N., Kaiser, C. R., Heckman, T. M., & Kauffmann, G. 2006, MNRAS, 368, L67
Béthermin, M., Daddi, E., Magdis, G., et al. 2012, ApJLett, 757, L23
Blain, A. W., Barnard, V. E., & Chapman, S. C. 2003, MNRAS, 338, 733
Blain, A. W., Moller, O., & Maller, A. H. 1999, MNRAS, 303, 423
Blanton, M. R., Lupton, R. H., Schlegel, D. J., et al. 2005, ApJ, 631, 208
Bolatto, A. D., Wolfire, M., & Leroy, A. K. 2013, ARA&A, 51, 207
Bothwell, M. S., Maiolino, R., Kennicutt, R., et al. 2013, MNRAS, 433, 1425
Bouché, N., Cresci, G., Davies, R., et al. 2007, ApJ, 671, 303
Bouché, N., Dekel, A., Genzel, R., et al. 2010, ApJ, 718, 1001
Bower, R. G., Benson, A. J., Malbon, R., et al. 2006, MNRAS, 370, 645
Bower, R. G., McCarthy, I. G., & Benson, A. J. 2008, MNRAS, 390, 1399
Bowler, R. A. A., Hewett, P. C., Allen, J. T., & Ferland, G. J. 2014, MNRAS, 445, 359
Boyle, B. J., Shanks, T., Croom, S. M., et al. 2000, MNRAS, 317, 1014
Bradley, L. D., Trenti, M., Oesch, P. A., et al. 2012, ApJ, 760, 108
Briggs, D. S., Schwab, F. R., & Sramek, R. A. 1999, in Astronomical Society of the Pacific Conference Series, Vol. 180, Synthesis Imaging in Radio Astronomy II, ed. G. B. Taylor, C. L. Carilli, & R. A. Perley, 127
Brinchmann, J. 2004, Mon. Not. R. Astron. Soc., 351, 1151
Brusa, M., Bongiorno, A., Cresci, G., et al. 2015, MNRAS, 446, 2394
Cai, Z.-Y., Lapi, A., Xia, J.-Q., et al. 2013, ApJ, 768, 21
Calvi, V., Stiavelli, M., Bradley, L., Pizzella, A., & Kim, S. 2014, ApJ, 796, 102
Cano-Díaz, M., Maiolino, R., Marconi, A., et al. 2012, A&A, 537, L8
Capak, P. L., Carilli, C., Jones, G., et al. 2015, Nature, 522, 455
Carilli, C. L., Kohno, K., Kawabe, R., et al. 2002, AJ, 123, 1838
Carilli, C. L., Riechers, D., Walter, F., et al. 2013, ApJ, 763, 120

Carilli, C. L. & Walter, F. 2013, ARA&A, 51, 105
Carniani, S., Marconi, A., Biggs, A., et al. 2013, A&A, 559, A29
Centeno, R. & Socas-Navarro, H. 2008, ApJLett, 682, L61
Chapman, S. C., Blain, A. W., Smail, I., & Ivison, R. J. 2005, ApJ, 622, 772
Chapman, S. C., Ivison, R. J., Roseboom, I. G., et al. 2010, MNRAS, 409, L13
Chapman, S. C., Windhorst, R., Odewahn, S., Yan, H., & Conselice, C. 2003, ApJ, 599, 92
Chen, C.-C., Cowie, L. L., Barger, A. J., et al. 2013a, ApJ, 762, 81
Chen, C.-C., Cowie, L. L., Barger, A. J., et al. 2013b, ApJ, 776, 131
Cicone, C., Feruglio, C., Maiolino, R., et al. 2012, A&A, 543, A99
Cicone, C., Maiolino, R., Gallerani, S., et al. 2015, A&A, 574, A14
Cicone, C., Maiolino, R., Sturm, E., et al. 2014, A&A, 562, A21
Cid Fernandes, R., Heckman, T., Schmitt, H., González Delgado, R. M., & Storchi-Bergmann, T. 2001, ApJ, 558, 81
Ciotti, L. & Ostriker, J. P. 1997, ApJLett, 487, L105
Ciotti, L., Ostriker, J. P., & Proga, D. 2010, ApJ, 717, 708
Clark, B. G. 1980, A&A, 89, 377
Cole, S., Aragon-Salamanca, A., Frenk, C. S., Navarro, J. F., & Zepf, S. E. 1994, MNRAS, 271, 781
Combes, F., García-Burillo, S., Braine, J., et al. 2011, A&A, 528, A124
Conselice, C. J., Mortlock, A., Bluck, A. F. L., Grützbauch, R., & Duncan, K. 2013, MNRAS, 430, 1051
Coppin, K., Chapin, E. L., Mortier, A. M. J., et al. 2006, MNRAS, 372, 1621
Coppin, K., Halpern, M., Scott, D., Borys, C., & Chapman, S. 2005, MNRAS, 357, 1022
Costa, T., Sijacki, D., & Haehnelt, M. G. 2014, MNRAS, 444, 2355
Costa, T., Sijacki, D., & Haehnelt, M. G. 2015, MNRAS, 448, L30
Cowie, L. L., Barger, A. J., & Kneib, J.-P. 2002, AJ, 123, 2197
Cresci, G., Hicks, E. K. S., Genzel, R., et al. 2009, ApJ, 697, 115
Cresci, G., Mainieri, V., Brusa, M., et al. 2015, ApJ, 799, 82
Cresci, G., Mannucci, F., Maiolino, R., et al. 2010, Nature, 467, 811
Crockett, R. M., Shabala, S. S., Kaviraj, S., et al. 2012, MNRAS, 421, 1603
Croft, S., van Breugel, W., de Vries, W., et al. 2006, ApJ, 647, 1040
Croom, S., Boyle, B., Shanks, T., et al. 2004, in Astronomical Society of the Pacific Conference Series, Vol. 311, AGN Physics with the Sloan Digital Sky Survey, ed. G. T. Richards & P. B. Hall, 457
Croton, D. J. 2006, MNRAS, 369, 1808
Croton, D. J. 2009, MNRAS, 394, 1109
da Cunha, E., Walter, F., Decarli, R., et al. 2013, ApJ, 765, 9
Daddi, E., Alexander, D. M., Dickinson, M., et al. 2007, ApJ, 670, 173
Daddi, E., Elbaz, D., Walter, F., et al. 2010, ApJLett, 714, L118
Dayal, P., Ferrara, A., & Dunlop, J. S. 2013, MNRAS, 430, 2891
Dayal, P., Ferrara, A., Dunlop, J. S., & Pacucci, F. 2014, MNRAS, 445, 2545
De Breuck, C., Williams, R. J., Swinbank, M., et al. 2014, A&A, 565, A59
Decarli, R., Falomo, R., Treves, A., et al. 2010, MNRAS, 402, 2453
Dekel, A. & Birnboim, Y. 2006, Mon. Not. R. Astron. Soc., 368, 2
Dekel, A., Sari, R., & Ceverino, D. 2009, ApJ, 703, 785
Di Matteo, T., Springel, V., & Hernquist, L. 2005, Nature, 433, 604
Dole, H., Lagache, G., Puget, J.-L., et al. 2006, A&A, 451, 417
Downes, D. & Solomon, P. M. 1998, ApJ, 507, 615
Draine, B. T. 2006, ApJ, 636, 1114
Dressler, A. 1989, in IAU Symposium, Vol. 134, Active Galactic Nuclei, ed. D. E. Osterbrock & J. S. Miller, 217
Dutton, A. A., Conroy, C., van den Bosch, F. C., Prada, F., & More, S. 2010, MNRAS, 407, 2
Dwek, E., Staguhn, J. G., Arendt, R. G., et al. 2011, ApJ, 738, 36
Eales, S., Lilly, S., Gear, W., et al. 1999, ApJ, 515, 518
Eastman, J., Gaudi, B. S., & Agol, E. 2013, PASP, 125, 83
Elbaz, D., Dickinson, M., Hwang, H. S., et al. 2011, A&A, 533, A119
Elbaz, D., Jahnke, K., Pantin, E., Le Borgne, D., & Letawe, G. 2009, A&A, 507, 1359
Engel, H., Tacconi, L. J., Davies, R. I., et al. 2010, ApJ, 724, 233
Epinat, B., Contini, T., Le Fèvre, O., et al. 2009, A&A, 504, 789
Faber, S. M., Willmer, C. N. A., Wolf, C., et al. 2007, ApJ, 665, 265
Fabian, A. C. 1999, MNRAS, 308, L39
Fabian, A. C. 2002, in Astronomical Society of the Pacific Conference Series, Vol. 258, Issues in Unification of Active Galactic Nuclei, ed. R. Maiolino, A. Marconi, & N. Nagar, 185
Fabian, A. C. 2012, ARA&A, 50, 455
Fabian, A. C. & Canizares, C. R. 1988, Nature, 333, 829
Fabian, A. C., Celotti, A., & Erlund, M. C. 2006, MNRAS, 373, L16
Fabian, A. C., Vasudevan, R. V., & Gandhi, P. 2008, MNRAS, 385, L43
Fanaroff, B. L. & Riley, J. M. 1974, MNRAS, 167, 31P

Fanidakis, N., Baugh, C. M., Benson, A. J., et al. 2011, MNRAS, 410, 53
Fardal, M. A., Katz, N., Weinberg, D. H., & Davé, R. 2007, MNRAS, 379, 985
Faucher-Giguère, C.-A. & Quataert, E. 2012, MNRAS, 425, 605
Ferland, G. J., Porter, R. L., van Hoof, P. A. M., et al. 2013, RMxAA, 49, 137
Ferrarese, L. & Ford, H. 2005, Space Sci. Rev., 116, 523
Ferrarese, L. & Merritt, D. 2000, ApJLett, 539, L9
Feruglio, C., Bongiorno, A., Fiore, F., et al. 2014, A&A, 565, A91
Feruglio, C., Fiore, F., Carniani, S., et al. 2015, ArXiv e-prints
Feruglio, C., Fiore, F., Piconcelli, E., et al. 2013, A&A, 558, A87
Feruglio, C., Maiolino, R., Piconcelli, E., et al. 2010, A&A, 518, L155
Fixsen, D. J., Dwek, E., Mather, J. C., Bennett, C. L., & Shafer, R. A. 1998, ApJ, 508, 123
Förster Schreiber, N. M., Genzel, R., Bouché, N., et al. 2009, ApJ, 706, 1364
Fujimoto, S., Ouchi, M., Ono, Y., et al. 2015, ArXiv e-prints
García-Burillo, S., Combes, F., Usero, A., et al. 2014, A&A, 567, A125
Geach, J. E., Hickox, R. C., Diamond-Stanic, A. M., et al. 2014, Nature, 516, 68
Gebhardt, K., Bender, R., Bower, G., et al. 2000, ApJLett, 539, L13
Gehrels, N. 1986, ApJ, 303, 336
Genel, S., Genzel, R., Bouché, N., et al. 2008, ApJ, 688, 789
Genzel, R., Burkert, A., Bouché, N., et al. 2008, ApJ, 687, 59
Genzel, R. & Cesarsky, C. J. 2000, ARA&A, 38, 761
Genzel, R., Tacconi, L. J., Gracia-Carpio, J., et al. 2010, MNRAS, 407, 2091
Giavalisco, M. 2002, ARA&A, 40, 579
Gnerucci, A., Marconi, A., Cresci, G., et al. 2011a, A&A, 528, A88
Gnerucci, A., Marconi, A., Cresci, G., et al. 2011b, A&A, 528, A88
Gonçalves, T. S., Martin, D. C., Menéndez-Delmestre, K., Wyder, T. K., & Koekemoer, A. 2012, ApJ, 759, 67
González, V., Labbé, I., Bouwens, R. J., et al. 2010, ApJ, 713, 115
Graham, A. W. 2007, MNRAS, 379, 711
Graham, A. W. 2008, ApJ, 680, 143
Graham, A. W. & Scott, N. 2013, ApJ, 764, 151
Granato, G. L., De Zotti, G., Silva, L., Bressan, A., & Danese, L. 2004, ApJ, 600, 580
Greene, J. E., Zakamska, N. L., Ho, L. C., & Barth, A. J. 2011, ApJ, 732, 9
Greene, J. E., Zakamska, N. L., & Smith, P. S. 2012, ApJ, 746, 86
Greve, T. R., Bertoldi, F., Smail, I., et al. 2005, MNRAS, 359, 1165
Greve, T. R., Vieira, J. D., Weiß, A., et al. 2012, ApJ, 756, 101
Groves, B. 2007, in Astronomical Society of the Pacific Conference Series, Vol. 373, The Central Engine of Active Galactic Nuclei, ed. L. C. Ho & J.-W. Wang, 511
Gültekin, K., Richstone, D. O., Gebhardt, K., et al. 2009, ApJ, 698, 198
Guyon, O., Sanders, D. B., & Stockton, A. 2006, ApJS, 166, 89
Haarsma, D. B., Partridge, R. B., Windhorst, R. A., & Richards, E. A. 2000, ApJ, 544, 641
Hainline, L. J., Blain, A. W., Smail, I., et al. 2011, ApJ, 740, 96
Häring, N. & Rix, H.-W. 2004, ApJLett, 604, L89
Harrison, C. M., Alexander, D. M., Mullaney, J. R., & Swinbank, A. M. 2014, ArXiv e-prints
Harrison, C. M., Alexander, D. M., Swinbank, A. M., et al. 2012, MNRAS, 426, 1073
Hatsukade, B., Ohta, K., Seko, A., Yabe, K., & Akiyama, M. 2013, ApJLett, 769, L27
Hayward, C. C., Narayanan, D., Kereš, D., et al. 2013, MNRAS, 428, 2529
Heckman, T. M. & Best, P. N. 2014, ARA&A, 52, 589
Hickox, R. C., Mullaney, J. R., Alexander, D. M., et al. 2014, ApJ, 782, 9
Ho, L. 1999, in Astrophysics and Space Science Library, Vol. 234, Observational Evidence for the Black Holes in the Universe, ed. S. K. Chakrabarti, 157
Ho, L. C. 2008, ARA&A, 46, 475
Hogg, D. W. & Turner, E. L. 1998, PASP, 110, 727
Holmberg, E. 1958, Meddelanden fran Lunds Astronomiska Observatorium Serie II, 136, 1
Hopkins, A. M., Irwin, M. J., & Connolly, A. J. 2001, ApJLett, 558, L31
Hopkins, P. F. 2006, Astrophys. J. Suppl. Ser., 163, 1
Hopkins, P. F., Bundy, K., Croton, D., et al. 2010, ApJ, 715, 202
Hopkins, P. F., Bundy, K., Hernquist, L., & Ellis, R. S. 2007, ApJ, 659, 976
Hopkins, P. F., Hernquist, L., Cox, T. J., & Kereš, D. 2008, ApJS, 175, 356
Hopkins, P. F., Kereš, D., Oñorbe, J., et al. 2014, MNRAS, 445, 581
Hopkins, P. F., Murray, N., & Thompson, T. A. 2009, MNRAS, 398, 303
Hopkins, P. F., Quataert, E., & Murray, N. 2012, Mon. Not. R. Astron. Soc., 421, 3522
Hopkins, P. F., Somerville, R. S., Hernquist, L., et al. 2006, ApJ, 652, 864
Hu, E. M., McMahon, R. G., & Egami, E. 1996, ApJLett, 459, L53
Hu, J. 2008, MNRAS, 386, 2242

Imanishi, M. 2002, ApJ, 569, 44
Imanishi, M., Ichikawa, K., Takeuchi, T., et al. 2011, PASJ, 63, 447
Imanishi, M. & Wada, K. 2004, ApJ, 617, 214
Inskip, K. J., Jahnke, K., Rix, H.-W., & van de Ven, G. 2011, ApJ, 739, 90
Iono, D., Yun, M. S., Elvis, M., et al. 2006, ApJLett, 645, L97
Ishibashi, W. & Fabian, A. C. 2012, MNRAS, 427, 2998
Ishibashi, W. & Fabian, A. C. 2015, MNRAS, 451, 4612
Iwasawa, K., Sanders, D. B., Teng, S. H., et al. 2011, A&A, 529, A106
Jahnke, K. & Macciò, A. V. 2011, ApJ, 734, 92
Johansson, D., Sigurdarson, H., & Horellou, C. 2011, A&A, 527, A117
Karim, A., Schinnerer, E., Martínez-Sansigre, A., et al. 2011, ApJ, 730, 61
Karim, A., Swinbank, A. M., Hodge, J. A., et al. 2013, MNRAS, 432, 2
Kaspi, S., Smith, P. S., Netzer, H., et al. 2000, ApJ, 533, 631
Kauffmann, G. & Haehnelt, M. 2000, MNRAS, 311, 576
Kauffmann, G., Heckman, T. M., Tremonti, C., et al. 2003a, MNRAS, 346, 1055
Kauffmann, G., Heckman, T. M., White, S. D. M., et al. 2003b, MNRAS, 341, 33
Kauffmann, G., White, S. D. M., & Guiderdoni, B. 1993, MNRAS, 264, 201
Kaviraj, S., Cohen, S., Windhorst, R. A., et al. 2013, MNRAS, 429, L40
Kawakatu, N. & Wada, K. 2008, ApJ, 681, 73
Kellermann, K. I., Sramek, R., Schmidt, M., Shaffer, D. B., & Green, R. 1989, AJ, 98, 1195
Kennicutt, R. C. & Evans, N. J. 2012, ARA&A, 50, 531
Kennicutt, Jr., R. C. 1998, ApJ, 498, 541
Keres, D., Katz, N., Weinberg, D. H., & Dave, R. 2005, Mon. Not. R. Astron. Soc., 363, 2
Kewley, L. J., Dopita, M. A., Sutherland, R. S., Heisler, C. A., & Trevena, J. 2001, ApJ, 556, 121
Kewley, L. J., Groves, B., Kauffmann, G., & Heckman, T. 2006, MNRAS, 372, 961
Kewley, L. J., Maier, C., Yabe, K., et al. 2013, ApJLett, 774, L10
King, A. 2003, ApJLett, 596, L27
King, A. 2005, ApJLett, 635, L121
King, A. & Pounds, K. 2015, ArXiv e-prints
King, A. R. 2010, MNRAS, 402, 1516
Klypin, A., Kravtsov, A. V., Valenzuela, O., & Prada, F. 1999, ApJ, 522, 82
Knudsen, K. K., van der Werf, P. P., & Kneib, J.-P. 2008, MNRAS, 384, 1611
Kormendy, J. 2001, in Astronomical Society of the Pacific Conference Series, Vol. 230, Galaxy Disks and Disk Galaxies, ed. J. G. Funes & E. M. Corsini, 247–256
Kormendy, J. & Bender, R. 2011, Nature, 469, 377
Kormendy, J. & Ho, L. C. 2013, ARA&A, 51, 511
Kormendy, J. & Richstone, D. 1992, ApJ, 393, 559
Kormendy, J. & Richstone, D. 1995, ARA&A, 33, 581
Kovács, A., Chapman, S. C., Dowell, C. D., et al. 2006, ApJ, 650, 592
Kroupa, P. 2001, MNRAS, 322, 231
Lagache, G., Abergel, A., Boulanger, F., Désert, F. X., & Puget, J.-L. 1999, A&A, 344, 322
Laird, E. S., Nandra, K., Pope, A., & Scott, D. 2010, MNRAS, 401, 2763
Lamastra, A., Menci, N., Maiolino, R., Fiore, F., & Merloni, A. 2010, MNRAS, 405, 29
Laor, A., Jannuzi, B. T., Green, R. F., & Boroson, T. A. 1997, ApJ, 489, 656
Lapi, A., Raimundo, S., Aversa, R., et al. 2014, ApJ, 782, 69
Larson, R. B., Tinsley, B. M., & Caldwell, C. N. 1980, ApJ, 237, 692
Lilly, S., Carollo, C. M., Pipino, A., Renzini, A., & Peng, Y. 2013, Astrophys. J., 772, 119
Lilly, S. J., Le Fevre, O., Hammer, F., & Crampton, D. 1996, ApJLett, 460, L1
Liu, G., Zakamska, N. L., Greene, J. E., Nesvadba, N. P. H., & Liu, X. 2013, MNRAS, 436, 2576
Luhman, M. L., Satyapal, S., Fischer, J., et al. 2003, ApJ, 594, 758
Luridiana, V., Morisset, C., & Shaw, R. A. 2015, A&A, 573, A42
MacGregor, M. A., Wilner, D. J., Rosenfeld, K. A., et al. 2013, ApJLett, 762, L21
Madau, P. & Dickinson, M. 2014, ARA&A, 52, 415
Madau, P., Ferguson, H. C., Dickinson, M. E., et al. 1996, MNRAS, 283, 1388
Magnelli, B., Lutz, D., Berta, S., et al. 2010, A&A, 518, L28
Magnelli, B., Lutz, D., Santini, P., et al. 2012, A&A, 539, A155
Maiolino, R., Carniani, S., Fontana, A., et al. 2015, MNRAS, 452, 54
Maiolino, R., Cox, P., Caselli, P., et al. 2005, A&A, 440, L51
Maiolino, R., Gallerani, S., Neri, R., et al. 2012, MNRAS, 425, L66
Maiolino, R., Nagao, T., Grazian, A., et al. 2008, A&A, 488, 463
Malhotra, S., Kaufman, M. J., Hollenbach, D., et al. 2001, ApJ, 561, 766
Mannucci, F., Cresci, G., Maiolino, R., Marconi, A., & Gnerucci, A. 2010, MNRAS, 408, 2115
Marconi, A. & Hunt, L. K. 2003, ApJLett, 589, L21

Marconi, A., Risaliti, G., Gilli, R., et al. 2004, MNRAS, 351, 169
Markwardt, C. B. 2009, in Astronomical Society of the Pacific Conference Series, Vol. 411, Astronomical Data Analysis Software and Systems XVIII, ed. D. A. Bohlender, D. Durand, & P. Dowler, 251
Martin, D. C., Wyder, T. K., Schiminovich, D., et al. 2007, ApJS, 173, 342
Marziani, P., Sulentic, J. W., Stirpe, G. M., Zamfir, S., & Calvani, M. 2009, A&A, 495, 83
McConnell, N. J. & Ma, C.-P. 2013, ApJ, 764, 184
McConnell, N. J., Ma, C.-P., Gebhardt, K., et al. 2011, Nature, 480, 215
McConnell, N. J., Ma, C.-P., Murphy, J. D., et al. 2012, ApJ, 756, 179
McLure, R. J. & Dunlop, J. S. 2001, MNRAS, 327, 199
McLure, R. J. & Jarvis, M. J. 2002, MNRAS, 337, 109
Meidt, S. E., Schinnerer, E., Knapen, J. H., et al. 2012, ApJ, 744, 17
Menci, N., Fiore, F., Puccetti, S., & Cavaliere, A. 2008, ApJ, 686, 219
Mendez, A. J., Coil, A. L., Lotz, J., et al. 2011, ApJ, 736, 110
Merloni, A., Bongiorno, A., Bolzonella, M., et al. 2010, ApJ, 708, 137
Merloni, A. & Heinz, S. 2008, MNRAS, 388, 1011
Merritt, D. & Ferrarese, L. 2001, MNRAS, 320, L30
Michałowski, M., Hjorth, J., & Watson, D. 2010, A&A, 514, A67
Mo, H. J., Mao, S., & White, S. D. M. 1998, MNRAS, 295, 319
Modigliani, A., Goldoni, P., Royer, F., et al. 2010, in Society of Photo-Optical Instrumentation Engineers (SPIE) Conference Series, Vol. 7737, Society of Photo-Optical Instrumentation Engineers (SPIE) Conference Series, 28
Mor, R., Netzer, H., Trakhtenbrot, B., Shemmer, O., & Lira, P. 2012, ApJLett, 749, L25
Moster, B. P., Somerville, R. S., Newman, J. A., & Rix, H.-W. 2011, ApJ, 731, 113
Mullaney, J. R., Daddi, E., Béthermin, M., et al. 2012, ApJLett, 753, L30
Murray, N., Quataert, E., & Thompson, T. A. 2005, ApJ, 618, 569
Mutch, S. J., Croton, D. J., & Poole, G. B. 2013, MNRAS, 435, 2445
Nagao, T., Maiolino, R., & Marconi, A. 2006, A&A, 447, 863
Narayan, R. & Quataert, E. 2005, Science, 307, 77
Narayan, R. & Yi, I. 1995, ApJ, 444, 231
Narayanan, D., Bothwell, M., & Davé, R. 2012, MNRAS, 426, 1178
Nayakshin, S. 2014, MNRAS, 437, 2404
Nayakshin, S. & Zubovas, K. 2012, MNRAS, 427, 372
Nesvadba, N. P. H., Polletta, M., Lehnert, M. D., et al. 2011, MNRAS, 415, 2359
Netzer, H. 2009, MNRAS, 399, 1907
Netzer, H. 2015, ArXiv e-prints
Netzer, H., Shemmer, O., Maiolino, R., et al. 2004, ApJ, 614, 558
Netzer, H. & Trakhtenbrot, B. 2014, MNRAS, 438, 672
Newberry, M. V., Boroson, T. A., & Kirshner, R. P. 1990, ApJ, 350, 585
Ohyama, Y., Taniguchi, Y., & Shioya, Y. 2004, AJ, 128, 2704
Omont, A., Petitjean, P., Guilloteau, S., et al. 1996, in IAU Symposium, Vol. 178, Molecules in Astrophysics: Probes & Processes, ed. E. F. van Dishoeck, 501
Ono, Y., Ouchi, M., Kurono, Y., & Momose, R. 2014, ApJ, 795, 5
Ono, Y., Ouchi, M., Mobasher, B., et al. 2012, ApJ, 744, 83
Ota, K., Walter, F., Ohta, K., et al. 2014, ApJ, 792, 34
Ouchi, M., Ellis, R., Ono, Y., et al. 2013, ApJ, 778, 102
Pannella, M., Gabasch, A., Goranova, Y., et al. 2009, ApJ, 701, 787
Papadopoulos, P. P., van der Werf, P., Xilouris, E., Isaak, K. G., & Gao, Y. 2012, ApJ, 751, 10
Pei, Y. C. 1995, ApJ, 438, 623
Peng, C. Y. 2007, ApJ, 671, 1098
Peng, C. Y., Impey, C. D., Rix, H.-W., et al. 2006, ApJ, 649, 616
Peng, Y. 2010, Astrophys. J., 721, 193
Peng, Y., Maiolino, R., & Cochrane, R. 2015, Nature, 521, 192
Perna, M., Brusa, M., Cresci, G., et al. 2015, A&A, 574, A82
Peterson, B. M. 2011, ArXiv e-prints
Petric, A. O., Armus, L., Howell, J., et al. 2011, ApJ, 730, 28
Planck Collaboration, Ade, P. A. R., Aghanim, N., et al. 2014, A&A, 571, A16
Poggianti, B. M., Smail, I., Dressler, A., et al. 1999, ApJ, 518, 576
Pounds, K. A., King, A. R., Page, K. L., & O'Brien, P. T. 2003a, MNRAS, 346, 1025
Pounds, K. A., Reeves, J. N., King, A. R., et al. 2003b, MNRAS, 345, 705
Puget, J.-L., Abergel, A., Bernard, J.-P., et al. 1996, A&A, 308, L5
Quataert, E. 2001, in Astronomical Society of the Pacific Conference Series, Vol. 224, Probing the Physics of Active Galactic Nuclei, ed. B. M. Peterson, R. W. Pogge, & R. S. Polidan, 71
Read, J. I. & Trentham, N. 2005, Royal Society of London Philosophical Transactions Series A, 363, 2693
Reeves, J. N., Sambruna, R. M., Braito, V., & Eracleous, M. 2009, ApJLett, 702, L187

Renzini, A. 2009, MNRAS, 398, L58
Richards, G. T., Strauss, M. A., Fan, X., et al. 2006, AJ, 131, 2766
Richstone, D., Ajhar, E. A., Bender, R., et al. 1998, Nature, 395, A14
Riechers, D. A., Walter, F., Carilli, C. L., Bertoldi, F., & Momjian, E. 2008, ApJLett, 686, L9
Riechers, D. A., Walter, F., Carilli, C. L., & Lewis, G. F. 2009, ApJ, 690, 463
Robaina, A. R., Bell, E. F., Skelton, R. E., et al. 2009, ApJ, 704, 324
Rodighiero, G., Cimatti, A., Gruppioni, C., et al. 2010, A&A, 518, L25
Rodighiero, G., Daddi, E., Baronchelli, I., et al. 2011, ApJLett, 739, L40
Rodriguez, J., Cadolle Bel, M., Tomsick, J. A., et al. 2007, ApJLett, 655, L97
Rodríguez-Ardila, A. & Viegas, S. M. 2003, MNRAS, 340, L33
Rodríguez Zaurín, J., Tadhunter, C. N., Rose, M., & Holt, J. 2013, MNRAS, 432, 138
Rodríguez Zaurín, J., Tadhunter, C. N., Rupke, D. S. N., et al. 2014, A&A, 571, A57
Rupke, D. S. N. & Veilleux, S. 2011, ApJLett, 729, L27
Rupke, D. S. N. & Veilleux, S. 2013, ApJLett, 775, L15
Salomé, P., Guélin, M., Downes, D., et al. 2012, A&A, 545, A57
Salomé, Q., Salomé, P., & Combes, F. 2015, A&A, 574, A34
Salpeter, E. E. 1955, ApJ, 121, 161
Sanders, D. B., Soifer, B. T., Elias, J. H., et al. 1988, ApJ, 325, 74
Sani, E., Marconi, A., Hunt, L. K., & Risaliti, G. 2011, MNRAS, 413, 1479
Sargsyan, L., Lebouteiller, V., Weedman, D., et al. 2012, ApJ, 755, 171
Schechter, P. 1976, ApJ, 203, 297
Schiminovich, D., Wyder, T. K., Martin, D. C., et al. 2007, ApJS, 173, 315
Schmidt, K. B., Treu, T., Trenti, M., et al. 2014, ApJ, 786, 57
Schmidt, S. J., Ménard, B., Scranton, R., et al. 2015, MNRAS, 446, 2696
Scott, K. S., Wilson, G. W., Aretxaga, I., et al. 2012, MNRAS, 423, 575
Scott, K. S., Yun, M. S., Wilson, G. W., et al. 2010, MNRAS, 405, 2260
Shankar, F., Crocce, M., Miralda-Escudé, J., Fosalba, P., & Weinberg, D. H. 2010, ApJ, 718, 231
Shankar, F., Weinberg, D. H., & Miralda-Escudé, J. 2009, ApJ, 690, 20
Shemmer, O., Netzer, H., Maiolino, R., et al. 2004, ApJ, 614, 547
Shen, Y. 2013, Bulletin of the Astronomical Society of India, 41, 61
Shibuya, T., Kashikawa, N., Ota, K., et al. 2012, ApJ, 752, 114
Shimizu, I., Yoshida, N., & Okamoto, T. 2012, MNRAS, 427, 2866
Sijacki, D., Springel, V., & Haehnelt, M. G. 2011, MNRAS, 414, 3656
Silk, J. & Norman, C. 2009, ApJ, 700, 262
Silk, J. & Rees, M. J. 1998, A&A, 331, L1
Silverman, J. D., Kovač, K., Knobel, C., et al. 2009, ApJ, 695, 171
Simpson, J. M., Swinbank, A. M., Smail, I., et al. 2014, ApJ, 788, 125
Springel, V., Di Matteo, T., & Hernquist, L. 2005, ApJLett, 620, L79
Springel, V. & Hernquist, L. 2003, MNRAS, 339, 312
Stasińska, G., Cid Fernandes, R., Mateus, A., Sodré, L., & Asari, N. V. 2006, MNRAS, 371, 972
Sturm, E., González-Alfonso, E., Veilleux, S., et al. 2011, ApJLett, 733, L16
Sun, A.-L., Greene, J. E., Zakamska, N. L., & Nesvadba, N. P. H. 2014, ApJ, 790, 160
Tacconi, L. J., Genzel, R., Neri, R., et al. 2010, Nature, 463, 781
Tacconi, L. J., Genzel, R., Smail, I., et al. 2008, ApJ, 680, 246
Tacconi, L. J., Neri, R., Chapman, S. C., et al. 2006, ApJ, 640, 228
Toft, S., Smolčić, V., Magnelli, B., et al. 2014, ApJ, 782, 68
Tombesi, F., Cappi, M., Reeves, J. N., et al. 2010a, A&A, 521, A57
Tombesi, F., Meléndez, M., Veilleux, S., et al. 2015, Nature, 519, 436
Tombesi, F., Sambruna, R. M., Reeves, J. N., et al. 2010b, ApJ, 719, 700
Tran, Q. D., Lutz, D., Genzel, R., et al. 2001, ApJ, 552, 527
Tremaine, S., Gebhardt, K., Bender, R., et al. 2002, ApJ, 574, 740
Trentham, N. & Hodgkin, S. 2002, MNRAS, 333, 423
Trentham, N., Sampson, L., & Banerji, M. 2005, MNRAS, 357, 783
Trentham, N. & Tully, R. B. 2002, MNRAS, 335, 712
Tsuzuki, Y., Kawara, K., Yoshii, Y., et al. 2006, ApJ, 650, 57
Urry, C. M. & Padovani, P. 1995, PASP, 107, 803
Urry, C. M., Scarpa, R., O'Dowd, M., et al. 2002, NewA. Rev., 46, 349
Valiante, R., Schneider, R., Salvadori, S., & Bianchi, S. 2011, MNRAS, 416, 1916
van Dokkum, P. G. 2001, PASP, 113, 1420
Vanzella, E., Pentericci, L., Fontana, A., et al. 2011, ApJLett, 730, L35
Veilleux, S., Meléndez, M., Sturm, E., et al. 2013, ApJ, 776, 27
Veilleux, S. & Osterbrock, D. E. 1987, in NASA Conference Publication, Vol. 2466, NASA Conference Publication, ed. C. J. Lonsdale Persson, 737–740

Venemans, B. P., McMahon, R. G., Walter, F., et al. 2012, ApJLett, 751, L25
Vernet, J., Dekker, H., D'Odorico, S., et al. 2011, A&A, 536, A105
Vestergaard, M. & Osmer, P. S. 2009, ApJ, 699, 800
Viero, M. P., Moncelsi, L., Quadri, R. F., et al. 2013, ApJ, 779, 32
Vika, M., Driver, S. P., Cameron, E., Kelvin, L., & Robotham, A. 2012, MNRAS, 419, 2264
Wagg, J., Wiklind, T., Carilli, C. L., et al. 2012, ApJLett, 752, L30
Wang, R., Wagg, J., Carilli, C. L., et al. 2013, ApJ, 773, 44
Weiß, A., De Breuck, C., Marrone, D. P., et al. 2013, ApJ, 767, 88
Weiß, A., Kovács, A., Coppin, K., et al. 2009, ApJ, 707, 1201
Weller, J., Ostriker, J. P., Bode, P., & Shaw, L. 2005, MNRAS, 364, 823
Whitaker, K. E., van Dokkum, P. G., Brammer, G., & Franx, M. 2012, ApJLett, 754, L29
White, S. D. M. & Rees, M. J. 1978, MNRAS, 183, 341
Williams, R. J., Maiolino, R., Santini, P., et al. 2014, MNRAS, 443, 3780
Willott, C. J., Omont, A., & Bergeron, J. 2013, ApJ, 770, 13
Wyder, T. K., Martin, D. C., Schiminovich, D., et al. 2007, ApJS, 173, 293
Wyithe, J. S. B. 2006, MNRAS, 365, 1082
Yuan, W., Liu, B. F., Zhou, H., & Wang, T. G. 2010, ApJ, 723, 508
Yun, M. S., Scott, K. S., Guo, Y., et al. 2012, MNRAS, 420, 957
Zinn, P.-C., Middelberg, E., Norris, R. P., & Dettmar, R.-J. 2013, ApJ, 774, 66
Zubovas, K. & King, A. 2012, ApJLett, 745, L34
Zubovas, K. & King, A. R. 2014, MNRAS, 439, 400
Zubovas, K., Nayakshin, S., King, A., & Wilkinson, M. 2013, MNRAS, 433, 3079

Appendix

The assembly of "normal" galaxies at z~7 probed by ALMA

Maiolino, R.; Carniani, S; et al. 2015

We report new deep ALMA observations aimed at investigating the [CII] line and continuum emission in three spectroscopically confirmed Lyman Break Galaxies at 6.8< z <7.1, i.e. well within the re-ionization epoch. With Star Formation Rates of SFR ~ 5 - 15 $M_{\odot}$/yr these systems are much more representative of the high-z galaxy population than other systems targeted in the past by millimetre observations. For the galaxy with the deepest observation we detect [CII] emission at redshift z=7.107, fully consistent with the Lyα redshift, but spatially offset by 0.7″ (4 kpc) from the optical emission. At the location of the optical emission, tracing both the Lyα line and the far-UV continuum, no [CII] emission is detected in any of the three galaxies, with 3σ upper limits significantly lower than the [CII] emission observed in lower redshift galaxies. These results suggest that molecular clouds in the central parts of primordial galaxies are rapidly disrupted by stellar feedback. As a result, [CII] emission mostly arises from more external accreting/satellite clumps of neutral gas. These findings are in agreement with recent models of galaxy formation. Thermal far-infrared continuum is not detected in any of the three galaxies. However, the upper limits on the infrared-to-UV emission ratio do not exceed those derived in metal- and dust-poor galaxies.

The MAGNUM survey: Positive feedback in the nuclear region of NGC 5643 suggested by MUSE

Cresci, G.; Marconi, A.; Zibetti, S.; Risaliti, G.; Carniani, S.; et al. 2015

We study the ionisation and kinematics of the ionised gas in the nuclear region of the barred Seyfert 2 galaxy NGC 5643 using MUSE integral field observations in the framework of the MAGNUM (Measuring Active Galactic Nuclei Under MUSE Microscope) survey. The data were used to identify regions with different ionisation conditions and to map the gas density and the dust extinction. We find evidence for a double sided ionisation cone, possibly collimated by a dusty structure surrounding the nucleus. At the centre of the ionisation cone, outflowing ionised gas is revealed as a blueshifted, asymmetric wing of the [OIII] emission line, up to projected velocity v10 ~-450 km/s. The outflow is also seen as a diffuse, low luminosity radio and X-ray jet, with similar extension. The outflowing material points in the direction of two clumps characterised by prominent line emission with spectra typical of HII regions, located at the edge of the dust lane of the bar. We propose that the star formation in the clumps is due to 'positive feedback' induced by gas compression by the nuclear outflow, providing the first candidate for outflow induced star formation in a Seyfert-like radio quiet AGN. This suggests that positive feedback may be a relevant mechanism in shaping the black hole-host galaxy coevolution.

Is there any evidence that ionised outflows quench star formation in type 1 quasars at $z < 1$?

Balmaverde, B.; Marconi, A.; Brusa, M.; Carniani, S.; et al. 2015

Aims. The aim of this paper is to test the basic model of negative AGN feedback. According to this model, once the central black hole accretes at the Eddington limit and reaches a certain critical mass, AGN driven outflows blow out gas, suppressing star formation in the host galaxy and self-regulating black hole growth. Methods. We consider a sample of 224 quasars selected from the Sloan Digital Sky Survey (SDSS) at $z < 1$ observed in the infrared band by the Herschel Space Observatory in point source photometry mode. We evaluate the star formation rate in relation to several outflow signatures traced by the [OIII]λ5006 4959,5007 and [OII]λ3726,3729 emission lines in about half of the sample with high quality spectra. Results. Most of the quasars show asymmetric and broad wings in [OIII]λ5006 which we interpret as outflow signatures. We separate the quasars in two groups, "weakly" and "strongly" outflowing, using three different criteria. When we compare the mean star formation rate in five redshift bins in the two groups, we find that the SFRs are comparable or slightly larger in the strongly outflowing quasars. We estimate the stellar mass from SED fitting and the quasars are distributed along the star formation main sequence, although with a large scatter. The scatter from this relation is uncorrelated with respect to the kinematic properties of the outflow. Moreover, for quasars dominated in the infrared by starburst or by AGN emission, we do not find any correlation between the star formation rate and the velocity of the outflow, a trend previously reported in the literature for pure starburst galaxies. Conclusions. We conclude that the basic AGN negative feedback scenario seems not to agree with our results. Although we use a large sample of quasars, we did not find any evidence that the star formation rate is suppressed in the presence of AGN driven outflows on large scale. A possibility is that feedback is effective over much longer timescales than those of single episodes of quasar activity.

The multi-phase winds of Markarian 231: from the hot, nuclear, ultra-fast wind to the galaxy-scale, molecular outflow

Feruglio, C.; Fiore, F.; Carniani, S; et al. 2015

We present the best sensitivity and angular resolution maps of the molecular disk and outflow of Mrk 231, as traced by CO observations obtained with IRAM/PdBI, and we analyze archival Chandra and NuSTAR observations. We constrain the physical properties of both the molecular disk and outflow, the presence of a highly-ionized ultra-fast nuclear wind, and their connection. The molecular outflow has a size of 1 kpc, and extends in all directions around the nucleus, being more prominent along the south-west to north-east direction, suggesting a wide-angle biconical geometry. The maximum projected velocity of the outflow is nearly constant out to 1 kpc, thus implying that the density of the outflowing material decreases from the nucleus outwards as r^{-2}. This suggests that either a large part of the gas leaves the flow during its expansion or that the bulk of the outflow has not yet reached out to 1 kpc, thus implying a limit on its age of 1 Myr. We find $\dot{M}_{OF} = [500 - 1000]\ M_{\odot}\ yr^{-1}$ and $\dot{E}_{kin,OF} = [7 - 10] \times 10^{43}$ erg s^{-1}. Remarkably, our analysis of the X-ray data reveals a nuclear ultra-fast outflow (UFO) with velocity -20000 km s^{-1}, $\dot{M}_{UFO} = [0.3 - 2.1]\ M_{\odot} yr^{-1}$, and momentum load $\dot{P}_{UFO}/\dot{P}_{rad} = [0.2 - 1.6]$.We find $\dot{E}_{kin,UFO} \sim \dot{E}_{kin,OF}$ as predicted for outflows undergoing an energy conserving expansion. This suggests that most of the UFO kinetic energy is transferred to mechanical energy of the kpc-scale outflow, strongly supporting that the energy released during accretion of matter onto super-massive black holes is the ultimate driver of giant massive outflows. We estimate a momentum boost $\dot{P}_{OF}/\dot{P}_{UFO} \approx [30 - 60]$. The ratios $\dot{E}_{kin,UFO}/L_{bol,AGN} = [1 - 5]\%$ and $\dot{E}_{kin,OF}/L_{bol,AGN} = [1 - 3]\%$ agree with the requirements of the most popular models of AGN feedback.

Acknowledgments

I wish to thank my supervisor Professor Alessandro Marconi for his guidance, encouragement, and patience over these three years. His support was fundamental to my PhD thesis. Thanks to the people at Arcetri observatory who were interested in this work: Fillippo Mannucci, Giovanni Cresci, Anna Gallazzi, Stefano Zibetti, Guido Risaliti, and Beta Lusso.

Thanks to the my coffe-break group of Arcetri, who accompanied me all these years: Barbara, Susanna, Sara, Mirko, Antonio, Claudia, Eleonora, Greta, Teresa, and Giacomo.

I would like to thank Roberto Maiolino for guide me through the mystery of the high-z Universe and for giving me the opportunity to join in group at the Institute of Astronomy in Cambridge during my PhD. I wish also to thank all the people that I met over there: Francesco B., Claudia, Sara, Rebecca, Matt, Matthew, Bethan, Ciro, Marina, Alberto, and Yingjie.

Last but not least, thanks to my family who always believed in me and supported me along my scientific way.